2020

Microbeam Radiation Therapy: Development of Instrumentation and Software Tools for Quality Assurance

Matthew John Cameron
University of Wollongong

UNIVERSITY
OF WOLLONGONG
AUSTRALIA

Microbeam Radiation Therapy: Development of Instrumentation and Software Tools for Quality Assurance

Matthew John Cameron

Supervisors:
Michael L. F. Lerch, Susanna Guatelli, Jeremy A. Davis

This thesis is presented as part of the requirement for the conferral of the degree:
Doctor of Philosophy

This research has been conducted with the support of the Australian Government Research Training Program Scholarship

Centre for Medical Radiation Physics, School of Physics,

University of Wollongong

April 2020

Abstract

Despite constant advancements in the treatment of cancer using chemotherapy, radiotherapy, and surgical intervention, the rate of survival for patients with head-and-neck cancers has remained steady at 30% for almost 30 years in Australia. Microbeam Radiation Therapy (MRT) is a preclinical radiotherapy modality that shows promise in improving positive treatment outcome rates for such patients.

MRT takes advantage of the specialised properties of synchrotron radiation generated from an insertion device, namely the high intensity and small divergence of the resulting photon beam. This allows the incident photon beam (a.k.a the broadbeam) to be collimated to produce an array of micrometre-width, spatially fractionated, high dose rate microbeams. The resulting shape of the lateral dose profile is that of high dose rate 'peaks' separated by low dose rate 'valleys'. Typical widths and pitch of the microbeams are 25–50 μm and 200–400 μm, respectively.

By taking advantage of the Dose-Volume Effect, where the tolerance of normal tissue to radiation damage increases dramatically as the radiation field size decreases, much higher treatment doses may be delivered than possible with conventional radiotherapy techniques. The low divergence of synchrotron radiation allows the microbeam array to maintain its structure even at depth in a patient, which leads to greater preferential damage to tumours and less normal tissue damage, thus leading to better positive treatment outcomes. Combined with the small field sizes of MRT compared to conventional radiotherapy techniques, MRT is well suited to treatment of small, radioresistant cancers that are in close proximity to sensitive normal tissue, such as brain gliomas. However, the small field sizes and high dose rates (hundreds to thousands of Gy/s) pose a challenge for dosimetry and treatment due to the increased risks and severity of consequence of errors in dose delivery.

In order to progress to clinical trials in humans, rigorous quality assurance (QA) is necessary, both in the field of experimental dosimetry and in simulations for treatment planning.

This thesis addresses the simulation requirement with G4IMBL, a Geant4 Monte Carlo model of the Australian Synchrotron Imaging and Medical Beamline (AS IMBL), which was developed to investigate the potential of Geant4 to simulate synchrotron radiation-based radiotherapy and provide theoretical treatment dose profiles for treatment planning and verification. G4IMBL's geometry, physics models, and two-stage execution philosophy are discussed. G4IMBL results are compared against third-party program (SPEC) theoretical energy spectra, and experimental dosimetry using

ionisation chambers and radiographic film. Discrepancies were found between the photon flux predicted by G4IMBL and SPEC, the cause of which was identified as low-energy overresponse of the Geant4 synchrotron radiation physics model. Normalisation of the energy spectra produced excellent agreement between G4IMBL and SPEC results. Normalised Depth Dose Profiles were compared against experimental results and good agreement was achieved in the broadbeam case and microbeam peak. Further investigation is required to compare valley dose profiles and for different beamline configurations.

The dosimetry requirement is addressed through the introduction of a novel n-type silicon-on-oxide single strip detector (SSD), the 3D-Mesa SSD, as a prospective candidate for MRT QA dosimetry. The defining feature of the 3D-Mesa SSD is the use of plasma etching to remove excess silicon surrounding the sensitive volume (SV) to produce a 3D freestanding structure above the silicon-oxide insulating layer. The resulting SV is 10 μm thick; either 22.5- or 36-μm wide; and 50-, 100-, or 250-μm long, depending on the sample design. Multiple samples underwent electrical characterisation and an Ion Beam Induced Charge study. Results indicate optimal bias of 2-3 V due to a parasitic MOS structure wanted charge collection above 3 V, which will be addressed in the next-generation of 3D-Mesa SSD.

3D-Mesa SSDs were exposed at the AS IMBL for a variety of different beam configurations to evaluate the performance of the device in broadbeam and microbeam cases. Results were promising, showing the 3D-Mesa SSD meets the requirements for MRT QA: possessing good radiation-hardness, large dynamic range, micrometre-scale spatial resolution, and real-time readout. Good agreement was found between 3D-Mesa SSD, radiographic film, and ion chamber normalised depth dose profiles for a variety of beamline configurations, speeds, and field sizes. Further investigation is required to determine energy dependence of the device, and more comparisons are required against competing MRT dosimeter candidates (e.g. epitaxial silicon SSDs, PTW microDiamond detector).

With further development, G4IMBL and the 3D-Mesa SSD should serve as excellent candidates for MRT QA in future human trials.

Keywords: Microbeam Radiation Therapy, Synchrotron Radiation, Dosimetry, Monte Carlo

Acknowledgments

I would like to thank AIIM and the Accelerator Operations Team, Institute of Environmental Research (IER), ANSTO, for use of their facilities and their assistance in the characterisation of the 3D-MESA SSD.

I would also like to thank UNSW ANFF and Monash University's MASSIVE cluster for their collaboration, allowing access to Synopsis TCAD.

I acknowledge the support of the NH&MRC (grant APP1093256) and AINSE (grant RPP10102).

Special thanks to the staff of the Australian Synchrotron Imaging and Medical Beamline, in particular Andrew Stevenson, for their support during synchrotron experiments and in benchmarking of the Geant4 Monte Carlo model of the beamline.

Special thanks also to my ANSTO contacts Dale Prokopovich and Rainer Seigele for their assistance in preparation and performance of IBIC measurements at ANSTO.

Thanks to Monash University and the National Computing Infrastructure Australia for the use of their supercomputing clusters, M2-MASSIVE and RAIJIN, respectively.

Thanks to Dr. Iwan Cornelius, without whom neither the Geant4 model of the IMBL nor the predecessor model of ESRF ID17 would exist.

Thanks to my colleagues: Andrew Dipuglia, Jason Paino, James Archer, and Matt Crowther, for their company during the long night shifts during experiments, for sharing the load during data acquisition and analysis, and for finding G4IMBL useful enough to use in your own research.

My deepest gratitude to my supervisors: Jeremy Davis, Susanna Guatelli, Michael Lerch, Anatoly Rosenfeld, and all of the staff of CMRP for their time, expertise, and enthusiasm.

Finally, my love to my entire family for all of their support over the years.

In memory of my mother, Jackie Cameron.

Certification

I, Matthew John Cameron, declare that this thesis submitted in fulfilment of the requirements for the conferral of the degree Doctorate of Philosophy in Physics, from the University of Wollongong, is wholly my own work unless otherwise referenced or acknowledged. This document has not been submitted for qualifications at any other academic institution.

_____

Matthew John Cameron
31st August 2019

List of Abbreviations

3DCRT — 3D Conformal Radiotherapy

AIIM — Australian Institute of Innovative Materials

ANSTO — Australian Nuclear Science and Technology Organisation

AS IMBL — Australian Synchrotron Imaging and Medical Beamline

BDA — Beam-Defining Aperture

BB — Broadbeam

C–V — Capacitance-Voltage

CMRP — Centre for Medical and Radiation Physics

CT — Computed Tomography

I–V — Current-Voltage

DIL — Dual in-line

DCAT — Dynamic Conformal Arc Therapy

ESRF — European Synchrotron Radiation Facility

EBRT — External Beam Radiation Therapy

FWHM — Full-Width at Half-Maximum

FWTM — Full-Width at Tenth-Maximum

GEANT4 — GEometry ANd Tracking Toolkit 4

HDR — High Dose-Rate Brachytherapy

IBIC — Ion Beam Induced Charge

IGRT — Image-Guided Radiotherapy

IMRT — Intensity-Modulated Radiotherapy

IC — Ionisation Chamber

KERMA – Kinetic Energy Released per unit MAss

LDR — Low Dose-Rate Brachytherapy

MOS — Metal-Oxide-Silicon

MB — Microbeam

MRT — Microbeam Radiation Therapy

MLC — Multi-leaf Collimators

MSC — Multi-slit Collimator

PVDR — Peak-to-Valley Dose Ratio

PDD — Percentage Depth-Dose profiles

SV — Sensitive Volume

SNR — Signal-to-Noise Ratio

SOI — Silicon on Insulator

SSD — Silicon Single-Strip Detector

SRS — Stereotactic Radiosurgery

SRT — Stereotactic Radiotherapy

TCAD — Sentaurus Technology Computer Aided Design

UOW — University of Wollongong

VMAT — Volumetric Modulated Arc Therapy

Table of Contents

Contents

List of Figures

List of Tables

List of Publications

First author publications:

1. M. J. Cameron, I. Cornelius, D. Cutajar, J. A. Davis, A. B. Rosenfeld, M. L. F. Lerch, S. Guatelli, "Comparison of Phantom Materials for Use in Quality Assurance of Microbeam Radiation Therapy," J. Synch. Rad. 24(4):866–76, 2017.
2. M. J. Cameron, J. A. Davis, A. Dipuglia, L. Chartier, L. T. Tran, D. A. Prokopovich, M. Petasecca, V. L. Perevertaylo, A. B. Rosenfeld, M. L. F. Lerch. 2019. "Characterisation of 3D-Mesa SSD Silicon Single Strip Detectors for Use in Synchrotron Microbeam Radiation Therapy." IEEE Transactions on Radiation and Plasma Medical Sciences, (early access), 2019.
3. Dipuglia, M. J. Cameron, J. A. Davis, I. M. Cornelius, A. W. Stevenson, A. B. Rosenfeld, M. Petasecca, S. Corde, S. Guatelli, M. L. F. Lerch. "Validation of a Monte Carlo Simulation for Microbeam Radiation Therapy on the Imaging and Medical Beamline at the Australian Synchrotron." Scientific Reports 9, 2019. (Coequal authorship)

List of Conferences

Oral presentations:

1. “Comparison of different phantoms materials for Quality Assurance of Microbeam Radiation Therapy: a Geant4 Monte Carlo study.” MedPhys 2013, Sydney (5 December).
2. "The comparison of different phantom materials for Quality Assurance of Microbeam Radiation Therapy - a Geant4 based study." CSM 2014, Melbourne (4-7 September).
3. "Characterization of a novel 3D silicon strip detector for Quality Assurance of Microbeam Radiation Therapy (MRT)", MMND-IPCT 2014, Port Douglas (20-25 October).
4. “Optimisation of synchrotron-based microbeam radiation therapy Geant4 Monte Carlo simulations”, Innovations in Radiation Applications 2017, Wollongong (20-22 April).
5. “Optimisation of synchrotron-based microbeam radiation therapy Geant4 Monte Carlo simulations”, Geant4 User Workshop 2017, Wollongong (19-22 September).
6. “Validation of Geant4 for Microbeam Radiation Therapy”, Geant4 Collaboration Meeting 2017, Wollongong (25-29 September).
7. “Validation of Geant4 for Microbeam Radiation Therapy”, 3rd Mathematical Modelling in Biology and Medicine Workshop, Wollongong, (24 November 2017).
8. “Dosimetry of Synchrotron Microbeam Radiation Therapy using a Novel 3D Silicon Strip Detector,” NSS MIC 2018, Sydney.

Poster presentations:

1. "Characterization of a novel 3D silicon strip detector for Quality Assurance of Microbeam Radiation Therapy (MRT)”, IEEE NSS MIC 2014, Seattle (8-15 November).
2. "Development of a novel detector system, X-Tream, for high spatial resolution Quality Assurance for Microbeam Radiation Therapy", Universities Australia Higher Education Conference 2015, Canberra (11-13 March).
3. “Characterisation of a novel 3D silicon strip detector for use in Quality Assurance in Microbeam Radiation Therapy (MRT)”, AOFSRR 2015 in conjunction with Australian Synchrotron Users Meeting 2015, Melbourne (25-27 November).
4. “Characterisation of a Novel 3D Silicon Strip Detector for Microbeam Radiation Therapy (MRT) Quality Assurance”, IEEE NSS MIC 2016, Strasbourg (29 October – 6 November).

5. “Characterisation of a Novel 3D Silicon Strip Detector for Microbeam Radiation Therapy (MRT) Quality Assurance”, EPSM 2016, Sydney (6-10 November).
6. "Application of a 3D MESA Silicon Strip Detector for use in MRT Dosimetry at the Australian Synchrotron" presented at Australian Synchrotron Users Meeting 2016, Melbourne (24-26 November).

Chapter 1

Introduction and Literature Review

1.1 Thesis Aim

The aim of this thesis is to introduce and benchmark a simulated model of the Australian Synchrotron Imaging and Medical Beamline, and to characterize and evaluate the performance of a novel silicon detector, for use in quality assurance of Microbeam Radiation Therapy.

1.2 Thesis Outline

Microbeam Radiation Therapy (MRT) is a highly promising preclinical radiation therapy modality that takes advantage of the unique properties of synchrotron radiation. Research and development of this radiotherapy technique has been progressing for many years at synchrotron light sources internationally and locally at the Australian Synchrotron. After a number of successful experiments using small mammals (i.e. rats), the focus is now on progressing to large animal trials (e.g. sheep, dogs) and eventually human trials. To this end, accurate quality assurance (QA) is required: both in the form of high spatial resolution, radiation-hard, real-time detectors with large dynamic range; and also theoretical models and simulations for use in treatment planning systems. This thesis seeks to address both QA requirements by introducing a Geant4 Monte Carlo model of the Australian Synchrotron Imaging and Medical Beamline, and a novel 3D-Mesa Silicon Single Strip detector as prospective candidates for MRT QA.

Chapter 1 of this thesis contains introductory remarks regarding the importance of radiation-based cancer treatment in Australia and a literature review broadly covering the physics of synchrotron Microbeam Radiation Therapy and properties of interest that distinguish it from other modalities of radiation therapy. Microbeam Radiation Therapy is introduced along with dosimeters of interest for dosimetry and quality assurance. Familiarity with the physics of radiation interactions with matter is assumed. Details regarding production of synchrotron radiation, semiconductor device manufacturing, and Monte Carlo physics simulations are touched upon briefly; but as these are well-understood topics with a wealth of available literature, any in-depth explanations are considered to be beyond the scope of this thesis.

of this thesis begins with an overview of the components of the Australian Synchrotron (AS) Imaging and Medical Beamline (IMBL) to provide necessary background information and

nomenclature relating to beamline configurations used in the rest of the thesis. The chapter then introduces the new Geant4-based model of the AS IMBL: G4IMBL. Geometry and radiation interaction and tracking models are discussed along with the two-stage simulation philosophy of this program and variance reduction techniques. Simulation results are provided and compared to theoretical and experimental results for benchmarking and validation, respectively. These results include:

- the examination of wiggler interactions using the synchrotron radiation production physics model,
- the optimisation of the steering angle of the electron beam for various configurations,
- the comparison of the energy spectrum of the wiggler to theoretical model both before and after filtration,
- the analysis of the change in a spectrum at depth in a phantom and the contribution of backscattered photons to the spectrum
- the comparison of broadbeam (BB) and microbeam (MB) relative depth-dose profiles against experimental results.

Chapter 3 of this thesis introduces the novel '3D-Mesa SSD' silicon single strip detector (SSD) as a potential quality assurance dosimeter for use in microbeam radiation therapy. Some device design specifics are provided, along with a full electrical characterization of the device using current-voltage (I–V) and capacitance-voltage (C–V) characteristics. Ion Beam Induced Charge (IBIC) test results are supplied and compared against theoretical electric field and depletion zone distribution simulated with Sentaurus Technology Computer Aided Design (TCAD).

Chapter 4 of this thesis covers the study of the 3D-Mesa SSD in uncollimated synchrotron radiation fields. The most common detectors used at IMBL are identified and the experimental setup for dosimetry with the 3D-Mesa SSD detector at the AS IMBL is explained. Sources of systemic uncertainty are identified and the calculation of statistical uncertainty is discussed. A series of studies are provided to analyse the performance of the 3D-Mesa SSD under a variety of conditions. These include: a response linearity study; a radiation hardness (detector lifetime) study; an energy dependence study; and a comparison of the response of different 3D-Mesa SSD SV designs to identical conditions. An extensive study of relative depth dose profiles has been conducted under a variety of beamline configurations. 3D-Mesa SSD measurements are compared against other

commercially available and clinically relevant dosimeters and the performance of the 3D-Mesa SSD is evaluated. All experimental relative depth dose profiles in this chapter are also compared to G4IMBL simulated results under identical beamline conditions.

Chapter 5 of this thesis covers the study of the 3D-Mesa SSD in collimated Microbeam fields. Considerations for microbeam dosimetry of the intrinsic microbeam radiation field and the microbeam radiation treatment field, and analysis of microbeam dosimetry results using the 3D-Mesa SSD detector under a variety of conditions. These results include: treatment field dosimetry and comparison to radiographic film, the effect of vertical alignment of the detector in an intrinsic microbeam field, the effect of depth on dosimetric parameters of interest, and comparison of intrinsic field response between different 3D-Mesa SSD detector designs. Most experimental results in this chapter are also compared to G4IMBL simulated results under identical beamline conditions. The thesis then concludes with evaluation and recommendations regarding the use of G4IMBL and the novel 3D-Mesa SSD Detector for quality assurance of microbeam radiation therapy.

1.3 Literature Review

1.3.1 Cancer and radiotherapy in Australia

Cancer is an unfortunate fact of life in modern Australia. The Australian Institute of Health and Welfare (AIHW) estimates that 394 new cases of cancer will be diagnosed and 167 people will die from cancer every day in 2019 [1]. As detection and treatment methods improve, the proportion of patients receiving positive treatment outcomes improves. The AIHW states: "between 1986–1990 and 2010–2014 the relative 5-year survival for all cancers increased from 51% to 69%," [1]. Despite the trend of rising survival across all cancers, the rate of survival for head-and-neck cancers has remained steady at 30% since 1990. Head-and-neck cancers account for 8% of all rare cancer diagnostics (<6 in 100,000) in men (the third most common rare cancer diagnosed) and 3% in women (the fifth most common rare cancer diagnosed). Treatment of these cancers must account for the delicate sensitive organs around the site of the tumour and some options (e.g. surgery) may be unfeasible. Radiotherapy presents an opportunity to improve patient treatment outcomes in conjunction with surgery and chemotherapy.

Barton, 2014, [2] states that 49% of all patients diagnosed with cancer in 2012 received radiotherapy treatment. In certain cases, radiotherapy outcomes may match or even exceed the success rate of surgery (e.g. the rate of favourable patient outcomes for treatment of prostate cancer using

radiotherapy is ~90%— equivalent to surgical treatment outcomes when the prostate is removed completely). Unfortunately, while radiotherapy has great potential for positive patient outcomes it also has the capacity to lead to harmful side effects. In Low Dose-Rate (LDR) brachytherapy, where encapsulated radioactive material ('seeds') are inserted into the cancer target volume directly, the omnidirectional emission of radiation from the seeds must be accounted for in adjacent non-target organs. Implanted LDR brachytherapy seeds generally remain permanently in the patient, which exposes themselves and the public to above average background radiation over the course of several half-lives. Additionally, swelling and motion of organs may shift seed positions from the planned sites, thus resulting in insufficient dose-delivery to the target and unsuccessful treatment outcomes. In High Dose-Rate brachytherapy, high-activity seeds are instead mechanically inserted and removed along temporary surgically implanted pathways in order to deliver treatment doses. This avoids the long-term excess dose of LDR brachytherapy due to implanted seeds, but swelling and motion of organs may shift the implanted pathways from their required positions. Additionally, the high activity of the radioactive seeds presents a potential risk if mechanical failure results in the seed remaining in the patient any longer than planned. HDR brachytherapy seeds also require frequent replacement as the source decays to insufficient dose-rates. Both forms of brachytherapy are dependent upon radioactive seeds; therefore, any problems in supply may affect or even prohibit treatment with this modality of radiotherapy.

External Beam Radiation Therapy (EBRT) as an alternative to brachytherapy provides its own advantages and limitations. Dose delivery through a medical linear accelerator (LINAC) is completely computer-controlled and is limited to when the machine is in operation, eliminating the risk of irradiating members of the public. Modern EBRT produces radiation through acceleration of electrons and the bremsstrahlung radiation that arises from the interaction of the electron beam with a high-Z target; thus, it requires no supply, storage, or disposal of radioactive material. Furthermore, it does not require surgery or lengthy hospital stays – treatment is performed in multiple fractions over 24-hour periods for approximately 30 days (i.e. approximately 30 fractions). Advanced EBRT systems are capable of delivering dose to complex target geometries through use of Intensity-Modulated Radiotherapy (IMRT) techniques, such as the use of time-dependent beam-intensity modulation and geometric beam shaping with dedicated sets of multileaf collimators (MLCs). IMRT relies on extensive pre-treatment planning and simulation in order to optimise the shape of each

complex 2D-field produced by the MLCs, and the dose rate and duration of treatment for each projection such that the convolution of doses of all projections conforms well to the target volume. The effectiveness of IMRT may be enhanced further via combination with 3D Conformal Radiotherapy (3DCRT), where dose is delivered from multiple different angles around the patient such that the dose delivered conforms to the target located at the converging point of the treatment fields. This serves to lower the dose delivered to non-target volume without compromising on the dose delivered to the target volume. Many other forms of EBRT exist that extend upon 3DCRT and IMRT techniques to address specific challenges for patient treatment, but rigorous discussion and explanation of these methods is beyond the scope of this thesis. These advanced EBRT techniques include, but are not limited to, such methods as:

- Volume Modulated Arc Therapy (VMAT), where IMRT techniques are used as the LINAC gantry rotates continuously (as opposed to discrete angular positioning in 3DCRT);
- Image-Guided Radiotherapy (IGRT), where X-ray images are taken before, during, and after treatment to verify accurate patient positioning;
- Dynamic Conformal Arc Therapy (DCAT), where the gantry MLCs dynamically shape the radiation field during rotation to match the shape of the target volume as the gantry rotates about the patient.
- Stereotactic Radiotherapy (SRT) and Stereotactic Radiosurgery (SRS), where higher doses are delivered to small target volumes in fewer fractions than standard EBRT (e.g. 5 fractions and 1 fraction for SRT and SRS respectively)
- Time-Gated Radiotherapy, where the treatment beam is turned on and off to match patient breathing and cardiosynchronous motion in order to reduce the effect of organ motion

When assessing the benefits and the risks of the use of conventional EBRT treatment for the patient, a major consideration is the fact that dose is delivered along the entire path of the MeV-energy photons through the patient, not just in the target volume. Due to the nature of photon interactions with matter, photons exhibit a depth-dose profile with a short build-up region of dose delivery as the field reaches charged-particle equilibrium, which first occurs near the point of maximum dose delivery (D_{max}), then a roll-off of dose delivery with increasing depth (Figure 1.1). This results in larger doses being delivered to shallower organs in the path to the target when compared with the

intended target dose, and excess dose deposited deeper than the target as well. The unwanted and unavoidable dose delivery to tissue deeper and shallower than the target was a significant impetus that led to the development of some of the advanced EBRT modalities mentioned above (3DCRT, VAMT, and DCAT) to achieve the goal of reducing the unwanted extra dose delivery in the path of the beam, without compromising the dose delivery to the target.

These considerations show the need for good quality assurance and powerful treatment planning systems to support the efforts of radiation oncologists, radiation therapists, and medical physicists in the careful planning of dose delivery to target volumes whilst sparing normal tissue.

Other advanced radiation therapy modalities exist, such as proton radiotherapy and heavy ion radiotherapy (collectively known as, ion radiotherapy), and neutron therapy. These exploit the physical and radiobiological properties of other types of radiation and may potentially reduce the dose to surrounding organs and tissues while delivering a therapeutic dose to the cancer target. Ion radiotherapy is the subject of much interest due to the fact that the majority of dose delivered by an ion is near the end of a given range (differing by material of interaction and the energy and type of ion) in a dosimetric structure known as the Bragg peak (Figure 1.1).

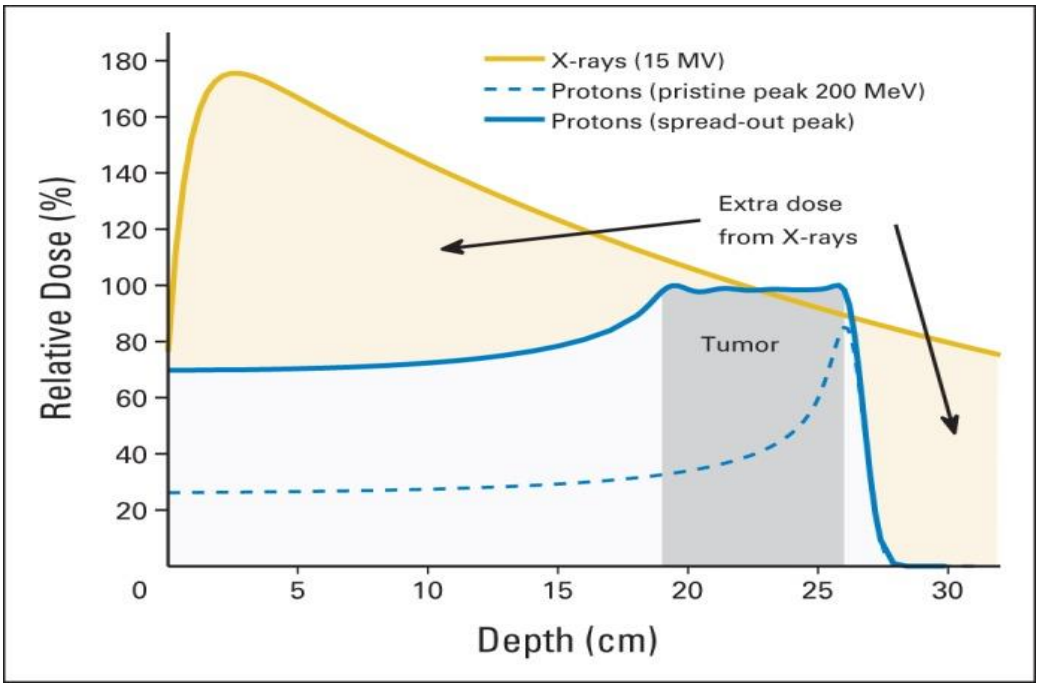

Figure 1.1: Normalised relative depth-dose profiles for EBRT and ion therapy, (Mitin and Zietman, 2014) [3].
EBT3 build-up region and unwanted overdose region shallow to the target depth, and characteristic ion therapy Bragg Peak are shown.

The combination of the relatively lower entrance dose (compared to photon dose profiles), the Bragg

peak structure at depth, and the sharp cut-off of dose delivery deeper than the Bragg peak, makes ion therapy well-suited for addressing the needs of radiotherapy. By adjusting the energy of the ion beam the Bragg peak may be 'scanned' across multiple depths and thus deliver dose to the entire target volume, whilst minimising excess dose deeper and shallower than the target.

Unfortunately, ion radiotherapy and neutron radiotherapy require the use of dedicated facilities — none of which currently exist in Australia. Therefore, ion radiotherapy and neutron radiotherapy do not yet exist as clinical options within Australia.

However, with the construction of the Australian Synchrotron in Clayton, Victoria, synchrotron radiation has become a possible avenue of investigation for the purposes of improved radiotherapy. Since achieving first light in June 2006 and commencing normal operation in 2007, the Australian Synchrotron has been undertaking research and development with the goal of utilising synchrotron radiation for clinical treatment of humans.

1.3.2 Synchrotron radiation

The properties of synchrotron radiation are well-understood and detailed examinations are available in a number of textbooks [4]–[6]. Fundamentally, synchrotron radiation is produced by any charge accelerating in a magnetic field at relativistic speeds. In the classical paradigm, electromagnetic radiation is produced equally in the direction of motion and opposite the direction of motion. At relativistic speeds, the observer effect prompts emission of electromagnetic radiation in a narrow cone (with a solid angle of approximately $\frac{2}{\gamma}$ where γ is the Lorentz factor) in the direction of motion.

In the simplest case, an electron is accelerated through a constant magnetic field (such as found in a bending magnet) at relativistic speed. The radius of curvature arises as:

$$\rho = \frac{p}{eB} = \frac{m\gamma_0\beta c}{eB} \qquad (1.1)$$

where ρ is the radius of curvature, p is the particle momentum, e is the particle charge, B is the magnetic flux strength in Tesla, m the rest mass of the particle, γ_0 and β the Lorentz factors, and c the speed of light in a vacuum.

From this Synchrotron radiation is produced according to:

$$\frac{d^2\check{S}_B(\omega)}{d\theta d\psi} = \frac{3\alpha}{4\pi^2}\gamma^2\frac{\Delta\omega}{\omega}\frac{I}{e}\,y^2(1+X^2)^2 \times \left[K_{2/3}^2(\xi) + \frac{X^2}{1+X^2}\,K_{1/3}^2(\xi)\right] \qquad (1.2)$$

where $\check{S}_B$ is the photon flux; θ and ψ are the horizontal and vertical observation angles respectively;

α is the fine-structure constant; $\gamma = \frac{E}{m_e c^2}$ is the ratio of the total electron energy E and the rest energy of the electron; ω is the angular frequency of photons; I is the beam current; $y = \frac{\omega}{\omega_c}$ which is the ratio of the angular frequency (ω) of the produced photon to the critical angular frequency (ω_c) of the spectrum $\left(\omega_c = \frac{3\gamma^3 c}{2\rho}\right)$, which divides the emitted power of the spectrum into equal halves; $X = \gamma\psi$; $\xi = \frac{y(1+X^2)^{\frac{3}{2}}}{2}$; and $K_{\frac{1}{2}}$ and $K_{\frac{2}{3}}$ are modified Bessel functions of the second kind (Weber functions). More detailed information may be found in the X-ray data booklet [6] and Classical Electrodynamics by J. D. Jackson [4].

Bending magnets by nature produce a broad spectrum that sweeps across a large area akin to a lighthouse spotlight passing. To improve upon the brightness and divergence of bending magnet, synchrotron radiation physicists utilise insertion devices. Insertion devices are, in simplest form, arrays of bending magnets that produce a sinusoidal magnetic field structure that 'wiggles' the charged particle beam back and forth. Depending on the strength and placement of each magnetic pole, one can tune the resulting spectrum according to the radius of curvature of the particle. If the insertion device is designed for broad-spectrum generation using incoherent interference, it is named a 'wiggler'. If the insertion device instead utilises coherent destructive interference to produce near-monochromatic synchrotron radiation it is referred to as an 'undulator'.

The most important properties of synchrotron radiation with respect to the potential for the treatment of cancer are high brightness and low divergence. To this end, wigglers are chosen as insertion device to produce synchrotron radiation for cancer treatment. Synchrotron institutions around the world are progressing towards clinical trials but the most pertinent to this thesis are the European Synchrotron Radiation Facility's ID17 Biomedical beamline (ESRF ID17, Grenoble, France) and the Australian Synchrotron Imaging and Medical beamline (AS IMBL, Clayton, Australia). Investigations are well underway to develop synchrotron-based radiotherapy — a leading candidate for which is Microbeam Radiation Therapy.

1.3.2.1 Microbeam radiation therapy

Microbeam radiation therapy (MRT) is a promising pre-clinical radiotherapy modality aimed at treating inoperable tumours, i.e. brain tumours in children and adolescents, where traditional treatment options cannot be utilized due to lack of tumour control and/or unwanted harmful side-effects [7]. MRT makes use of highly brilliant synchrotron radiation passing through a multi-slit

collimator (MSC) to create micrometre-scale, spatially fractionated X-ray beams known as ‘microbeams’ (MBs). An array of microbeams produces a radiation field profile characterised by thin, high dose-rate ‘peaks’ (where synchrotron radiation passes through the slits in the tungsten block) that are separated by low dose-rate ‘valleys’, which arise due to scattered radiation from the peaks. The width and pitch of these microbeams are dependent upon the geometrical design of the MSC, with typical widths between 25–100 μm and pitch of 100–400 μm. The uncollimated field (i.e. with the multi-slit collimator removed from the beam) is denoted as the ‘broadbeam’ (BB) radiation field to differentiate it from the collimated microbeam field.

Microbeams take advantage of the phenomenon known as the Dose-Volume Effect — where the tolerance of normal tissue to radiation dose increases dramatically inversely proportional to the size of the radiation field. Zeman et al. (1959) published the first known instance of this observation using a beam of deuterons incident upon mouse brain tissue, which was confirmed in subsequent publications [8] (Figure 1.2).

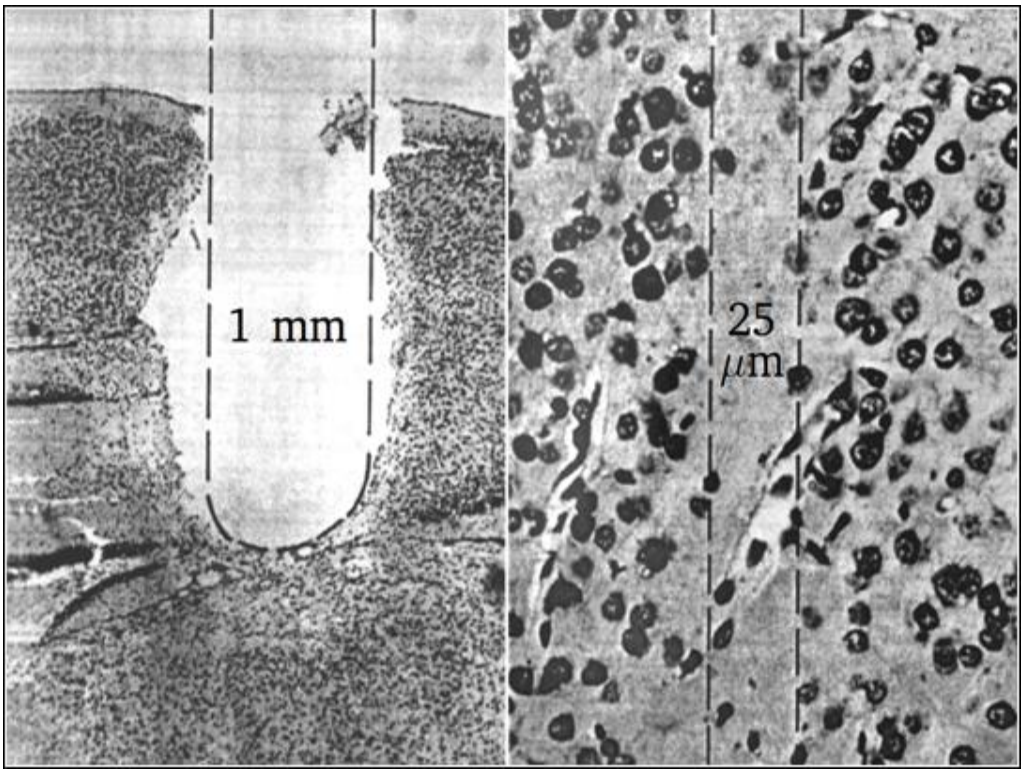

Figure 1.2: Demonstration of the dose-volume effect.
Left: 280 Gy with a 1 mm beam of deuterons; Right: 4 kGy with a 25-μm beam of deuterons.
from Zeman, Curtis, and Baker (1961) [8]

By a combination of the Dose-Volume effect and the heightened radiation-tolerance of normal tissue compared to cancerous tissue, MRT is capable of improved treatment outcomes compared to standard EBRT techniques. However, in order to maintain the width and pitch of the microbeams

in the microbeam array, a very low-divergence photon field is required, which is currently only possible with third-generation synchrotron light sources and dedicated insertion devices (i.e. wigglers). Without low divergence, the width of individual microbeam fields and the spacing of the microbeam array increases with depth and becomes a conventional broadbeam, thus losing the special properties of MRT.

Additionally, due to the small size of the radiation field, cardiosynchronous motion, breathing, and fidgeting of the patient become an issue. Any patient movement during treatment leads to blurring of the delivered dose profile and reduces the efficacy of the MRT treatment. The solution to this issue arises from the high brightness of synchrotron radiation from an insertion device – which may have dose-rates orders of magnitude larger than conventional EBRT (kGy/s as opposed to Gy/min, respectively). With such higher dose-rates, MRT treatment may occur in a fraction of the time of EBRT – thus reducing the impact of target motion on the treatment plan. Conversely, the high dose-rate requires even more stringent quality assurance due to the increased severity of the risk of over-dosing the patient. This risk is managed via electronic beam-monitoring patient safety systems that are intended to trigger emergency safety shutters and/or kill the electron beam within fractions of a second.

Finally, synchrotron MRT also deviates from megavoltage EBRT in the energy spectrum of the incident photon beam. EBRT machines require megavoltage sources to produce photon spectra in the 0.1–18 MeV energy range with sufficient energy and intensity to deliver dose to a target deep in the patient. Insertion devices are capable of 1–300 keV photon spectra at significantly higher intensities – which has an impact on the shape of the depth-dose profile.

MRT is currently under development at a number of synchrotron institutions around the world (e.g. Australian Synchrotron, European Synchrotron Radiation Facility) [9]–[14].

1.3.3 Microbeam dosimetry: current status

As with any other radiotherapy technique, accurate Quality Assurance (QA) prior to treatment is required to ensure appropriate dose delivery according to the prescribed treatment plan. Experimental dosimetry for MRT is a challenging task, as dosimeters require a large dynamic range, high spatial resolution, high radiation-hardness and real-time readout. Very few of the dosimetry techniques that are currently available satisfy the stringent dosimeter requirements necessary for use in MRT. A preliminary assessment of multiple candidates for QA dosimetry of MRT may be found

in Bräuer-Krisch et al. (2010) [15], some of which are outlined below.

Small ionisation chambers (e.g. the PTW PinPoint™ ionisation chamber range) are sufficient for reference dosimetry of large-field (e.g. 20 × 20 mm²) broadbeam (BB) dosimetry due to their well-understood operating principles and the calibration services available at multiple global Physical Standards Laboratories. However, the spatial resolution of such ionisation chambers are insufficient for resolving micrometre-scale radiation fields, therefore they are only recommended for large-field broadbeam dosimetry. In broadbeam QA, ionisation chambers are used to determine dose-count calibration factors by way of comparison to the response of other dosimeters in identical field conditions.

The PTW microDiamond detector is capable of real-time dosimetry of synchrotron microbeams, with a resolution of 1 μm when properly set up [11]. It is able to interface with the same electrometers that PinPoint™ ionisation chambers use, so customised readout systems are not necessary. However, proper set-up of the microDiamond requires a lengthy and difficult alignment process to avoid geometric effects degrading spatial resolution. Additionally, even when properly aligned, the height of the detector will be 2.2 mm and so volume-averaging effects may be present in fields smaller than the height of the detector.

Radiographic film is another option that satisfies the requirements of high spatial resolution, if the film can be scanned using a scanner with sufficient resolution. In broadbeam cases, traditional flatbed scanners are sufficient, but for analysis of microbeam structures, the scanner may need to be substituted with a microscope capable of acquiring images. An example of the use of a microscope for analysis of Gafchromic™ EBT3 film for MRT dosimetry may be found in Dipuglia et al (2019) [16]. However, radiographic film has a limited dynamic range and so may not be able to correctly record peak and valley doses simultaneously. Additionally, it does not allow for real-time dosimetry, as it requires at least 24 hours of development time post-irradiation before scanning and analysis, so it is better used for post-treatment dose verification as opposed to pre-treatment QA.

Fibre-optic detectors coupled with milled scintillators have been investigated at the AS IMBL in BB and MB modes [17], [18]. These have potential as a cheap, water-equivalent dosimeter for MRT, but improved data acquisition systems are necessary to overcome the reduced signal as scintillators approach single-micrometre-scale thicknesses. The effect of high-Z reflective paints used for enhancement of the signal-to-noise-ratio (SNR) and the effect of Cherenkov radiation in the length

of the fibre-optic cable exposed to the beam both require further investigation.

1.3.3.1 Silicon detectors

Unique silicon single strip detectors (SSDs), specially mounted in kapton probe packaging, have been the subject of investigation by the Centre for Medical Radiation Physics (CMRP, University of Wollongong) for several years as candidates for MRT real-time dosimetry [19]–[26]. MOSFET devices have been exposed at the ESRF ID17 beamline in an Edge-On configuration (see Figure 1.3) to take advantage of the much smaller thickness of the device (as compared to the width of the sensitive volume (SV)). While desired spatial resolution was achieved in this method, the devices are not sufficiently radiation-hard to withstand the long-term doses delivered by kGy/s beams; thus, device turnover would become an issue.

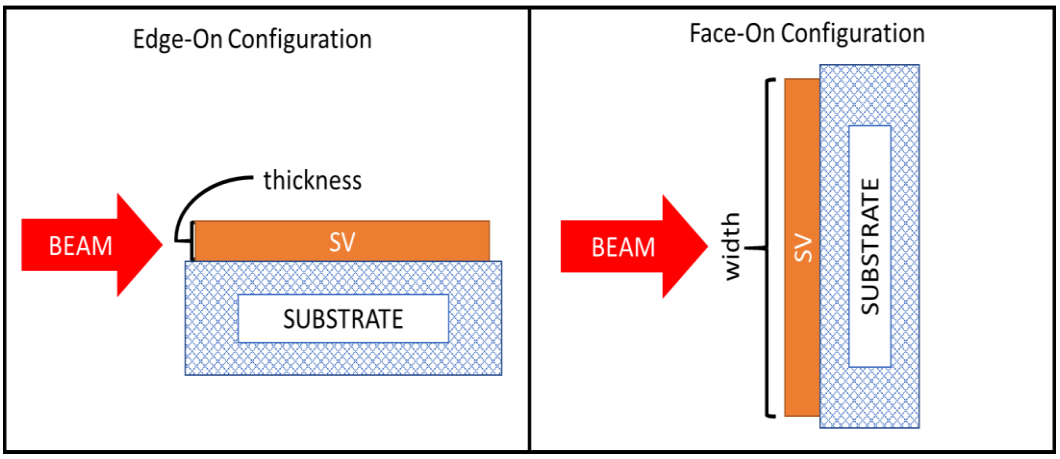

Figure 1.3: Diagram of edge-on and face-on configurations for an SSD, with the sensitive volume (SV) normal vector perpendicular and parallel to the incident beam, respectively.

The successor to the MOSFET, a 50 µm-thick epitaxial silicon single strip detector (henceforth, the EPI50 SSD), was designed to address the challenge of micrometre-scale dosimetry whilst retaining radiation harness of the device. The EPI50 SSD was designed to use an electronic 'guard-ring' system that acted to electronically limit the collection volume in the device by draining charge generated too far from the collecting strip. A limiting factor for the use of EPI50 SSDs is the requirement of a custom-built real-time readout system and thus an increased difficulty in performing maintenance in the event of damage. Nevertheless, the EPI50 SSD presents a strong case for use in QA of MRT.

The 3D-Mesa SSD, designed at CMRP and fabricated at a microelectronic foundry by SPA-BIT (Kiev, Ukraine), is a novel and alternative SSD prototype [23], [25] and is a promising candidate for QA in MRT. It is specifically designed with the goal of reducing the impact of the silicon

material that typically surrounds the SV in previous planar SSD designs (such as the aforementioned EPI50). It has been hypothesized that reducing the surrounding silicon may improve the ability of the device to work in low energy (<100 keV) photon environments (like MRT) (Ch.4: Energy dependence of hypothetical detectors, [27]) where the ratio of mass energy absorption coefficients (μ_e/ρ) of silicon to water (C_E at E keV) differs significantly from unity (1.3).

$$C_E = \left(\frac{\mu_e}{\rho}\right)_{Si} \div \left(\frac{\mu_e}{\rho}\right)_{H_2O} \qquad (1.3)$$

This work aims to characterise the performance of the first generation of 3D-Mesa SSDs and determine the potential of the 3D-Mesa SSD design as a QA dosimeter for MRT.

1.3.4 Electrical characterisation of silicon detectors

Before a new detector may be used for dosimetry, it is essential to determine optimal operating conditions and examine the behaviour of the charge generated during irradiation. In this work, the optimal operating conditions of the 3D-Mesa SSD device are determined via electrical characterisation measurements, specifically: current-voltage (I–V) and capacitance-voltage (C–V) characteristic curves. Current-voltage curves are used to understand the leakage current of the device under optimal bias. The leakage current must be small compared to the expected charge that will be generated in order for useable signals to be differentiable from the electronic noise of the device and readout system. Capacitance-voltage curves are used to estimate the propagation of the depletion layer within the device as a function of bias. The inverse-squared capacitance is a useful extension of the capacitance-voltage curve and may be used to estimate the built-in bias and doping concentration for an abrupt PN junction. In the case of non-ideal 'abrupt' PN junctions the approximation is less accurate but is still useful for rough estimates of magnitude.

The electrical behaviour of a simple semiconductor device under reverse bias conditions is well understood and is covered in many textbooks relating to the study of electronic materials. This provides a good estimate for SSD electrical characteristic behaviour; though deviations from the ideal are to be expected as the geometry of the device becomes more complicated. It is also important to acknowledge the effect that the device packaging may have upon the experimental results. For instance, experimental capacitance measurements will provide a value that is the sum of the SSD capacitance, the packaging capacitance, and the capacitance of the connecting wires. If the packaging of the device is much larger than the device itself, then small-magnitude features may be

completely dominated by the much larger capacitance of the packaging. To avoid such complications, it is good practice to order a set of sample detectors for testing with minimal mounting, such as a dual in-line (DIL) packaging, in addition to 'production' mounted devices suitable for experimental dosimetry. The relative smaller size of DIL packaging compared to 'production' packaging also makes DIL-packaged samples ideal for charge-collection studies of the device – which are best undertaken in vacuum and thus much easier in smaller vacuum chambers.

1.3.5 Charge collection studies

Electrical characterisation alone is not enough to completely understand the behaviour of a solid-state dosimeter, and so the device must be irradiated under known conditions in order to determine whether the device is suitable for use as a dosimeter. Depending on the eventual use of the device, it may need to undergo spectroscopy studies or charge-collection studies. As the dosimetry of MRT is unconcerned with extraction of particle-energy information, but is very concerned with spatial resolution and total energy deposition, Ion Beam Induced Charge (IBIC) studies are best suited for evaluating device performance. IBIC collection measurements are used to determine the intrinsic spatial resolution of the device when operated in a face-on orientation and evaluate the fabrication technologies utilized to fabricate the 3D-Mesa SSD device. The principle of IBIC is the raster-scanning of a micrometre-sized low-current ion beam of known energy across the surface of the detector. With appropriate calibration, signal shaping, and analysis, energy deposition as a function of position can be extracted. This information can then be compared against the theoretical energy deposition of an ion of identical energy within the device structure and the charge released during that interaction to determine the charge collection efficiency of the device at each location at that bias. This also allows identification of unwanted charge collection that may occur in the device and thus verification of optimal operating conditions to reduce the impact of such events.

1.3.6 Technology Computer Aided Design

It is good practice in the field of detector fabrication to supplement experimental testing of new devices with theoretical modelling and simulations that may provide insight into electrical characteristics that experimentation is ill equipped to examine. Indeed, device simulation often precedes fabrication, as commercial detector fabrication programs are able to estimate the feasibility of the device design before fabrication and thus prevent wasted investment of resources into poor designs.

Sentaurus TCAD [28] is capable of modelling device fabrication procedures (etching, doping, etc.) in addition to simulation of circuit behaviour and physical characteristics of the device geometry during operation. These characteristics include electric field distribution, electron-and-hole densities, current density, capacitance, carrier lifetime and charge collection efficiency. This is accomplished using analytical methods – where Poisson and electron-hole continuity equations are solved at many points within the device model under user-defined conditions. Many different models are available to TCAD that allow the user to define carrier mobility, recombination, charge trap formation, and other electronic behaviour as required.

Models of the 3D-Mesa SSD detector have been constructed to investigate electric field distribution in the device to understand the current design and aid future improvement of 3D-Mesa SSD designs. While analytical methods are excellent for examining physical and electrical properties of the device, they are, however, less suited to simulation of energy deposition within the device during irradiation. For this, Monte Carlo modelling must be used.

1.3.7 Geant4 Monte Carlo modelling

Monte Carlo modelling is the best method for simulating the stochastic nature of radiation interactions within matter. This is achieved using pseudorandom number generation that is used to select a 'random' result from a pool of possible results according to the probability of each result. In the case of radiation interaction simulations, the type of interaction at any given location is selected from the pool of all possible interactions for the chosen particle based on the cross-section of interaction of each process.

If the models used are accurate and a large sample size of particles are simulated, Monte Carlo modelling will provide accurate and reliable results directly comparable to experimental data. However, the need for large sample sizes means that Monte Carlo simulations are often much slower than well-optimised analytical simulations that employ approximations rather than simulating and tracking every particle and interaction.

The GEometry ANd Tracking toolkit 4 (Geant4) was developed at CERN as a tool for high-energy physics Monte Carlo simulations [29], [30]. The toolkit was soon discovered to have applications in the field of medical physics simulations and has been improved upon and extended for many years. The most recent public release as of the time of writing is version 10.6. Geant4 is well documented and so will not be discussed in detail, but a brief overview is provided below.

A Geant4 simulation is broadly divided into three main components: 'geometry', 'physics', and 'run action'. First, the user defines the geometry to be modelled in a 3D Cartesian 'world' space. Geometries of varying complexity are available, from simple rectangular prisms and cylinders to complicated voxelised reconstructions of computed tomography (CT) images. The material of each object is defined and then the object is positioned within the world geometry.

The user then defines the physics models to be used to simulate particle interactions. A number of electromagnetic physics models have been benchmarked and validated for use in Geant4 in published literature, such as the PENELOPE and Livermore models. Recent versions of Geant4 also contain models to simulate hadronic physics as well as more complicated physics processes, such as interaction of particles with electric and magnetic fields, and radioactive decay of materials.

Finally, the simulation begins a 'run' where particles are simulated individually (as 'events') according to user-defined specifics (energy, position, momentum, etc.) and transported in discrete 'steps' through the geometry. At the vertex of each step is a physics interaction, which is selected from a pool of all possible interactions based on the probability of each interaction. The probability of any possible interaction is defined as the inverse of the mean-free path length between two of the same interaction (photoelectric effect, Compton scattering, pair production, etc.). Information regarding the particle interaction may be extracted at any step along the path or only in defined 'sensitive detector' volumes according to user requirements and may be stored in a number of file formats for analysis.

Geant4 simulations perform well in parallel computing architectures where identical 'runs' with different pseudorandom number generator seeds may be simulated simultaneously and simulation output files merged upon completion. This is an excellent way to increase statistics and save time for those with access to supercomputing clusters and is highly recommended.

1.3.7.1 Previous Geant4 synchrotron beamline models

The Geant4 model of the Australian Synchrotron Imaging and Medical Beamline discussed in this thesis is a successor to a Geant4 model of the European Synchrotron Radiation Facility's ID17 Biomedical Beamline developed by Dr. Iwan Cornelius and discussed in detail in [31], henceforth referred to as G4ESRF.

It was designed to be an up-to-date model of the ID17 beamline with time-dependent geometry and to remove the need for parameterised source models based on experimentally generated Phase Space

Files (PSFs) to produce synchrotron radiation. In this context, a PSF refers to a file that record information about a large number individual particles in a radiation field. In essence, a table of M rows and N columns is constructed wherein each of the M rows defines a unique particle and each of the N columns stores information regarding one physical property of the particle (such as position, momentum, energy, polarisation, etc.).

G4ESRF interfaces with the third-party program SHADOW3 [32] to generate synchrotron radiation and import into the Geant4 geometry for transport and interaction. Broadbeam depth-dose profiles were compared to PENELOPE simulations [33] with excellent agreement across multiple field sizes, at the centre of the field, to a depth of 150 mm in a 200 × 300 × 300 mm^3 RW3 (PTW Freiburg, Freiburg, Germany) phantom. Good agreement was achieved between G4ESRF, PENELOPE, and experimental HD-810 Gafchromic® film measurements [34] for peak and valley depth dose profiles in a 300 × 300 × 300 mm^3 water phantom. After the accuracy of the model had been assessed, work began on the construction of a successor model.

Chapter 2

Geant4 simulation of the Australian Synchrotron Imaging and Medical Beamline

2.1 Introduction

In this chapter, the Geant4 model of the Australian Synchrotron Imaging and Medical Beamline (AS IMBL) is discussed. First, the specific geometry of the Australian Synchrotron Imaging and Medical Beamline (IMBL) is outlined and important elements discussed in detail. Of note is the explanation of beamline configuration nomenclature and coordinate system to be used in the rest of the thesis.

The new Geant4 simulation model of the AS IMBL, G4IMBL, is then introduced. This involves explanation of the choice of physics models for transportation and particle interaction (including associated user-defined limits) and the outlining of geometrical information (including material composition and placement of all relevant components of the beamline). The design-flow of the simulation and information output and analysis methods used in the simulation are briefly discussed. Phase Space Files (PSFs) for various configurations of the beamline and at various positions have been analysed with an emphasis on average particle position and resulting energy spectrum. PSF energy spectra are compared against the third-party program SPEC, developed by IMBL staff [35]. A theoretical investigation into the change of photon energy spectra at various depths in a phantom has been presented, highlighting the ability of this simulation to separate incident and backscattered components of a photon spectrum within a phantom. Finally, comparisons have been made for broadbeam and microbeam relative depth dose profiles against experimental measurements using a PTW PinPoint™ IC and EBT3 Gafchromic® film for a known beamline configuration.

2.2 IMBL beamline geometry and setup

At the AS IMBL (and in the Geant4 model of the beamline) the coordinate directions are as follows: the +X direction of travel of the photon beam, the Y-direction is perpendicular to the +X direction and forms the horizontal XY plane corresponding to the motion of the electron beam in the storage ring; and the Z-direction is perpendicular to the XY plane and defines verticality (more positive towards the ceiling of the hutch).

2.2.1 Electron beam specifics

For the majority of experiments performed at the IMBL synchrotron radiation was produced by an

electron beam with an energy of 3.022 GeV. The electron beam current in the 216 m–circumference storage ring is generally held at 200.0 mA with an uncertainty of 0.3% [35] in continuous top-up mode with a fresh injection of electrons into the storage ring every 10 minutes. Electron bunches are of 25 ps duration and are separated by 2 ns. During one experimental beam time, industrial action lead to the electron beam current being lowered to 175.0 mA, which affects brightness of the synchrotron radiation, but not polarisation, or energy spectrum characteristics compared to a 200 mA beam with identical wiggler and filtration conditions.

2.2.2 IMBL hutches

The IMBL itself is ~150 m long and divided into discrete sections in order from closest to the ring: the Front End, Hutch 1A/1B, Hutch 2A/2B, the transfer line, and Hutch 3A/3B. All experiments in this thesis were performed in Hutch 2B and thus components in all upstream sections will affect the shape, intensity, and spectrum of the radiation field in Hutch 2B. The transfer line, and Hutches 3A and 3B do not feature in any results contained herein and so are not described further, but full details are contained within [35].

2.2.2.1 Front End – generation of synchrotron radiation

The Front End consists of the section exposed to the storage ring and contains the wiggler, bending magnet, diamond filtration, copper shaping mask, and the upstream lead wall of Hutch 1A.

The AS IMBL Superconducting Multi-Pole (SCMP) Wiggler is 1.612 m long, consisting of 59 full-strength pole-pairs and a pair of -¾ and +¼ strength pole pairs at the entrance and exit of the aperture channel. The centre-to-centre distance between magnet poles is 52 mm. The SCMP wiggler is able to produce a maximum magnetic field strength of up to 4.2 T, though in practice 1.4, 2, 3, and 4 T are the most common setups provided at IMBL. For convenience, the midpoint of the wiggler is defined as the radiation ‘source’, though this is primarily to simplify discussion of distances between components as synchrotron radiation is produced along the entire length of the wiggler, not exclusively at the midpoint.

The bending magnet positioned immediately after the insertion device is of 1.4 T magnetic field strength and functions to divert the electron beam away from the IMBL to continue around the storage ring. Some synchrotron radiation produced by the bending magnet is capable of entering the beamline, but this is negligible compared to the magnitude of radiation intensity from the wiggler.

A thin sheet of diamond is fixed in place after the bending magnet to act as the first filtration element

upon the synchrotron radiation from the wiggler. This attenuates the lowest energy photons in the spectrum and also lowers the intensity of the radiation field a small fraction.

The copper (Cu) mask block contains an aperture to serve as an initial geometrical definition of the beam such that the beam forms a solid angle from source to downstream face of the mask of 0.0038 rad and 0.0003 rad in the Y and Z directions respectively.

The lead (Pb) wall contains an aperture of width 200 mm (Y) and height 200 mm (Z) to allow particles to pass through into the beamline hutches beginning with Hutch 1A. The Pb wall marks the boundary between the storage ring and the beamline, beyond which the radiation is transported under vacuum within large stainless steel cylindrical pipes.

2.2.2.2 Hutch 1A–2A – shutters, filtration, shaping, and transport

Hutch 1A contains the photon stop shutter, primary shaping slits (a.k.a the high heat-load slits), filtration paddles, monochromators, and the secondary safety shutter. All of these components are held under vacuum at all times within specially designed chambers, though some components may be translated into or out of the path of the beam to adjust radiation field shape, photon intensity, and energy spectrum.

Because of the nature of synchrotron radiation production, whenever there are electrons present in the storage ring synchrotron radiation is always produced by a non 0 T wiggler and the 1.4 T bending magnet. In order to permit ‘turning the photon beam on or off’ without affecting the electron ring current, a set of motorised large Cu blocks are used to obstruct the photon beam and attenuate all incoming radiation to zero. A very large He-cooled block sits at the border between the Front End and the rest of the beamline, capable of attenuating the maximum output of the wiggler and bending magnet. However, its mass makes it too slow to act as a fast safety switch in an emergency. Instead a second set of two smaller Cu blocks (denoted collectively as the ‘safety shutter’) are positioned at the border of Hutch 1A and Hutch 2B, which are designed to attenuate a filtered spectrum (and thus lower intensity radiation field), but are correspondingly faster to move and thus ‘shut off’ the beam (within tenths of second). The safety shutter is the primary shutter used for controlling the presence or absence of radiation in downstream hutches during experimentation and setup.

Prior to Hutch 2B where dosimetry experiments are performed, three separate sets of cooled copper paddles, collectively known as ‘shaping slits’, are available to provide coarse spatial shaping of the beam. Each set consists of two paired vertically separated Cu sheets and two paired horizontally

separated Cu sheets which may all be moved individually to construct a rectangular aperture in the negative space where the slits do not overlap. The aperture of desired width and height (and positioning) allows the beam to pass through while the Cu bodies of the slits attenuate the remainder of the beam. Adjustment of slit-aperture sizes and aperture central position have a significant effect on the shape and dose rate of final treatment beam and may be restricted to reduce dose rate and improve beam uniformity, or expanded to deliver greater flux and larger beam size. The primary shaping slits (a.k.a. the high heat-load slits (HHLS)), secondary shaping slits, and tertiary shaping slits are positioned at 14, 20, and 25 m from the centre of the wiggler, respectively. The HHLS closest to the source are designed to withstand the greatest heat load from the radiation field and provide coarse beam shaping and so have superior cooling but coarser positioning resolution compared to the secondary and tertiary shaping slits. Finer spatial field-shaping may be performed by the tertiary shaping slits in Hutch 2A (closest to the phantom in Hutch 2B), where effects of beam divergence may be minimised, though final shaping of the beam generally occurs in Hutch 2B using a tungsten block with a channel milled to specific aperture dimensions, known as the Beam-Defining Aperture (BDA). In certain cases where the beam size required by the experiment exceeded the maximum size of the BDA dimensions the BDA was removed entirely and beam definition is entirely due to the shaping slits.

Following the primary shaping slits, there are five optional filter paddles for attenuating the beam load and determining the final photon spectrum incident on the sample. The first three filters are carbon and fixed for all subsequent results. Filters 4 and 5 may be a combination of Cu, Al, or Mo of specific thicknesses. Each set is oriented as noted in Table 2-1. Most of the spectral shaping is performed by the first set of paddles, which are He-cooled and thus designed to handle much higher heat-load than subsequent paddles.

For clarity and conciseness, a naming scheme to define a beamline configuration of specific wiggler magnetic field strength and filtration combination will be implemented for the rest of this thesis in the format of: “A-BC”, where A is the magnetic field strength of the wiggler, B the material of filter 4, and C the material of filter 5. For example, under this scheme a 3T wiggler with a filtration combination where Filter 4 is Cu and Filter 5 is Al will be referred to as ‘3T-CuAl’ in text.

Table 2-1: Most common filtration combinations used experimentally at the AS IMBL.

	Very High Dose Rate (Al-Al)	**High Dose Rate (Cu-Al)**	**Medium Dose Rate (Cu-Cu)**	**Low Dose Rate (Al-Mo)**
Filter 1	C (0.45 mm)			
Filter 2	C (1.49 mm) 45º			
Filter 3	C (10 mm) 45º			
Filter 4	Al (1mm) 45º	Al (2 mm) 45º	Cu (1 mm) 45º	Al (2 mm) 45º
Filter 5	Al (1mm) 45º	Cu (1 mm) 45º	Cu (1 mm) 45º	Mo (2 mm) 45º

The photon energy spectrum depends strongly on both the filtration and wiggler magnetic field strength and different spectra produce significant differences in dosimetric results. The mean energy of the spectrum and air-KERMA rates (private correspondence with Dr. Andrew Stevenson, AS IMBL staff) as produced via "spec.exe", IBML's in-house program for beam analysis (Stevenson et al, 2017) [35] — henceforth referred to as SPEC — is provided for the configurations to be examined in this thesis in Table 2-2.

Table 2-2: Example mean energy and air-KERMA rate of relevant beam configurations.

	3T-CuCu	3T-AlAl	3T-CuAl	2T-CuAl	1.4T-AlAl
Mean energy (keV)	94.63	54.47	82.28	70.73	39.72
Air-KERMA rate (Gy/s)	356	6440	786	137	690

The energy spectrum of the beam is not significantly affected by manipulation of shaping slit positioning or the aperture size and so the weighted average energy of the spectrum as provided by Table 2-2 may be considered constant. However, the air-KERMA rate provided above should be taken as a rough guide only – as individual experiments will alter shaping slit aperture sizes depending on the requirements of the experiment. Optimisation of the aperture size and central position is required for every individual experiment to achieve a maximum air-KERMA rate that agrees with theoretical values for that beamline configuration.

In this thesis, the shaping slit aperture sizes and positions have not been recorded due to the difficulty we experienced in replicating shaping slit positioning between experiments that could be months apart. Because of this, the dose rate and shape of the beam should be considered unique to every set of data. This means that results in this thesis may not be directly comparable to published experimental data and all measurements should be taken as relative dosimetry within the unique beam configuration. In order to directly compare data in this thesis to experimental data the shaping

slits will need to be adjusted in order to produce a field that delivers an identical dose to the reference dosimeter at reference depth in a phantom.

The IMBL is also capable of producing a mono-energetic beam using the double-crystal Laue monochromator (DCLM) in Hutch 1A, which uses refraction of the beam through crystalline planes of a pair of Si crystals to select energies of interest. The DLCM is capable of producing monochromatic beams ranging from ~20–120 keV, though higher order harmonic contamination may be present at low energies and must be accounted for.

2.2.2.3 Hutch 2B – experimental hutch

Hutch 2B is the dynamic MRT hutch, located approximately 35 m from the source. Final spatial shaping of the broadbeam is accomplished by passing it through the BDA in Hutch 2B. The BDA is a tungsten inset of 10 mm thickness (X) with an aperture of known dimensions to shape the beam prior to interaction with MSC, conformal mask, and phantom. In most cases, final definition of beam geometry is performed with a 30 × 2.014, 30 × 1.053, or 30 × 0.532 mm aperture (Y, Z). In some cases, the BDA is removed and shaping of the beam is performed only by shaping paddles at an earlier point in the beamline.

The AS IMBL's MSC may be chosen from either a solid block of tungsten carbide-cobalt alloy (WCCo) with apertures milled into it (Hutch 1B Horizontal MSC) or an array of multiple 'C' shaped WCCo [36] plates pressed together to create an array of near-rectangular apertures (Hutch 2B Vertical MSC) — see Figure 2.1 for a simplified model.

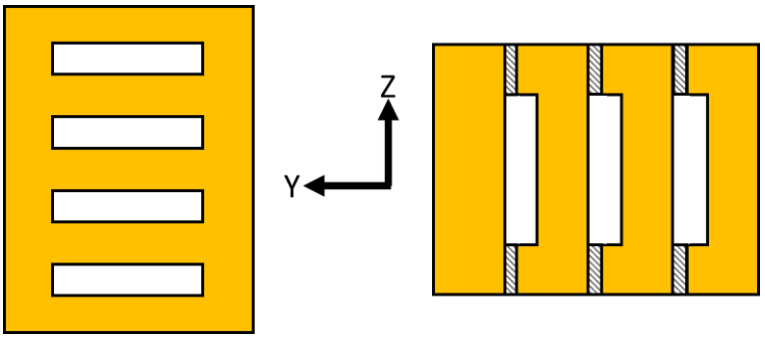

Figure 2.1: Schematic of the AS IMBL Horizontal MSC (Left) and Vertical MSC (Right). X-axis is into the page.

The '50–400' Vertical MSC of Hutch 2B utilises the 'stacked' architecture to produce 125 apertures of 30 mm high (Z), 50 µm wide (Y) and separated in Y by 350 µm of tungsten. The tungsten block through which the aperture is milled has a geometry of 8 × 40 × 40 mm³. All MRT experiments discussed in this thesis used the Vertical '50–400' MSC and so subsequently 'MSC' will refer to

this design exclusively.

The maximum vertical beam size limited by the BDA is 2.014 mm, which is much smaller than most tumour sizes. In order for the smaller beam to fully treat the entire volume of the target, the beam must be scanned over the target, thus delivering dose across a larger treatment field. As the beam is of fixed position, the motorised stage upon which the phantom sits may be moved through the beam as required to 'paint' the dose over the required area (see Figure 2.2). Spatial definition of the treatment field is accomplished by scanning the beam across a tungsten conformal mask.

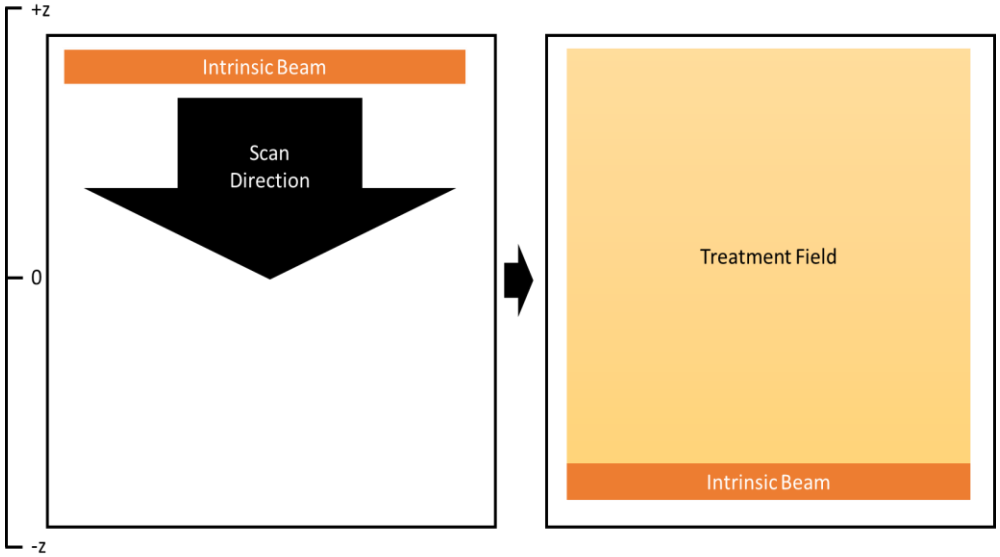

Figure 2.2: Delivery of a treatment field using a smaller intrinsic beam.
Note that the same effect may be achieved with a stationary beam by moving the target relative to the beam or vice versa.

The conformal mask geometry is 8 × 40 × 40 mm^3 with an aperture of known dimensions milled through it (typically 20 × 20, 10 × 10, or 5 × 5 mm^2 square apertures). The conformal mask is placed into a raised arm on the phantom stage and moves in parallel with the stage, remaining at a fixed height and distance relative to the phantom. For targets smaller than the conformal mask, both the mask and the target move together. For targets larger than the conformal mask (as illustrated in the figure), the Pb mask and the target move together, while the conformal mask is stationary with respect to the target and is centred on the X-ray beam. The white Pb mask is not present in beam setups discussed in this thesis and so should be ignored.

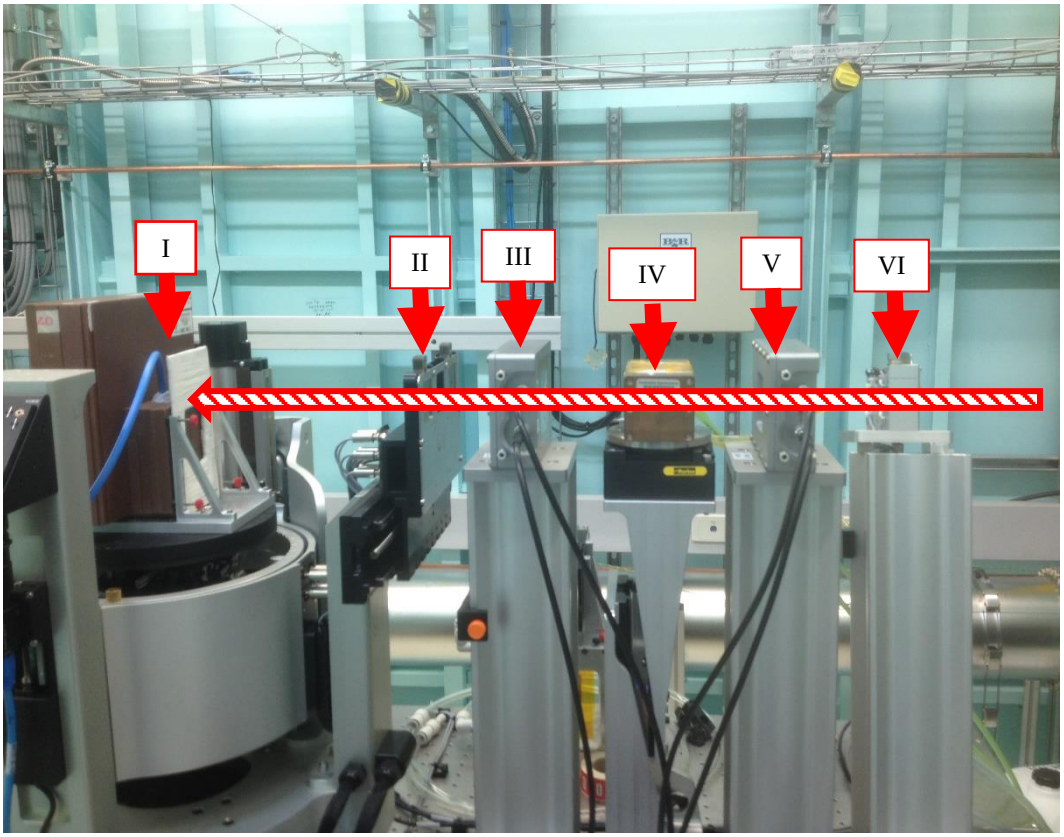

Figure 2.3: Basic setup of Hutch 2B.
Components from left to right: (I) phantom with PinPoint™ IC and white Pb mask, (II) conformal W mask holder, (III) beam monitor chamber #2, (IV) MSC, (V) beam monitor chamber #1, (VI) BDA. The direction of beam is shown in red.

The most common phantom used for the following experiments is a set of specially prepared varied-thickness slabs of water-equivalent RMI457 Gammex (Gammex, Inc., Middleton, USA) Solid Water, generally 100 × 100 × 100 mm³ in total. Specific slabs have channels milled into them to allow for consistent positioning of dosimeters while minimising air-gaps. The solid phantom may be replaced by a water tank phantom (137 × 158 × 120 mm³) with motorised arm for water-tank measurements.

Accurate positioning of phantom and detectors is aided by the use of vertical and horizontal guidance lasers coupled with alignment markings on phantom faces and stationary beamline components such as the BDA holder.

All important elements of Hutch 2B may be seen in Figure 2.3.

2.3 G4IMBL

The new GEometry ANd Tracking Monte Carlo toolkit 4 (GEANT4) model of the AS IMBL, henceforth G4IMBL, is an expansion on G4ESRF with the aim of generating synchrotron radiation for use in energy deposition simulations without the use of third-party programs. Initially developed

using Geant4 version 9.6 patch 4, it has since been ported to version 10.0 patch 0 with minimal alteration to the source code. This simulation is designed to be separated into two discrete stages of operation:

- Stage I — synchrotron radiation production from an electron beam and filtration and transportation of the resulting photons through the geometry to be recorded near a phantom;
- Stage II — energy deposition simulation within a parameterised, voxellised phantom to produce dose profiles for comparison to experimental measurements.

This simulation was developed to be highly modular, easily controllable with runtime macro commands, and capable of parallelisation with the use of supercomputing clusters.

Application specifics are discussed below in sections pertaining to the physics, geometry, and primary particle generation.

2.3.1 G4IMBL physics models

2.3.1.1 General physics options and particle transport

G4IMBL makes use of the G4EMLivermorePolarisedPhysics model – an extension of the Livermore low energy electromagnetic physics model which has been validated over the range of 250 eV to 10 MeV – which encapsulates our range of energy spectra entirely [37]–[40]. Physics options for fluorescence, auger electrons, and PIXE have not been activated. Production cuts apply a minimum threshold for secondary particle step length and any particle with a step length less than that threshold is killed and all kinetic energy is said to be deposited locally. Production cuts have been applied to be 1 mm for photons and positrons, and 0.01 mm for electrons throughout the world volume. A high-resolution region is available for the scoring volume of the phantom, which applies a maximum step-limit of 1 μm to improve track resolution and production cuts for photons and electrons of 10 μm.

Transport of the particles is managed in discrete steps from the initial position of the particle (the pre-step) to the interaction position (post-step) of the pseudo-randomly selected physics process. Step length is determined by calculating the mean-free-path of each possible physics process from their individual probability distributions using pseudo-random Monte Carlo methods, and then selecting the minimum mean-free-path as both step length and chosen interaction. Consequently, the state of the particle at any point along the step (excepting the post-step point) is considered to be equal to the pre-step state and any change in the particle position, momentum, polarisation, or

kinetic energy, or production of secondary particles will only occur at the post-step position. Pre- and/or post-step particle information may be extracted and recorded as required by the user.

2.3.1.2 Production of synchrotron radiation

Production of synchrotron radiation is handled by the G4SynchrotronRadiation process (referred to as synRad) [40], [41] which determines both the probability of interaction and the energy of the generated particle. The probability of interaction of an electron is handled by calculation of the mean-free-path of interaction using:

$$\lambda_{mfp} = \frac{2\sqrt{3}m_e}{5\alpha ec|B|} \qquad (2.1)$$

where λ_{mfp} is the mean-free-path of interaction (m), m_e the rest energy of the electron (MeV), α the fine-structure constant (≈1/137), e the charge of an electron (C), c the speed of light in vacuum (m/s) and B the magnetic field strength at the point of interaction (T). The energy of the synchrotron radiation is calculated using Chebyshev polynomials and simple transformations to approximate the inverse cumulative probability distribution function for synchrotron radiation interaction. It should be noted that the synRad process was developed for production of synchrotron radiation in constant magnetic field (i.e. bending magnets) as opposed to insertion devices such as the wiggler. The model is valid for regimes where the magnetic field is 'approximately constant' across the formation length (L_F) of synchrotron radiation:

$$L_F = \frac{\rho}{\gamma_0} \qquad (2.2)$$

where ρ is radius of curvature and γ_0 is the Lorentz factor.

2.3.1.3 Physics-related variance reduction

Two alterations were made to the standard G4SynchrotronRadiation model in the interest of variance reduction. Variance reduction is the implementation of biasing to the simulation with the intent of reducing simulation times by minimising computation of less statistically significant particles.

Firstly, a minimum-energy threshold for production of synchrotron radiation was applied based on the shape of expected energy spectra. Due to the filtration inherent in the IMBL model, the synchrotron beam undergoes significant hardening and attenuation during transport to the phantom and thus photons with energies below the minimum energy of the expected spectrum are not expected to survive to reach the phantom. Processing time is reduced by choosing not to generate

and transport particles below the minimum energy threshold for simulation. In most cases, a low-energy threshold of 40 keV could be applied without affecting the final energy spectrum, though for 1.4 T wiggler field strength this threshold had to be lowered to 20 keV.

Secondly, an option was added to clone all synchrotron radiation photons above the low energy limit by a user-defined quantity (e.g. 1000 times). In essence, time could be saved by reducing the number of total electrons simulated by a chosen factor (referred to as photon splitting number henceforth) and then cloning generated synchrotron photons by that same factor. This approach relies on the assumption that different electrons in reality may interact in identical positions and produce identical particles, and that identical particles will not interact identically due to the stochastic nature of radiation interactions with matter. The relationship between the electron fluence and photon fluence is preserved by assigning a 'weighting number' to every photon that records the equivalent number of electrons simulated to produce that phase-space file from the product of the number of electrons simulated and the photon splitting number.

2.3.2 G4IMBL geometry

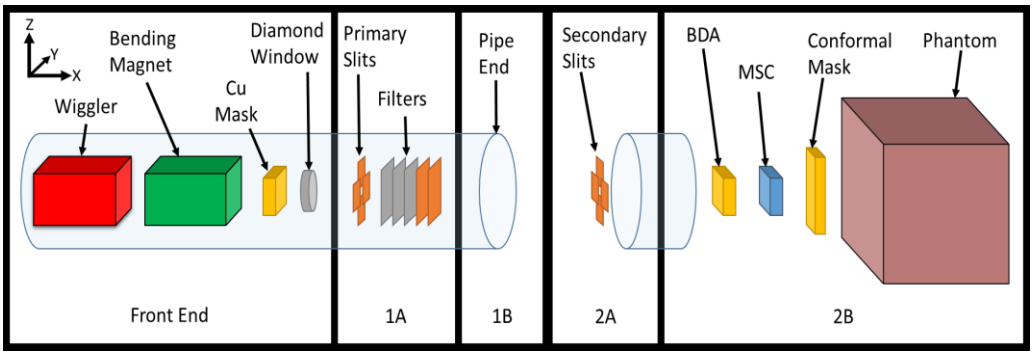

Figure 2.4: Conceptual diagram of G4IMBL geometry (not to scale).
Positive X-, Y-, and Z-directions are shown in the top left corner.

The geometry of the G4IMBL simulation is a simplified recreation of the real IMBL geometry introduced in section 2.2. A conceptual diagram of the simulation model is presented in Figure 2.4 with the positive axis directions indicated.

The simulation model is contained in a 'World' volume ($50 \times 1 \times 1$ m^3) of G4_Air centred at the origin (0, 0, 0). Modular design allows construction of groups of elements of the model independently as required by the user — decreasing both memory consumption and simulation time. The sections are:

- Front End (containing wiggler, bending magnet, G4_Cu mask block, diamond window, and lead wall of the hutch),

- Hutch 1A (containing high-heat load slits and filtration paddles),
- Hutch 1B (containing optional horizontal-slit multi-slit collimator (MSC) and 1B MRT stage),
- Hutch 2A (containing a He- or vacuum-filled pipeline and secondary shaping slits),
- Hutch 2B (containing beam-defining aperture (BDA), silicon beam monitors, vertical-slit MSC),
- Dynamic Stage (containing conformal mask and phantom).

The Front End is the only component that is required to be constructed in order to produce synchrotron radiation, but once synchrotron radiation has been stored in a phase-space file the stored particles may be read in from the output file and generated at the coordinates each particle was recorded in the model.

A phase-space scoring volume (2 × 100 × 100 mm^3) is constructed and assigned as a sensitive detector and may be positioned at any point (x, 0, 0) in the model to record particle information. The sensitive detector records G4ThreeVectors of hit position, momentum, and polarisation, kinetic energy and weight of the particle at the post-step, by default, and then stops and kills that particle. Only photon particle information is recorded, electrons that intersect with the scoring volume are stopped and killed.

Standard procedure is to position the phase-space scoring volume +10 mm (X-direction) from the 2B MSC and run a Stage I simulation to collect synchrotron radiation with all upstream components constructed. Following this, any Stage II simulation only requires Hutch 2B to be constructed – ideal, considering the memory demands of the voxelisation and parameterisation required for energy deposition in the phantom.

2.3.2.1 Front End

The Front End contains the wiggler, bending magnet, Cu mask block (with aperture), diamond window, and lead wall (with aperture) all contained within a mother volume (Front End pipe) filled with G4_Galactic material (i.e. vacuum). Coordinates and dimensions of the components are given in Table 2-3. The wiggler is constructed as 30 periods of G4_Galactic material with a length of 52 mm (X) each. This simplified wiggler has one extra full strength magnetic pole and lacks the ¼ and ¾ ending orbit correction poles which are used in reality to adjust the path of the electron beam away from the ideal orbit within the storage ring.

The wiggler geometry has a G4SinusoidalMagneticField applied with a maximum strength of default 3.0 T, a 1 mm maximum step-limit within this geometry, and uses a G4HelixSimpleRunge stepper and G4Mag_UsualEqRhs equation. The bending magnet is likewise a box of G4_Galactic material that is applied a G4UniformMagField with strength of 1.4 T and delta chord length of 0.1 mm. While synchrotron radiation is produced at random points in the wiggler and bending magnet according to the individual process' probability of interaction, for ease of reference the 'source' is defined as the midpoint of the wiggler.

Table 2-3: Front End simulation components.

Element	X-Coordinate (centre, mm)	X length (mm)	Y width (mm)	Z height (mm)	Material
Front End pipe	-1.801E+04	14,000	1,000	1,000	G4_Galactic
Wiggler	-2.422E+04	1,560	100	100	G4_Galactic
Bending magnet	-2.122E+04	2,000	100	100	G4_Galactic
Mask block	-1.662E+04	210	118	118	G4_Cu (& aperture)
Diamond filter	-1.602E+04	0.6	118	118	G4_C (3.5 mg/cm³)
Lead wall	-1.851E+04	1,000	1,000	1,000	G4_Pb

The mask block and lead wall are as defined above in 2.2.2.1. The diamond filter is constructed using 3.5 mg/cm³ G4_C and contains no aperture; thus, it is the first filtration element that the photon beam is exposed to during transport along the beamline.

In the interest of variance reduction, the upstream face of the lead wall is set to be a 'killzone' that stops and kills all particles that interact with it, as those particles would have 0% probability to interact with other downstream beamline components. Another killzone is placed on the -Y face of the bending magnet to kill the transportation of any particles that would in reality continue along the storage ring. Suppression of modelling the transport and interaction of particles that are no longer significant will provide slight improvements to overall simulation efficiency.

2.3.2.2 Hutch 1A

The G4_Cu primary shaping slits are constructed in Hutch 1A to assist in shaping beam geometry. In this model the slit positioning is static unless changed in the source code, but experimentally these slits (along with the tertiary shaping slits in Hutch 2A) are motorised and may restrict or enlarge the beam size to adjust beam intensity further down the beamline. As the number of particles capable of being simulated by Geant4 in a reasonable timeframe is massively smaller than the number of particles produced by the wiggler in reality, the aperture size has minimal effect on the

number of photons that reach the phantom. The horizontal and vertical slit pairs are separated by 20 mm (X) and are 15.11 mm and 2.52 mm apart respectively (Y, Z).

Table 2-4: Hutch 1A simulation components.

Element	X-Coordinate (centre, mm)	X length (mm)	Y width (mm)	Z height (mm)	Material
Hutch 1A pipe	-7.946E+03	6,148	200	200	G4_Galactic
High heat load slits	-1.022E+04	10	50	10	G4_Cu (& aperture)
Filter paddle 1	-9.83E+03	0.45	150	150	G4_C
Filter paddle 2	-9.69E+03	1.49	150	150	G4_C
Filter paddle 3	-9.55E+03	10	150	150	G4_C
Filter paddle 4	-9.41E+03	Variable	150	150	Variable
Filter paddle 5	-9.27E+03	Variable	150	150	Variable

The filtration paddles are constructed to reduce beam intensity and shape the photon energy spectrum. Thicknesses and material composition of paddles 1–3 are given in Table 2-4, but paddles 4 and 5 differ depending on spectrum or intensity requested. The most comment filtration configurations are listed in Table 2-1. The X-lengths of the paddles provided do not take into account that paddles 2–5 are rotated 45° about the Z-axis in order to increase effective filtration thickness.

2.3.2.3 Hutch 1B

Hutch 1B is the closest available hutch to the source at IMBL in which users may perform experiments. In this experimental mode, the hutch may have a horizontal multi-slit collimator and parameterised moving phantom constructed, but these components may be shifted laterally out of the path of the beam in a ‘hybrid’ configuration or replaced with a vacuum-filled tube in ‘pipe’ mode if experimentation is to be performed in Hutch 2B. The chief difference between pipe and hybrid modes is the construction of hybrid-mode’s upstream and downstream pipe-exit windows, which separate the interior of the pipe from the world volume (G4_AIR). If running in hybrid mode the downstream pipe that connects to Hutch 2A will be filled with G4_He instead of pipe-mode’s G4_Galactic vacuum. Because the primary configuration used in experiments by CMRP is the ‘hybrid’ mode for Hutch 2B experimentation, all results that follow will assume this configuration.

Table 2-5: Hutch 1B simulation components ('hybrid' mode).

Element	X-Coordinate (centre, mm)	X length (mm)	Y width (mm)	Z height (mm)	Material
Upstream 1B pipe	-3.947E+03	1,850	200	200	G4_Galactic
Beryllium window	-3.09525E+03	0.35	200	200	G4_Be
Helium	-3.05858E+03	73	200	200	G4_He
Aluminium window	-3.02204E+03	0.08	200	200	G4_Al
Air gap	-	3,701.95	1,000	1,000	G4_AIR
kapton window	6.79975E+02	0.05	200	200	G4_KAPTON
Downstream 1B pipe	9.3E+02	500	200	200	G4_He

2.3.2.4 Hutch 2A

Hutch 2A consists of upstream and downstream pipes to be filled with G4_He or G4_Galactic depending on Hutch 1B mode. In reality, the tertiary shaping slits and fast-MRT shutter are positioned here to define beam geometry and facilitate millisecond-scale beam shuttering for the patient-safety system, respectively. As previously mentioned, the timescale of the simulation compared to reality is miniscule; therefore, dose artifacts due to shutter motion would be difficult to reproduce. Additionally, users may alter Hutch 2B's BDA aperture dimensions through the use of user-defined macro commands at runtime, thus obviating the need for construction and translation of the tertiary shaping slits.

Table 2-6: Hutch 2A simulation components.

Element	X-Coordinate (centre, mm)	X length (mm)	Y width (mm)	Z height (mm)	Material
Upstream 2A pipe	3.83E+03	5,300	200	200	G4_He
Be window	6.48018E+03	0.35	200	200	G4_Be
Helium	6.52085E+03	81	200	200	G4_He
Aluminium window	6.56137E+03	0.038	200	200	G4_Al
Air gap	6.88E+03	637	1,000	1,000	G4_AIR
Aluminium window	7.19863E+03	0.038	200	200	G4_Al
Helium	7.23915E+03	81	200	200	G4_He
Beryllium window	7.27983E+03	0.35	200	200	G4_Be
Downstream 2A pipe	7.43E+03	300	200	200	G4_He

2.3.2.5 Hutch 2B

Hutch 2B is the second available hutch in which users may perform experimentation at IMBL. It consists of upstream pipe, BDA, beam monitor chambers, MSC, conformal mask block, and

phantom. The aperture of the BDA is by default 30 × 2.014 mm (YZ) but height and width of the aperture may be adjusted at runtime through user-defined commands. The MSC is a tungsten carbide-cobalt alloy (WCCo) construct [36] contained within a 70 × 140 × 70 mm³ G4_He mother volume. The base volume is constructed as a solid 8 × 70 × 6 mm³ WCCo box with 125 G4_Air apertures of 8 × 0.05 × 3 mm³, centred at the origin of the mother volume with a centre-to-centre distance of 0.4 mm (Y). Beam monitors 1 and 2 have identical construction detailed in Table 2-8.

The phantom is placed within a 500 × 500 × 500 mm³ G4PVParameterised mother volume in order to allow for Z-scanning the phantom through the beam. This pseudo-time-dependent movement is accomplished by translating the phantom's mother-volume position according to the equation:

$$Z\ position = Field\ Size \times \left(\frac{event\ number}{total\ events\ to\ simulate} - 0.5\right) \qquad (2.3)$$

The tungsten conformal mask is also constructed as a daughter-volume of the G4PVParametrised volume and thus its position is fixed relative to the phantom. The aperture of the mask is by default 20 × 20 mm² (YZ) and determines the final field size of the 'treatment field' that results from the integration of the beam across the surface of the moving phantom.

Table 2-7: Hutch 2B simulation components.

Element	X-Coordinate (centre, mm)	X length (mm)	Y width (mm)	Z height (mm)	Material
Hutch 2B pipe	7.98E+03	800	200	200	G4_He
kapton window	8.37998E+03	0.05	200	200	G4_KAPTON
BDA	9.135E+03	10	100	100	G4_W
Beam monitor 1	9.255E+03	40	100	100	See Table 2-8
MSC	9.375E+03	70	140	70	G4_He/ WCCo
Beam monitor 2	9.515E+03	40	100	100	See Table 2-8
Mask block	9.787E+03	4	50	50	G4_W
Phantom	9.935E+03	140	100	100	RMI457
Phase space scoring volume	9.42E+03	2	1,000	1,000	N/A

Due to the focus on comparison of simulation results with Hutch 2B experimental results the default position of the phase-space scoring volume was decided to be 10 mm (X) downstream of the MSC mother volume, just prior to the beam monitor 2 chamber, conformal mask and phantom.

Acquisition of energy deposition is handled by a scoring volume G4SensitiveDetector within the phantom geometry. The scoring volume is by default a 140 × 30 × 30 mm³ daughter volume of the phantom of identical material; though for microbeam analysis this is reduced to 140 × 2 × 2 due to memory consumption. Voxel resolution is provided by the user, generally 1 × 1 × 1 mm³ for

broadbeam study, 2 × 2 × 5 mm³ when comparing to the PinPoint™ Ion Chamber, and 1 × 0.01 × 0.1 mm³ for microbeam study. Voxelisation is handled via creation of a C++ standard library vector of G4doubles (double precision floating point numbers) of length equal to the product of the number of voxels in each dimension defined by scorer dimensions and resolutions. Functions to determine vector index corresponding to interaction position and to increment specified vector element by energy deposited are called for every non-zero-energy-deposition interaction within the scoring volume. The vector is then recorded as a numerical python file for post-simulation analysis.

Table 2-8: Hutch 2B beam monitor components (positions relative to He mother volume).

Element	X-Coordinate (centre, mm)	X length (mm)	Y width (mm)	Z height (mm)	Material
He Volume	0	40	100	100	G4_He
Al upstream window	-19.975	0.05	40	40	G4_Al
kapton upstream	-19.925	0.05	40	40	G4_KAPTON
Silicon	0	0.06	50	50	G4_Si
kapton downstream	19.925	0.05	40	40	G4_KAPTON
Al downstream window	19.975	0.05	40	40	G4_Al

2.3.3 G4IMBL primary generator action

For Stage I electron beam simulations, a Gaussian G4GeneralParticleSource electron beam is defined at (-25 m, 0, 0) with a momentum direction (1, 0, 0). The kinetic energy of the beam is defined by a 3.032 ± 0.006 GeV Gaussian energy distribution and a Gaussian position distribution of the particle is applied with Y- and Z-sigma of 320 μm and 16 μm, respectively. Finally, the momentum direction is rotated about the Z-axis in order to account for electron beam excursion in the wiggler. This rotation is henceforth referred to as the electron injection steering angle and must be determined for each particular wiggler field strength to optimise flux intensity and symmetry of the beam about the Y- and Z-origins.

For Stage II energy deposition simulations, a G4ParticleGun is defined to import photon information from the user-specified PSF. The position, momentum, polarisation, energy, and weighting data of the photon is read from the file prior to each event. Users may generate a specified number of particles from the PSF (provided that there are more particles in the PSF than are requested by the user) or they may use a G4UserDefinedFunction to allow the program to automatically obtain and run the total number of particles in the PSF.

The use of PSFs containing a population of shaped, filtered, and collimated photons near to the

entrance of the photon is the most significant variance reduction technique in this simulation, as once a PSF of satisfactory statistics has been produced, it may be used in Stage II simulations indefinitely, without the need for Stage I simulations of that particular beamline configuration again. However, this introduces the requirement that PSFs be produced for every unique beamline configuration that one desires to investigate – any alteration to the wiggler strength, filtration, beam dimensions, physical parameters, or geometry upstream of the PSF position will require production of a new PSF through Stage I simulations.

2.4 Stage I simulations

Prior to the production of PSFs for Stage II simulations, the production of synchrotron radiation within the wiggler was examined.

2.4.1 Electron interactions with the wiggler magnetic field

To confirm correct functioning of the sinusoidal magnetic field a sample electron was transported through the wiggler and information was recorded for each interaction. The path of the electron through the wiggler was mapped in Figure 2.5.

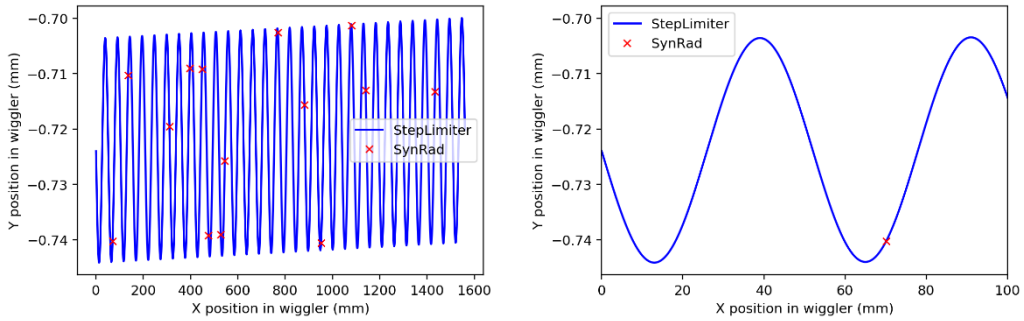

Figure 2.5: Path (XY) of an electron through the wiggler, showing positions of all interactions. A snapshot of the first two periods is shown to the right.

The step limit of 1 mm is necessary to correct pathing through the wiggler because the initial step into the volume calculates a probability of interaction based on a magnetic field strength of 0 T. This results in a mean-free-path of interaction that is set to Geant4's maximum float value and thus, lacking any other process to force interaction within the wiggler, the particle is transported to the end of the volume. The current step size is sufficient to force recalculations that interact with a non-zero magnetic field, thereby tracing a sinusoidal path as required.

2.4.2 Geant4 synchrotron radiation production in a wiggler

A limitation of the G4SynchrotronRadiation (synRad) process is that it was designed for use in

uniform magnetic fields, such as may be found in the bending magnet, rather than the sinusoidal magnetic field throughout the length of the wiggler. A changing magnetic field strength implies a changing mean-free-path of interaction, as described by (2.1), and thus a variable probability of synchrotron radiation production depending upon the position in the wiggler. An investigation of synchrotron radiation production in the wiggler is necessary to determine the presence of artifacts due to using the model outside of the conditions for which it was designed.

2.4.2.1 Mean-free-path of synchrotron radiation production

The mean-free-path of interaction of synchrotron radiation production is displayed graphically for one period of a 3.0 T wiggler in Figure 2.6.

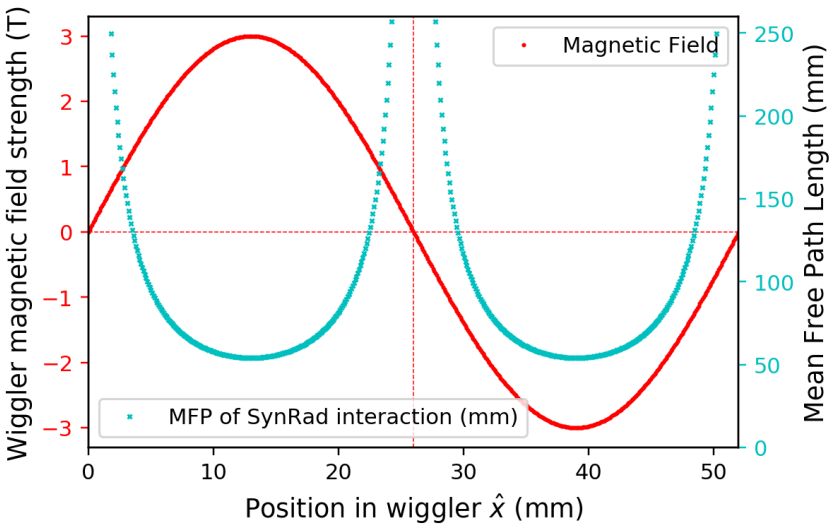

Figure 2.6: Magnetic field strength and mean-free-path of interaction for a single period in the 3.0 T wiggler.

An average mean-free-path of synRad interaction in the wiggler is difficult to calculate due to the mean-free-path asymptotes that arise when magnetic field strength is 0 T. An alternative is to divide the wiggler length by the average number of synRad interactions in the wiggler per electron to produce an 'effective' mean-free-path. Simulations were performed for single electrons using unique random seeds, for a variety of step sizes, and synRad process interaction numbers were obtained (Table 2-9).

Table 2-9: SynRad interactions in the wiggler for different step sizes.

Step limit (mm)	Mean number of synRad interactions across 10 runs	Std. Dev. of synRad interactions across 10 runs	Relative uncertainty
0.5	19.9	5.66	28.5%
1	15.9	3.67	23.1%
5	20.7	4.34	21.0%
10	18.1	3.65	20.1%
25	15.4	3.8	24.7%
50	15.5	4.03	26.0%
60	18	3.71	20.6%
Mean	17.64		
Standard deviation	2.14		
Relative uncertainty	12%		

Using the mean number of synRad interactions across all simulated step sizes of 17.64, an effective mean-free-path of interaction of 88.44 ± 10.61 mm may be calculated for the 3 T wiggler. This is larger than the calculated mean-free-path of 54 mm in a uniform magnetic field of 3.0 T and does not agree within uncertainty. Alteration of the step limit size does not appear to display a trend over the range tested, though step sizes much larger than the period of the wiggler are not advised. Likewise, decreasing the step limit size does not appear to effect total number of synRad interactions, but smaller step limits will require greater memory and runtime due to the larger number of forced transportation interactions.

2.4.2.2 Formation length of synchrotron radiation

The formation length described by (2.2) is also of interest as the limiting factor determining the validity of synRad production in a magnetic field. The formation length changes with respect to magnetic field strength due to the change in radius of curvature of the electron and follows the trend of the mean-free-path of synRad interaction, with minima at the maximum amplitude of magnetic field strength and asymptotes as the magnetic field strength approaches 0 T. The formation length for the 3.0 T wiggler is shown in Figure 2.7.

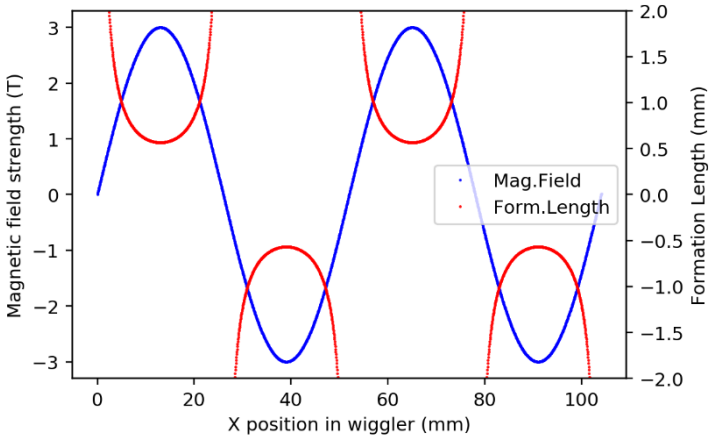

Figure 2.7: Formation length in a 3.0 T wiggler (2 periods).

This wiggler has a formation length of less than 2 mm for part of its length and formation length increases inversely proportional to magnetic field strength. To determine validity of the model for this insertion device the change in magnetic field across the formation length was determined at each point across two periods of the wiggler (Figure 2.8).

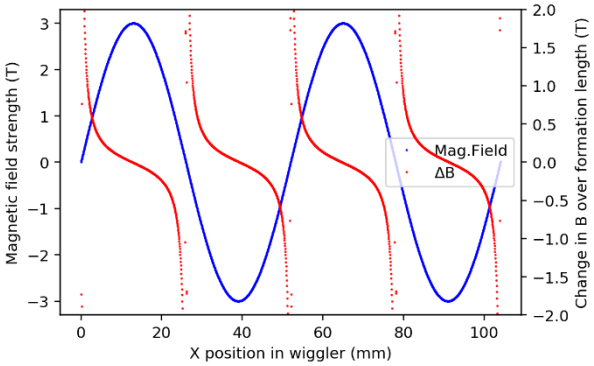

Figure 2.8: Change of magnetic field strength and formation length in a 3.0 T wiggler (2 periods).

The magnetic field is most stable across small formation lengths and thus closest to the magnetic field peaks, with increasing difference as magnetic field strength approaches 0 T. Approximately 49% of the wiggler has a change in magnetic field strength over the formation length of less than 0.2 T (6.67% of max strength). Approximately 30% of the wiggler has a change in magnetic field strength over the formation length of less than 0.1 T (3.33% of maximum strength).

2.4.2.3 Discussion of the validity of synRad in a wiggler

No quantitative values are provided in the Geant4 Physics Reference Manual for determining what magnitudes of change of the magnetic field may be considered ‘approximately constant over the formation length’. The smaller the restriction for ‘approximately constant,’ the smaller the areas of the wiggler that the synRad process may be considered valid. However, there may be a mitigating

factor in that the probability of synchrotron radiation production is low in areas of large change of magnetic field strength, due to the similar trend of the mean-free-path of interaction. This is supported by Figure 2.5, which shows very few interactions at the middle of the wave-trajectory, where the magnetic field is close to 0 T.

In the absence of a model of synchrotron radiation production within insertion devices, the current synRad process must be used in spite of concerns regarding the stated area of validity. These factors will simply be taken into account should major discrepancies to theoretical or experimental results arise.

2.4.3 Electron steering angle optimisation

The electron injection steering angle for each wiggler field strength was optimised by simulating Stage I PSF accumulation for a number of angles with an identical number of primary electrons, then determining the average Y-position of all particles at that angle. An optimised beam trends towards maximum photon flux and a symmetrical distribution about the Y-axis; that is, a mean Y-position of zero. Determination of optimised electron injection for 1.4 T, 2.0 T, and 3.0 T fields are shown in Figure 2.9, Figure 2.10, and Figure 2.11 respectively. Plots of the energy spectra and the Y-intensity profiles of a portion of the total number of angles are included to illustrate the effect of improper electron steering angle on spectral shape and intensity, and beam position. In the case of 3.0 T, the PSF was placed 10 mm after the end of the wiggler, hence the shape of the 3.0 T energy spectrum is different to subsequent 3T-AlAl spectra. As the primary concern of the electron steering angle study is the position of particles the low-energy threshold of 40 keV was retained as the lack of the low energy component has minimal effect on mean photon position. The effect of different field shape on optimised electron steering angle are shown in Figure 2.12 for the standard field shape, a negative sinusoid, and a square-wave shape. Optimised electron steering angles are tabulated in Table 2-10.

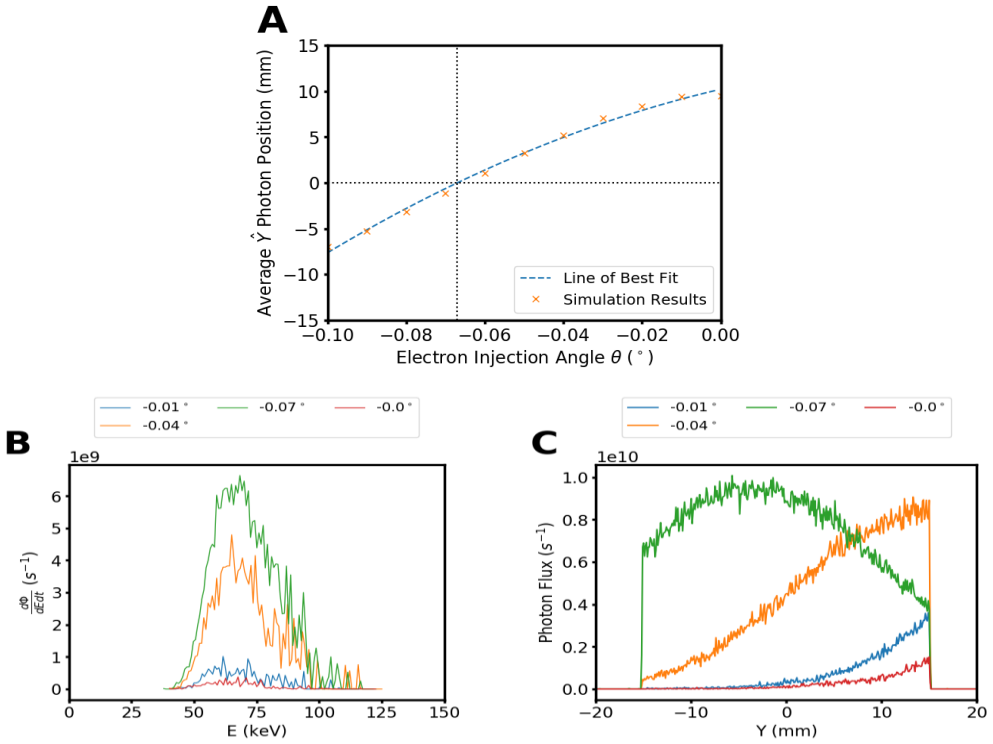

Figure 2.9: 1.4 T electron steering angle study (PSF at phantom).
(A) Mean Y-position for each angle; (B) energy spectrum at some angles; (C) Y-intensity profile at some angles.

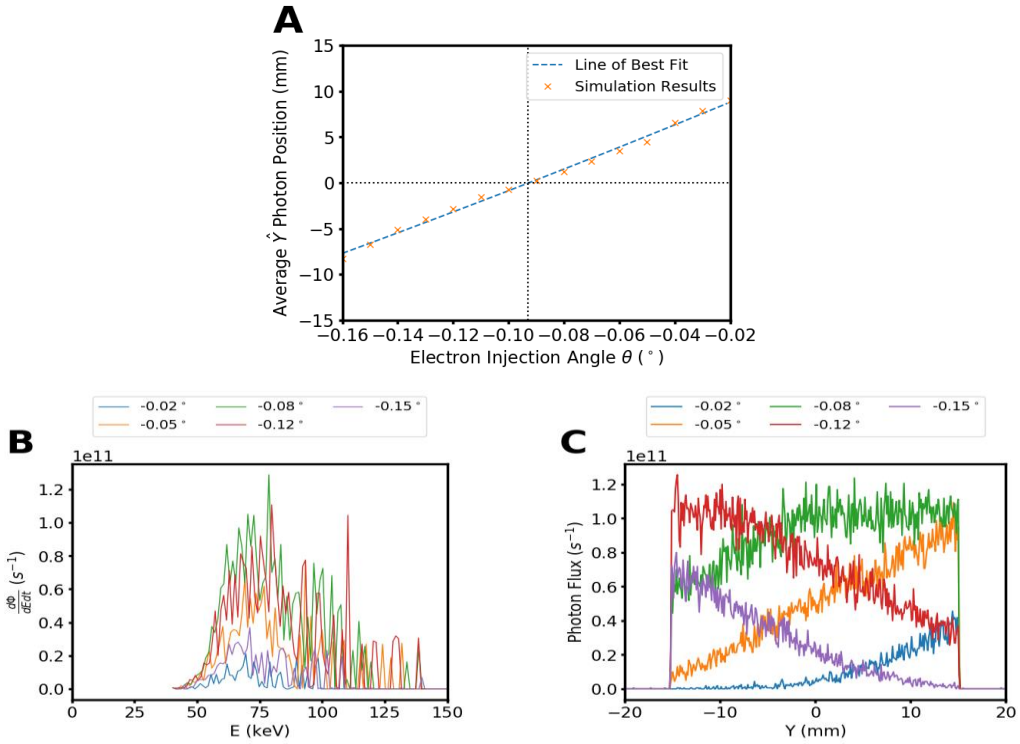

Figure 2.10: 2 T electron steering angle study (PSF at phantom).
(A) Mean Y-position for each angle; (B) energy spectrum at some angles; (C) Y-intensity profile at some angles.

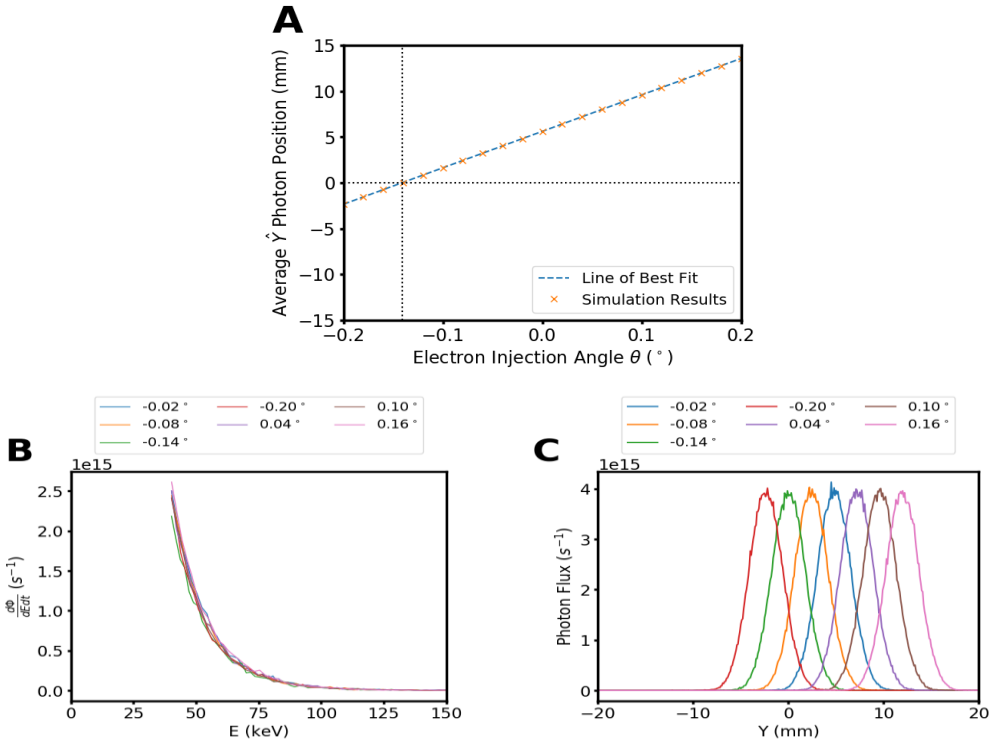

Figure 2.11: 3 T electron steering angle study (PSF at wiggler, 40 keV low-energy threshold). (A) Mean Y-position for each angle; (B) energy spectrum at some angles; (C) Y-intensity profile at some angles.

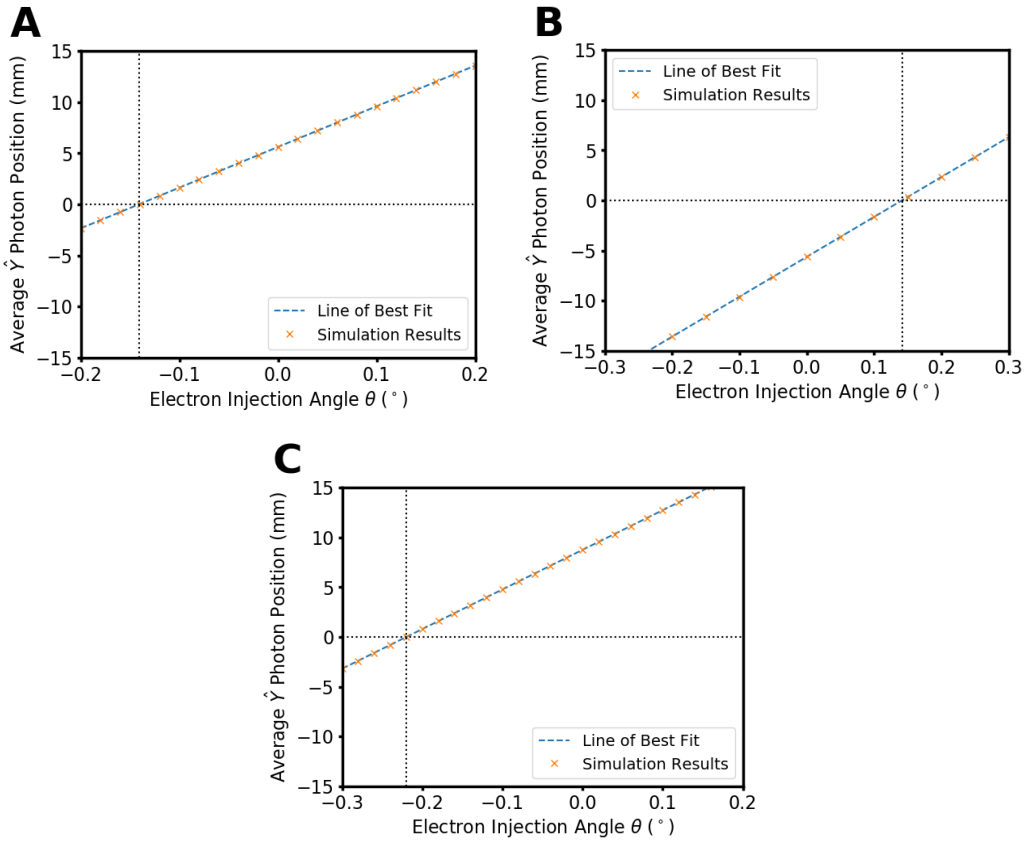

Figure 2.12. Electron steering angles for nonstandard 3T wiggler fields. (A) 3T sinusoid, (B) 3T negative sinusoid, (C) 3T square-wave wiggler.

Table 2-10: Optimised electron steering angle for standard wiggler field strengths.

	1.4 T	2.0 T	3.0 T	3.0 T (-sin)	3.0 T (Square)
Electron steering angle (°)	-0.065	-0.093	-0.141	+0.142	-0.22

A trend is observed that stronger magnetic fields require larger electron steering angles to correct beam excursion in the wiggler. Additionally, it is observed that a negative sinusoid of otherwise identical parameters will result in an electron steering angle that is of the same magnitude but opposite sign. A square wave magnetic field of identical frequency and amplitude as the normal sinusoid requires a greater magnitude of electron steering angle to correct for beam excursion. Optimised electron steering angle can therefore be assumed to differ for all wiggle fields and must be determined for any new beamline models for all relevant field strengths and shapes in order to maximise beam intensity and symmetry.

2.4.4 Populating PSFs near the phantom

2.4.4.1 Methods

Once the electron steering angle has been optimised for the chosen beam configuration, validation of the photon energy spectrum may proceed. The G4IMBL energy spectrum is compared against

the theoretical energy spectrum for the chosen beam configuration as generated via SPEC. Generation of the theoretical spectrum requires distance from the source, wiggler field strength, and thicknesses of all intervening materials, which are recorded for standard simulation configurations in Table 2-11. All G4IMBL energy spectra were analysed using numerical python by placing PSF photons into a weighted energy histogram of range 0 to 1000 keV and resolution of 0.1 keV. The weighting applied to each energy bin converts number of photons into flux (s^{-1}) by dividing histogram bin counts by equivalent experimental time (s). Equivalent experimental time (T) is calculated using

$$T = N_e \times \frac{I}{e} \qquad (2.4)$$

where N_e is the total number of electrons simulated to generate the PSF as discussed in 2.3.3 , *I* the beam current (200 mA), and e the charge of an electron in coulombs. This method permits comparison of PSFs with differing numbers of simulated electrons, and comparison against SPEC energy spectra given in units of s^{-1}.

The targeted configurations were 1.4T-AlAl, 2T-CuAl, and 3T-CuCu, as these were common beamline configurations for experimentation by CMRP at the AS IMBL during this thesis. Previous experimental setups also informed the selection of beam sizes to simulate for each configuration.

For 1.4T-AlAl the beam sizes were 30 × 1.2 mm², 30 × 0.6 mm², and 30 × 0.2 mm² (YZ) and the low-energy threshold was set to be 20 keV to allow for resolution of the full energy spectrum.

For 2T-CuAl and 3T-CuCu the beam sizes were 30 × 2.014 mm², 30 × 1.053 mm², 30 × 0.532 mm² (YZ), and the low-energy threshold was set to be 40 keV due to the harder expected energy spectra.

The dotted horizontal line in single-beam-size energy spectra represents 50% of the maximum flux of the SPEC energy spectrum. The resolution of the eponymous axis in Y- and Z-intensity profiles was set to be 0.1 mm and 0.01 mm respectively.

Table 2-11: Total thickness of materials from source to phantom (excluding filter paddles 4 and 5).

Element	Total thickness (mm)
G4_Galactic	21,185.46
G4_He	1,915
G4_C	12.54
G4_Al	0.25
G4_Be	1.05
G4_KAPTON	0.2
G4_AIR	5,059.17
G4_Si	0.12

2.4.4.2 Results

The 1.4T-AlAl case is shown in Figure 2.13. The Z-intensity profile full widths at the half-maximum (FWHMs) agree with geometrical size of the BDA within the uncertainty of 0.01 mm. Y-intensity profiles show some divergence from the 30-mm-wide BDA as FWHMs vary between 35.1 and 34.7 mm. Comparisons between SPEC and G4IMBL show a disagreement in flux, with G4IMBL results for all field sizes ~70% of the flux expected by SPEC

The 2T-CuAl and 3T-CuCu cases, are shown in Figure 2.14 and Figure 2.15, respectively. Z-intensity profile FWHMs agree with geometrical size of the BDA within the uncertainty of 0.01 mm and Y-intensity profiles agree within 0.1 mm. Comparisons between SPEC and G4IMBL show a disagreement in flux, with G4IMBL results for all field sizes ~45% of the expected flux in 2T-CuAl and ~50% in 3T-CuCu.

The good agreement of the Z-profiles with the expected FWHMs in all cases show that the geometry attenuates and shapes the beam as expected. Good agreement is seen for Y-profile FWHMs with expected values in the 2T-CuAl and 3T-CuCu cases, but there is an approximately ~20% greater simulated FWHM than expected for the 1.4T-AlAl case. Because of the fact that most experiments in Hutch 2B involve the use of conformal masks with apertures of 20 × 20 mm^2 or less, this broadening of the lateral FWHM should not be significant for any simulations involving the conformal mask.

Due to the large discrepancies in the calculated flux in the PSFs it is not advised to use G4IMBL spectra in their current state for simulation of dose deposition in a phantom. Further investigation is necessary to determine and correct the cause of the discrepancies in flux.

However, visual comparison between G4IMBL and SPEC spectra shows that the overall shape of the energy spectra is as expected. This suggest that the use of normalised spectra may be worth investigating.

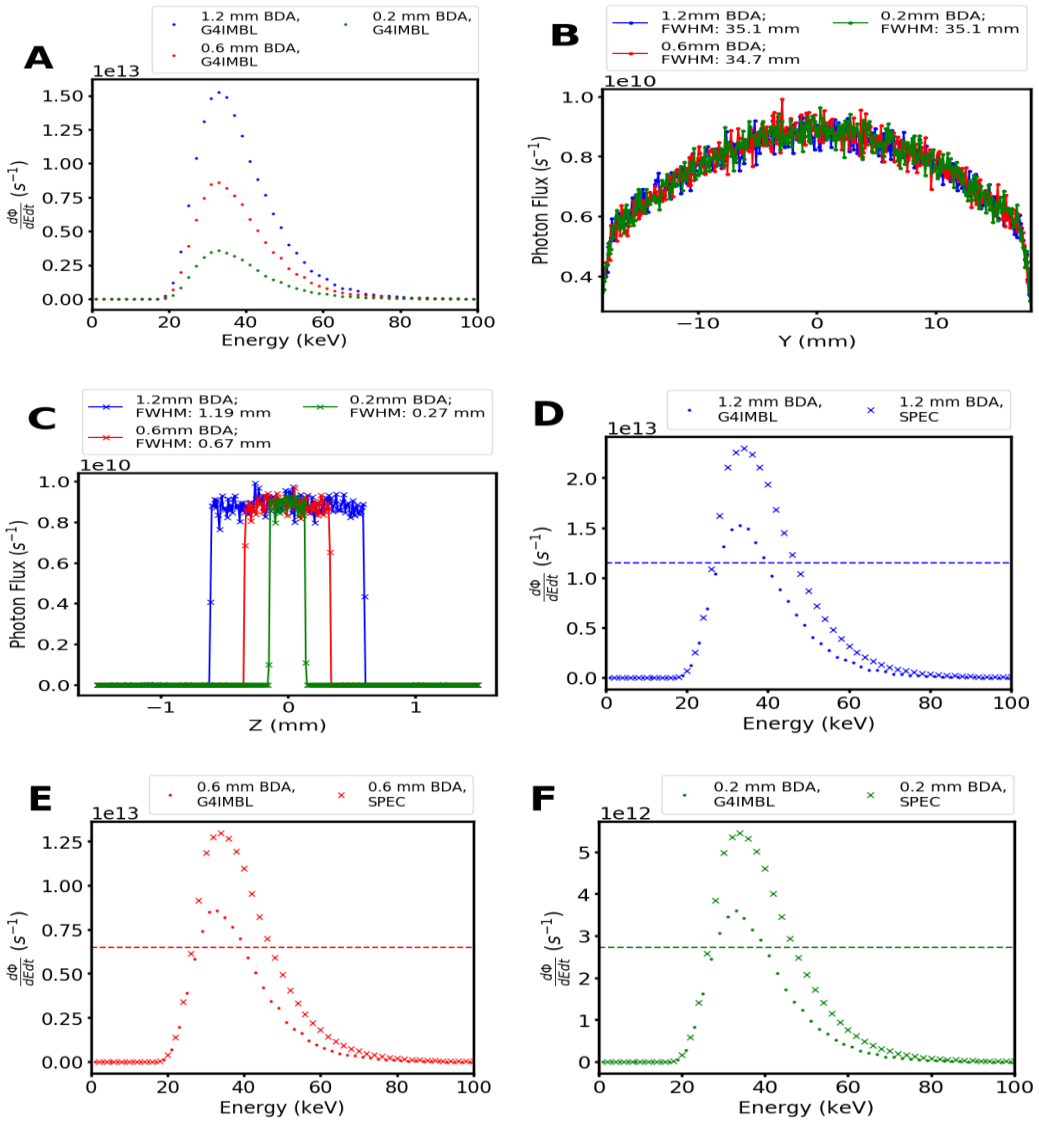

Figure 2.13: Analysis of G4IMBL 1.4T-AlAl PSF spectral properties.
(A) energy spectra for all BDAs; (B) Y-intensity profile for all BDAs; (C) Z-intensity profile for all BDAs; (D) energy spectrum for 2.014 mm BDA, compared with SPEC; (E) energy spectrum for 1.053 mm BDA, compared with SPEC; (F) energy spectrum for 0.532 mm BDA, compared with SPEC.

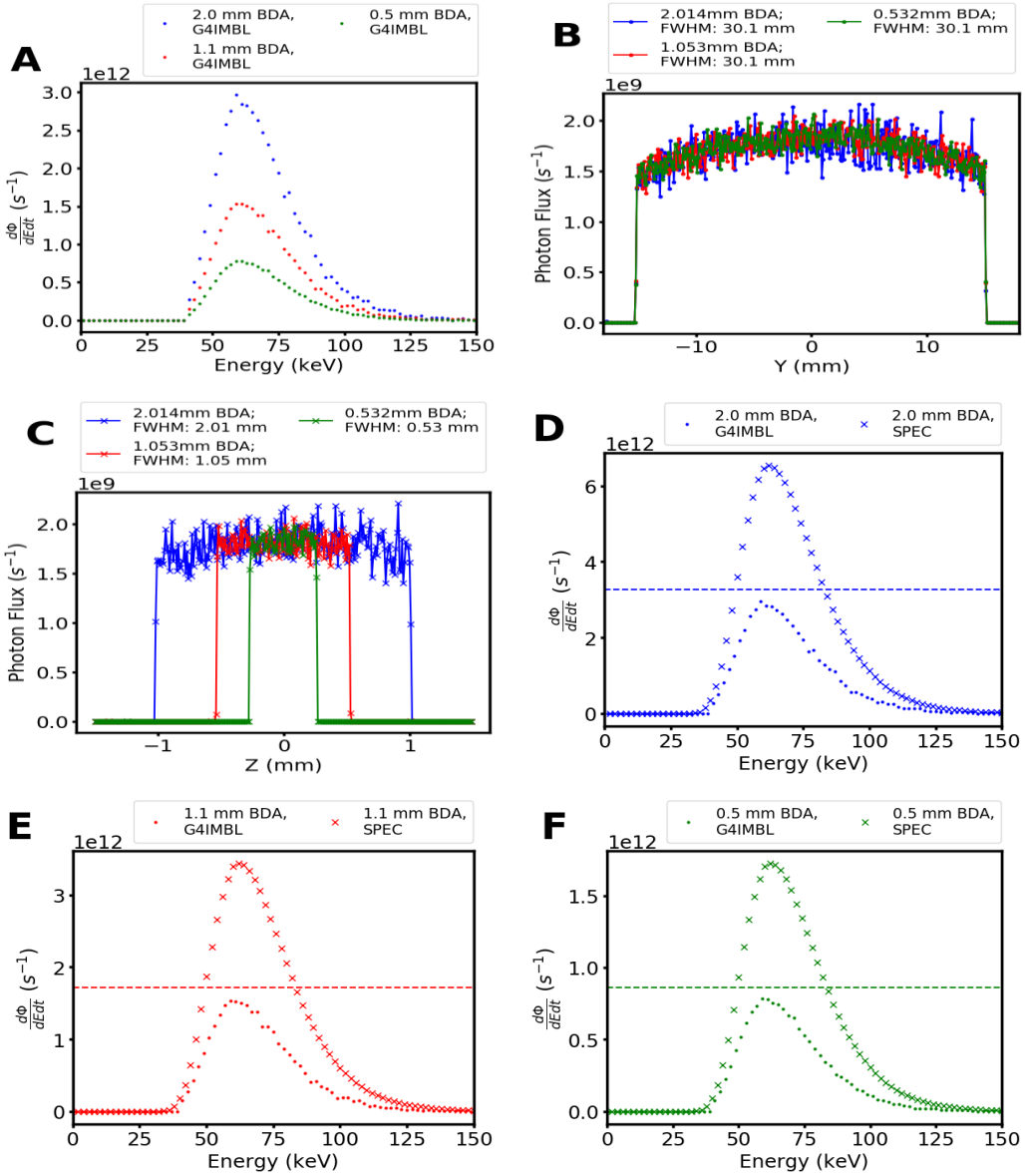

Figure 2.14: Analysis of G4IMBL 2T-CuAl PSF spectral properties.
(A) energy spectra for all BDAs; (B) Y-intensity profile for all BDAs; (C) Z-intensity profile for all BDAs; (D) energy spectrum for 2.014 mm BDA, compared with SPEC; (E) energy spectrum for 1.053 mm BDA, compared with SPEC; (F) energy spectrum for 0.532 mm BDA, compared with SPEC.

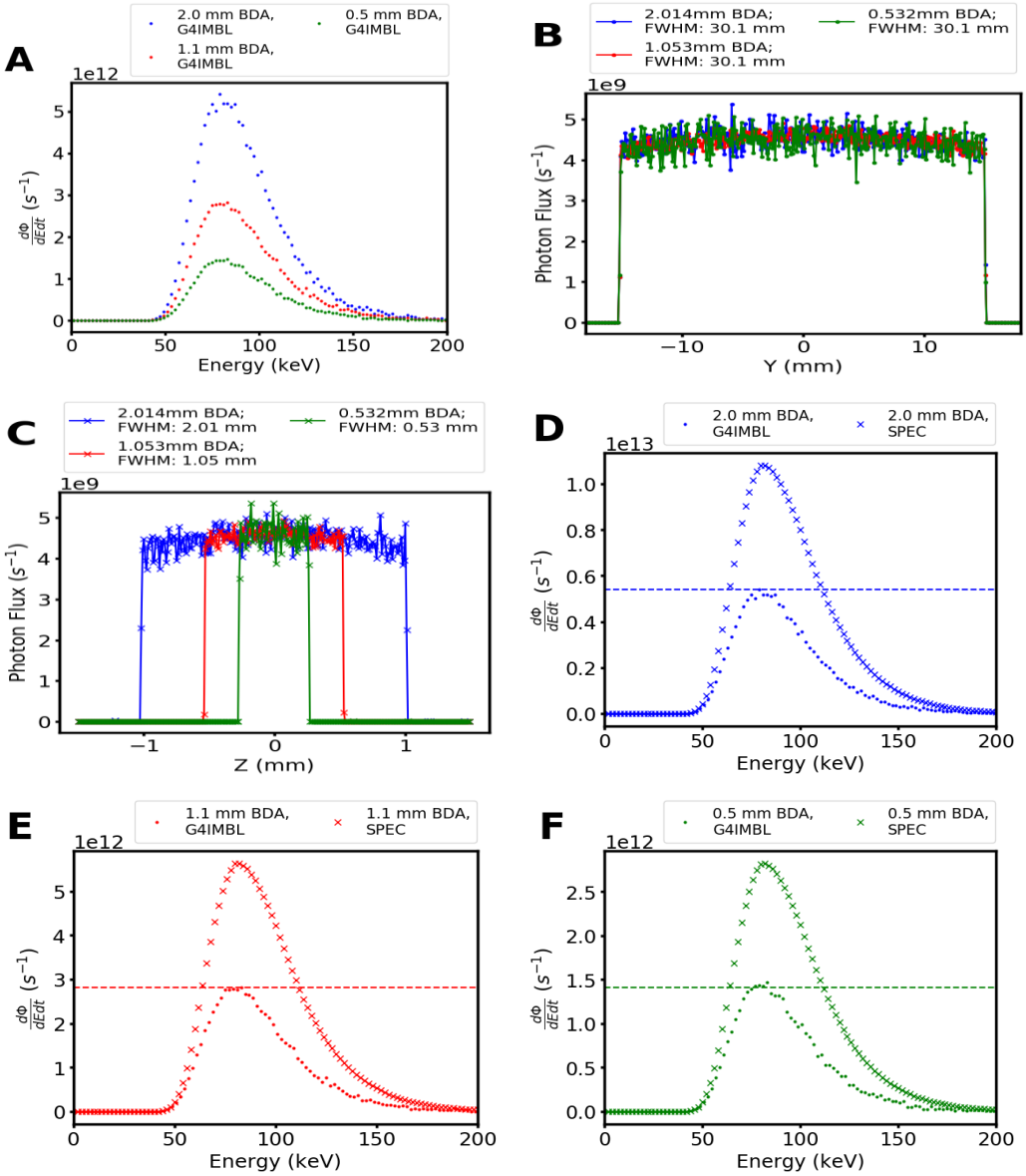

Figure 2.15: Analysis of G4IMBL 3T-CuCu PSF spectral properties.
(A) energy spectra for all BDAs; (B) Y-intensity profile for all BDAs; (C) Z-intensity profile for all BDAs; (D) energy spectrum for 2.014 mm BDA, compared with SPEC; (E) energy spectrum for 1.053 mm BDA, compared with SPEC; (F) energy spectrum for 0.532 mm BDA, compared with SPEC.

2.4.4.3 Normalised results and discussion

To address the issue of flux discrepancy it was decided to examine the normalised energy spectra of the three PSF configurations against normalised SPEC spectra, shown in Figure 2.16.

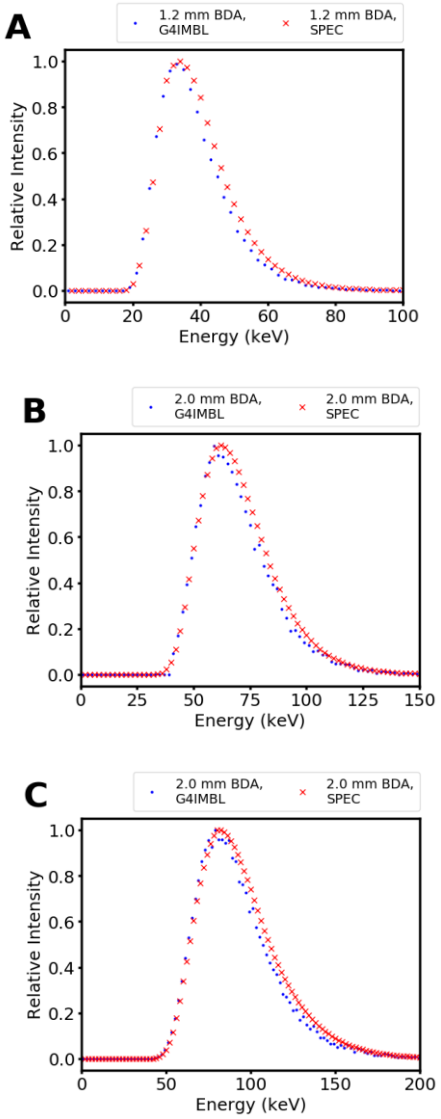

Figure 2.16: Normalised G4IMBL energy spectra compared with SPEC.
(A) 1.4T-AlAl, 1.2 mm BDA; (B) 2T-CuAl, 2.014 mm BDA; (C) 3T-CuCu, 2.014 mm BDA.

It is immediately apparent that the normalised PSF spectra are much closer to agreement with normalised SPEC spectra. Note that only the largest BDA is shown for each configuration in Figure 2.16 because normalisation to the integral flux of the spectrum cancels out flux deviations due to BDA size. Thus, all normalised spectra for smaller BDAs are nearly identical to the normalised spectrum of the largest BDA for that configuration. Relevant spectral quantities have been calculated and tabulated (Table 2-12) to determine agreement between the normalised G4IMBL and SPEC spectra.

Table 2-12: Comparison of G4IMBL to SPEC for normalised energy spectra.

	1.4T-AlAl		2T-CuAl		3T-CuCu	
	G4IMBL	SPEC	G4IMBL	SPEC	G4IMBL	SPEC
Mean energy (keV)	38.16	39.72	69.31	70.73	91.78	94.63
Modal energy (keV)	32	33.7	60.9	61.9	79	81
Standard deviation (keV)	10.43	11.02	16.65	17.21	24.04	25.09
Standard error of the mean (keV)	0	0	0.01	0	0.01	0
Critical energy (keV)	36.3	37.7	66.5	67.9	87.6	90.2

The mean energies of G4IMBL are smaller than expected by SPEC by 1.56, 1.42, and 2.85 keV for 1.4 T, 2 T, and 3 T respectively. The most frequent photon energies of G4IMBL are also consistently lower than SPEC values by 1.7, 1, and 2 keV respectively. Additionally, the mode is a lower energy than the mean in all cases, with consistent difference of ~6, ~9, and ~13 keV for G4IMBL and SPEC under each configuration. The G4IMBL standard deviation of the spectra are smaller than SPEC in all cases: 0.59, 0.56, and 1.05 keV respectively. The standard error of the mean of all spectra are near zero as expected for such large sample sizes in G4IMBL and small histogram bin width in G4IBML and SPEC results.

Finally, the critical energy (the energy that divides the spectrum flux equally both above and below) was calculated from the cumulative frequency distributions of the spectra. G4IMBL calculates critical energies that are 1.4, 1.4, and 2.6 keV smaller than SPEC results for 1.4 T, 2 T, and 3 T, respectively. Overall, normalised G4IMBL spectra are slightly softer than SPEC predicts, but the single-digit differences are small compared to the range of the spectra (e.g. a 2 keV difference for a 50–150 keV spectrum, which is ~2% of the median value, 100 keV).

These results indicate that the normalised photon energy spectra produced by G4IMBL are in agreement with normalised SPEC spectra. A closer examination of the output of the wiggler absent all attenuation is necessary to reconcile the agreement of normalised spectra with SPEC results and the disagreement of non-normalised spectra with SPEC results.

2.4.5 Output of the 3 T wiggler (G4IMBL vs SPEC)

The discrepancies in photon flux between G4IMBL results and SPEC were investigated by comparison of the spectrum exiting the 3.0 T wiggler using a PSF positioned at 1 m from the source, between the wiggler and the bending magnet. The low-energy limit for production of synchrotron radiation was set to 1 keV, and the step size in the wiggler was set to 0.1 mm. Photons were collected for 1000 electrons over 1000 jobs and resulting PSFs were merged.

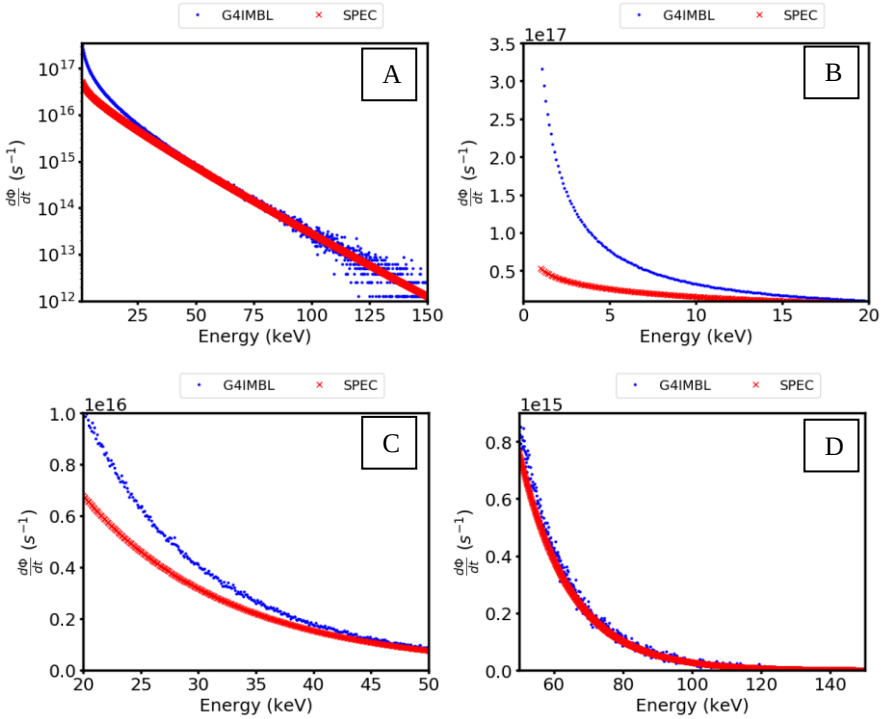

Figure 2.17: Comparison of simulated G4IMBL spectrum from 3.0 T wiggler to SPEC spectrum. (A) logarithmic scale of 0–150 keV window; (B) 0–20 keV window; (C) 20–50 keV window; (D) 50–150 keV window.

2.4.5.1 Results

G4IMBL is shown in Figure 2.17 to overestimate the low-energy component of the 3.0 T wiggler spectrum significantly for energies lower than 30 keV. Across the entire spectrum, G4IMBL produces 9.26×10^6 photons, which may be converted to photon flux by calculation of time elapsed for the number of simulated electrons to pass through the wiggler in reality for a 3 GeV, 200 mA electron beam. The photon flux is determined to be 1.16×10^{19} photons per second. SPEC is calculated to produce 4.42×10^{18} photons per second and thus the ratio of G4IMBL flux to SPEC flux is 2.576. This particular ratio does not properly account for the changing magnitude of difference across the entire spectrum and so analysis of smaller windows is necessary to properly describe the relationship of G4IMBL and SPEC photon fluences.

For a 0–20 keV window, G4IMBL produces 8.16×10^6 photons, which corresponds to 1.02×10^{19} photons per second. SPEC predicts 3.5×10^{18} per second in this window, and thus the ratio of G4IMBL production to SPEC is 2.922. This improves for a window of 20–50 keV, where G4IMBL produces 8.43×10^5 photons corresponding to 1.05×10^{18} per second, SPEC predicts 8.13×10^{17} per second. The flux ratio is 1.299 for this window. For the window 50–150 keV G4IMBL produces 9.7×10^5 photons (1.2×10^{17} per second), SPEC produces 1.13×10^{17} per second, and the flux ratio

becomes 1.07. As 98% of spectrum is below 150 keV, there is no need to examine agreement for windows greater than 150 keV.

2.4.5.2 Conclusion

Based on the windowed approach, the photon fluxes agree (7% difference in integrals) for energies >50 keV but diverge at lower energies as G4IMBL overestimates the photon flux compared to SPEC. Therefore, it appears that the probability distribution of G4IMBL photon energies is weighted to lower energies, which produces a greater proportion of lower energy photons than expected. This does not appear in the filtered photon spectra at the phantom because transportation through the beamline and filtration all energies lower than 50 keV have been absorbed, but the remaining higher energy flux is less than it should be based off of the number of electrons simulated. This disagreement at low energies has been reported to the Geant4 development team and further investigation is underway. In the meantime, G4IMBL will be used only for spectra with a minimum photon energy of 30 keV, and all comparisons to theoretical spectra will be performed using normalisation. Stage I PSFs are recommended to be used for Stage II dose delivery simulations under the condition that Stage II results be compared to experimental doses:

- using appropriate calibration factors to account for the systematic flux discrepancy of the simulated energy spectra to the expected energy spectra, or,
- as relative dose-profiles, normalised to an appropriate response (e.g. the response at 20 mm depth, or the maximum response of a lateral profile).

2.5 Stage II: Energy deposition and dose delivery in the phantom

With the completion of the study of Stage I simulation outputs, the production of a library of BB and MB PSFs for a variety of beamline configurations was able to commence and, following that, the execution of Stage II simulation studies. Of particular importance for the purposes of MRT treatment planning and dose verification are the behaviour of the energy spectrum at different locations within a phantom (or patient) and the accurate simulation of energy deposition in voxellised volumes, both of which are discussed below.

2.5.1 Spectral changes in the phantom

The low energy spectra available to synchrotron radiation is of interest to researchers that require targeted energy deposition to a sample (e.g. targeted nanoparticle therapy) in conjunction with microbeam field geometry. Selection of appropriate wiggler strength and filtration allows users to

select an appropriate incident energy spectrum to suit their needs, which may be verified by SPEC and G4IMBL. Depending on the phantom material and the depth required, hardening of the energy spectrum is expected, thus the behaviour of the spectrum as it traverses the phantom was investigated.

2.5.1.1 Methods

The typical phase-space scoring volume dimensions were altered to 140 × 100 × 100 mm³, identical to the phantom geometry, and placed overlapping the phantom position. A Stage II simulation was performed with both parameterised motion and voxelised energy-deposition volume not activated. Pre-step and post-step positions and particle kinetic energy were recorded for all interactions for all photons within the phantom to be analysed with numerical python post-simulation. 140 energy-histograms were created for each 1 × 100 × 100 mm³ slice of the phantom and kinetic energy of all photons that traversed each slice without interacting were binned and recorded (that is, the pre-step energy). Comparison of pre-step and post-step positions of each interaction for each unique photon allows identification of backscattered particles. For each slice, three energy histograms were produced: the total energy spectrum, the backscattered spectrum, and the spectrum without backscatter; denoted 'full', 'backscatter-only' (BSO), and 'backscatterless' (BSL) henceforth. Full, BSO, and BSL spectra at various depths have been produced for 3T-CuCu and are compared to the incident spectrum from the PSF in the first slice (0–1 mm X), and to the first-slice spectrum at subsequent depths. To quantify the overall behaviour of the spectra the mean energy and standard error of the mean were determined for all spectra in each slice.

2.5.1.2 Results

3T-CuCu results for full, BSL, and BSO spectra are shown in Figure 2.18, Figure 2.19 , and Figure 2.20 respectively. The full spectrum at 0–1 mm (X) is softer than the incident spectrum due to the presence of backscattered photons from deeper in the phantom. It also displays smaller peak intensity due to photon interaction in the first slice via photoelectric effect, which is not recorded by the PSF. Between 10 and 101 mm (X) the spectrum loses intensity but does not soften or harden particularly. The means of the photon spectrum at each depth follow a parabolic softening, then hardening as the amount of backscattered particles increases, then decreases closer to the downstream face of the phantom. However, the range of values is 5 keV, approximately a 6% uncertainty assuming a 'mean-of-all-means' of 85 keV.

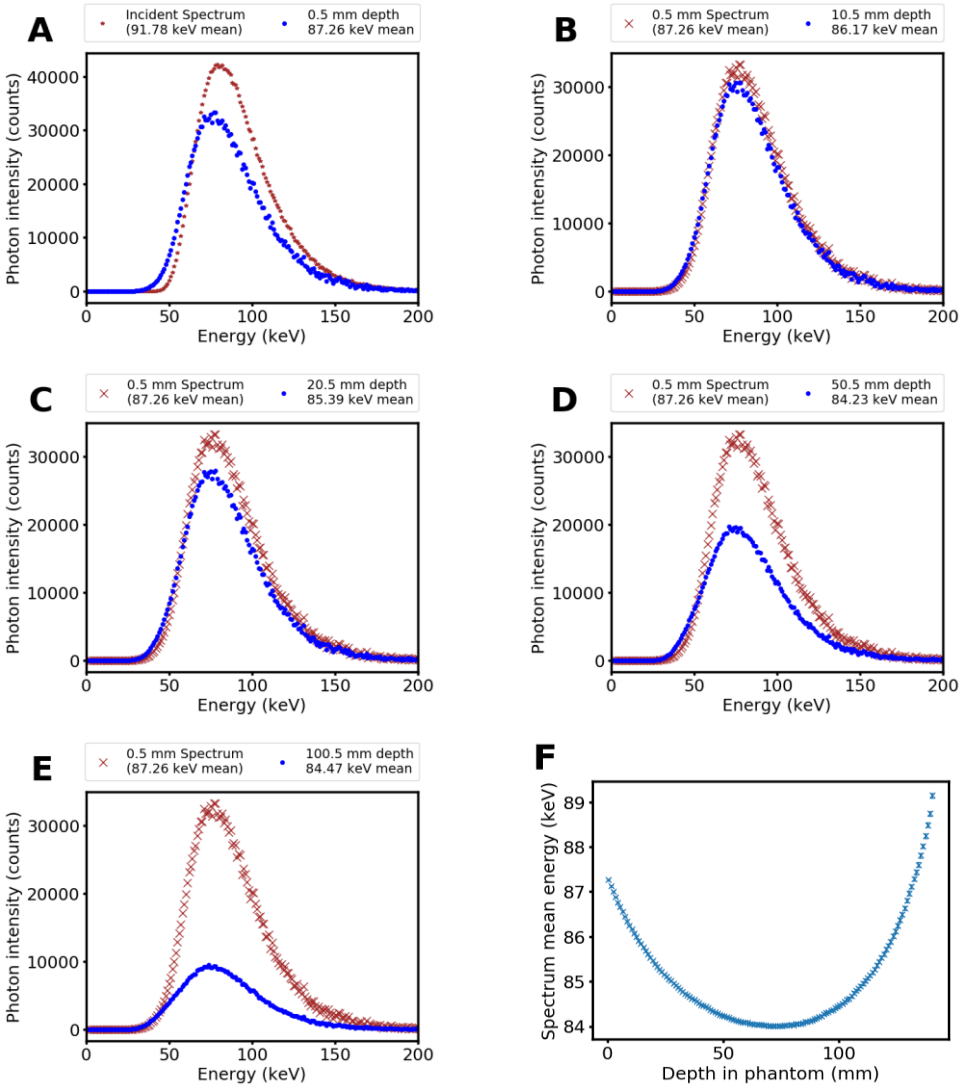

Figure 2.18: Spectral changes with depth in an RMI457 phantom.
(A) 0.5 mm depth with incident spectrum; (B) 10.5 mm depth; (C) 20.5 mm depth; (D) 50.5 mm depth; (E) 100.5 mm depth; (F) Mean energy of full spectrum at each depth.

The BSL spectrum has a lower intensity at shallow depths than the full spectrum due to lack of backscattered photons; at 0–1 mm (X) the full spectrum intensity is ~29,000 counts, where the BSL spectrum is ~27,000 counts. The discrepancy does not appear to change with increasing depth in the phantom; at 100-101 mm the full spectrum has an intensity of ~10,000 and BSL spectra has an intensity of ~6,000 counts. The lack of contribution from backscatter means that the BSL spectrum does not undergo hardening or softening to the same extent as the full spectrum. The range of means is ~1.5 keV, less than half that of the full spectrum range, and the minimum mean of 91.5 keV is greater than the maximum mean of 89 keV in the full spectrum.

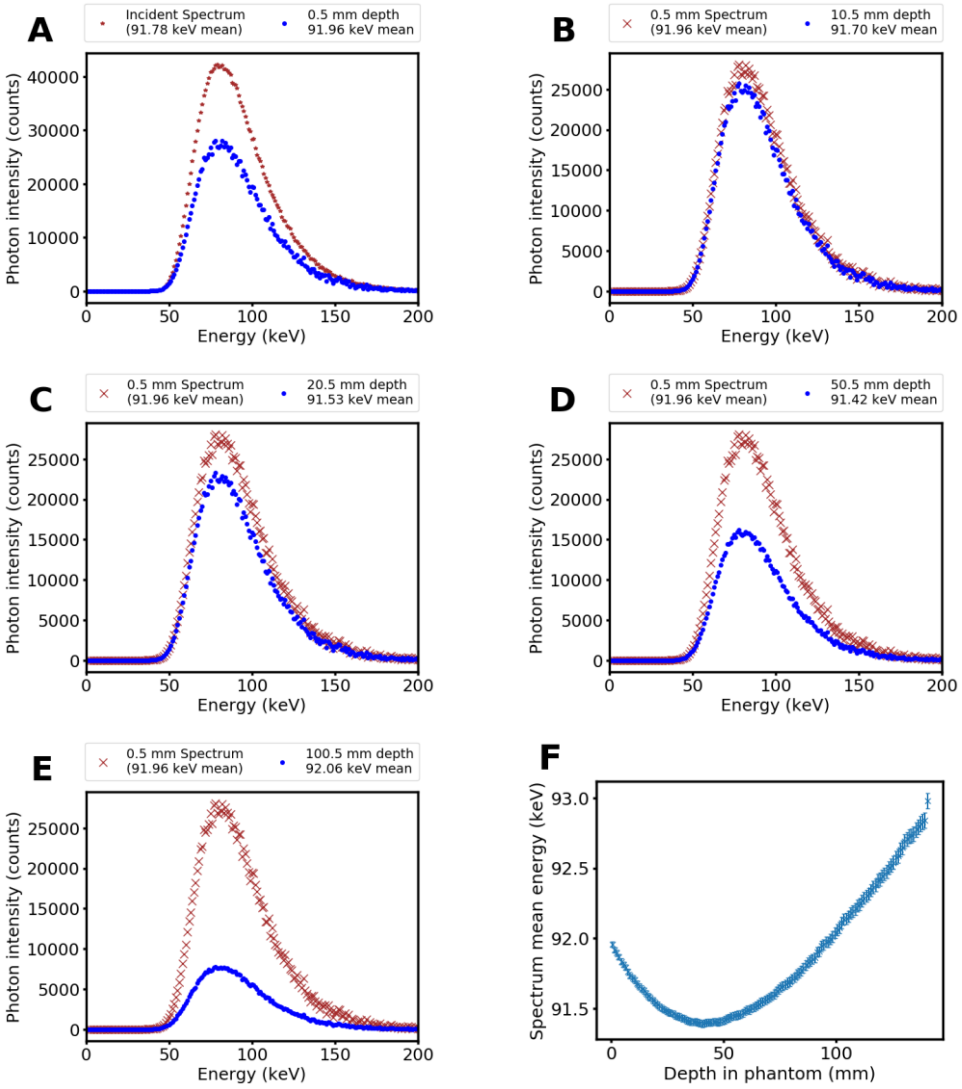

Figure 2.19: Spectral changes at depth in an RMI457 phantom, without backscatter.
(A) 0.5 mm depth with incident spectrum; (B) 10.5 mm depth; (C) 20.5 mm depth; (D) 50.5 mm depth; (E) 100.5 mm depth; (F) Mean energy of BSL spectrum at each depth.

The BSO spectrum is significantly softer and less intense than the incident, full, and BSL spectra, with a maximum intensity of ~10,000, nearly a third of the maximum intensity of the full or BSL spectra. Additionally, the BSO spectra exhibits a constant softening with depth, as opposed to the parabolic motion of the other spectra. The range of means is 10 keV, covering 66 to 56 keV, and thus is both a larger range than the other spectra and has lower maximum than either other spectra's minimum means.

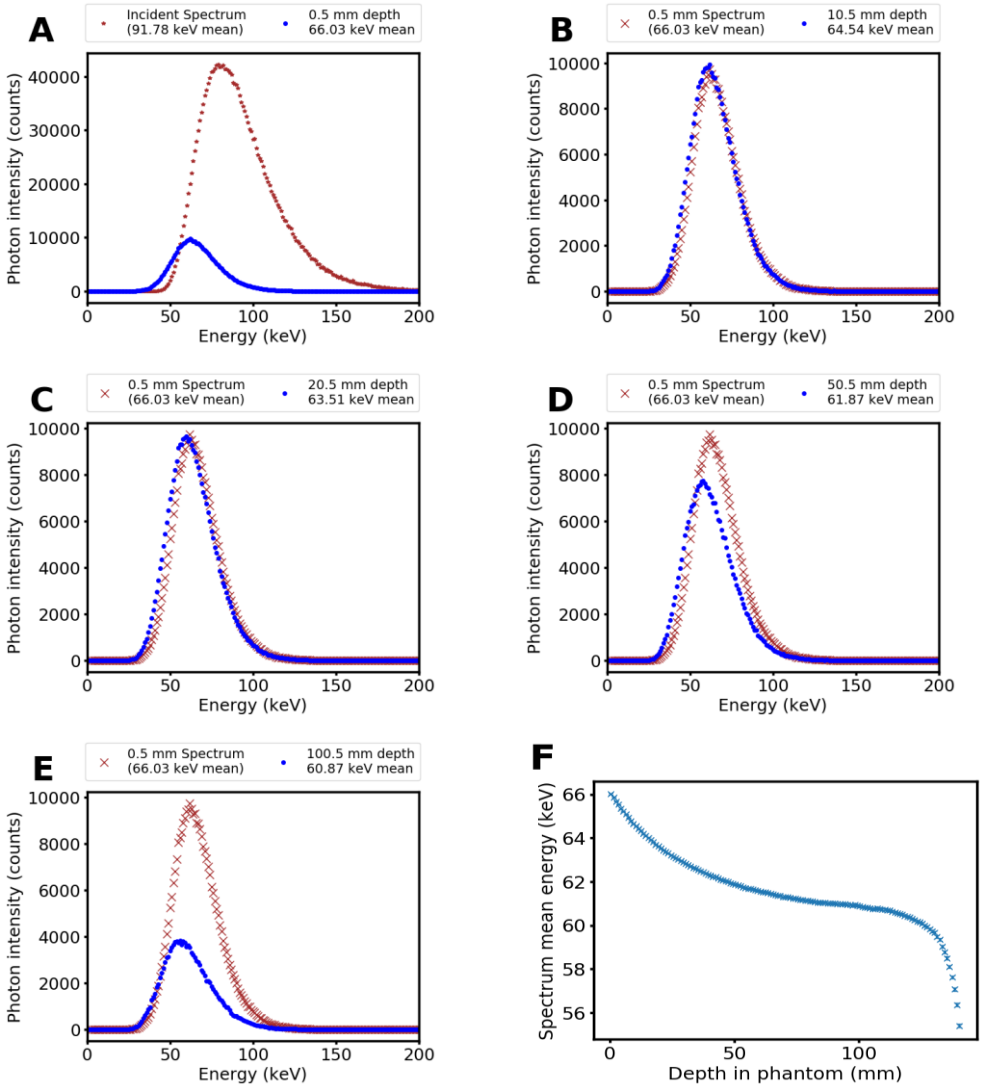

Figure 2.20: Spectral changes at depth in an RMI457 phantom, backscatter only.
(A) 0.5 mm depth with incident spectrum; (B) 10.5 mm depth; (C) 20.5 mm depth; (D) 50.5 mm depth; (E) 100.5 mm depth; (F) Mean energy of BSO spectrum at each depth.

From these results, it can be shown that the spectrum inside the phantom at depth may be significantly different to the incident spectrum due to backscattered photons. Spectral simulations at depth are recommended to be performed by all IMBL users that require precision energy targeting tailored to the specific beamline configuration for their experiments. Alterations in wiggler strength, filtration, and the size and composition of the phantom will alter the spectrum at depth significantly compared to the incident spectrum.

2.5.2 Comparison of G4IMBL dose delivery with experimental results

Validation of energy deposition by comparison to experimental results has been investigated in detail for 3T-CuCu and 2T-CuAl configurations in Dipuglia et al (2019) [16]. For brevity, only the 3T-CuCu results for the 20 × 2.014 mm² field size are discussed here.

2.5.2.1 Method

Stage II dose deposition was simulated for 3T-CuCu with a 30 × 2.014 mm² (YZ) beam with a tungsten mask defining a 20 × 20 mm² (YZ) treatment field size. Simulated results were to be compared against experimental results from a PinPoint™ 31014 Ion Chamber (PTW, Freiburg), and EBT3 Gafchromic® film (International Specialty Products, Wayne, NJ, USA) in a RMI457 Solid Water (Gammex, Middleton, WI, USA) phantom (100 × 100 × 100 mm³). In the broadbeam case, 2 × 2 × 5 mm³ voxels were chosen to match the dimensions of the PinPoint™ sensitive volume for a 100 × 30 × 30 mm³ scoring volume. Production cuts of 1 mm for photons, 0.01 mm for electrons, and a maximum step-limit of 10 µm was applied in the scoring volume. For the microbeam case, 1 × 0.01 × 0.1 mm³ voxels were applied to a 100 × 2 × 2 mm³ scoring volume in order to examine the central five microbeams with 10-µm resolution in the direction of greatest change of dose rate. Production cuts of 0.01 mm for photons and 0.01 mm for electrons, and a step limit of 1 µm in the scoring volume were applied.

One hundred (100) jobs with unique seeds were run and the results averaged prior to analysis. In the broadbeam case the depth-dose profile was taken from the mean dose over a 10 × 10 mm² YZ cross-section for each depth and normalised to the dose at 20 mm depth (Figure 2.21).

2.5.2.2 Results

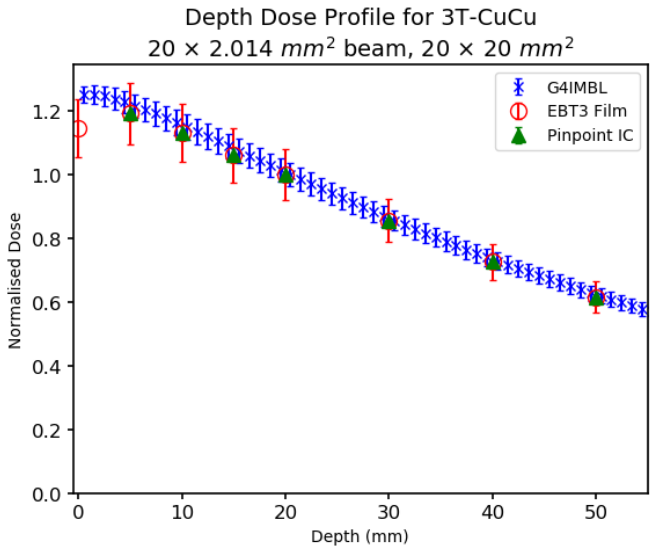

Figure 2.21: Normalised BB dose deposition (to 20 mm depth) in an RMI457 Solid Water phantom. 3T-CuCu, 20 × 2.014 mm² broadbeam dimensions for a 20 × 20 mm² field.

Due to the size constraints of the microbeam array, simulated microbeam results can only be compared against EBT3 and not the pinpoint ionisation chamber. The full width at the half-maximum (FWHM) and the full width at the tenth-maximum (FWTM) were calculated from

simulated results via fitting a Gaussian distribution to the middle microbeam with a resolution of 1-µm steps. The peak-to-valley dose ratio (PVDR) was extracted from the central peak value and an average over 0.2 mm in the valley Y-direction (centred at +0.2 mm (Y) from the peak) and 2 mm in the Z-direction. Analysis of the FWHM, FWTM, and PVDR of the central microbeam was performed at 20 mm depth and is shown in Figure 2.22 and tabulated in Table 2-13.

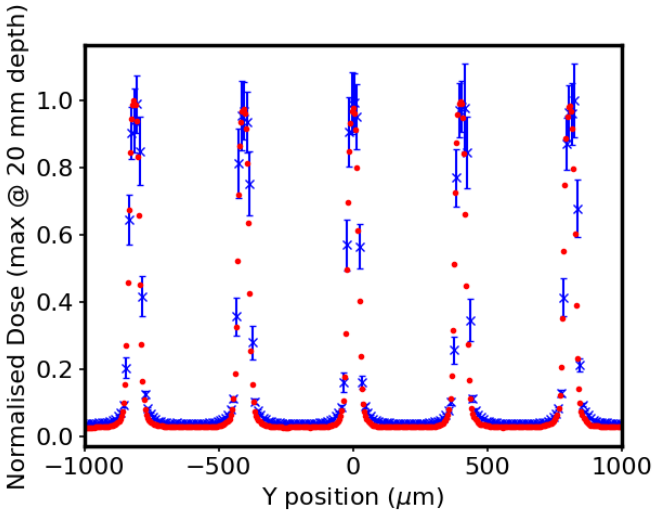

Figure 2.22: Normalised dose profile (to maximum) for a 3T-CuCu 2.014 mm² microbeam heights for a 20 × 20 field in an RMI457 Solid Water phantom.

Table 2-13: Comparison of microbeam Y-profile against EBT3 film.

	G4IMBL	EBT3
FWHM (µm)	48.68	42.39
FWTM (µm)	88.70	77.26
PVDR	26.58 ± 2.75	26.25

Both the fitted FWHM and FWTM of G4IMBL are ~15% larger than the corresponding EBT3 results, though remain in the same magnitude; and the PVDRs agree within the calculated uncertainty.

Normalised depth-dose profiles, also known as percentage depth-dose profiles (PDDs), were also obtained for the central peak and the central valley. In order to boost statistics, the peak profile values were obtained through averaging over 2 mm in the Z-direction and the valley profile was obtained by the average value over 0.2 mm (Y) about the valley centre and 2 mm in the Z-direction. Simulated microbeam profiles are compared with EBT3 in Figure 2.23, for peak and valley PDDs.

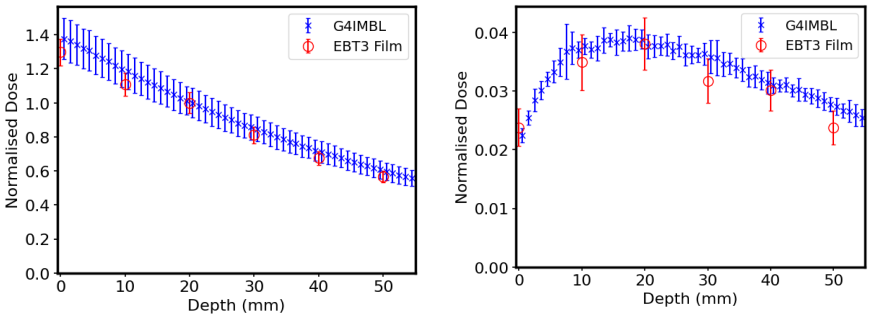

Figure 2.23: Microbeam normalised depth dose profiles at central peak (left) and central valley (right).

The microbeam valley normalised dose profile are normalised to the peak dose at 20 mm depth for the respective dosimeter. The microbeam peak normalised depth dose profile agrees with EBT3 results within uncertainty at all depths. A trend can be noted that G4IMBL overestimates both the peak and the valley dose in comparison to EBT3 at all depths except 0 mm depth in the valley (and 20 mm in both peak and valley, though this is due to normalisation at this depth). This consistent overresponse in G4IMBL's PDDs with respect to EBT3 may explain the slightly larger PVDR calculated by Table 2-13, due the larger magnitude of the relative peak response providing a more significant impact on the ratio compared to the smaller magnitude of difference in the relative valley dose. Both G4IMBL and EBT3 valley PDDs show the larger build-up region observed in [31] compared to the peak PDDs.

These results suggest that G4IBML Stage II simulations may be useful for comparison against 3T-CuCu 30 × 2.014 mm² beam experimental results for broadbeam and microbeam peak-normalised depth dose profiles. G4IMBL should be suitable for experimental comparison for different BDAs and conformal mask aperture sizes for 3T-CuCu due to normalisation being unaffected by flux. G4IMBL must be validated against experimental results for other wiggler magnetic field strengths and filtration combinations before being used as a theoretical standard for experiments under identical conditions.

2.6 Conclusion

A simplified Geant4-based model of the AS IMBL has been produced for use in quality assurance and treatment planning for MRT experiments in Hutch 2B. Normalised energy spectra match theoretical energy spectra as calculated by a third-party program (SPEC) and normalised dose deposition profiles in a RMI457 phantom agree with experimental measurements under identical conditions. This program has the capability to perform predictive simulated dosimetry for MRT experiments in Hutch 2B. Further investigation is needed into Geant4's capacity to model

synchrotron insertion devices with a focus on confirming the correct photon flux per electron in order to allow benchmarking of absolute dose simulations. Future work on this program will include extension of the geometry to Hutch 3B, and implementation of Geant4-DICOM interface to allow construction of geometry from CT imaging.

Chapter 3

Characterisation of 3D-Mesa SSD silicon single strip detectors for use in synchrotron microbeam radiation therapy

3.1 Introduction

This chapter introduces the 3D-Mesa SSD detector and provides simplified schematics and electron-microscope images to show the intended topography of the devices. Current-Voltage and Capacitance-Voltage characteristics are shown and explained, along with $\frac{1}{C^2}-$Voltage characteristics. Ion Beam Induced Charge (IBIC) results for both one-sided and two-sided samples at multiple biases and explains the results. Sentaurus Technology Computer Aided Design (TCAD) simulations to examine electric field distribution and depletion zone behaviour are shown and explained. The results of the electrical characterisation are discussed and the suitability of the 3D-Mesa SSD detector for synchrotron radiation is evaluated.

The contents of this chapter have been previously published in IEEE Transactions on Radiation and Plasma Medical Sciences [42].

3.2 3D-Mesa SSD technology

The 3D-Mesa SSD silicon single-strip detector (SSD) was fabricated on an n-SOI wafer with a 10 μm thick, high-resistivity (4 kΩ cm) n-Si active layer and 2 μm thick SiO_2 insulating layer, bonded to a 350 μm thick low-resistivity Si substrate. The Si ingots were fabricated using Floating Zone methods and were doped with phosphorus to a concentration of 1.104×10^{12} cm^{-3}. The SV of the 3D-Mesa SSD has had all the surrounding silicon removed down to the insulating layer using plasma etching to produce pseudo-3D geometry and improve electric field distribution. Etching 10 μm deep down to the insulating layer was accomplished by noting the change in etching rate when the beam transitioned from Si to the SiO_2 as indication of correct depth.

Two ion-implanted regions, one N+ (phosphorus) and the other P+ (boron), are connected via an Al bus placed over a passive silicon bridge to contact pads 200 μm from the end of the SV. An approximately 0.75 μm-thick oxide layer is formed on the outer surfaces of the etched silicon SV (i.e. the 'sides' of the SV, bridge, and pads) along with a thin layer of hydrophobic phosphosilicate glass (PSG) on top.

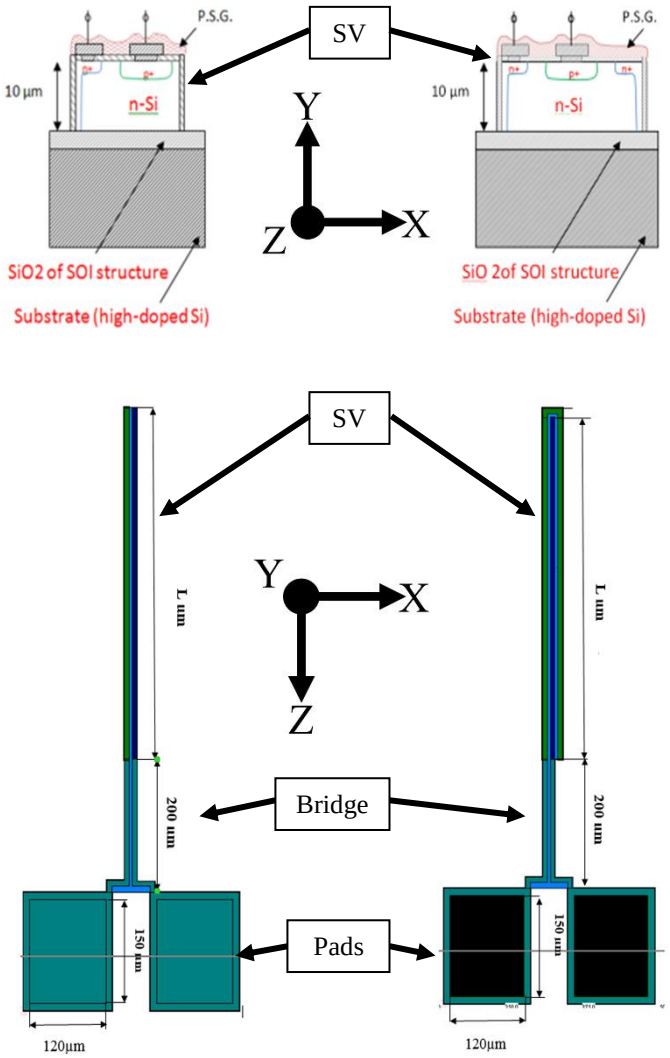

Figure 3.1: Schematic of the 3D-Mesa SSD.
Left: single-sided. Right: double-sided.

Two options of the 3D-Mesa SSD were produced: 'single-sided' and 'double-sided' as shown in Figure 3.1. Each option was fabricated with three different lengths (L) of the SV: 50 µm, 100 µm, or 250 µm. The 'single-sided' SSD has a 3D SV of 10 µm × 22.5 µm × L µm consisting of only one P+ and one N+ doped region. The 'double-sided' variant has a larger SV of 10 µm × 36 µm × L µm and consists of one continuous N+ doped region 'wrapped' around the middle P+ region.

In the double-sided case the N+ doped region extends vertically down both sides of the SV structure similar to an 'active-edge planar sensor' [43]. This was accomplished using multiple implantation angles as in visually tolerable tiling (VTT) fabrication processes [44], although unlike the edgeless detector there is no N+ implantation at the bottom of the active layer. No N+ or P+ doping is present down the P+ side of the SV in the single-sided case, which introduces asymmetry that is not present in the double-sided case.

3.3 Methodology

3.4 Scanning electron microscopy study

The structure of the 3D-Mesa SSD was investigated using Scanning Electron Microscopy (SEM) techniques. This was performed using a Japan Electron Optics Laboratory (JEOL) JSM-7001F Thermal Field Emission Scanning Electron Microscope at the Australian Institute for Innovative Materials (AIIM), University of Wollongong. The resolution of the results is approximately 2 nm [45].

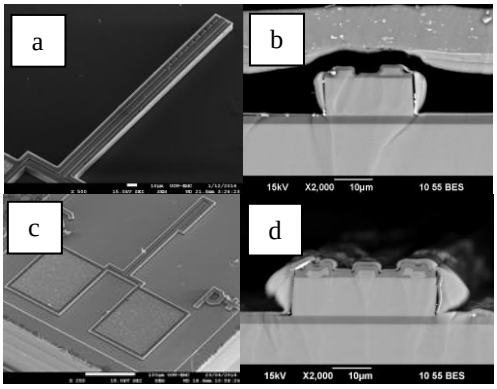

Figure 3.2: SEM images of the 3D-Mesa SSD.
(a) Plan view of the single-sided 3D-Mesa SSD,
(b) Cross-sectional view of the single-sided 3D-Mesa SSD,
(c) Plan view of the double-sided 3D-Mesa SSD,
(d) Cross-sectional view of the double-sided 3D-Mesa SSD.

The cross-sectional images and composition maps (Figure 3.2) show that silicon surrounding the SV was fully etched down to 10 μm (SiO_2 layer). No noticeable physical defects were present in either single-sided or double-sided option.

3.5 Electrical characterisation

Current-voltage (I–V) measurements of the 3D-Mesa SSD were undertaken using a Keithley 6517A electrometer. Measurements were undertaken with reverse bias (from 0 V to -50 V) applied to the strip and back connected to the ohmic contact corresponding to an input of electrometer. A 1 s delay between each step was implemented in order to allow measured currents to stabilise. A current threshold of 1 μA was set to protect the devices from overload.

The leakage current of a device may be determined through analysis of I–V characteristics.

Capacitance-voltage (C–V) measurements were performed upon a Boonton capacitance meter (Model 7200) controlled by a PC via an IEEE-488 interface at ANSTO. The system is calibrated prior to testing without the device connected to cancel out capacitance contributions inherent in the experimental set-up. The Boonton 7200 provides measurements of capacitance at 1 MHz, and has a

resolution of 0.01 pF with an uncertainty of 0.01 pF under the chosen scale [46]. The operational frequency of 1 MHz is larger than ideal for capacitance measurements of high-resistivity silicon, and may affect the accuracy of C–V results.

C–V measurements may provide insight into the intrinsic doping concentration and P-N junction potential of the silicon detector. Assuming a single-sided abrupt PN junction, this is accomplished using the equation:

$$\left(\frac{A}{C}\right)^2 = \frac{2}{q_e \epsilon_{si} N_d}(\phi_i - V) \qquad (3.1)$$

Where C is capacitance, A the cross-sectional area of the PN junction, q_e the charge of an electron, ε_{si} the permittivity of silicon, N_d the concentration of donors (Phosphorus), V the applied voltage, and ϕ_i the built-in potential of the junction.

Fitting a straight line to the inverse square capacitance at low biases, where the curve is mostly linear, allows extraction of N_a and ϕ_i from the gradient and intercept of the line respectively.

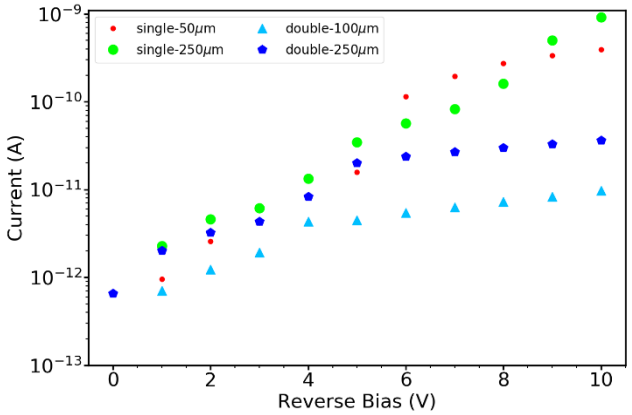

Figure 3.3: I–V profiles of the 3D-Mesa SSD.

I–V profiles show that all devices produce a leakage current less than 1 nA when below 10 V reverse bias (Figure 3.3), with single-sided devices producing a current less than 1 nA when below 10 V and double-sided devices producing a current less than 0.05 nA when below 10 V. Both single-sided devices show a more linear trend from 1–8 V compared to the double-sided devices, which reach saturation at 5 V. In both single-sided and double-sided cases, the shorter SV appears to saturate at a slightly lower current than the other length.

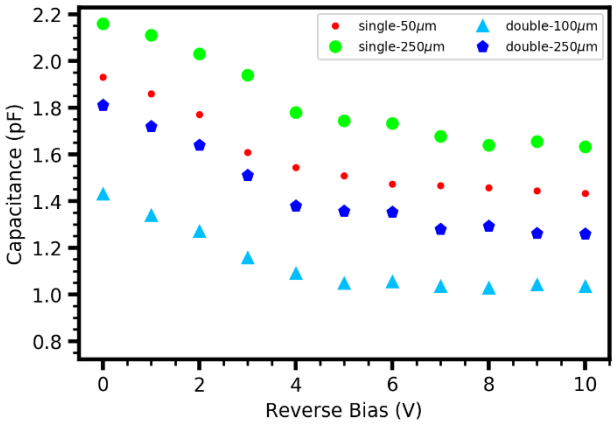

Figure 3.4: C–V profiles of the 3D-Mesa SSD.

C–V profiles are consistent between devices, with differences in zeroing between samples contributing to the 1 pF offset (Figure 3.4). Results suggest that all samples reached vertical depletion (from the P+ to the insulating layer) at -4 V where the gradient changes, and lateral depletion (from the P+ across the width of the Si strip) at approximately -7 V when the gradient has flattened completely. These results indicate that a bias of -3 V will be sufficient for full depletion of the detectors.

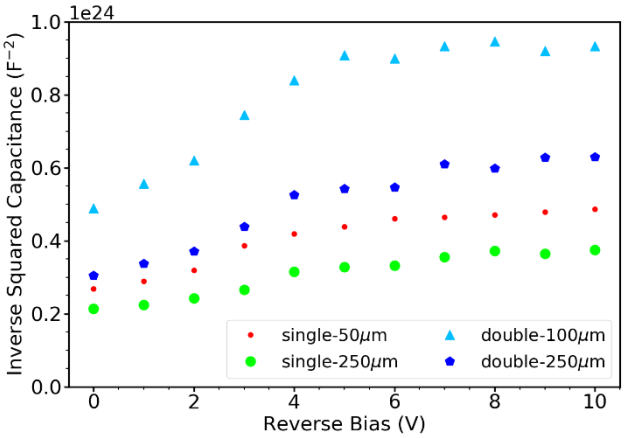

Figure 3.5: $1/C^2$ vs V profiles of the 3D-Mesa SSD.

A least-squares 1-D polynomial fit was applied to $1/C^2$-V curves (Figure 3.5) for biases 0–5 V and (3.1) was used to calculate N-bulk doping concentration and built-in potential for each device. The results are shown in Table 3-1 and disagree with manufacturer's stated N-doping concentration by a factor of ~10^6. Thus, the assumption of device behaviour approximating an abrupt PN junction is not valid, as expected from the complex device geometry and lack of doping at the bottom SiO_2 insulating layer, and parasitic MOS contribution from the bridge and pad regions.

Table 3-1: N-bulk doping concentration of 3D-Mesa SSD using (3.1).

Detector Configuration	N-bulk Doping Concentration ($\times 10^{19}$ cm^{-3})
Single-sided — 50 µm	1.29
Single-sided — 250 µm	0.08
Double-sided — 100 µm	0.14
Double-sided — 250 µm	0.04

3.6 Charge collection characterisation

The charge collection efficiency (CCE) for the 3D-Mesa SSD was investigated using the IBIC technique. This experiment was performed upon the Australian National Tandem for Applied Research (ANTARES) heavy ion microprobe at the Australian Nuclear Science and Technology Organisation [47].

The IBIC study was performed using 5.5 MeV He^{2+} ions, which were calculated to have a range of 28.02 µm in silicon using the program 'SRIM' (Stopping Range of Ions in Matter) [48]. A low ion beam current of 1000 ± 100 ions/s was maintained during the experiment to avoid pile-up. The ions were incident normal to the silicon, focussed to approximately 1–2 µm spot size resolution and raster scanned across the device. The detector was AC coupled to the preamplifier and reverse biased as desired. The detector in IBIC experiment was connected to a charge sensitive preamplifier (Amptek A250), followed by a shaping amplifier and the ADC. A shaping time of 1 µs was deemed sufficient by estimating minority carrier lifetime for a high-quality Si device and comparing to estimate time taken for a charge carrier to traverse the bulk of the SV to the contact.

For a 10 µm thick SV (h) with an electron mobility (μ_e) of ~1400 cm^{2}V^{-1}s^{-1} biased at 1 V (V_b), the drift velocity (v_{drift}) is

$$v_{drift} = \mu_e V_b / h \qquad (3.2)$$

thus, time taken to traverse h is

$$t_{drift} = \frac{h}{v_d} = \frac{h^2}{\mu_e V_b} \qquad (3.3)$$

which is 3.57×10^{-10} s. Carrier recombination lifetime (τ) can be estimated with

$$\tau = (\sigma v_{thermal} N_d)^{-1} \qquad (3.4)$$

where σ is trapping cross-section of the initial defects, $v_{thermal}$ is carrier thermal velocity, and N_d the carrier volume density [49]. As $v_{thermal}$ is approximately 1×10^7 cm/s, N_d is 1.104×10^{12} cm^{-3}, and using a trap cross-section of 1×10^{15} cm^2 as in [49], the carrier lifetime is calculated to be

approximately 1×10^{-4} s. Since τ is six orders of magnitude greater than t_{drift} it is safe to assume that all charge generated by an ion will be collected by the contact before it is able to recombine. Thus, as the preamplifier shaping time is four orders of magnitude greater than t_{drift}, the entirety of that charge will be properly shaped by the preamplifier.

The generated signal has an amplitude corresponding to the collected charge induced by each ion impact and was recorded along with beam position to form data triplets (x, y, energy). Energy calibration was then performed using a pulse generator calibrated with a 300-µm thick windowless silicon PIN diode with known Charge Collection Efficiency (CCE) of 100% for 5.5 MeV alpha particles. Energy spectra and median energy maps were then generated using python MatPlotLib [50].

IBIC studies were performed in vacuum on each of the above electrically-characterised samples for multiple voltages between 0 and 10 V. IBIC results were similar for 1–3 V and for 4–10 V across all samples, therefore the two voltages with the greatest discrepancy for the single-sided 250 µm SV are shown for brevity's sake.

Figure 3.6a shows the energy spectrum for He^{2+} ions with an energy of 5.5 MeV, obtained during IBIC for a SV reverse-biased at 3 V. A pronounced peak is observed in the spectrum at an energy of 1384 keV. Figure 3.6b shows a median energy map demonstrating that charge collection is confined to within the 250-µm-length SV with minor low-energy charge collection in the bridge close to the SV (corresponding to the 0–100 keV feature in Figure 3.6a).

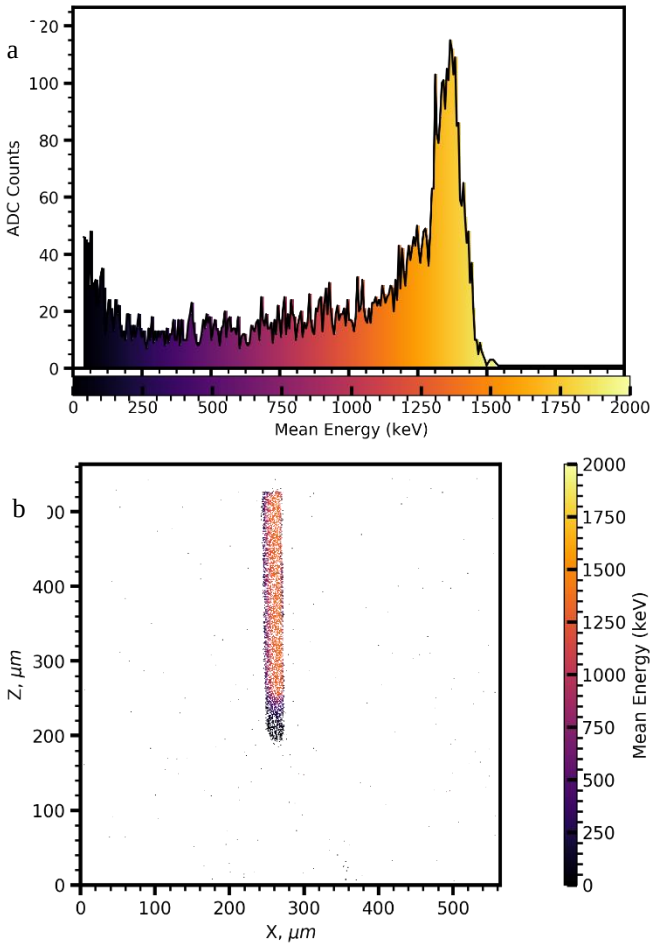

Figure 3.6: Energy spectrum (a) and median energy map (b) for single-sided, 250 µm 3D-Mesa SSD at 3 V.

Figure 3.7a shows the energy spectrum for the same SSD reverse-biased at 4 V. The peak of 1384 keV previously observed at the 3 V bias remains, but a larger-statistic peak with an energy of 1050 keV was also observed. The median energy map on Figure 3.7b demonstrates that charge collection events now occur under the bridge and pad, as well as within the SV; thus, the new 1050 keV peak is due to events in the bridge region and under the pad. This conclusion is supported by consideration of the greater area of the bridge and pad compared to that of the SV.

The CCE was calculated for the detector by comparison of energy of the experimental spectrum against theoretical energy deposition in the device, calculated by SRIM code. The energy deposited by He^{2+} ions with an energy of 5.5 MeV in a SV thickness of 10 µm and an Al overlayer of 2 µm was calculated by SRIM code to be 1384 keV. This is in good agreement with observed highest-energy peak in both the 3 and 4 V biased devices and corresponds to a 98% CCE in the SV. This indicates that even a not-fully-depleted SV allows almost full charge collection due to the large diffusion length of the high-resistivity Si. Using the energy peak at 1050 keV the Bridge and Pad are calculated to have a CCE of 76%.

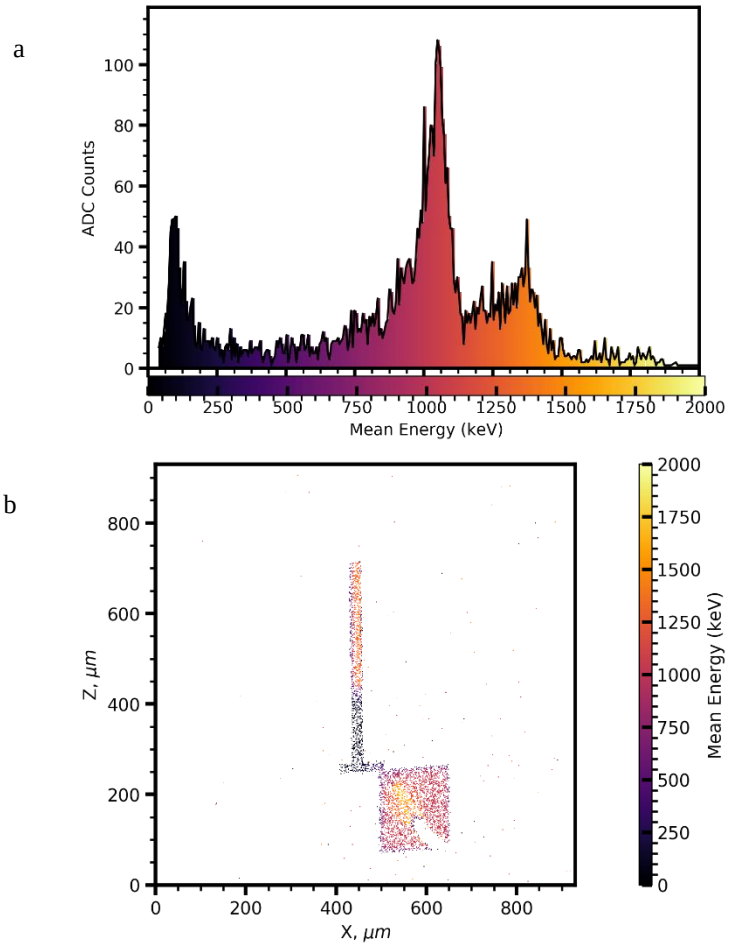

Figure 3.7: Energy spectrum (a) and median energy map (b) for single-sided, 250 µm 3D-Mesa SSD at 4 V.

At biases greater than 3 V, charge collection was observed from the SV of all devices, but also from under the connecting bridge, and even the contact pad (at higher biases). The undesired excess charge is collected from a region that is much greater in area than the SV and this is evident in the energy spectra in Figure 3.8, where the area associated with the SV charge collection peak at 1360 keV is overshadowed by the area associated with the bridge-and-pad peak at 1050 keV.

Using a window from 1250-1500 keV on the normalised spectra the percentage of total counts corresponding to the SV peak were found to be 38.29 and 17.14% for 3 and 4 V respectively. Conversely, a window from 800–1200 keV was used to determine total percentage of the 4 V spectrum corresponding to the pad-and-bridge peak as 39%. The same window in the 3 V spectrum contributes to 22.98 % of the total counts.

The magnitude of the undesired charge collection increases with voltage to dominate the spectrum at 10 V.

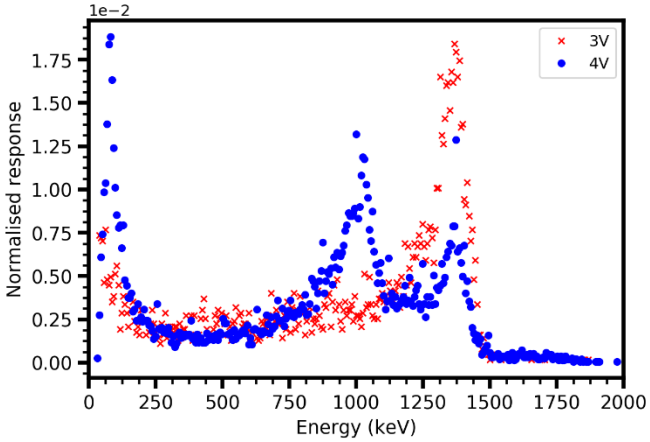

Figure 3.8: Overlayed and normalised spectra for 3 V and 4 V.

3.7 TCAD simulations

Analytical finite-element simulations were performed to supplement experimental results. 3D models of the single-sided 3D-Mesa SSD and double-sided 3D-Mesa SSD, with 150-µm length SV, were constructed in Synopsis TCAD. 2D cross-sectional models of the SV were generated from cutplanes of the 3D models 20 µm from the bridge. The silicon was doped with phosphorus to a density of 1.104×10^{12} cm^{-3} and to 1.0×10^{19} cm^{-3} in the N+ region under the Al contact and down the side closest to that strip (as in Figure 3.1). The P+ region was doped with boron to 1.0×10^{19} cm^{-3} only underneath the Al contact.

Poisson and continuity equations for electrons and holes were solved at multiple biases in order to study the depletion region and electric field distribution throughout the device. The carrier mobility models used in the physics section handles Doping-Dependent mobility [51], High-Electric-Field-Saturation mobility [52], and mobility degradation typical to semiconductor-insulator interfaces [53], [54]. The Recombination models used handle Shockley–Read–Hall (SRH) recombination and doping dependence of SRH lifetimes using the Scharfetter relation [55]–[58], and Auger recombination [59]–[61]. The intrinsic carrier concentration is defined by the Bennett-Wilson model [61], including bandgap narrowing. Fixed-charge traps induced during the fabrication process were introduced at all Si-SiO_2 interfaces with an initial concentration of trapped charge of 5.0×10^{10} cm^{-2} as implemented in similar TCAD models [62].

Simulations were performed for mesh-grids with 100,000–440,000 vertices and were analysed for a cross-section of the SV 30 µm from the bridge. An additional lengthways cross-section through the centre of the SV and bridge was also examined.

TCAD simulations were performed to investigate the change in depletion within the device when

unbiased and during undesired charge collection conditions above 4 V bias.

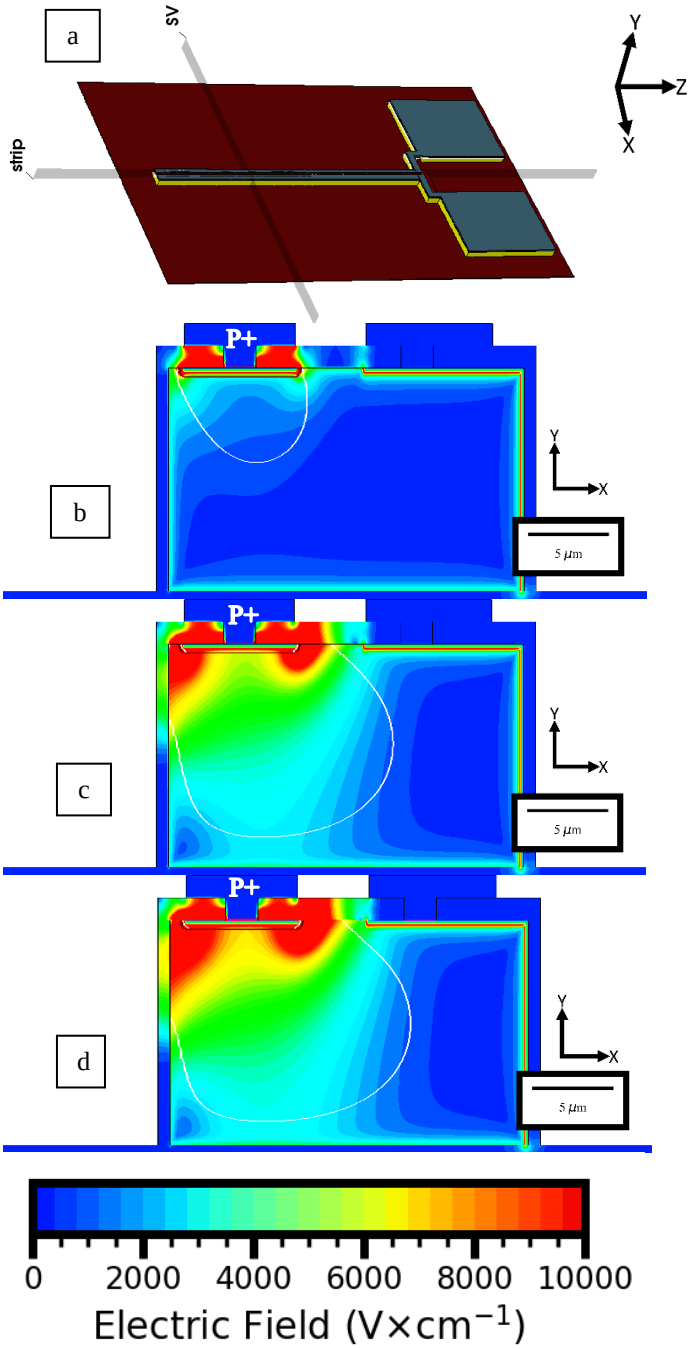

Figure 3.9: TCAD simulation of electric field in single-sided 3D-Mesa SSD.
(a) Location of SV and strip cut-planes on device model,
(b) Cross-plane SV electric field distribution, bias 0 V,
(c) Cross-plane SV electric field distribution, bias 3 V ,
(d) Cross-plane SV electric field distribution, bias 4 V.
(Vertical direction is not in scale.)

At 0 V the depletion zone (denoted by the white line) extends from the P+ contact vertically 4 µm down to the SiO_2 insulating layer, and laterally a maximum of 5 µm into the Si bulk (Figure 3.9b). At this bias, the depletion zone exists only underneath the P+ contact and does not propagate to underneath the bridge (Figure 3.10a). The lateral spreading of the electric field is inhibited by the

presence of traps included in the SiO_2-Si interface.

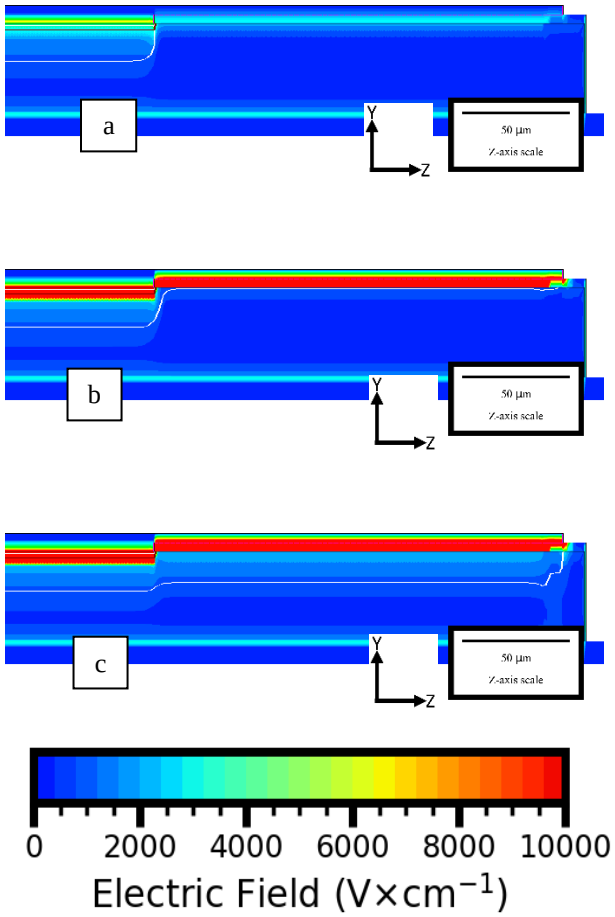

Figure 3.10: TCAD simulation of in-plane electric field distribution in single-sided 3D-Mesa SSD (under P+ strip and bridge).
(a) Bias 0 V; (b) bias 3 V; (c) bias 4 V.
(Vertical direction is not in scale.)

At 3 V, the depletion zone extends down 8 µm approaching the SiO_2 layer and 10 µm laterally towards the N+ region in the SV (Figure 3.9c) and makes contact with the closest SiO2 side surface. At 4 V the depletion zone and electric field distribution in the SV has changed very little compared to 3 V (Figure 3.9d).

Under 3 V bias conditions the depletion zone has begun to spread longitudinally under the bridge region compared to the unbiased SV less than 10 µm (Figure 3.10b), but extends the full 200 µm length under the bridge (Figure 3.10c) under 4 V bias, thus leading to unwanted charge collection.

The double-sided model displays the same characteristics as the single-sided model, which can be attributed to the design of the double-sided SVs as two symmetrical single-sided SVs joined through the lengthwise cross-section about the P+ contact. At 0 V the depletion zone extends approximately 4 µm downwards and towards both sides from the middle P+ region (Figure 3.11a). At 3 V the

depletion zone extends 8 µm downwards to contact the SiO_2 layer and extends approximately 7.5 µm towards both sides from the middle P+ region to cover a total distance of 15 µm (Figure 3.11b).

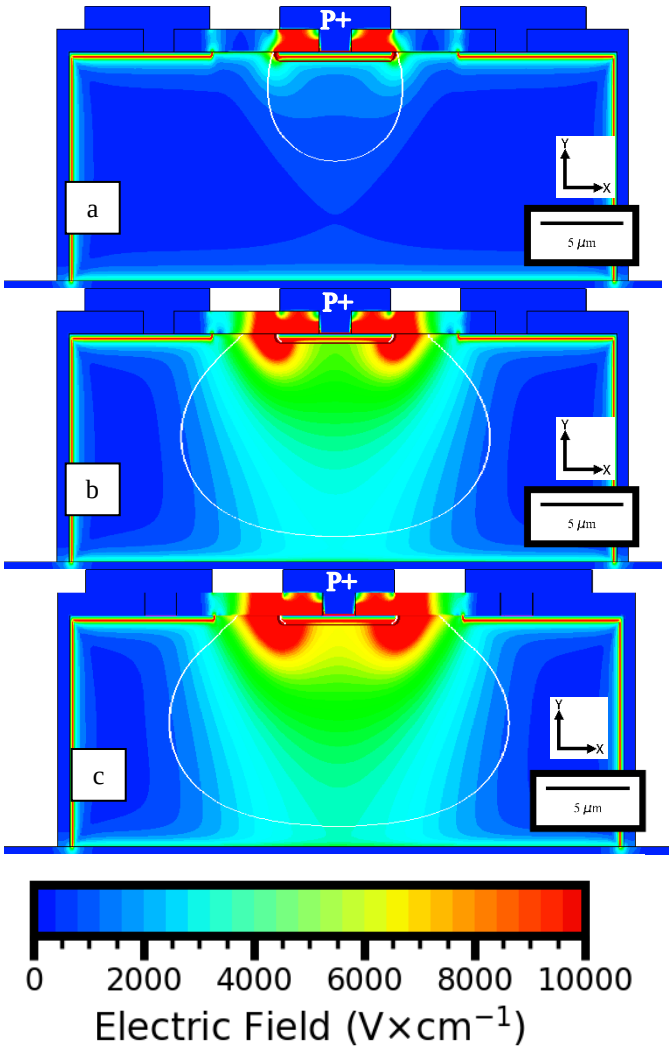

Figure 3.11: TCAD simulation of cross-plane electric field in double-sided 3D-Mesa SSD SV. (a) Bias 0 V; (b) bias 3 V; (c) bias 4 V; (Vertical direction is not in scale).

At 4 V the depletion zone and electric field distribution in the SV has changed very little compared to 3 V (Figure 3.11c). The results for the in-plane SV-bridge cross-section for the double-sided model are identical to the results for the single-sided model and have thus been omitted.

I–V and C–V characteristic curves for the single-sided and double-sided 2D and 3D 250 µm-length models have been produced between 0 V and 10 V reverse bias. I–V characteristics (Figure 3.12) show a sharp increase between 0 V and 0.25 V from 2.0×10^{-14} to 1.0×10^{-12} A for the 2D models and 1.0×10^{-16} A to 1.0×10^{-12} A for the 3D models. Between 0.25 V and 3.75 V all models behave very similarly, rising from 1.0 × 10-12 A to 4.0 × 10-12 A, then the 2D models continue along the same trajectory while the 3D models show a second increase before flattening again. It was observed

that the 2D single-sided model always exhibited lower current than the 2D double-sided model, whereas the 3D single-sided model achieved higher currents than the 3D double-sided model above 3.75 V. Between 0.25 and 4 V the TCAD simulated characteristic profiles roughly agree (i.e. are within the same magnitude) with the experimental 250 µm 3D-Mesa SSD I–V profiles in Figure 3.3. Above 4 V, the experimental I–V profiles show significantly greater current with increasing voltage compared to the simulated profiles by up to two orders of magnitude.

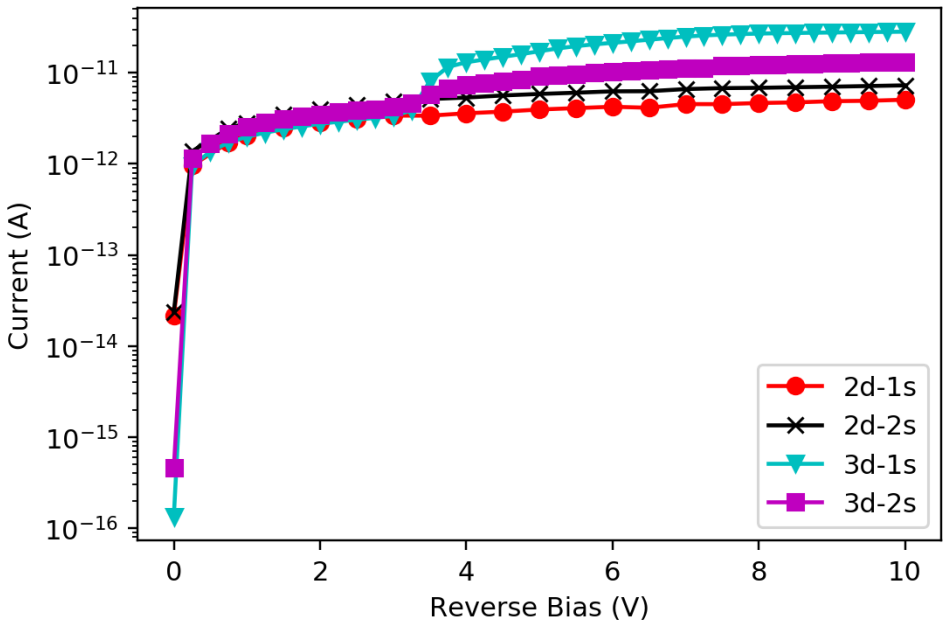

Figure 3.12: TCAD simulated I–V characteristic profiles.

The 2D and 3D simulated C–V profiles differ much more strongly than the simulated I–V profiles because the 3D model contains the bridge and pad structures, whereas the 2D model simply extrapolates a 1 µm-thick slice of the SV to the desired length. Thus, the 2D models do not exhibit the effect of the parasitic MOS structure and so are approximately 25% of the magnitude of the 3D models. Additionally, the 2D models do not show a sharp decrease in capacitance at 2.5 V, instead showing a smooth curve that plateaus between 5 V and 10 V. The structure at 2.5 V in the 3D models is likely due to interference from the bridge as the electric field strengthens and the depletion zone extends under the bridge. Compared to the experimental C–V profiles (Figure 3.4), the simulated 2D profiles do not match either the shape or magnitude of the 250-µm 3D-Mesa SSD results. The simulated 3D C–V profiles are closer to experimental results than the 2D, but still do not agree. The simulated C–V magnitude ranges from approximately 0.4 pF to 0.2 pF and a corresponding experimental profile ranges from 1.8 pF to 1.4 pF. Even accounting for increased experimental

capacitance due to the device packaging and connectors, the difference in capacitance between 0 V and 10 V is twice that of the simulated results.

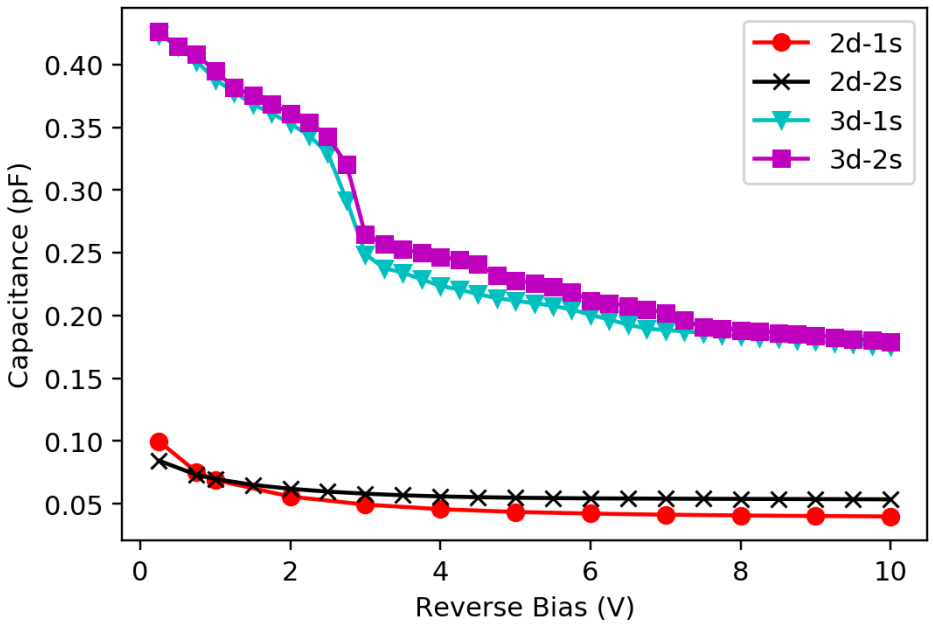

Figure 3.13: TCAD simulated C–V characteristic profiles.

Based on the lack of agreement with experimental results, it is recommended that care should be taken when using the TCAD simulated I–V and C–V characteristics as a theoretical point of comparison for this complex geometry, with its associated parasitic MOS structure. It is possible that better agreement would be achieved with a more accurate model, a greater number of mesh-vertices, or if the effect of the parasitic MOS structure could be reduced.

3.8 Discussion

Electron microscopy has confirmed the effectiveness of the etching method to produce the isolated protruding 3D-Mesa SSD SV to the specified dimensions. The cross-sections in Figure 3.2b and Figure 3.2d demonstrate a near-ideal rectangular parallelepiped shape proposed in Figure 3.1, with excess material on either side of the SV due to the adhesive used in the electron microscopy process. I–V results demonstrate a low current less than 1 nA for both single-sided devices and a current less than 0.05 nA in the double-sided detectors when biased less than 10V. Both single-sided devices achieved greater current at high voltage than double-sided devices by a factor of ~100. This may be attributed to the asymmetric doping of the single-sided devices where a lack of doping on the vertical side of the SV near the P+ contact results in more surface recombination and thus higher leakage current.

Leakage current may be deemed acceptable if the current generated during operation of the device greatly exceeds the magnitude of the leakage current. Theoretical charge generated within the 3D-mesa in a 100 Gy/s synchrotron beam of 100 keV photons may be estimated using:

$$\dot{D} = \frac{\dot{E}}{m} = \frac{\dot{N_\gamma}\overline{E_\gamma}}{\rho_{Si}V_{Si}} \rightarrow \dot{N_\gamma}\overline{E_\gamma} = \dot{D}\rho_{Si}V_{Si} \quad (3.5)$$

$$I = \frac{q_e\dot{N_\gamma}\overline{E_\gamma}}{C_{ion}} \quad (3.6)$$

Where $\dot{D}$ is dose rate $\dot{E}$ is energy deposition rate, m is mass of detector, $\dot{N_\gamma}$ is photon flux, $\overline{E_\gamma}$ is average photon energy, ρ_{Si} is density of silicon, V_{Si} is volume of sensitive volume, I the detector current, q_e the charge of an electron, and C_{ion} the mean ionisation energy in Si (~3.62 keV).

Substitution and conversion to standard units arrives at a detector current in the synchrotron beam of ~3.62 µA, which is greater than the maximum leakage current at 10 V of 1 nA by a factor of 3000. Thus, the leakage current is not expected to impact normal operation of the device in high dose-rate synchrotron beams.

C–V results demonstrate saturation at 8–10 V, which corresponds to a silicon resistivity of approximately 3–4 kΩ-cm — considering lateral depletion to be 35 µm. The estimated doping concentrations using (3.1) did not agree with the expected doping concentrations supplied by the manufacturer. Thus, the assumption of 'abrupt P-N junction'-like behaviour of the 3D-Mesa SSD is false. The complex 3D geometry, lack of N+ doping at the SV-Insulator interface, and the MOS structure of the bridge and pads are not taken into account in (3.1)'s assumption, hence ideal linear behaviour of $1/C^2$ vs V is not expected. In the 1s case the asymmetrical lack of doping on the P+ vertical side of the SV further influences the electrical characteristics of the 1s device due to excess surface recombination.

To extract the true SV capacitance a 3D-Mesa SSD MOS test structure would be investigated to determine quantitatively the contribution of the bridge and pads to the measured capacitance. Absent the MOS capacitance, (3.1) may approximate the behaviour of the SV better, which will be the subject of future investigation.

IBIC results indicate the optimal operating bias of the 3D-Mesa SSD to be 3 V for all devices on length of SV. Greater bias leads to charge collection in the bridge region. This occurs because build-up of positive charge in a thick field-oxide blocks depletion under low negative voltages (below 3 V), while for higher voltages the positive charge accumulation results in inversion of the charge and

propagation of depletion in depth. The incomplete charge collection in the bridge region at 4 V bias (Figure 3.7) corresponds to this partial depletion. This problem will be addressed in next-gen 3D-Mesa SSD by implantation of N 'stop layers' under the Al of the bridge to avoid inversion. IBIC results demonstrated that full depletion in SV is achieved under 3 V and further increase of bias does not improve charge collection in the SV.

TCAD and IBIC results suggest that the effective spatial resolution of the device at low bias is better than the physical dimensions of the width of SV as the majority of deposited charge will be collected mostly under P+ region only slightly larger in width than the Al contacts.

These results support the hypothesis that the 3D-Mesa SSD is suitable for use in quality assurance of MRT with the ability to perform dose mapping in edge-on configuration in the penumbra region, with spatial resolution better than 10 μm (the geometrical 'height' of the SV). Preliminary results of the double-sided 3D-Mesa SSD in edge-on mode at the Australian Synchrotron Imaging and Medical Beamline Hutch 1B may be found in [23]. Further tests under a variety of experimental conditions have been performed and shall be the subject of future papers.

3.9 Conclusion

The Centre for Medical Radiation Physics has produced novel n-type Silicon-On-Insulator silicon single strip detectors (3D-Mesa SSD) for the purpose of Quality Assurance of Microbeam Radiation Therapy. These devices have undergone experimental and simulation-based electrical characterisation to determine an ideal operating bias.

Examination of the topology and cross-section of two version of the SSD detectors using scanning electron microscope techniques confirmed that almost an ideal rectangular parallelepiped shape was formed via plasma etching and that fabrication of the device to provided specifications was achieved.

Electrical characterisation with a combination of I–V and C–V measurements and IBICC techniques determined optimal biasing to be -3 V in order to maximise charge collection of the SV without inducing excess charge collection from under the bridge and connecting pad, thus providing spatial resolution of the SSD relevant to SV only. Leakage current at this bias was below 1 nA. The CCE within the SV is ~100% — indicative of the quality of the fabrication techniques utilised in the construction of the 3D-Mesa SSD device. The plasma etching technique used to remove silicon from outside the strip region is proven to stop charge collection laterally from outside the SV region.

However, further processing will be required to limit charge collection from the bridge and underneath the electrode regions. Analysis of $1/C^2$ vs V slopes allowed extraction of estimated bulk-N doping concentration, which was found to agree with expected doping concentration used in TCAD simulations.

Sentaurus TCAD simulations were performed to examine depletion zone distribution within the device at different biases. At 0 V bias, the depletion zone only exists underneath the P+ region and is confined vertically and laterally to approximately 5 µm from the P+ Al strip in the SV. At -3 V, the depletion zone extends vertically to almost the full depth of the SV but is still confined laterally to the P+ region. This provides spatial resolution in face-on operation better than the width of the SV. However, depletion appeared under the bridge as discussed above.

These devices were determined to be good candidates for further testing at a synchrotron radiation facility under MRT conditions.

Chapter 4

3D-Mesa SSD broadbeam experimentation at IMBL

4.1 Introduction

In this chapter a number of experimental studies of the 3D-Mesa SSD under broadbeam conditions are presented. As this chapter involves discussion of experimental studies performed at the Australian Synchrotron Imaging and Medical Beamline (AS IBML), the contents of Chapter 2.2: IMBL beamline geometry and setup, should be considered mandatory pre-reading in order to be aware of beamline specifics and nomenclature.

First, an overview is provided of the properties of current standard dosimeters used for experiments on the IMBL to be compared the 3D-Mesa SSD results. These dosimeters include ionisation chambers, Gafchromic® film, the PTW microDiamond detector, and the precursor to the the 3D-Mesa SSD, the Epitaxial SSD. The methods of operation and challenges of usage are briefly outlined for each detector, including the 3D-Mesa SSD, and a nomenclature is defined to concisely relate 3D-Mesa SSD bridge design, sensitive volume length, and unique sample identification number.

Next, a number of small studies are performed to examine the operational behaviour of the 3D-Mesa SSD, including:

- An optimal operating bias voltage is confirmed, based on X-Tream data acquisition system response to a broadbeam field.
- The characteristic profile of a vertical scan through the BB treatment field is acquired and all relevant features are identified.
- A response linearity study is conducted in a ~100 Gy/s BB field and the difference between treatment field dose rate and intrinsic field dose rate is analysed.
- A lifetime study is performed on a number of 3D-Mesa SSD samples to evaluate the effect of radiation damage on response over ~100 kGy.
- A number of samples are also exposed to monochromatic beams to examine the effect of the various 3D-Mesa SSD designs on device energy dependence.
- Dose-ADC count calibration factors are calculated for a number of devices and preamplifiers to determine uniformity of response across different device designs and batches.

An extensive study of BB relative depth dose profile acquisition by 3D-Mesa SSDs is performed for a large number of beamline configurations in several different phantoms for several different field sizes. 3D-Mesa SSD PDDs are compared against other standard detector PDDs and G4IMBL simulated BB PDDs for specific beamline configurations.

Finally, synchrotron broadbeam results are summarised and the suitability of the 3D-Mesa SSD for broadbeam dosimetry is evaluated.

4.2 Dosimetry at IMBL

4.2.1 PTW PinPoint™ IC dosimetry

The gold standard for BB dosimetry at IMBL is the PTW (Freiburg, Germany) PinPoint™ IC (31014) (0.015 cm^3 SV) read out with a UNIDOS webline Universal Dosemeter at 400 V bias. The PinPoint™ IC probe has a corresponding 10 × 100 × 100 mm^3 RMI457 phantom slab with a cylindrical channel of known dimensions bored into it. During dosimetry the PinPoint™ IC is inserted into the channel and positioned with respect to the reference marks on the PinPoint™ IC shell and the remaining air-gap filled with water (Figure 4.1). This ensures consistent positioning of the phantom while also restricting the PinPoint™ IC placement to a minimum achievable depth of 5 mm deep to the phantom surface.

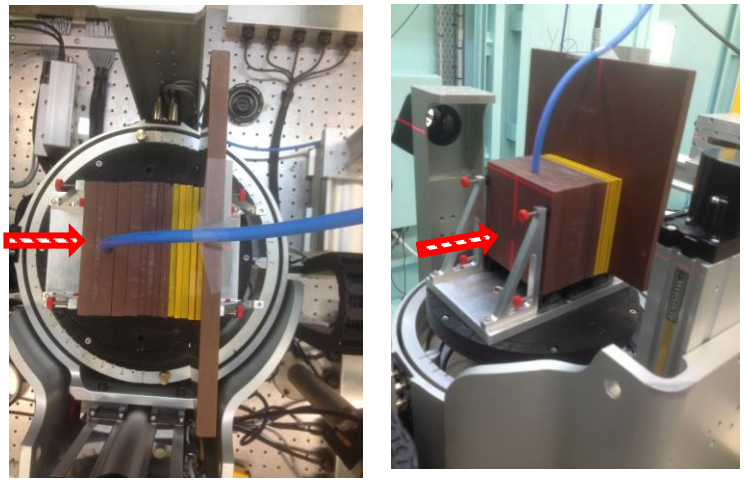

Figure 4.1: PinPoint™ IC calibration setup: top view and front view. The direction of the beam is shown in red.

The PinPoint™ IC SV is cylindrical and has a radius of 1 mm and length of 5 mm. The length is greater than our maximum vertical beam height as defined by the BDA, which limits the PinPoint™ IC to use in treatment field dosimetry according to small field methods. Prezado et al [63] provides an empirical derived formalism that states that the dose (D) measured in a uniform field is equivalent to the dose rate ($\dot{D}$) of the beam of known height (h) integrated over the SV when scanned at a

constant and known speed (v):

$$D = \frac{\dot{D}h}{v} \qquad (4.1)$$

A key assumption for this equation is that the majority (or, ideally, the entirety) of the dose delivered to the volume of interest is due to the beam and not scattered radiation when the beam is far from the volume of interest.

The PinPoint™ IC response at 20 mm depth in a phantom is the standard reference dose for synchrotron radiation dosimetry at AS IMBL, but it is incapable of dosimetry of intrinsic BB fields or MB fields of any type. According to the manufacturer (PTW), the minimum field size for dosimetric measurements using the PinPoint™ IC is 20 × 20 mm².

The PinPoint™ was calibrated at PTW on a TH 200 source (~100 keV) according to IAEA-TRS 398 [64] protocols and has a beam-quality correction factor (k_{Q_0}) for that standard field of 0.95. k_{Q_0} corrects the PinPoint™ IC measured dose at the reference depth in the reference field Q_0 to equal the absorbed dose in water and is unique to that particular PinPoint™ IC. Absolute dosimetry using ion chambers requires correction of the measured dose to account for deviation of the measured radiation field and device setup to standard conditions using:

$$D_{corr} = k_{Q,Q_0} k_s k_{TP} k_{pol} D_{meas} \qquad (4.2)$$

Where correction factors apply for beam quality (k_{Q,Q_0}), IC recombination (k_s), readout polarity effect (k_{pol}), and temperature and pressure variation (k_{TP}) for a measured dose (D_{meas}). Of note is the k_{Q,Q_0} factor, which is the ratio of beam quality correction factors for the field of interest (beam quality Q) and the reference field (beam quality Q_0). As beam quality is dependent upon radiation field dimensions, uniformity, energy spectrum, and intensity it is impractical to determine beam quality of every beamline configuration due to the difficulty of positioning all beamline components identically every time. Therefore, the k_{Q,Q_0} correction factor is chosen to be unity for all beamline configurations in this thesis and is acknowledged as a source of error when determining dose with the PinPoint™ IC. Correction factors for recombination and polarisation are close to unity and so have negligible impact on the PinPoint™ dose measurements for these beamline configurations. A correction factor for local temperature and pressure should also be applied to IC measurements to account for deviations from laboratory standard temperature and pressure (293.15 K and 101.325 kPa, respectively). Hutch 2B is both air-conditioned and sealed when in use, and so variations in

temperature and pressure for each experiment over the years were found to be ± 0.5 K and ± 4 kPa about the means. Utilising the average values of 297.12 K and 101.21 kPA produces a temperature-and-pressure correction factor of 1.02 ± 2%.

4.2.2 PTW microDiamond dosimetry

An alternative detector with micrometre-scale spatial resolution potential is the PTW microDiamond (60019) detector (0.004 mm^3 SV), also read out using the UNIDOS webline Dosemeter at a bias of 0 V [11]. The diamond detector itself has a 1.1 mm radius and 1 µm thickness, though the outer shell is of identical dimensions to that of the PinPoint™ IC. This allows the microDiamond to be set up and read out identically to the PinPoint™ IC, using the same dedicated phantom slab with milled channel. Great care must be taken to align the microDiamond such that the circular face of the SV is normal to the XZ plane, as a misalignment of even 0.1° will produce a geometric SV y-width as seen by the beam of $2200\ \mu m \cdot sin(0.1°) + 1\ \mu m \cdot \cos(0.1°)\ \sim 4.8\ \mu m$, which is almost 5 times the thickness of the disc.

4.2.3 Radiographic film dosimetry

Some experiments were also compared against EBT3 Gafchromic® film (recommended range 2–20 Gy) and HDV2 film (recommended range 10–1000 Gy). 20 × 20 mm^2 film were prepared at CMRP laboratories and scanned on-site at the AS IMBL using a Leica (Leica Microsystems, Wetzlar, Germany) DMI4000B microscope with an 8-bit Leica DMC2900 camera coupled to a 10x objective lens prior to irradiation. The Leica microscope used a 10-× objective lens to achieve a field-of-view of 2 × 2 mm^2. Use of the motorised sample stage and Leica software allowed the stitching-together of multiple fields of view (6 horizontal × 5 vertical) to achieve combined field size of 12 × 10 mm^2 at the centre of the film with effective DPI of ~3630 (or pixel size ~7 µm).

Positioning of films for irradiation was accomplished using large scrap film cut-offs and the laser guidance system to determine proper placement of films. Films were affixed to the phantom faces using tape at the edges of the film to avoid perturbation of the dose.

All films were allowed 24–26 Hrs after irradiation for development before being scanned again. This is the minimum development time necessary for reliable dosimetry of the films. The full development time of 72 hours would be ideal, but this is impractical due to time constraints during experiments at the AS IMBL. Careful timing of post-irradiation scanning allows consistent development across all films, and thus consistent calibration of the optical density.

Analysis was performed by comparison of average red-channel pixel values pre- and post-irradiation to determine change in optical density (OD) as a function of dose delivered. Films are calibrated on-site via dose delivery using the beam of interest according to PinPoint™ IC dose measurements at 20 mm depth in an RMI457 phantom for a 20 × 20 mm² field by adjusting speed of vertical scan to deliver the required dose. This ensures that beam quality of the calibration films and the films of interest are consistent.

The significantly greater resolution of the film scans using the Leica microscope (as compared to standard 250 DPI flatbed scanners) allows for dosimetry of micrometre-scale dose structures. This methodology is also used to extend the linear region of the film OD-dose calibration curve beyond the manufacturer's recommended range, thus allowing accurate dosimetry in both peak and valley simultaneously (provided both dose in the peak and the valley are within the linear range of the calibration curve). This improvement is offset by interference of the granular structure of the film that is visible on the micrometre scale, which acts to increase OD wherever the granular structure of the film is darker, thus complicating determination of OD.

An extensive MRT film dosimetry protocol is under development of CMRP PhD student Andrew Dipuglia using Gafchromic® film so is not described in detail in this thesis. However, this film protocol was utilised as part of the research described in this thesis.

4.2.4 50 µm Epitaxial SSD dosimetry with the X-Tream readout system

50 µm thick epitaxial silicon strip detectors (EPI SSDs) described in [24], [65] were used in some experiments as a point of comparison to the 3D-Mesa SSD. All EPI SSDs designated for use in MRT dosimetry are affixed within a flexible kapton probe [21] with a thickness of 600 µm, a width of 10 mm, and a length of 30 cm. The silicon wafer containing the EPI SSD and contacts is covered by kapton tape to create an airtight and watertight seal around the silicon device and then the flexible mount is wrapped in conductive aluminium tape to provide support, protection, and electrical grounding. The kapton probe terminates in a male USB mount with 4 pins providing connection to the EPI SSD N+, P+, 'guard ring', and ground contacts. The grounded contact is electrically continuous with the aluminium wrapping. Data was acquired for EPI SSDs using the CMRP-designed X-Tream data acquisition and readout system [21] and associated probe-packaging compatible preamplifiers.

The EPI SSD may be set up in edge-on mode awith a 0 V bias applied, allowing the thickness of the

SV to determine spatial resolution, or set up in face-on mode and biased to 50 V to allow the 'guard ring' to electrically restrict the depletion zone and thus determine the spatial resolution. Positioning of the EPI SSD was accomplished using dedicated RMI457 phantom slabs with dimensions of 20 × 100 × 100 mm³, with a specially-milled channel matching the dimensions of the kapton probe in edge-on or face-on orientation. Channels were milled such that the position of the SSD at the end of the mount would be in the centre of the phantom's YZ plane. In the edge-on configuration, this forces a minimum available depth of measurement of 5 mm in the phantom due to the width of the probe. Permanent marker has been used to add guidelines to the front face of the phantom to aid in positioning the SSD with assistance from the laser-guidance system (Figure 4.2).

The X-Tream system is controlled by a purpose-built GUI, 'RadPlot,' which is also capable of basic MRT-relevant data analysis (e.g. determination of baseline counts, integration of regions, MRT peak identification, calculation of FWHMs, PVDRs, etc.). EPI SSD output data as acquired by X-Tream may be analysed manually with 'RadPlot' or by the use of Python-based scripts.

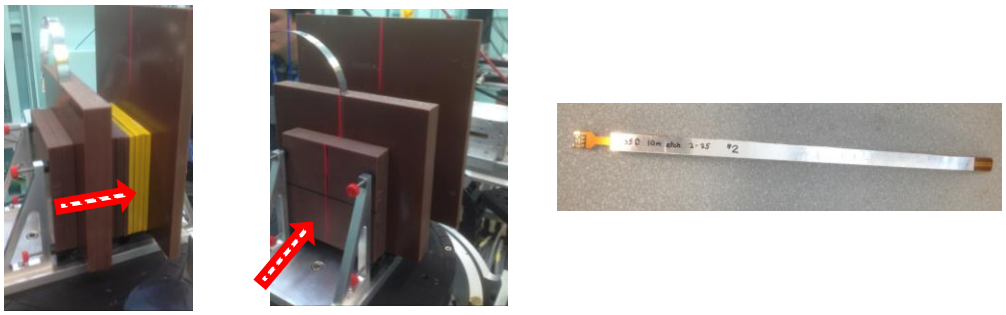

Figure 4.2: Setup of the Epitaxial 50 µm SSD.
The direction of the beam shown in red.
a. Side view of edge-on setup; b. Front view of edge-on setup; c. Flexible kapton probe packaging

4.2.5 3D-Mesa SSD dosimetery with the X-Tream readout system

The 3D-Mesa SSD device itself is mounted similarly to the EPI SSD in order to interface with the X-Tream readout system. Each 3D-Mesa SSD is mounted at the end of a kapton probe and requires the same preparation as the EPI SSD before use (i.e. wrapping with kapton and aluminium tape). The USB pins at the end of the 3D-Mesa SSD probe provide connection to the N+, P+ strip contacts and ground only, as there is no guard ring structure on the 3D-Mesa SSD. Like the EPI SSD, the 3D-Mesa SSD is also capable of edge-on or face-on mode measurements (see Figure 4.3) and uses the same custom-milled phantoms. Thus, the 3D-Mesa SSD is positioned using the same method as the EPI SSD. However, the dimensions of the 3D-Mesa SSD 3D volume are much smaller than that of the EPI SSD and so the spatial resolution in face-on mode is roughly equivalent to that of edge-

on mode, especially at low bias (Figure 3.9).

3D-Mesa SSD output data as acquired by X-Tream is stored in the same format as EPI output data and may be analysed using RadPlot or the same Python scripts used to analyse EPI SSD results.

Due to the large number of 3D-Mesa SSD samples that have been studied, a shorthand naming-scheme has been implemented to simplify identification of devices. The shorthand identifying name is in the format 'A's-'L'µm-#'N' where 'A' refers to a single (1) or double (2) sided SV design, 'L' is the length of the SV, and "N' is the 3D-Mesa SSD device's unique identifier number. Therefore, a single-sided 100-µm length SV device with a sample number 13 is denoted 1s-100µm-#13.

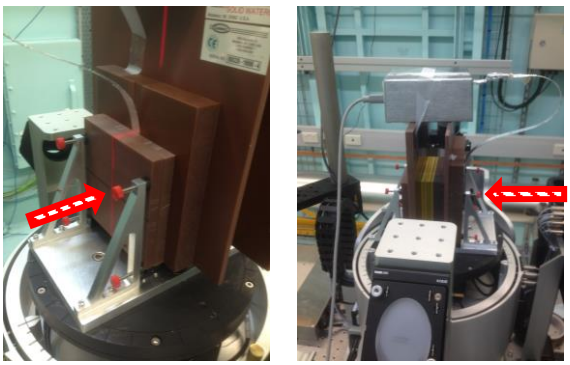

Figure 4.3: Face-on setup of the 3D-Mesa SSD showing alignment at depth and preamplifier. The direction of the beam is shown in red.

4.3 Sources of systemic uncertainty in 3D-Mesa X-Tream dosimetry

Calculation of the uncertainty of a measurement is essential for determining the accuracy of experimental results. Throughout Chapter 4 and Chapter 5 3D-Mesa SSD measurements are primarily performed utilising the X-Tream dosimetry system, though in rare cases 3D-Mesa SSDs may utilise the UNIDOS webline universal Dosemeter instead.

The vertical size of the radiation field is also a factor, as the entire 3D-Mesa SSD (including bridge and pads) should be entirely contained within the beam for most stable performance. This is a concern because the use of sensitivity of the detector to any transient charge produced under the bridge and pads. Fortunately, the smallest vertical (Z) size of any radiation field in this thesis (0.5 mm) is still larger than the combined lengths of the SV, bridge, and pad (L + 200 µm + 150 µm) for all but the longest SV, so this is rarely a concern provided proper placement within the field.

Additionally, the positioning of the 3D-Mesa SSD silicon chip within the kapton probe packaging also influences the spatial resolution and uncertainty of the measurements. For instance, if the chip is placed in the packaging such that there is a non-zero angular difference between the lengthways axis of the 3D-Mesa SSD SV and the lengthways axis of the kapton probe then the SV may exhibit

a ‘wider’ SV due to geometric effects. The change in width (W) for a rectangle of length (L) rotated by θ is approximated by

$$\Delta W = L \cdot sin(\theta) + W \cdot cos(\theta) - W \qquad (4.3)$$

A single-sided 3D-Mesa SSD SV of length 250 μm and width of 22.5 μm will present a SV ‘width’ of 26.8 μm at 1° (a 19% increase) and 44.2 μm at 5° (a 96% increase). This may result in volume averaging effects in small fields (such as MB peaks), leading to broadening of the penumbra of the field.

The energy dependence of the Si SSD is also a source of uncertainty within the polychromatic energy spectra used at IMBL. The response of Si at <150 keV energies is known to vary significantly relative to the response of a water-equivalent dosimeter. Under a constant spectrum the discrepancy can be accounted for with proper calibration factors, but the spectrum is known to change depending on depth in a phantom (due to attenuation). The spectrum of radiation will also be different in MB peaks when compared to MB valleys, even at the same depth, because the radiation field in the valley is comprised of lower energy photons that have scattered from the peak. This is an area where utilisation of Monte Carlo simulations such as in section 2.5.1 would be very valuable to quantify the spectral change between peak and valley. Work is already underway at CMRP utilising G4IMBL as a scaffold, but the complexity of this task for a single spectrum (let alone the multiple spectra examined within this thesis) renders it beyond the scope of this thesis. Therefore, uncertainty due to spectral change within the phantom is a source of error that is too complicated to fully quantify yet.

Dose rate dependence may be a source of uncertainty, but this is difficult to characterise without good control of the radiation source dose rate. Ideally, a dose-rate dependence study would be performed for a given set of filters at a fixed wiggler magnetic field strength and the dose rate of the beam would be altered by adjusting the ring current of the electron beam. Practically, it is rare to be able to be permitted to alter the electron beam ring current as that affects the radiation quality for every other beamline at the synchrotron. Alternatively, varying the wiggler magnetic field strength would allow for alteration of the synchrotron radiation dose rate, but this also alters the spectrum of the photon field more than may be easily compensated for with available filtration. This would result in interference from energy dependence that would complicate a dose-rate study. This is an area that would benefit from future investigation and further study.

Due to these sources of systemic uncertainty, some of which are not quantifiable, it has been decided

that the majority of results in this thesis be presented as ‘relative dosimetry’ (that is, measurements that have been normalised to a specific response – such as the response at a given depth, or a maximum response) rather than ‘absolute dosimetry’ (where calibration and correction factors are applied to the detector response resulting in a measurement of ‘dose to water’).

4.4 Discussion of statistical uncertainty in 3D-Mesa SSD dosimetry

4.4.1 Leakage current baseline uncertainty

When using X-Tream, data is acquired with a very high (1 MHz) sampling rate using a transimpedence amplifier with a high gain to convert the instantaneous photocurrent within the 3D-Mesa SSD into a voltage signal that can be interpreted as ADC ‘counts’ (2.51 counts/nA [21]). Consequently, the leakage current (a.k.a dark current) of the reverse-biased 3D-Mesa SSD, the gain of the preamplifier, and the electrical noise of the X-Tream system and associated cabling have an impact on the quality of the signal. This manifests as a variable non-zero baseline signal as recorded by RadPlot as a base ~100 counts when the device is connected, but not irradiated. This baseline signal can be offset slightly using inbuilt voltage offset as necessary. Generally, the baseline is characterised for every scan by allowing approximately one second of data acquisition prior to exposing the device to radiation. This baseline region is then averaged and subtracted from all data points in that measurement so that all meaningful signal is generated by interaction with the radiation field. When analysing data using python scripts, it is also possible to evaluate the standard deviation of the baseline measurement and apply a threshold to the entire measurement such that any signal below one standard deviation above the baseline is set to be zero counts. This may have use in measurements with high signal but may be dangerous in areas of low signal — for instance, in the valley regions of MRT profiles if the signal in the valley is too small.

4.4.2 Determining the uncertainty of a single measurement

In most cases in Chapter 4 and Chapter 5, the majority of results presented were derived from analysis of a single scan’s response profile. For BB results and MRT SNS results, the relevant data of interest was the integral of the signal received by the 3D-Mesa SSD during irradiation, less the baseline. For MRT intrinsic studies, the relevant data of interest was derived from analysis of individual dosimetric structures present in the dose profile (i.e. peak signal, valley signal, width of structures), less the baseline. In order to determine the statistical uncertainty of the signal at any given point the simplest method is to assume that the uncertainty of the baseline signal encompasses

the uncertainty due to electronic noise. Thus, the baseline uncertainty is the average uncertainty of any point. However, this does not take into account statistical error introduced by the moment-to-moment differences in the radiation field that produces the signal.

A better option is to take advantage of the 1 MHz sampling rate of the X-Tream dosimetry system and apply an averaging factor to the measured data. For instance, an averaging factor of 100 could be applied by finding the average of every 100 points (i.e. the average signal over 100 µs, for an adjusted sampling rate of 0.1 kHz) and performing analysis on the resultant profile. This method allows the construction of a secondary 'error profile' from the standard deviation of each set of averaged points. This does result in smoothing of the profile and artificial reduction of large signals that may be noticeable for large averaging factors, but the magnitude of the initial sampling rate is such that some averaging is feasible without losing noticeable resolution. For instance, the fastest scan speed in this thesis is 20 mm/s, which corresponds to 0.02 µm/µs. An averaging factor of 100 changes the effective sampling rate to 0.1 kHz and thus the time between samples to be 100 µs, which corresponds to a distance of 2 µm. This is much less than the dimensions of the 3D-Mesa SSD and will only decrease with slower scan speeds, and thus should not negatively impact upon the quality of the measured profile.

4.4.3 Determining uncertainty of the average of several measurements

For the BB PDD study, the response of the 3D-Mesa at any given depth was obtained through the averaging of three individual scans through the beam. The statistical uncertainty of the average was therefore determined to be the standard deviation of the three samples. In an ideal case, the number of samples would be increased from three to at least ten samples, thus reducing the calculated uncertainty and improving the estimate of the mean. In practice, this was not feasible de to the limited time available for each experiment and so the choice of three repetitions per point was decided upon as a compromise between experimental time restrictions and the need for meaningful uncertainty measurements. However, the use of RadPlot for data acquisition allowed for a degree of quality control of the measured response of the detector, because the response profile is shown on-screen after each successful acquisition. Thus, any major deviations between scans (e.g. resulting from a delay in the opening or closing of the beamline shutter) could be identified and the scan repeated promptly. In rare cases, the response of the 3D-Mesa SSD was too unstable for repeated re-scans to produce consistent response profiles and so the average was performed on the 'best of

three' and resulting in a larger uncertainty than other data points in the PDD.

4.5 3D-Mesa SSD bias study

Prior to any dosimetry, the effect of the excess charge collection from under the bridge and pad that was identified in Chapter 3 was investigated. The results of this study were used to determine the optimal operating bias of the 3D-Mesa SSD detector to provide consistent response to irradiation.

4.5.1 Methods

The bias study was conducted for 1s-250µm-#14 for a 3.2T-CuCu intrinsic BB field generated by a 200 mA ring current, at 0 mm depth in a 95 × 100 × 100 mm^3 RMI457 phantom. The beam size was 20 × 2.014 mm^2 as defined by the largest BDA and the phantom was positioned such that the SV was centred in the middle of the beam. The device was read out using X-Tream with a preamplifier gain of 1.8×10^3 and a sampling frequency of 1 MHz. The stationary sample was then exposed for 500 ms duration at differing biases for a large acquisition time (5 s). The sample was not scanned through the beam during exposure, as this was a purely qualitative test of response to a radiation field. A delay of 1 s was enforced before exposure to allow for acquisition of the dark current related baseline ADC response, which is subtracted from the signal when performing the data analysis.

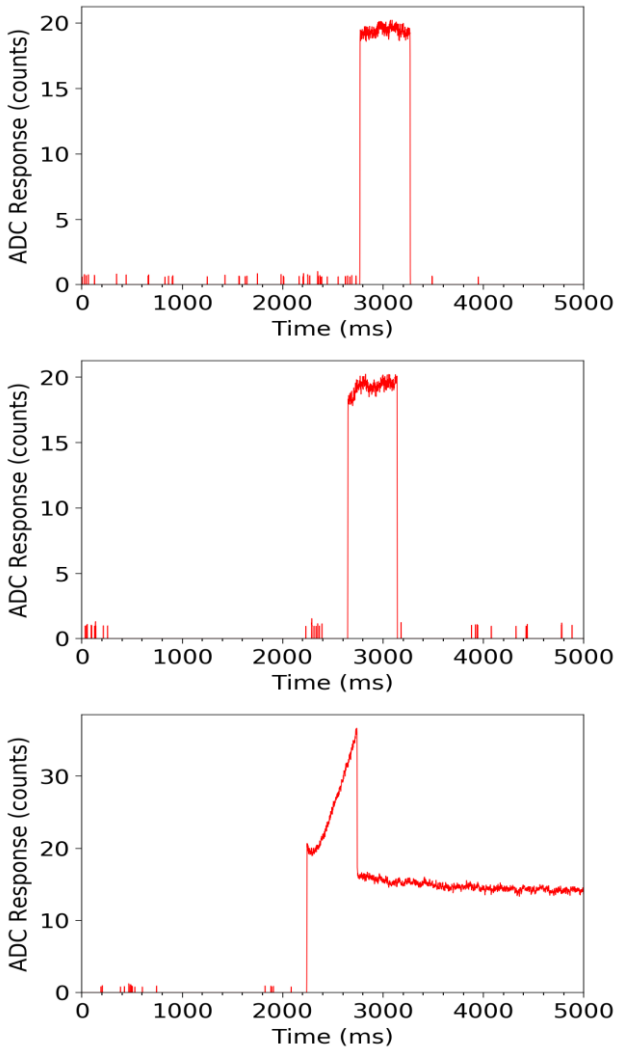

Figure 4.4: 3D-Mesa SSD Bias study – response to a 500 ms exposure.
a. 2.733 V bias; b. 3.514 V bias; c. 4.392 V bias;

4.5.2 Results and discussion

The results shown in Figure 4.4 correlate with the IBIC and TCAD results from the prior chapter, with expected square-wave-like response from the exposure at biases of 2.7 and 3.5 V. The 2.7 V response lacks the slight slope of the 3.5 V measurement, which may be due to slight variation in beam intensity due to electron beam top-up or slower charge collection at the higher voltage. At 4.4 V the charge-collection from under the bridge and pad leads to the charge build-up during irradiation and very long discharge (>2 s) after the beam is shut off.

To avoid any interference with dosimetry the 3D-Mesa SSD devices have been selected to be biased at 2.733 V or less during experimentation.

4.6 The characteristic response of a treatment field

The high sampling frequency (1 MHz) of the X-Tream readout system allows for analysis of

structures of the radiation field when the detector is dynamically scanned through the broadbeam treatment field. With a detector of sufficient sensitivity and spatial resolution the photon beam, penumbral region, and scattered radiation field (as defined by the conformal mask) may be resolved.

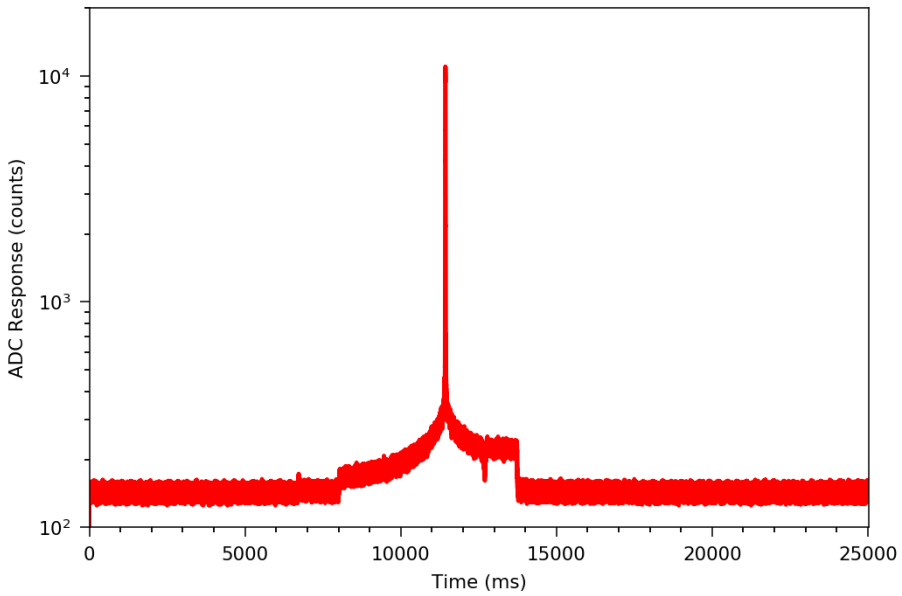

Figure 4.5: Characteristic shape of a broadbeam treatment field.

The characteristic shape of a vertical (Z) scan of a 3D-Mesa SSD through a broadbeam treatment field is shown in Figure 4.5. In the logarithmic scale, the scattered field may be seen as a plateau rising above the baseline ADC response, with edges at approximately 8,000 ms and 14,000 ms as the detector enters and leaves the field, respectively. The photon broadbeam is visible as a thin spike in ADC response at approximately 11,000 ms. If the width of the radiation field is known, then the speed of motion of the detector may be extracted, or vice versa. A small spike may be seen at approximately 7,000 ms, which may indicate when the upstream photon stop was removed and the photon beam first entered the hutch, though the sensitivity of the 3D-Mesa SSD in this field was not sufficient to determine this with confidence. A sufficiently sensitive detector (or a sufficiently intense photon spectrum) should form a second plateau of small magnitude above the baseline response and of longer duration than the scattered field plateau, which would indicate when radiation is present and absent in the hutch.

This demonstrates the ability of the 3D-Mesa SSD and X-Tream readout system to analyse the spatial features of the radiation field. If necessary, multiple vertical scans may be taken at different horizontal positions to construct a 2D ‘map’ of the radiation field at any given depth, allowing for analysis of beam uniformity — though this would be a time-consuming process if high resolution

is required.

It should be noted that the characteristic shape of the broadbeam treatment field shown above would be nearly identical if instead the detector was vertically scanned through the centre of a microbeam peak. The further away (horizontally) from the peak of the microbeam, the wider the 'spike' of the photon beam would appear. With a sufficiently sensitive detector, the two plateaus should remain visible above the baseline even when vertically scanned through the treatment field in the centre of a valley.

4.7 Response linearity study

4.7.1 Introduction

In order to perform accurate dosimetry the relationship between the dose that is delivered to the device and the response of the device (e.g. charge produced) must be well understood, generally by acquisition of a dose-response calibration curve. While it is usually more convenient to use a device with a linear response (and, ideally, a directly proportional response) to radiation exposure, nonlinear dosimeters may also be used, provided that the dose-response characteristics of that dosimeter are well-understood. Radiographic film is well known for its nonlinear response beyond the linear portion of the dose calibration curve, which can limit its use in certain radiotherapy applications. This is a concern for MRT, where the difference in magnitude of dose between the peaks and the valleys of microbeams is very large, which may cause nonlinear responses due to saturation in areas of high dose, or insufficient change in optical density in areas of low dose.

The 3D-Mesa SSD response linearity was tested for sample 2s-250µm-#2 between 0.5 Gy and 880 Gy, using the method described below, with the results shown in Figure 4.6.

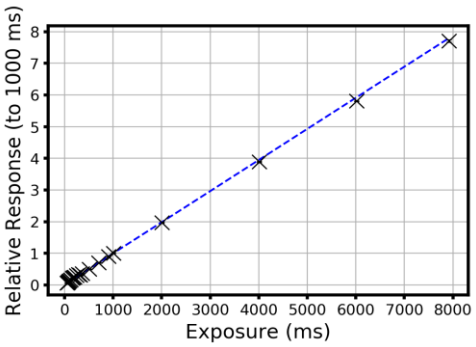

Figure 4.6: Response linearity of a double-sided 3D-Mesa SSD 250 µm SV in a ~110 Gy/s beam.

4.7.2 Method

The 3D-Mesa SSD sample was exposed to a 3T-CuCu intrinsic BB field generated by a 200 mA

ring current, at 20 mm depth in a 95 × 100 × 100 mm³ RMI457 phantom. The beam size was 36 × 0.5 mm² as defined by the tertiary shaping slits in Hutch 2A and the phantom was positioned such that the SV was centred in the middle of the beam. The device was read out using X-Tream with a bias of 2 V applied to the sample, a preamplifier gain of 1.0×10^7 and a sampling frequency of 1 MHz. The stationary sample was then exposed for increasing time increments (50 ms to 6 s) using a fast beam exposure shutter, certified by IMBL staff. The integral of the ADC response of the sample was then compared to the exposure duration to determine linearity of response. A 1 s delay before exposure ensured accurate measurement of baseline ADC response. Beam duration was controlled via the fast MRT shutter, which has a beam-off transient time of less than 1 ms. Three exposures were acquired for each time interval and the average of the integrals was calculated along with the sample standard deviation (σ) according to (4.4), where N is total number of samples, $\bar{x}$ mean value of samples, and x_n the nth sample value.

$$\sigma = \sqrt{\frac{\sum(x_n - \bar{x})^2}{N-1}} \qquad (4.4)$$

4.7.3 Results

The detector appears to perform in a linear fashion under these beam conditions (Figure 4.6). Two possible linear least-squares lines-of-best-fit were calculated for the relative response for two cases: where the intercept is forced to be 0, and where the intercept is not forced to be zero – representing device dose proportionality and device dose linearity, respectively. Fischer F-statistics have been acquired for both curves using the LINEST function of Microsoft Excel to determine the validity of the models calculated to fit the data, shown in Table 4-1, along with other data regarding the curves.

Table 4-1: Statistical analysis of response linearity line-of-best-fit.

	SSD dose proportionality	SSD dose linearity
Slope	1E-3 ± 0.34%	9.93E-4 ± 0.24%
Intercept	0	3.50E-2 ± 16%
Degrees of freedom	20	19
Fischer F-statistic	8.44E+4	1.77E+5
Critical F-value for 99% confidence	8.096	8.185

In order to be 99% confident that either model is a good fit for the data the Fisher F-statistic must be greater than the Critical F-value for 99% confidence for that dataset's degrees of freedom. This is the case for both possible models, but the linear fit with a non-zero intercept has a slightly smaller error of the slope of 0.24% (as opposed to 0.34%) and so shall be considered the better approximation. Thus, our model of 3D-Mesa SSD response linearity is a straight line with a gradient

of 9.93×10^{-4} relative response/ms (or 0.993 relative response/s, where a perfect linear fit would be a gradient of 1.0 s^{-1}) and an intercept of 3.5×10^{-4} relative response – corresponding to the dark current and other noise present without radiation delivered to the detector.

The 3D-Mesa SSD sample was then calibrated to PinPoint™ IC readings to determine ADC-dose calibration factor. Calibration scans were performed by scanning the 3D-Mesa SSD through the 36 × 0.5 mm² beam across a 36 × 100 mm² treatment field at 20 mm/s at 20 mm depth in the RMI457 phantom. Field size was defined by the beam only as no conformal mask was in place before the phantom, thus the 36 mm wide beam was scanned across the entire front face of the 95 × 100 × 100 mm³ phantom. Calibration scans were used to benchmark the integral ADC response against the dose measured by a PinPoint™ IC under the same conditions. This approach is valid under the assumption that the reference dosimeter has been properly calibrated at a national standards laboratory (e.g., ARPANSA) and that all necessary correction factors are applied to the measured PinPoint™ IC dose — as in (4.2) — to determine absolute dose in Gy. A calibration factor (C) may then be calculated from the reference dose (D) and the detector response (R) by:

$$C = \frac{D}{R} \qquad (4.5)$$

For a dose of 6.75 Gy the 3D-Mesa SSD received $4.31 \times 10^8 \pm 1\%$ counts and thus using (4.5) has a calibration factor of 1.57×10^{-8} Gy/count. This becomes a treatment field dose rate of 270 Gy/s at 20 mm depth in the RMI457 phantom according to (4.1) when rearranged for $\dot{D}$. Applying the calibration factor to the dose linearity response at 1000 ms (~6.9×10^9 ADC counts) provides an intrinsic field dose rate of ~110 Gy/s at 20 mm depth in the phantom.

4.7.4 Discussion of results – treatment field dose rate vs intrinsic field dose rate

The expected air-KERMA rate for a 3T-CuCu configuration according to SPEC (Table 2-2) is 356 Gy/s and differs significantly from both treatment field and intrinsic field dose rates, allowing for slight decrease in dose rate due to 20 mm phantom depth. This highlights the magnitude of the impact of the primary and secondary shaping slits on the dose rate expected at the phantom. It is recommended that treatment field dose rates calculated for PinPoint™ IC measurements later in this thesis be compared to expected air-KERMA rates under the acknowledgement that primary and secondary shaping slits are unique to each experiment and may not be configured to permit maximum dose rate at the phantom.

The treatment field dose rate is a factor of ~2.5 that of the intrinsic dose rate at centre of field. To account for the difference in calculated dose rates, the response of the treatment field is analysed in Figure 4.7. A logarithmic scale is applied to the vertical axis to allow easy identification of all features of the profile and the baseline response was calculated from the average of all counts in the first second of acquisition, then subtracted from the rest of the profile. The extents of the FWHM, the full width of the peak above the plateau of scattered dose, and the full width of the plateau of dose acquired by the 3D-Mesa SSD are shown with dotted lines. The integral over the full plateau is $3.76 \times 10^6 \pm 10\%$ counts and the peak response is 8895 counts ± 5% for a sampling rate of 1 MHz and an averaging factor of 100. The integral over the FWHM is calculated to be 33.9% of the total integral over the field, and the full width of the peak was calculated to be 43.7 % of the total integral of the field (thus, the integral of the full plateau without the peak is 56.3%). Therefore, for the 0.5 mm height beam over the 100 mm treatment field, more than half of the dose contribution is from scattered photons, not from the beam itself.

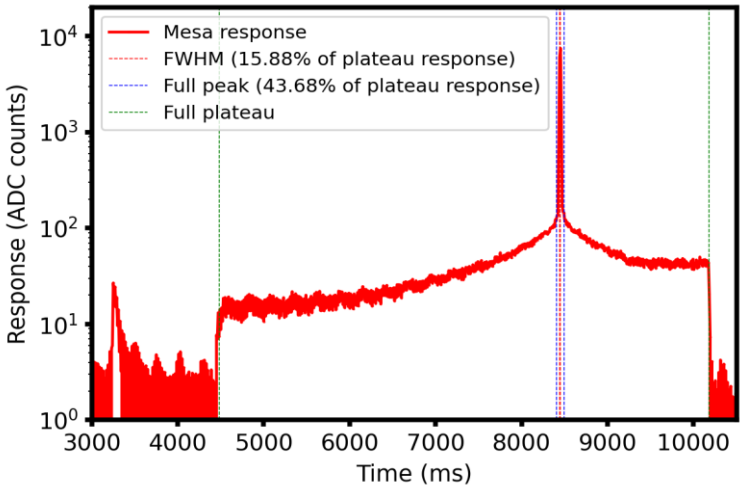

Figure 4.7: BB dose profile for comparison to expected dose linearity.

This indicates that these field conditions do not fulfil the assumption of (4.1) that the majority of the dose delivered must be due to the direct beam and not the scattered photons from the penumbral region of the beam. If an additional factor of 0.437 (i.e. 43.7%) is multiplied to the treatment field dose rate to account for the dose delivered only within the peak, the dose rate of the beam is corrected to 118 Gy/s – which agrees within 10% to the dose rate calculated via the stationary scan in the centre of the beam (110 Gy/s). An alternative intrinsic dose rate may also be calculated by multiplying the maximum response of the peak by the sampling rate and the calibration factor to produce ~140 Gy/s.

These calculations indicate that the magnitude of the out-of-beam dose contribution for large treatment fields (relative to the size of the intrinsic beam), and the distinction between the intrinsic field dose rate and the treatment field dose rate, are both important considerations when characterising a synchrotron BB treatment field. This also highlights the effect of the use of a conformal mask to restrict the dimensions of the treatment field, thereby reducing the relative magnitude of the contribution of scattered out-of-beam photons to the total dose delivered.

With these corrections, the results of this study indicate that the 3D-Mesa SSD exhibits a linear response to irradiation for intrinsic field dose rates of ~100 Gy/s.

4.8 Lifetime study

Radiation hardness of a dosimeter is essential for cost-efficient and time-efficient dosimetry of high-dose-rate synchrotron radiation fields. This was investigated by exposure of 3D-Mesa SSD samples to an intrinsic BB field of known dimensions and dose-rate for extended intervals of time to observe the degradation in the response as the radiation damage accumulated.

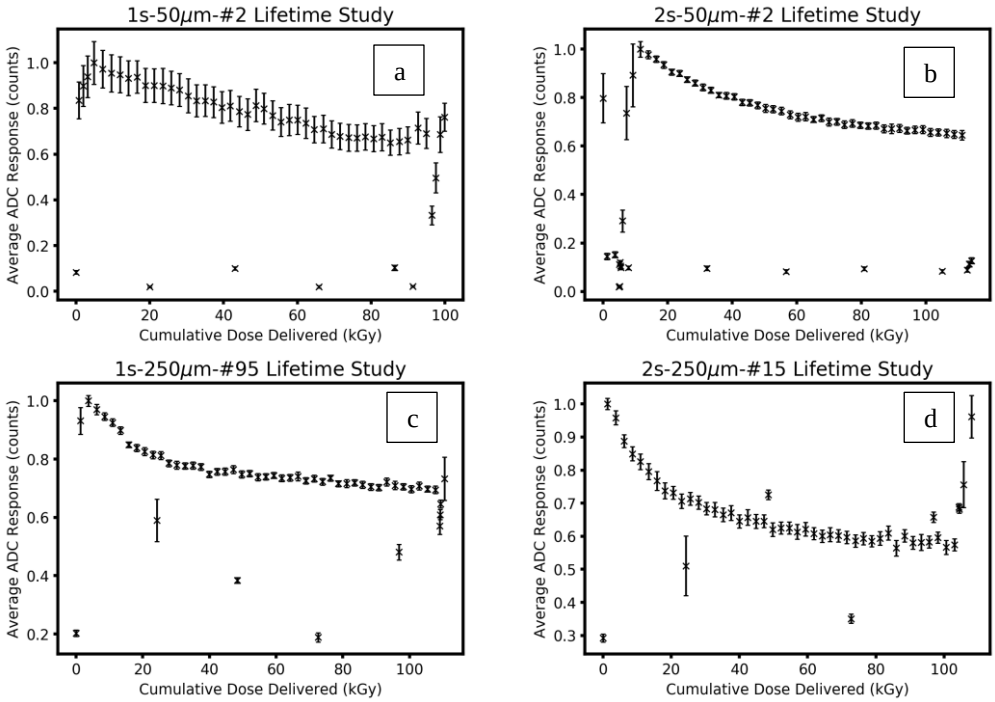

Figure 4.8: Average ADC response over 100 kGy delivered.
a. 1s-50µm-#2 b. 2s-50µm-#2 c. 1s-250µm-#95 d. 2s-250µm-#15.

4.8.1 Methods

Multiple 3D-Mesa SSD samples were exposed to a 3T-CuCu intrinsic BB field generated by a 200 mA ring current, at 20 mm depth in a 95 × 100 × 100 mm³ RMI457 phantom. The beam size was 20 × 2.014 mm² and the phantom was positioned such that the SV was centred in the middle of the

beam. The device was read out using X-Tream with a bias of 2 V, a preamplifier gain of 1.8×10^4 and a sampling frequency of 1 MHz. The treatment field dose rate was determined to be 242 Gy/s by the PinPoint™ IC, but the intrinsic field dose rate was not measured by that detector. As the beam size is a factor of 4 times larger in the vertical direction and the treatment field size is one fifth of the size used in the response linearity study, it is assumed that contribution of scatter to treatment field dose is smaller. The ratio of treatment field size to beam height in the response linearity study is ~200 times larger, whereas the ratio for this configuration is ~10 times larger. Thus, it is assumed that (4.1) holds and the treatment field dose rate is assumed to approximate the intrinsic dose rate for this case.

Once positioned, samples were exposed for various intervals of time up to a cumulative dose of ~100 kGy and average ADC response in the plateau was calculated, with the standard deviation of the plateau providing uncertainty. The average response (in ADC units) vs cumulative dose delivered has been plotted and shown in Figure 4.8. Outliers are the result of a mismatch between the MRT fast-shutter trigger and ADC automatic collection trigger, or due to initial positioning of the detector close to 0 kGy delivered.

4.8.2 Results and discussion

All detector samples show a gradual degradation of ADC response over the dose delivered as radiation damage accumulates and increases charge accumulation within the Si-SiO_2 interface. All models tested were still functional after >100 kGy were delivered but could not be tested to point of failure due to time limitations of the synchrotron experiment. Nevertheless, devices were not expected to function after 150 kGy due to observed failure of other samples with similar estimated cumulative dose deposition.

The graphs in Figure 4.8 show evidence that the 3D-Mesa SSD device should be irradiated by approximately 40 kGy prior to use in order for the device to perform in the most stable section of the Response-Cumulative Dose curve. The calibration factor of the device should also regularly (every ~30 kGy) recalculated in order to compensate for long-term changes in the device response behavior due to radiation damage.

The judgment can be made that the 3D-Mesa SSD is sufficiently radiation-hard to allow for use in MRT dosimetry. Normal calibration of the 3D-Mesa SSD in BB fields and then intrinsic MB y-profile scans for a ~100 Gy/s 2.014 mm (Z) beam with a scanning speed of 10 mm/s are estimated

to accumulate 60–100 Gy and thus are capable of being performed ~1000 times before replacement of the detector becomes necessary. Based on the above results and the assumption of a single MRT treatment fraction per patient, it is feasible to expect that the total treatment QA could be carried out (including detector alignment) before recalibration of the detector would definitely need to be made.

4.9 Mono-energetic study

The ideal dosimeter provides an energy-independent response — that is, the response of the detector is the same for beams of identical dose-rate regardless of the energy of the incident spectrum of radiation. Silicon is known to over-respond relative to water at energies lower than 100 keV by a factor of up to 8 times the response at approximately 40 keV. Above 100 keV, the response is approximately constant. This is due to the ratio of the differing mass-energy-absorption coefficients of silicon relative to water as obtained from Hubbell and Seltzer [66] and which are shown in Figure 4.9.

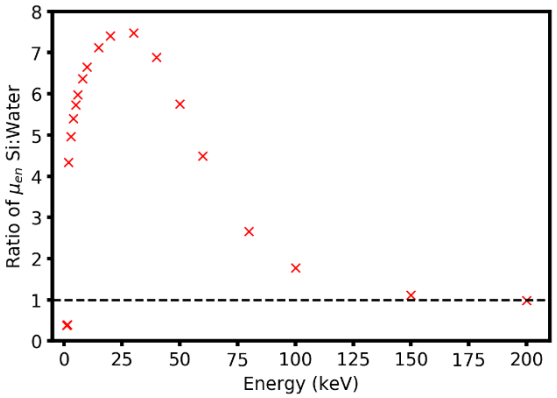

Figure 4.9: Ratio of the mass-energy absorption coefficient of Si to water.

4.9.1 Methods

A mono-energetic study was performed to investigate the 3D-Mesa SSD energy dependence at energies less than 100 keV. A similar experimental setup of monochromatic experiments is described in detail in [67]. Briefly, the synchrotron radiation field is passed into the monochromator directly after Hutch 1A filtration where the field is diffracted off a Si single crystal. Adjustment of the angle and distance to a secondary Si crystal allows selection of the desired energy, although higher-order harmonic contamination may occur at low energies (e.g., at 25 keV the 3rd order harmonic of 75 keV contributes 10–30 % of the dose). The resulting monochromatic beam is shaped as a standard polychromatic beam and measured with the same method for dosimetry of a BB treatment field. 3D-Mesa SSD samples are compared to PinPoint™ IC readings at 20 mm depth for

calibration at each energy.

Mono-energetic X-ray beams between 20 and 100 keV were produced from a 3T-CuAl primary beam incident on the monochromator, generated by a 200 mA synchrotron storage ring current. A PinPoint™ IC was placed at 20 mm depth in a 100 × 100 × 100 mm³ RMI457 phantom and scanned through multiple monochromatic 20 × 2.014 mm² beams with 20 × 20 mm² field size at 10 mm/s. Primary and secondary shaping slit apertures were reduced to reduce dose rate of the beam. The dose rate at each energy was determined through application of (4.1) to PinPoint™ IC results. The PinPoint™ IC was then replaced with various 3D-Mesa SSD samples both at 20 mm depth and scanned through the same energies for the same beam conditions to determine calibration factor and relative response as a factor of energy. 3D-Mesa SSD devices were also exposed at 0 mm depth after calibration to PinPoint™ IC results. The PTW microDiamond detector was also scanned at 20 mm depth as a point of comparison.

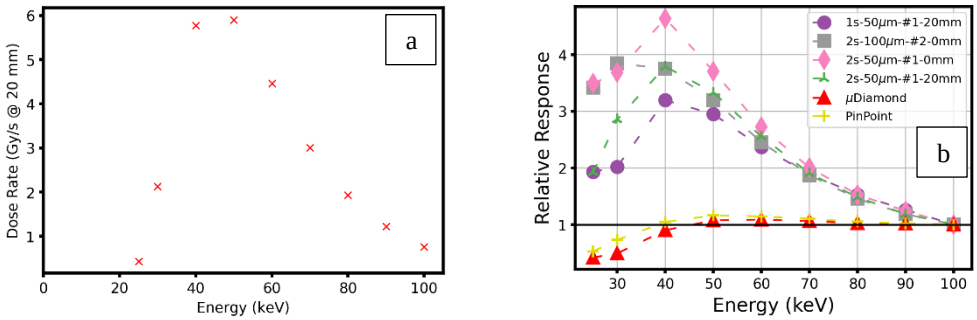

Figure 4.10: Energy dependence of 3D-Mesa SSDs of varied design.
a. PinPoint™ IC Dose rate *b. Normalised responses relative to 100 keV.*

The 3D-Mesa SSD devices were read out using the UNIDOS webline Dosemeter rather than X-Tream in order to test 3D-Mesa SSD response with a different readout system. This also allowed us to take advantage of monochromatic experimental control script which interfaced with beamline controls and the UNIDOS webline Dosemeterreadout to allow automation of the monochromatic study. The 3D-Mesa SSD devices were biased at 0 V for this study due to limitations on the prototype USB-BNC converter that was constructed to allow 3D-Mesa SSD readout with the UNIDOS webline Dosemeter.

All treatment field scans were acquired at 0.35 mm/s scan speed rather than adjusting the speed based on PinPoint™ IC treatment field dose rate to deliver equal dose at each energy. Instead, the response of the Hutch 2B in-air ICs were monitored during scans and were chosen to provide a measurement of difference in the air-KERMA rate at each energy. Thus, all results were normalised

against the in-air IC measurements for each energy to account for differing dose delivered per energy. After this, results were then normalised against the 100 keV response to observe energy dependence trends of each detector.

4.9.2 Results and discussion

The dose rate at each energy as determined by PinPoint™ IC results is shown in Figure 4.10.a to display the difference in flux at each point on the energy spectrum and thus highlight the importance of normalisation to the air-KERMA rate estimation.

Figure 4.10.d. shows the relative response of each 3D-Mesa SSD sample, the PinPoint™ IC, and the microDiamond detector, normalised first to the in-air IC measurement of air-KERMA, then normalised again to the response at 100 keV (the highest energy tested). A trend is observed that all 3D-Mesa SSD devices have increased relative response at low energy between three to five times that at 100 keV. At 0 mm depth, the low-energy overresponse is even more pronounced at greater than five times that at 100 keV. Energy dependence appears to be improved compared to the theoretical energy dependence described in Figure 4.9, with an experimental over-response of 3× at 50 keV compared to the theoretically expected 5× at 50 keV.

Both the PinPoint™ IC, and the microDiamond detector show superior energy dependence between 40 keV and 100 keV, with relative reponses to 100 keV of near unity. Beneath 40 keV, both detectors show an under-response relative to 100 keV, which should be accounted for in the event of very low energy dosimetry at IMBL.

Further investigation is needed to examine the energy dependee of the full range of 3D-Mesa SSD detector designs (such as the 250 µm SV length designs, which were not available for this experiment), but 1s-50µm design appears to have slightly smaller deviation from unity at 20 mm depth than the 2s-50µm design, and thus appears to be the best design candidate (from this limited sample selection) for future devices with respect to energy dependence of the response.

Based on these results it is recommended that care should be taken to utilise different Dose-ADC calibration depending on the energy of the beam. Furthermore, it is cautioned that 3D-Mesa SSD overresponse may be a factor for radiation fields with a large energy range encompassing <70 keV to >100 keV or rapidly changing photon spectral conditions.

4.10 Calibration factors of 3D-Mesa SSD designs

Reliable dosimetry requires repeatable measurements and thus depends on uniformity of response

across all dosimeters of identical design. A uniformity study on 3D-Mesa SSD samples of identical design fabricated on the same Si wafer and a comparison of 3D-Mesa SSD samples of different design that were fabricated using the same Si wafer has been obtained. This study examined calibration factors among all SV designs to examine the effect of the SV geometry upon the ADC response under identical conditions.

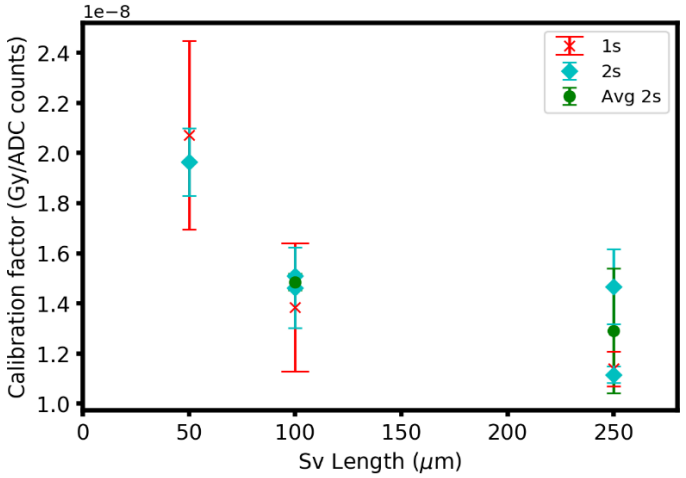

Figure 4.11: Calibration factors of 3D-Mesa SSDs in a 3.2T-CuCu field.

4.10.1 Methods

3D-Mesa SSD samples of each SV design were exposed to a 3.2T-CuCu BB treatment field generated by a 200 mA ring current, at 20 mm depth in a 95 × 100 × 100 mm³ RMI457 phantom. The beam size was 36 × 0.5 mm² as defined by the Hutch 2A tertiary shaping slits and the phantom was scanned across the entire 100 mm height of the face of the phantom with no conformal mask in place to produce a 36 × 100 mm² treatment field. The device was read out using X-Tream with a bias of 2 V, a preamplifier gain of 1.0×10^7 and a sampling frequency of 1 MHz. The sample was then exposed for various durations and the integral of ADC response was compared to expected dose. A 1 s delay before exposure ensured accurate measurement of baseline ADC response. Three measurements of the treatment field were taken for each dosimeter and the average response was calculated, (with an uncertainty equal to the standard deviation of the samples), and calibration factors were compared. Calibration factors for this beam configuration are shown in Figure 4.11 and numerically in Table 4-2.

Table 4-2: Calibration factors of 3D-Mesa SSDs in a 3.2T-CuCu field.

Detector design	Calibration factor (Gy/Count)	Uncertainty
1s-50µm-#1	2.0723E-08	18.2%
1s-100µm-#2	1.38478E-08	18.5%
1s-250µm-#2	1.13946E-08	6.1%
2s-50µm-#1	1.96451E-08	6.9%
2s-100µm-#1	1.50893E-08	0.3%
2s-100µm-#2	1.50893E-08	10.9%
2s-250µm-#1	1.11598E-08	10.2%
2s-250µm-#2	1.11598E-08	3.0%
2s-100µm-AVG	1.48597E-08	2.2%
2s-250µm-#AVG	1.29185E-08	19.3%

4.10.2 Results and discussion

Calibration factors behave as expected: larger volume SVs generate more charge for the same dose delivered due to the larger cross-sectional area and thus the calibration factor determined is smaller. This is more pronounced when changing the SV length and compared to changing the SV type, due to the larger change in volume. The only outlier to this trend is the single-sided 100-µm length SV. The uncertainty of the calibration factors varied between 18.5 % and 0.3 % depending on the detector sample. Generally, larger devices had smaller uncertainties, but better statistics (i.e. more scans per device and more devices scanned) are necessary to identify trends with reliability.

These results show the non-uniformity of calibration factors across 3D-Mesa SSD SV designs, as expected. This may be useful for informing the selection of a specific 3D-Mesa SSD design to address specific requirements. For example, a larger device shows larger response and so may be useful for small-field and low-dose-rate dosimetry, whereas a smaller device could be used for higher dose-rate fields where loss of sensitivity is counteracted by increased photon flux.

Average calibration factors across each of the two samples of the 2s-100µm, and 2s-250µm SV designs were determined. Because only two sample of each design were used to determine mean and standard deviation, the reliability of results is small and the uncertainty is large. The 2s-100µm average resulted in an uncertainty of 2.2 % whereas the 2s-250µm average resulted in a 19.3 %

uncertainty. This indicates that while uniformity of response across samples of the same type is possible there may be discrepancies up to 20%, though repetition of this experiment will be required to improve statistics and reliability of results. Thus, it is recommended that every sample be treated as unique and a calibration factor determined for every experiment to minimise the probability of incorrect dosimetry.

Over subsequent experiments, calibration factors were determined for a number of different 3D-Mesa SSD devices in different beam configurations and with different preamplifiers. A summary of these calibration factors is shown in Table 4-3.

Table 4-3: Calibration factors for different beam configurations.

Beam configuration	3D-Mesa SSD sample	Calibration factor (Gy/ADC)	Preamplifier gain (±3%)	Gain-independent factor
1.4T-AlAl	2s-250µm-#2	2.78E-07	5.0E+05	1.39E-01
3T-CuCu	1s-250µm-#14	1.053E-05	1.8E+04	1.88E-01
2T-CuAl	1s-250µm-#13	8.15E-07	1.5E+05	1.22E-01
3T-CuAl	1s-250µm-#13	6.305E-07	1.8E+05	1.13E-01
3T-CuCu	1s-250µm-#100	1.00E-06	1.8E+05	1.80E-01

When different preamplifier gains are taken into account by extending (4.4) such that detector response R is divided by preamplifier gain a gain-independent calibration factor may be determined. The gain-independent factor appears relatively constant across a variety of 3D-Mesa SSD samples over a number of beam configurations at $1.48 \times 10^{-1} \pm 23\%$. This shows the consistency of the 3D-Mesa SSD device across samples for the 250 µm length SV with multiple beam configurations and the changing gain-independent factor for 1s-250µm-#13 for 2T-CuAl and 3T-CuAl shows the need for recalibration after large dose delivery or when changing beam configuration.

These results emphasise the need for recalibration of the 3D-Mesa SSD at the beginning of every experiment to avoid incorrect dosimetry.

4.11 Percentage depth-dose studies

4.11.1 Introduction

Acquisition of normalised depth-dose profiles (a.k.a. percentage depth-dose profiles, henceforth PDDs) is one of the most common and important dosimetry measurements that can be performed. Accurate and reliable PDDs in water-equivalent phantoms allow characterisation of the radiation field under known conditions at depth in a phantom (and eventually within a patient), which is the

foundation of precision delivery of the radiation dose. Quality Assurance of radiation fields for use on humans requires accurate, reliable, repeatable, and fast acquisition of results in order to verify patient-specific treatment. Each data point of a PDD is normalised to a response at a given reference depth such that:

$$D_{norm,x} = \frac{R_x}{R_{20}} \qquad (4.6)$$

Where $D_{norm,x}$ is the normalised dose (or response) at depth x, R_x the response at depth x, and R_{20} the response at the reference depth (20 mm in this case).

Percentage depth dose profiles have been acquired for a number of beamline configurations and 3D-Mesa SSD samples for comparison against other experimentally based techniques (e.g., PinPoint™ IC, EBT3 Film, PTW microDiamond) and G4IMBL simulated results. Unless stated otherwise, the 3D-Mesa SSD devices were biased to ~2 V and read out with a sampling frequency of 1 MHz using the X-Tream data acquisition system and associated QT-based software 'RadPlot', with further analysis performed with python scripts. A >1 s delay is introduced in all scans before exposure to allow acquisition of the measured baseline detector response.

Uncertainty is determined by repetition of each measurement a minimum of three times, and calculation of the mean response and the standard deviation of the sample measurements, as discussed in section 4.4.3 above. The 3D-Mesa SSD uncertainty of the dose at a given depth 'x mm' ($\Delta D_{norm,x}$), will be shown by the error bars on the graphs below, and will be scaled to account for normalisation to the 20 mm response using relative error equation:

$$\frac{\Delta D_{norm,x}}{D_{norm,x}} = \frac{\Delta R_x}{R_x} \qquad (4.7)$$

Substituting (4.8) into (4.7) for a given depth of x mm produces:

$$\begin{aligned} \Delta D_{norm,x} &= D_{norm,x} \times \frac{\Delta R_x}{R_x} \\ &= \frac{R_x}{R_{20}} \times \frac{\Delta R_x}{R_x} \\ &= \frac{\Delta R_x}{R_{20}} \end{aligned} \qquad (4.8)$$

where $D_{norm,x}$ is normalised response at x mm, R_x the response at x mm, and ΔR_x the uncertainty of response at x mm depth calculated from sample standard deviation.

It should be noted that secondary shaping slit position and aperture size was not recorded for the

majority of PDDs and may have been altered from optimal and well-defined settings (for very precise and reproducible data-sets) so as to reduce the dose rate or beam size for important concurrent experiments during the same experimental beam time. Therefore, the treatment field dose rate of the beam configurations as measured by the PinPoint™ IC should not be expected to match the optimised dose rates described in Table 2-2 and PDDs should be taken as relative measurements of the particular beamline configuration and beam geometry of each experiment. In order for direct comparison of future PDD measurements to the PDD results in this thesis, adjustment of shaping slits to produce an identical treatment field dose rate as measured by the PinPoint™ IC at an identical reference depth in an identical phantom would be necessary, though there is no guarantee that field-shape based artifacts would be faithfully reproduced.

4.11.2 RMI phantom 1.4T-AlAl

4.11.2.1 Methods

A PDD profile was acquired for a 1.4T-AlAl BB treatment field produced by a 165 mA ring current, in a 100 × 100 × 100 mm^3 RMI457 phantom for comparison against PinPoint™ IC results. Beam size was 36 × 0.5 mm^2, the treatment field size was 20 × 20 mm^2, and the phantom was scanned across the field at 20 mm /s. The 2s-250µm-#2 3D-Mesa SSD was chosen for the experiment to provide maximum SV for maximum sensitivity and was read out using X-Tream with a bias of 2 V, a preamplifier gain of 1.0×10^7 and a sampling frequency of 1 MHz. EBT3 film measurements were performed simultaneously at all depths to provide a point of comparison for surface dose. The treatment field dose rate of 1.4T-AlAl for the 165 mA ring current is approximately 464.4 Gy/s at 20 mm depth in the phantom due to the Al-Al filtration combination allowing for the minimum amount of attenuation of the beam. Comparatively, 3T-CuCu (moderate filtration) for a 200 mA ring current provides a treatment field dose rate of approximately 200 Gy/s at 20 mm depth. The lower beam current for this experiment (due to industrial action at the time) produced a lower dose-rate and thus smaller signal than the same wiggler-and-filtration configuration normally produces.

4.11.2.2 Results and discussion

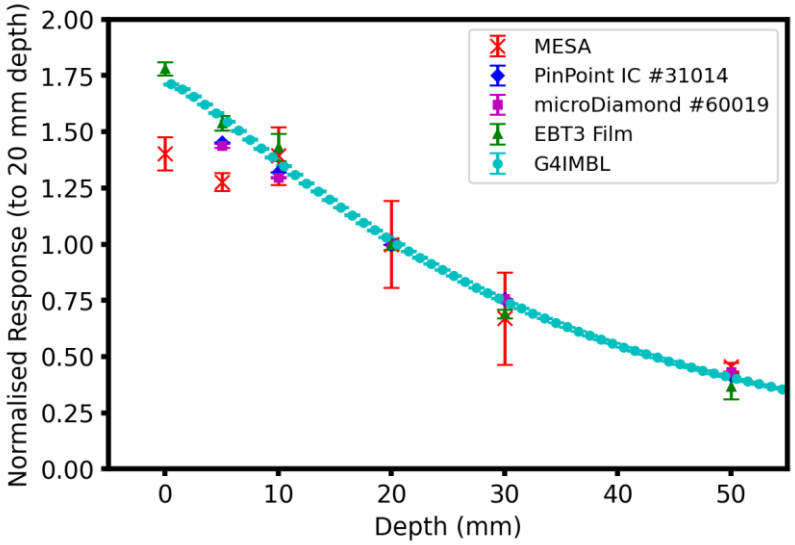

Figure 4.12: 1.4T-AlAl, RMI457 BB PDD.
165mA electron beam current, 100 × 100 × 100 mm³ RMI457 phantom; 20 × 1.2 mm² photon broadbeam, 20 × 20 mm² treatment field size, 20 mm/s; 2 V detector bias, 1.0 × 10^7 preamplifier gain, 2s-250µm-#2.

Figure 4.12 shows comparison of the 3D-Mesa SSD results with the PinPoint™ IC, microDiamond, EBT3 film, and G4IMBL for a range of depths 0–50 mm in the phantom. 3D-Mesa SSD results have a wide range of uncertainties from 3% to 31% relative to the response at that depth.

Mesa results agree with PinPoint™ IC, EBT3, and G4IMBL at depths of 10, 20, 30, and 50 mm within uncertainty and under-responds by 12% relative to the PinPoint™ IC response at 5 mm depth. Agreement at the 20 mm depth is expected as that depth was chosen as the reference point for normalisation to the PinPoint™ IC dose and so is only shown to provide the uncertainty of the 3D-Mesa SSD response at that depth. The 3D-Mesa SSD also under-responds at 0 mm depth relative to EBT3 results by 20%.

The 3D-Mesa SSD's large uncertainty at 20 and 30 mm (19 % and 31 %) depth is not ideal and reduces accuracy and reliability of results. Increasing the sample size at each depth and elimination of outliers are the best way to improve uncertainty.

Based on the large range of uncertainty the 3D-Mesa SSD is not recommended for dosimetry at 1.4T-AlAl filtration despite agreement, within uncertainty, to other dosimeters at 10 mm depth or greater, though no judgement may be made for different 1.4T filtrations. Using slower scan-speeds to provide more acquisition time may also improve uncertainty. The small volume size (i.e. reduced sensitivity) of the 3D-Mesa SSD along with the low gain of the electronics imply that that the 3D-Mesa SSD is not suitable in this regime. Improvements in the pre-amplifier must be addressed if this application is to be considered.

4.11.3 RMI phantom 2T-CuAl

4.11.3.1 Methods

PDDs were acquired for 2T-CuAl BB treatment field produced by a 200 mA ring current, in a 100 × 100 × 100 mm³ RMI457 phantom for comparison against equivalent PinPoint™ IC results. The beam size was defined by the BDA and the treatment field size was 20 × 20 mm². The 20 mm/s max speed of 1.4T-AlAl experiments was determined to be non-reproducible due to stage-motor limitations (discovered through the post analysis of the data and later confirmed by IMBL beamline staff) and so was lowered to 10 mm/s for this experiment performed at a later date. The phantom was scanned across the treatment field at 10 mm/s and again at 5 mm/s for all BDA sizes. The 3D-Mesa SSD 1s-250-#13 was chosen for maximum sensitivity and was read out using X-Tream with a bias of 2 V, a preamplifier gain of 1.5×10^5 and a sampling frequency of 1 MHz. The treatment field dose rate is 111 Gy/s at 20 mm depth in the phantom; calculated using (4.1) based on PinPoint™ IC data.

4.11.3.2 X-Tream results

Figure 4.13 shows the 3D-Mesa SSD PDD results compared to PinPoint™ IC, and G4IMBL PDDs between 5 and 50 mm depth in the RMI457 phantom at 10 mm/s. For the three beam sizes tested 3D-Mesa SSD results agreed within uncertainty with PinPoint™ IC and G4IMBL results at almost every depth and the reasonable uncertainties (<7% for all depths barring 43% uncertainty in Figure 4.13 c. at 50 mm depth) render the agreement reliable and repeatable for scientific work. It should be noted that all field sizes saw consistent under-response of the 3D-Mesa SSD at 5 mm depth by 40%, 20%, and 20% relative to the PinPoint™ IC results in order of decreasing BDA. This may be due to dose-rate dependence effects that sees charge created close to or under the bridge, which is not collected properly.

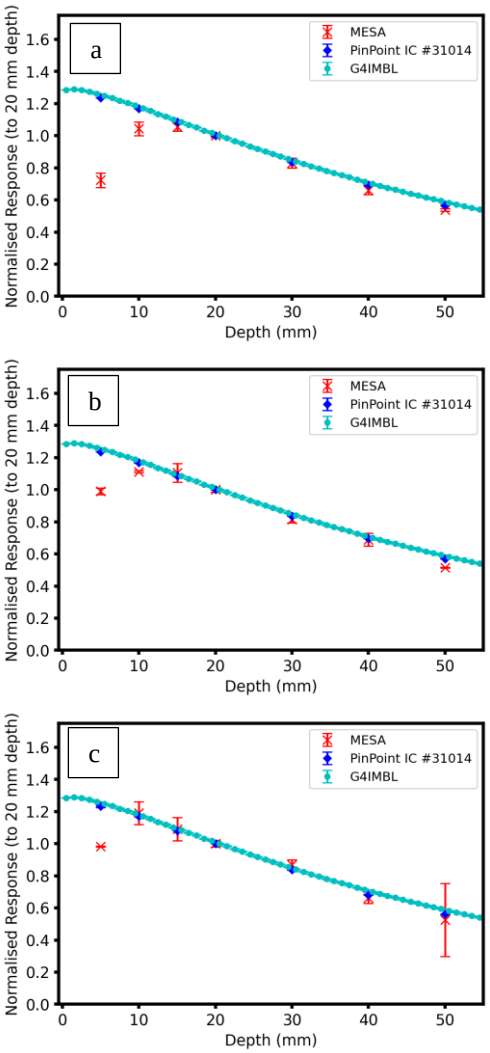

Figure 4.13: 2T-CuAl RMI457 BB PDDs, at 10 mm/s.
200 mA electron beam current, 100 × 100 × 100 mm³ RMI457 phantom; 20 × 20 mm² treatment field size; 2 V detector bias, 1.50 × 10^5 preamplifier gain, 1s-250µm-#13:
a. 20 × 2.014 mm²; b. 20 × 1.053 mm²; c. 20 × 0.532 mm².

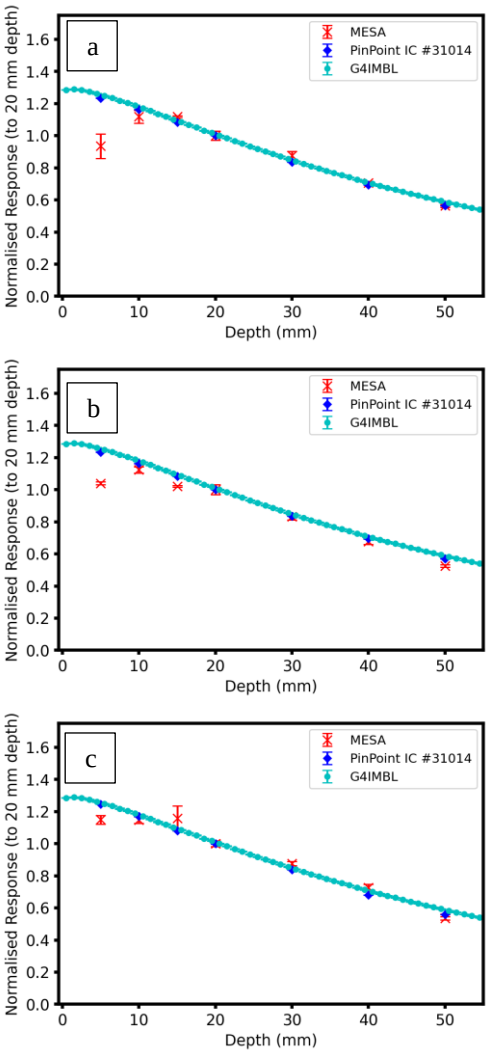

Figure 4.14: 2T-CuAl RMI457 BB PDDs, at 5 mm/s.
200 mA electron beam current, 100 × 100 × 100 mm³ RMI457 phantom; 20 × 20 mm² treatment field size; 2 V detector bias, 1.0 × 10^7 preamplifier gain, 1s-250µm-#13:
a. 20 × 2.014 mm²; b. 20 × 1.053 mm²; c. 20 × 0.532 mm².

PDDs for the 2T-CuAl 5mm/s experiment confirm the trends from the 10 mm/s experiment and are shown in Figure 4.14. 3D-Mesa SSD results achieved good agreement within a maximum of 7% uncertainty at all depths greater than 10 mm for all field sizes, but also displayed shallow under-response by 25%, 16%, and 8% relative to PinPoint™ IC at 5 mm depth in order of decreasing BDA. Of note is that improvement in relative difference to PinPoint™ IC at 5 mm occurred for both speeds as BDA size decreased, suggesting that non-uniformity of the intrinsic BB field contributes to the under-response. It is recommended that upstream filtration and shaping elements of the beamline be examined prior to every dosimetry to identify and correct unwanted attenuation of the beam.

This particular beam configuration is also reported in [17] where PDDs for a Fibre-optic-scintillator Detector (FOD) found systemic overresponse at all speeds and depths compared to PinPoint™ IC

at 10 mm depth and good agreement with PinPoint™ IC results between 20 and 50 mm.

4.11.3.3 UNIDOS webline Dosemeter results

This experiment (2T-CuAl RMI) was repeated in a separate beam time to evaluate consistency of the 3D-Mesa SSD response to identical spectrum on a different beam time. The second experiment had a treatment field dose rate of 55.26 Gy/s at 20 mm depth — almost half of the treatment field dose rate of the previous experiment, thus this experiment also shows any effects due to dose rate dependence. This difference is due to contraction of the Hutch 2A shaping slits to limit dose rate for cell dosimetry. Primary and secondary shaping slit positions were not recorded and so exact beam dimensions prior to the BDA cannot be compared. The 2T-CuAl repetition was performed at only a single speed and single beam height (1.25 mm/s and 0.532 mm, as opposed to 5 mm/s and 10 mm/s for all BDAs above), so direct comparison may only be made against one BDA dataset from the previous experiment. The experiment was performed with 3D-Mesa SSD, PinPoint™ IC, G4IMBL, and 50 µm thick EPI SSD read out using the UNIDOS webline Dosemeter at 0 V for the SSDs and standard operating bias for the PinPoint™ IC and microDiamond (Figure 4.15).

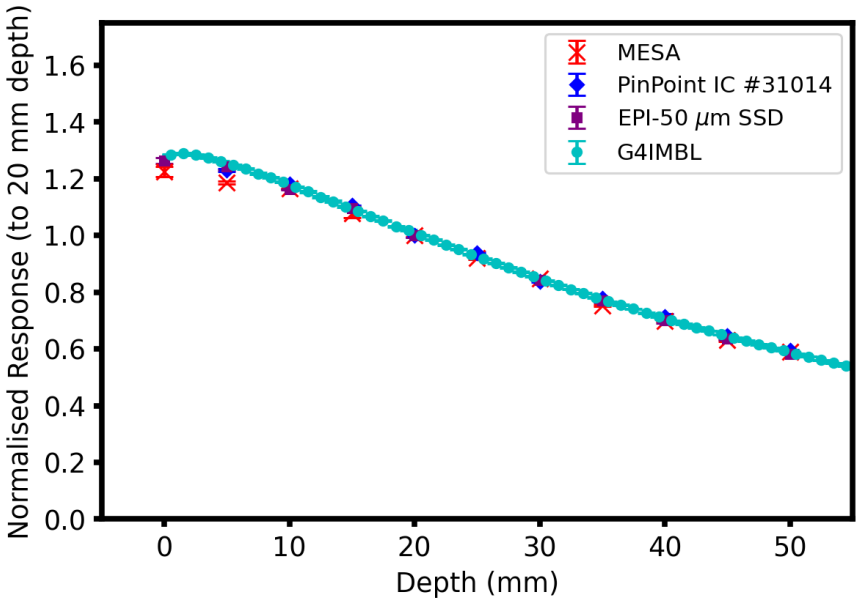

Figure 4.15: 2T-CuAl RMI457 BB PDD, UNIDOS webline Dosemeter readout. 200 mA electron beam current, 100 × 100 × 100 mm³ RMI457 phantom; 20 x 0.532 beam, 1.25 mm/s, 20 × 20 mm² treatment field size; 0 V detector bias, 2s-250µm-#13.

Statistical uncertainty of the UNIDOS webline Dosemeter was negligible because scan repetitions produced very consistent integrated charge measurements (<1% 3D-Mesa SSD uncertainty at all depths). Nevertheless, all devices agree well at depths from 10 to 50 mm under these conditions when normalised to their respective response at 20 mm depth. At 5 mm depths the EPI SSD agreed

with PinPoint™ IC within uncertainty but the 3D-Mesa SSD did not (3% relative difference for 1% uncertainty), and at 0 mm the EPI and 3D-Mesa SSD did not agree.

4.11.3.4 Discussion

These results show the potential of the 3D-Mesa SSD to perform dosimetry using the UNIDOS webline Dosemeter readout system, though several differences to the standard X-Tream readout system should be acknowledged. The UNIDOS webline Dosemeter acquires measurements by directly reading integrated charge collected over a user-defined time period for in current ranges of 0.2–250 pA, 0.01– 25 nA, or 0.001–2.5 µA, without the need for an external preamplifier. Detector readout is printed to a linked computer terminal command line as a single integral number for each measurement and may be logged in ASCII file format for ease of analysis, which would be prohibitively storage-expensive for the much larger X-Tream data files. Additionally, the UNIDOS webline Dosemeter may be controlled remotely via python-based scripts along with beamline component shutters and motors, allowing for ease of automation for a number of dosimetry techniques. However, integration of charge across the entire measurement removes the ability to examine specific features of the radiation field that X-Tream is capable of discerning, due to its MHz-scale sampling rate. The choice of readout system thus must be determined by the nature of the analysis one wishes to perform – the UNIDOS webline Dosemeter is better suited to integral-based measurements for dosimetry of entire fields (e.g., PDDs) whereas X-Tream is better suited for analysis of field features (e.g., examination of rolloff, field size, microbeam structures).

Once the issue of charge collection at large biases (>5 V) is addressed then UNIDOS webline Dosemeter measurements may be made with applied bias greater than 0 V to improve charge collection in the SV.

Based on this and the prior experiment, the 3D-Mesa SSD device is recommended for BB dosimetry of 2T-CuAl either using X-Tream or the UNIDOS webline Dosemeter readout systems at depths greater than 10 mm and speeds less than 10 mm/s for all field sizes.

4.11.4 RMI phantom 3T-CuCu

4.11.4.1 Methods

PDDs were acquired for 3T-CuCu BB treatment field produced by a 200 mA ring current, in a 100 × 100 × 100 mm³ RMI457 phantom for comparison against PinPoint™ IC, Gafchromic® film, and simulation results. Beam size was defined by the BDA and the treatment field size was 20 × 20

mm². The treatment field Dose Rate was calculated to be 218 Gy/s. The 1s-250µm-#14 3D-Mesa SSD was chosen for increased sensitivity and was biased at 2 V and read out by X-Tream for a 1.8 × 10^3 Gain preamplifier. Experimental results were compared against normalised G4IMBL simulated PDDs at the centre of the field in a voxelised RMI phantom of 1 × 1 × 1 mm^3 resolution as described in Chapter 2. EBT3 Film was irradiated for all field sizes at scan speeds of 20 and 10 mm/s; and HDV2 Film was irradiated for all field sizes at scan speeds of 10 and 5 mm/s. These speeds were chosen to ensure the calibrated range of the particular film was within the range of doses expected in the PDD according to PinPoint™ IC measurements.

4.11.4.2 Results and discussion

The uncertainty in the 3D-Mesa SSD measurements was large for all depths and BDAs at 20 mm/s and varied from 5–40%, with uncertainty trending to increase as beam size decreases (Figure 4.16). Due to the large uncertainty, the 3D-Mesa SSD results agree with PinPoint™ IC and G4IMBL results at almost all depths within uncertainty excepting two outliers, but results are not reliable enough for regular MRT QA.

EBT3 shows best agreement for the largest BDA – agreeing with the 3D-Mesa SSD, PinPoint™ IC, and G4IMBL within 3% uncertainty at all depths — but poor agreement with PinPoint™ IC and G4IMBL at smaller BDAs due to relative differences of response greater than the ability for 3% uncertainty to compensate. G4IMBL results agreed within 5% uncertainty with PinPoint™ IC results at all depths. The trend of increasing agreement of the 3D-Mesa SSD with other detector measurements as the beam size decreases has been noted, but cannot be attributed to large-field artifacts, as this would have affected results for all devices equally. Further investigation into this discrepancy is required, but the high speed of motion and low gain of the preamplifier are possible contributors to the poor performance of the 3D-Mesa SSD under these conditions.

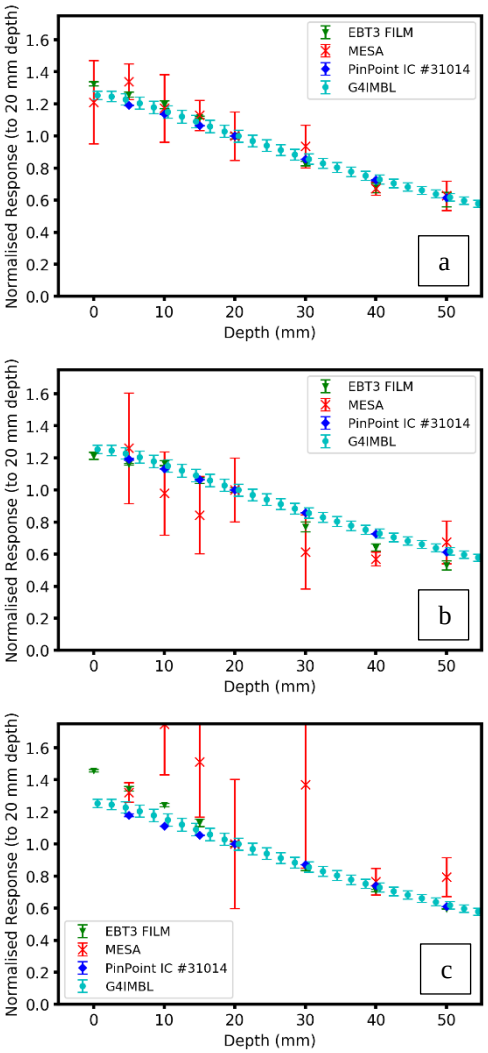

Figure 4.16: 3T-CuCu RMI457 BB PDDs, at 20 mm/s.
200 mA electron beam current, 100 × 100 × 100 mm³ RMI457 phantom; 20 × 20 mm² treatment field size; 2 V detector bias, 1.8 × 10³ preamplifier gain, 1s-250µm-#14:
a. 20 × 2.014 mm²; b. 20 × 1.053 mm²; c. 20 × 0.532 mm².

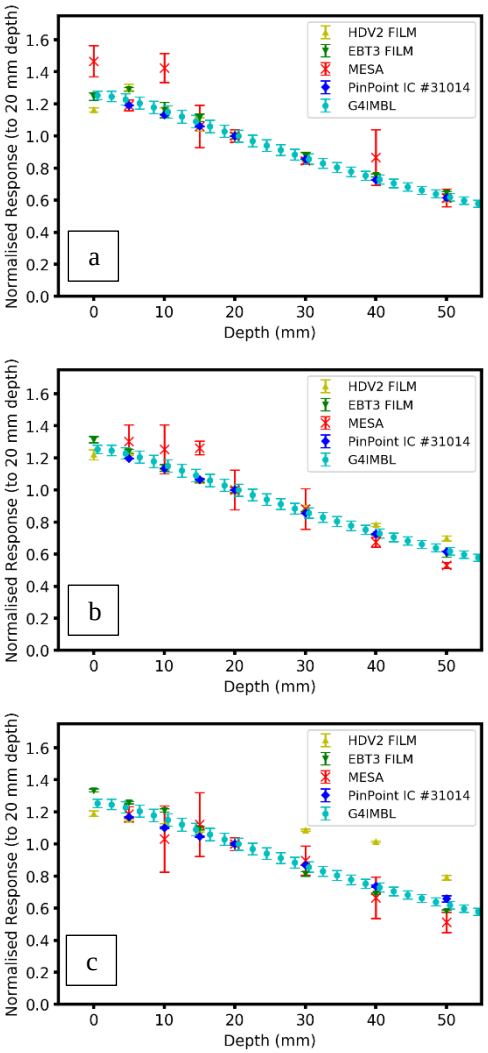

Figure 4.17: 3T-CuCu RMI457 BB PDD, at 10 mm/s.
200 mA electron beam current, 100 × 100 × 100 mm³ RMI457 phantom; 20 × 20 mm² treatment field size; 2 V detector bias, 1.8 × 10³ preamplifier gain, 1s-250µm-#14:
a. 20 × 2.014 mm²; b. 20 × 1.053 mm²; c. 20 × 0.532 mm².

Mesa results for the 10 mm/s scans are slightly improved (Figure 4.17) — covering a range of uncertainties from 2–20% — and follow the same trend of increased uncertainty as BDA size decreases. There is disagreement for the largest field size for 10 mm/s scan speed at 0 and 10 mm between the 3D-Mesa SSD and other dosimeters due to the smaller uncertainty combined with 25% overresponse relative to other dosimeters. Otherwise, all dosimeters agree within the uncertainty for the largest BDA at depths greater than 15 mm. For the 1.053 mm BDA uncertainties are low <5% for PinPoint™ IC, EBT3, HDV2, and simulation and agreement good between all dosimeters except the 3D-Mesa SSD. Because of the large uncertainty of the 3D-Mesa SSD results (3–14%), the normalised response of the 3D-Mesa SSD may agree with the normalised response of all other detectors at 5, 10, 20, 30, and 40 mm depths within that range of uncertainty. However, from a dosimetric perspective, the large uncertainty makes the 3D-Mesa SSD response unreliable.

Therefore, the 3D-Mesa response under these conditions should be treated with caution.

At 0.532 mm BDA HDV2 has a large over-responses deep in the phantom (>10% relative difference to PinPoint™ IC) and EBT3 agrees with G4IMBL and 3D-Mesa SSD results, but no longer with PinPoint™ IC results within error (~7% relative difference to PinPoint™ IC).

It is likely that the large disagreements for the largest field were due to an under-response at 20 mm depth, which exacerbates the relative difference of the remaining 3D-Mesa SSD data points to other results due to normalisation to an outlier.

G4IMBL simulation results agree with PinPoint™ IC within 5% at all reliably measureable depths.

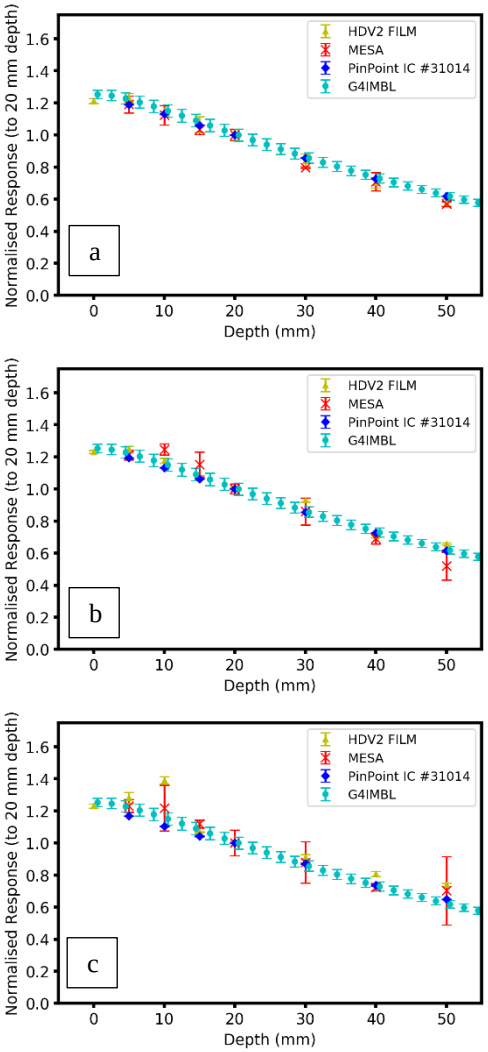

Figure 4.18: 3T-CuCu RMI457 BB PDD, at 5 mm/s.
200 mA electron beam current, 100 × 100 × 100 mm³ RMI457 phantom; 20 × 20 mm² treatment field size; 2 V detector bias, 1.8 × 10³ preamplifier gain, 1s-250µm-#14:
a. 20 × 2.014 mm²; b.20 × 1.053 mm²; c.20 × 0.532 mm².

The 5 mm/s scan speed shows the least uncertainty and best agreement of all three speeds tested. This is to be expected as the slower scan speed allows the SV to be exposed to the beam for a longer duration than other scan speeds. As such, a greater amount of data is available to be integrated, thus

improving the stability of the integral over the three repetitions.

The 3D-Mesa SSD results agree with PinPoint™ IC and G4IMBL results within uncertainty for all BDAs and depths; excepting 0 mm (which is too large to be shown at this scale) for all BDAs, and at10 mm depth for the 1.053 mm BDA (Figure 4.18). Results are more reliable with smaller uncertainties of 1–8 % for 2.014 mm, 3–17 % for 1.053 mm, and 2–30 % for 0.532 mm BDAs. The 3D-Mesa SSD results have smaller relative difference to (<8 %, <15 %, and <10 % to PinPoint™ IC for decreasing BDA) closer to the theoretical PDD curve. Notably, the 3D-Mesa SSD results at 0 mm depth do not agree for any field size due to great over-response (>50 % relative to PinPoint™ IC). HDV2 is also more stable at this slowest scan speed, agreeing within uncertainty (2%) with PinPoint™ IC, and G4IMBL results deeper than 0 mm (and 3D-Mesa SSD results greater than 5 mm depth) for both 2.014 mm and 1.053 mm BDAs. Over-responses (>7% relative to PinPoint™ IC) at multiple depths for the 0.532 mm BDA prohibit HDV2 agreement with other dosimeters at depth, though 0 mm depth does agree with predicted G4IMBL surface dose.

The increased uncertainty at smaller beam-sizes is expected because, despite the slow scan speed allowing for charge collection in the beam for longer durations, the smaller beam sizes result in both a less intense photon flux and a shorter time of measurement in the beam (though the total time for measurement in the out-of-beam field remains the same).

It should be noted that the X-Tream readout system displayed unusual baseline behaviour due to rough handling during transport, which impacted negatively on the reliability and accuracy of these results. For future experiments, an X-Tream readout system was permanently stored at the AS IMBL to eliminate the risk of damage during transport. The preamplifier also provided the lowest gain of all experiments discussed in this chapter and the low signal coupled with high noise in the system increased the uncertainty of 3D-Mesa SSD measurements.

Nevertheless, even with the unusual behaviour of the readout system the 3D-Mesa SSD detector may still be recommended for 3T-CuCu RMI457 for scan speeds of 5 mm/s or lower and especially for larger field sizes. G4IMBL PDD results agreed with PinPoint™ IC results for all speeds and BDAs, showing the potential usefulness of G4IMBL for dose verification purposes at other beam configurations.

4.11.5 Water phantom 3T-CuCu

4.11.5.1 Methods

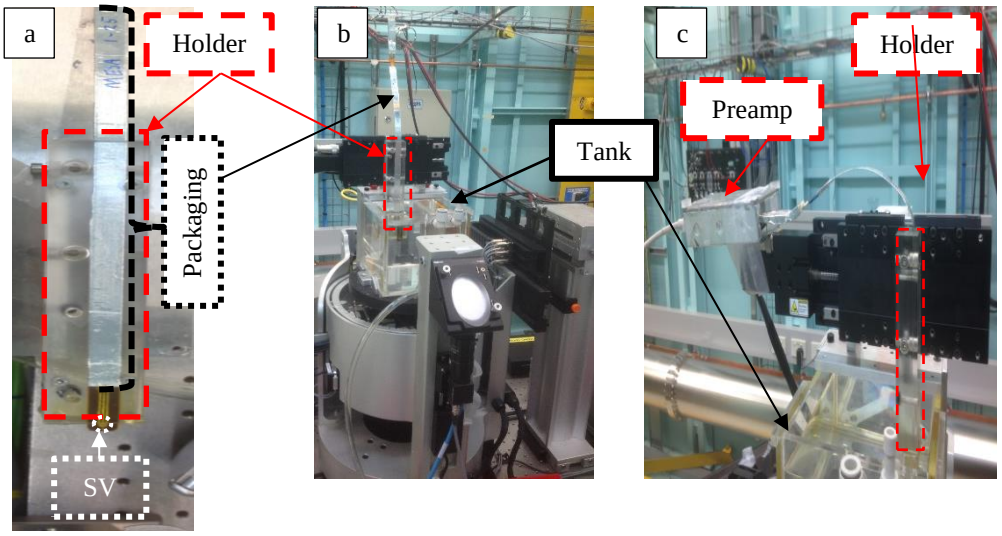

Figure 4.19: 3D-Mesa SSD water tank setup.
a. 3D-Mesa SSD in Perspex device holder; b. 3D-Mesa SSD Edge-on mode;
c. 3D-Mesa SSD Face-on mode.

The 3T-CuCu configuration was repeated during a later beam time under near-identical conditions (treatment field of 210 Gy/s within 4% of previous treatment field dose rate) with a 137 × 158 × 120 mm³ IMBL water tank phantom to compare against RMI457 PDDs. The mounting of the 3D-Mesa SSD on the moveable arm imposes a limit upon the minimum depth achievable (5 mm) for all detector types, owing to the physical size of the arm containing the detector and the need to prohibit contact between the front face of the phantom and the arm (Figure 4.19). The maximum limits of the motors driving movement of the arm also introduce a maximum depth for dose measurements, but the differing mounts specific to each detector type (PinPoint™ IC, 3D-Mesa SSD) are mounted slightly differently and so the maximum possible depth differs depending on the detector used. In this case, the maximum depth possible for the 3D-Mesa SSD was 60 mm depth. Dose measurements were acquired at depths from 5–60 mm using a different detector sample with identical SV design compared to the 3T-CuCu RMI457 experiment above.

4.11.5.2 Results and discussion

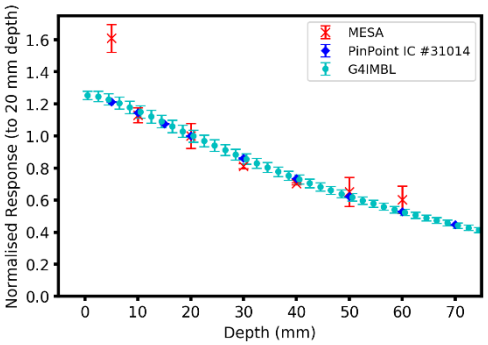

Figure 4.20: 3T-CuCu water tank BB PDD.
20 × 2.014 mm² BB, 10 mm/s, Face-on mode, 200 mA electron beam current, 137 × 158 × 120 mm³ water phantom; 20 × 20 mm² treatment field size; 2 V detector bias, 1.8 × 10^3 preamplifier gain, 1s-250µm-#100.

The 3D-Mesa SSD sample agreed with PinPoint™ IC and G4IMBL results within uncertainty at all depths within the water phantom, barring an outlier at 5 mm depth with a relative difference of +33% compared to the PinPoint™ IC result at that depth (Figure 4.20). Of note is that the uncertainty at 50 and 60 mm depth is significantly larger (~14 %) than at shallower positions (<8 %) in the phantom. This may be due to smaller signal-to-noise ratio as dose decreases and readout system noise remains constant, or due to poor contact between 3D-Mesa SSD kapton probe packaging and the preamplifier at the extremity of displacement. 3D-Mesa SSD measurements were only acquired for a single scan speed and BDA, and so direct comparison with 3T-CuCu RMI457 results is limited. Even so, the improved uncertainty in Figure 4.20 compared to Figure 4.17a. is promising for future 3T-CuCu RMI457 PDD repetitions and highlights the problems associated with the data collected with the damaged X-Tream system previously.

4.11.6 Water phantom 3T-CuAl

4.11.6.1 Methods

PDDs were acquired for 3T-CuAl BB treatment field produced by a 200 mA ring current, in a 137 × 158 × 120 mm^3 water tank phantom for comparison against PinPoint™ IC, G4IMBL, and microDiamond results. Beam size was defined by the BDA and the treatment field size was 20 × 20 mm^2. The phantom was scanned across the treatment field at 10 mm/s for all BDA sizes. The 3D-Mesa SSD 1s-250-#100 was read out using X-Tream with a bias of 2 V, a preamplifier gain of 1.8 × 10^3 and a sampling rate of 1 MHz. The treatment field dose rate is 219 Gy/s at 20 mm depth in the phantom (Figure 4.21).

4.11.6.2 Results and discussion

3D-Mesa SSD results showed a trend of improving agreement with microDiamond and PinPoint™ IC results after initial poor agreement as BDA size decreased under these beam conditions. Uncertainty of 3D-Mesa SSD measurements was less than 3% at all depths for all BDAs; microDiamond uncertainties are similarly low and relative difference to PinPoint™ IC results is less than 6% for all depths and BDAs (and less than 3% excluding 5 mm depths).

For the 2.014 mm BDA, 3D-Mesa SSD results over-responded by up to 60% compared to PinPoint™ IC results and thus do not agree with PinPoint™ results, except at 10-, 15-, and 30-mm depths. This may be due to a difference in the relative position of the 3D-Mesa SSD and PinPoint™ IC with respect to the field, which contributes to 3D-Mesa SSD response less at smaller and more uniform fields. For the 1.053 mm BDA the 3D-Mesa SSD achieves relative difference to PinPoint™ IC results of less than 15% across all depths but does not agree within uncertainty due to small magnitude of uncertainty. For 0.532 mm, the 3D-Mesa SSD achieves agreement at all depths within 3% uncertainty; barring the 100 mm depth, which has a relative difference of 12% compared to PinPoint™ IC results.

Further testing is required for this configuration, specifically acquisition of RMI457 PDDs, but good performance for the 0.532 mm BDA is very promising.

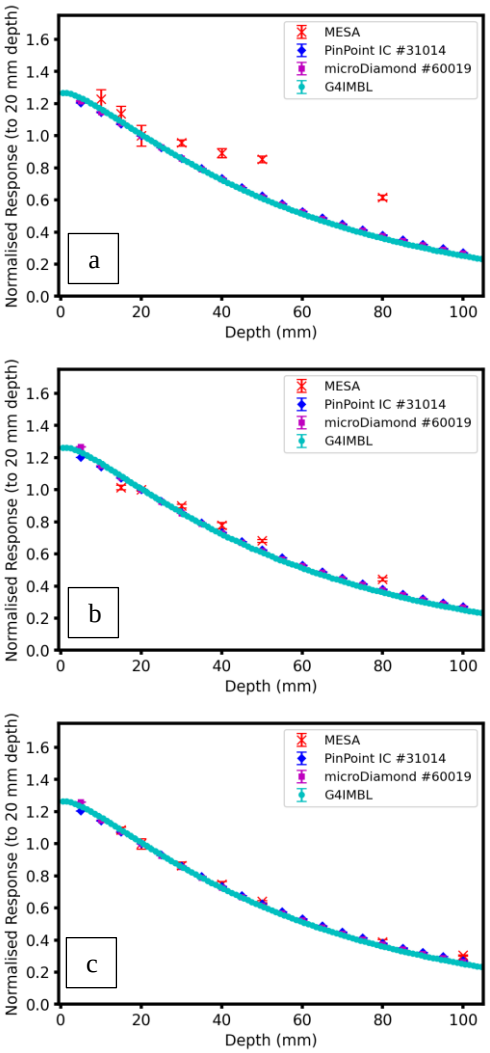

Figure 4.21: 3T-CuAl water tank BB PDD.
Face-on mode, 200 mA electron beam current, 137 × 158 × 120 mm³ water phantom, 20 × 20 mm² treatment field size, 10 mm/s, 2 V detector bias, 1.8 × 10³ preamplifier gain, 1s-250µm-#100
a. 20 × 2.014 mm²; b. 20 × 1.053 mm²; c. 20 × 0.532 mm².

4.11.7 Water phantom 3T-AlAl (intrinsic PDD)

4.11.7.1 Methods

A 3D-Mesa SSD device was used to measure an intrinsic BB PDD profile for a 3T-AlAl BB intrinsic field produced by a 200 mA ring current, in a 137 × 158 × 120 mm³ water tank phantom with a 2.014 mm height beam. The treatment field dose rate as measured with the PinPoint™ IC was ~ 3 kGy/s, but the intrinsic field dose rate could not be independently determined. The phantom was scanned laterally across the width of the intrinsic field at 2 mm/s for 10 mm and 20 mm widths as defined by the conformal mask. The 3D-Mesa SSD 1s-250-#100 was read out in edge-on mode using X-Tream with a bias of 2 V, a preamplifier gain of 1.8×10^5 and a 1 MHz sampling frequency. Data was acquired by positioning the 3D-Mesa SSD SV at the centre of the beam (Y) to optimise

height, then once positioned in the vertical centre of the beam (Z), the phantom stage was shifted laterally (-Y) 30 mm out of the beam, then scanned through the full width of the field at each depth at 2 mm/s. The resulting intrinsic BB field was then integrated and plotted in Figure 4.22.

The size of an intrinsic profile limits the number of dosimeters capable of providing a comparison to Film, EPI SSD, and microDiamond but time constraints rendered acquisition of a secondary dosimeter profile for comparison to the 3D-Mesa SSD result unfeasible. Additionally, the use of the 3D-Mesa SSD in edge-on mode enforces a deeper minimum achievable depth than face-on mode for data acquisition due to the physical dimensions of the perspex mount. The minimum achievable depth in the water tank phantom in this setup was 20 mm and maximum achievable depth was 80 mm.

4.11.7.2 Results and discussion

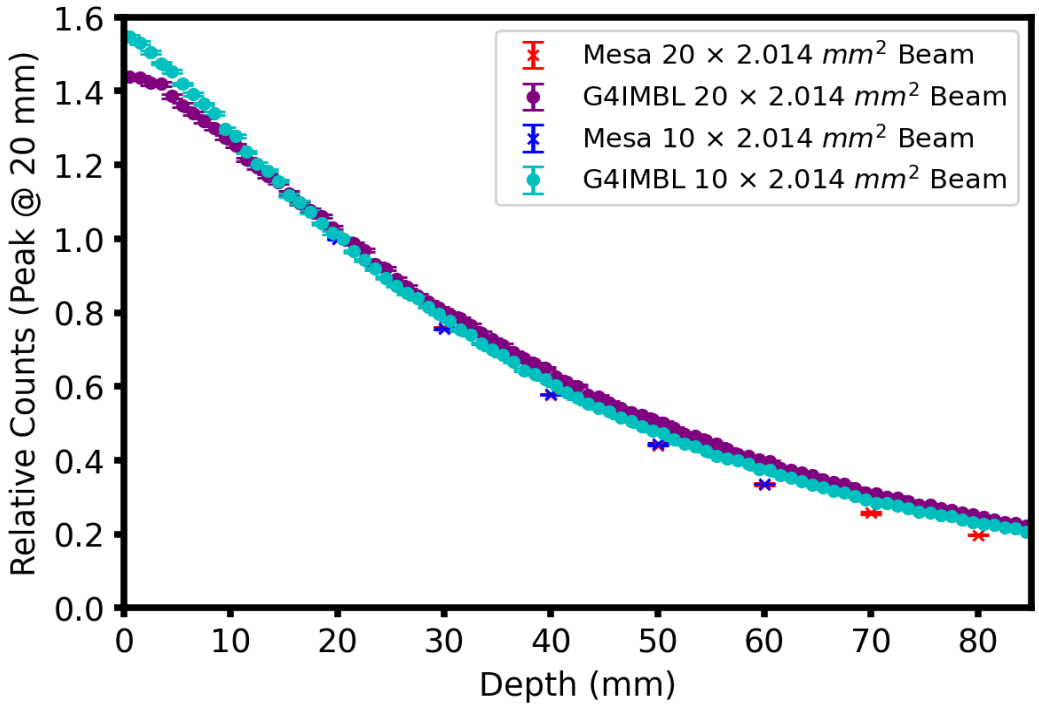

Figure 4.22: 3T-AlAl, water tank intrinsic BB PDD.
Edge-on mode, 200 mA electron beam current, 137 × 158 × 120 mm³ water phantom; 2.014 mm height beam, intrinsic lateral field scan at 2 mm/s; 2 V bias, 1.8 × 10³ preamplifier gain, 1s-250µm-#100.

Normalised 3D-Mesa SSD results for both field sizes agree within <1% uncertainty at all depths. The large field sizes (20, 10 mm) in comparison to standard treatment field Z-scanning (2.014 mm or less) generate significantly greater charge and so have small uncertainty when integrated. The small uncertainty is also indicative of good positioning of the SV, as it did not drift out of the vertical centre of the beam at greater depths, which would have led to larger roll-off at the edges of the field

and thus larger standard deviation over the integral curve.

G4IMBL results under these conditions show discrepancy in the relative response at the surface of the phantom – with the 10 × 2.014 mm² field exhibiting a slightly higher relative response (~1.6) compared to the larger field (~1.4). The gradients of the PDD curves also differ slightly, with the smaller field showing a sharper dose attenuation. Both G4IMBL PDDS overestimate the relative response as measured by the 3D-Mesa SSD at all depths, but not by a particularly large magnitude. With a slightly larger uncertainty in either 3D-Mesa SSD measurements or G4IMBL results, all four PDDs could be considered to have excellent agreement.

Comparison of these results to other experimental dosimeter results under the same conditions is necessary to recommend the 3D-Mesa SSD for use in 3T-AlAl — however, the intrinsic BB PDD is useful as a comparison to 3T-AlAl intrinsic MRT PDD performed under the same conditions, discussed in Chapter 5.

4.12 Summary of BB results

Under appropriate measurement conditions, the 3D-Mesa SSD results for synchrotron broadbeam dosimetry are promising and the data certainly warrants further development of such device technology for high resolution dosimetry. The bias study confirms the presence of excess charge collection under the bridge at ~4.7 V. Implantation of an N-stop region under the bridge and pad is recommended to solve this issue.

The 3D-Mesa SSD device design has shown good radiation hardness across multiple designs (>100 kGy) and has good response linearity (99.9% confidence of linearity) for a beam with a 110 Gy/s intrinsic field dose rate and a treatment field dose rate of 270 Gy/s. The relationship of treatment field dose rate to intrinsic field dose rate was discussed in depth and further investigation is required to determine a model that permits conversion from one to the other, or at least well-defined limits.

The mono-energetic study suggests that the device exhibits energy dependence at low energy (50 keV) of three to five times that at 100 keV normalised to the delivered dose, which is less than the expected theoretical overresponse factor of six at that energy. Further investigation is required to examine the energy dependence of the entire set of fabricated 3D-Mesa SSD designs.

The calibration factor study indicates that the response of the device in a known beam is approximately proportional to the length of the SV; thus, smaller SVs are recommended for intense beams and high-dose-rate fields where avoiding current saturation is important and loss of

sensitivity is less crucial. Larger SVs are recommended for lower dose-rates to maximise low-dose-rate response and provide higher sensitivity at the cost of greater electronic noise. Additionally, devices of the same SV design may show uniformity of calibration factor between 2 and 20 %. Repetition of this experiment with a greater sample number of identical design detectors is recommended.

Finally, a number of PDDs were performed for various beamline configurations. The 3D-Mesa SSD is recommended for use in 2T-CuAl (1.053 mm or smaller, 5 mm or deeper, 10 mm/s), 3T-CuCu (2.014 mm or smaller, 5 mm or deeper, 10 mm/s or slower) and 3T-CuAl (0.532 mm, 10 mm/s). 3T-CuCu RMI PDDs and 1.4T-AlAl PDDs may show improvement in uncertainty if performed again with more than 3 repetitions at each depth for each speed and BDA, due to improved standard deviation, or using lower scan speeds. 3T-AlAl and 4T configurations require more investigation before judgements can be made.

Chapter 5

3D-Mesa SSD microbeam experimentation at IMBL

5.1 Introduction

In this chapter, the nomenclature and types of MRT radiation fields are identified, and dosimetry options outlined. 3D-Mesa SSD results are compared against EBT3 film and G4IMBL MRT simulations for treatment MRT fields and dosimetric quantities of interest are extracted and evaluated. 3D-Mesa SSD results for intrinsic MRT fields are then analysed to determine the effect of non-optimal positioning within the MRT intrinsic field and the effect of displacement with respect to depth in an RMI457 phantom — specifically, the effect on PVDR at the surface compared to the reference depth. A comparison study on the response of the different architectures of the 3D-Mesa SSD was performed in order to evaluate their effectiveness for dosimetry in MRT. The PDD of an intrinsic MRT field measured in a water tank phantom for two different MRT field sizes was obtained for a 3T-AlAl beam and the effect of field-size on all relevant dosimetric quantities at multiple depths was assessed. Finally, an overall summary of 3D-Mesa SSD MRT results and recommendations for future work are presented.

5.2 MRT treatment and intrinsic field dosimetry

The introduction of the MSC into the broadbeam introduces extra factors that must be considered in the dosimetry of the MRT field. The MRT field is produced by placing the Hutch 2B '50-400' MSC in the path of the beam — at the same height as the BDA upstream. The array of microbeams that exit the MSC is named the intrinsic MRT field and is unable to be moved from its fixed Z-position, though it may be shaped before the MSC using the BDA or tertiary shaping slits, or afterwards using a conformal mask.

The horizontal extents of the MRT profile are defined in most cases by the conformal mask aperture width and the vertical extents defined by the BDA vertical width (or the vertical separation of the tertiary shaping slits, provided that this distance is smaller than the BDA vertical width). Depending on the size of the conformal mask aperture and its Y-position relative to the central Y-position of the MSC, the conformal mask may occasionally partially obstruct MBs at the edge of the treatment field and produce undesirable 'half-peaks' where the intensity of that peak is significantly different from the other MB peaks in the spectrum.

The MSC is capable of rotation about the Z-axis, which may perturb the beam, introduce roll-off in the dose profile, decrease the cross-sectional silt-size as seen by the beam, or even block the beam partially or entirely. Generally, the MSC is effective at preventing transmission of photons through the bulk WCCo material, but at large angle rotations excess photon transmission may arise when the thickness of the WCCo around the slits as seen by the beam is too thin to be an effective attenuator. Wave nature effects such as total external reflection of X-rays also play a significant effect at small rotation angles of the MSC. Thus, confirmation of the MSC rotation is important to allow for the cross-sectional face of the slits to be as close to perpendicular to the direction of beam traversal as possible. An optimised MSC rotation exhibits the greatest response magnitude in peaks and a symmetrical MRT profile about the central peaks.

Intrinsic field dosimetry may be performed on the intrinsic beam at any phantom depth in the X-direction by scanning a detector in the horizontal Y-direction through the vertical Z centre of the beam at a known speed (maximum horizontal Y motor speed 4 mm/s at IMBL) or (in the case of Gafchromic® films) by exposure on the stationary dosimeter for a known duration. This is an excellent dosimetry technique for optimisation of MSC rotation, and identification of unwanted 'half-peaks' that might be removed from the MRT profile with slight adjustments to the conformal mask Y-postion.

As in the case for a broadbeam, when a phantom is scanned vertically through the intrinsic field the resulting integral of the dose delivered to the point of measurement (whether in or out of the target area) from the intrinsic field over the duration of dose delivery is known as the treatment field dose. In order to construct a lateral dose profile of the treatment field it is not sufficient to simply scan the detector laterally through the field at a fixed height. Instead, dosimetry measurements of the treatment field must be performed in a manner similar to BB treatment field dosimetry at multiple Y positions — a technique henceforth referred to as the step-and-scan (SNS) method.

Firstly, the detector is scanned vertically through the intrinsic beam and the treatment field as defined by the BDA and conformal mask respectively, and then it is horizontally repositioned by a known distance using the phantom stage motor, then finally rescanned in the same direction as the prior measurement at the new Y-position and repeated as necessary. Measurement of the treatment field by the SNS method will result in a resolution equal to the Y-step distance chosen by the user in order to compromise between the need for high spatial resolution, the total desired width of the

scan, and the time constraints of the experiment. As the number of required data points increases, the SNS method becomes significantly more time-consuming than Y-scans of intrinsic fields. For this reason, SNS results shown in this thesis are coarser than intrinsic scan results and generally show only a few peaks and valleys due to time constraints during experiments.

Dosimetry of the treatment field by Gafchromic® film differs in that the entire field may be measured at once with a single scan (provided that the film is large enough to cover the treatment field), but demands a minimum 24 hours of development time and a set of dose-calibration films exposed to the same beam in order to determine the delivered dose. The relevant quantities of interest to define an MRT field are PVDR, FWHM, FWTM — which provide information regarding ratio of treatment dose to target tumour in peaks to limiting dose to normal tissue in valley, collimator rotation, divergence of the beam, and presence of artifacts due to stage-motor jitter or unwanted collimation or attenuation of the beam profile.

5.3 MRT treatment field studies – step-and-scan method

In order to deliver MRT to target tumour volumes, exposure to the intrinsic MRT field will not be sufficient. MRT treatment fields will be used instead by scanning the patient through the small intrinsic field to deliver dose across the larger field size defined by the conformal mask aperture and therefore deliver dose to the entire height of the target. Thus, fast, accurate, and reliable acquisition of treatment field dosimetric quantities (PVDR, FWHM and FWTM) is essential to bring MRT into clinical practice. At the current stage, using only single detectors, dosimetric characterisation of a MRT treatment field is too time-consuming for use in patient-specific pre-treatment dose verification, as every Y-position requires an individual scan to estimate the dose at the respective point of measurement. As field size and resolution requirements increase, the time required for full field dosimetry becomes prohibitive.

Nevertheless, analysis of small sections of the field, such as those that follow, are necessary to characterise the performance of the 3D-Mesa SSD as a potential treatment field dosimeter. Provided good performance, it becomes feasible to fabricate 3D-Mesa SSDs in large quantities and design new readout systems capable of in-parallel readout of multiple 3D-Mesa SSDs simultaneously. With proper mounting, such arrays of 3D-Mesa SSDs could be used to acquire many Y-position doses simultaneously — which fulfils the requirements for routine patient-specific quality assurance of MRT treatment.

MRT SNS studies have been performed for four different beamline configurations to assess the ability of the 3D-Mesa SSD to perform treatment field dosimetry as compared to G4IMBL simulations of the five central MBs, and EBT3 film in some cases. G4IMBL simulated lateral dose are performed with a voxel resolution of 10 µm in the Y-direction, and some discrepancies between the simulated and experimental profiles are to be expected if the experimental SNS did not specifically target the middle MB peak. To achieve sub-10 µm resolution necessary for comparison of FWHMs and FWTMs a Gaussian peak fitting scheme was applied as described below.

5.3.1 1.4T-AlAl SNS MRT treatment field

5.3.1.1 Methods

A 3D-Mesa SSD (sample 2s-250µm-#2) was exposed to a 1.4T-AlAl MRT treatment field generated by a 165 mA ring current, at 20 mm depth in a 95 × 100 × 100 mm³ RMI457 phantom. Beam size was 20 × 1.28 mm² and the phantom was scanned vertically through a 20 x 20 mm² field at 20 mm/s (the maximum vertical Z motor speed). The device was biased to 2 V and was read out using X-Tream with a preamplifier gain of 1.0×10^7 and a sampling frequency of 1 MHz.

A MRT treatment field lateral dose profile for 1.4T-AlAl has been acquired with the 3D-Mesa SSD using the SNS method at a coarse step resolution of 20 µm over three peaks. 3D-Mesa SNS results have been compared to EBT3 film that was scanned once through the treatment field at 20 mm depth under the same conditions. Repetition of Z-scans at each position for a total of three sample measurements, as in BB treatment field analysis, was deemed too time-consuming and so an alternative method of determining the measurement uncertainty was required. The chosen method for SNS experiments was comparison of measured data to fitted Gaussian data.

A Gaussian function was fitted over the measured peak at position 1.0 mm for both dosimeters to provide relevant dosimetric quantities. The Gaussian function was fitted using Scientific Python (SciPy) package non-linear least-squares fitting function based on the Gaussian equation:

$$f(x) = Ae^{-\frac{(x-\mu)^2}{2\sigma^2}} + C \qquad (5.1)$$

where A is the peak height, μ is the centroid position, σ is the FWHM, and C is a constant equalling the baseline response of the detector in the middle of the valley between two microbeam peaks.

The PVDR was calculated as the maximum of the peak at 1.0 mm divided by the average of the valley from 0.6–0.9 mm position and the uncertainty was defined using propagation of error as:

$$\left(\frac{\Delta PVDR}{PVDR}\right)^2 = \left(\frac{\Delta V}{V}\right)^2 + \left(\frac{\Delta P}{P}\right)^2 \quad (5.2)$$

where ΔV is the standard deviation of the samples from 0.6–0.9 mm and ΔP the difference between the maximum measured value at the peak and the maximum value of the fitted Gaussian curve. Using this method of calculating uncertainty of PVDR introduces a possible artificial inflation of uncertainty in the case that the true maximum response of a microbeam peak was not found, due to step-sizes that were too large. In such cases, the 'true' uncertainty of the PVDR would be smaller than calculated using (5.2).

The FWHM and FWTM were obtained by subtracting the Half-Maximum and Tenth-Maximum values respectively from all points on the fitted Gaussian and then the roots of the curve were found. The uncertainty in these quantities is defined as the resolution of the fitted Gaussian curve, which is small enough that the uncertainty in the fitted FWHM and FWTM is rounded to zero. Practically speaking, assuming that the device is mounted such that the length of the SV is normal to the XY plane during data acquisition, the minimum uncertainty in the FWHM and FWTM would be half the size of the sensitive volume in the Y-direction. Based off TCAD results (Figure 3.9 and Figure 3.11), the depletion field is approximately half the width of the SV at 2 V.

5.3.1.2 Results

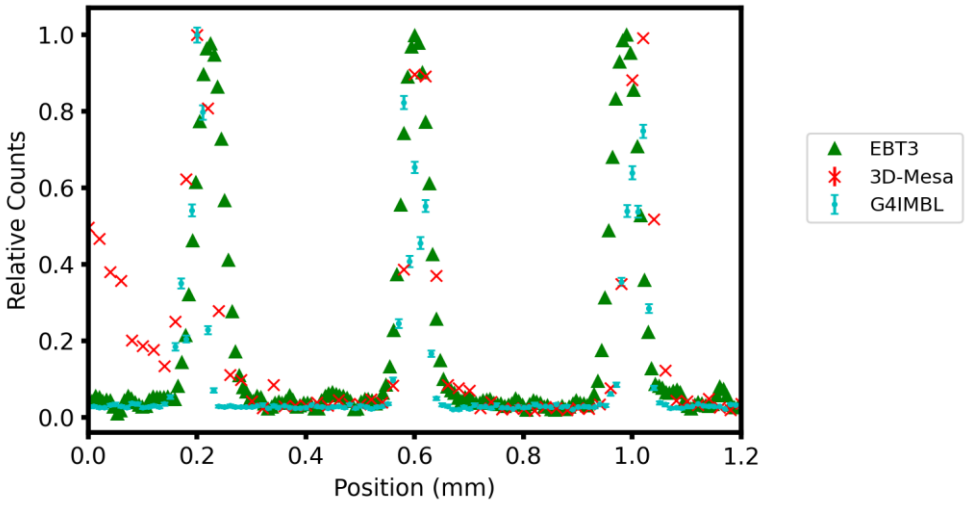

Figure 5.1: 1.4T-AlAl MRT treatment field lateral response profile.

Figure 5.1 shows the MRT treatment field measured by the 3D-Mesa SSD, EBT3 film, and simulated by G4IMBL under the same beamline conditions. 3D-Mesa SSD measurements were poor between 0.0 and 0.4 mm and so it was decided that analysis would be performed on the rightmost peak and the valley at 0.8 mm. Some positional mismatch is observed when overlaying the EBT3

and G4IMBL profiles – which may be attributed to the fact that 3D-Mesa SSD measurements were performed on peaks further from the centre of the MRT field, but the precise distance of the peaks from the centre is not known. Dosimetric quantities of interest for this beam are found in Table 5-1. The PVDRs of the dosimeters both display large uncertainty due to the large standard deviation of the points in the valley, 25.1% and 26.5% for the 3D-Mesa SSD and EBT3 respectively under these particular irradiation conditions. The PVDR uncertainty of G4IMBL is of similar magnitude at 25.2%. This could be improved for the 3D-Mesa SSD by choosing finer Y-step size to provide more samples or for both dosimeters by increasing the dose delivered in order to improve statistics in the valley.

Table 5-1: 1.4T-AlAl RMI457 MRT treatment field dosimetric quantities.

	PVDR	FWHM	FWTM
3D-Mesa SSD	40.7 ± 10.2	53.6 µm	100 µm
EBT3	28.0 ± 7.4	58.3 µm	110 µm
G4IMBL	29.76 ± 7.5	54.1 µm	102.2 µm

5.3.1.3 Discussion of results

Due to the large uncertainty, the three calculated PVDR agree within 25% uncertainty to provide an agreed PVDR within a range from 30.5–35.5, though a dosimetric uncertainty of such magnitude renders the results too imprecise for use in clinical practice.

Neither the FWHM nor the FWTM agree between the dosimeters, as the resolution of the fitted curve is significantly higher than dosimeter resolution and thus the uncertainty of FWHM and FWTM values of the fitted Gaussian are close to zero. An upper limit of the uncertainty for the 3D-Mesa SSD would be 10 µm (half the coarse step-size). The EBT3 uncertainty is estimated to be ~6.9 µm (using the readout image pixel size in µm). Under these uncertainties, the FWHM and the FWTM of both detectors would agree with the other. In this case, the relative uncertainty of 3D-Mesa SSD FWHM and FWTM would be 18.6% and 10%, and relative uncertainty of EBT3 FWHM and FWTM would be 11.8% and 6.3% respectively. The 3D-Mesa SSD uncertainty could be improved with finer step-size until the measured profile is limited by the spatial dimension of the 3D-Mesa SSD.

The uncertainty of the EBT3 FWHM and FWTM measurements is dependent either upon the resolution of the chosen Gaussian fit, or the parameters of the Leica microscope. A larger magnification (e.g. 20-× objective lens) would improve scanning resolution but may impact upon

determination of the dose-OD calibration curve due to the increased significance of the granular structure of the film in the image.

The magnitude of the FWHM is plausible for 50-µm MSC slit-width accounting for divergence and any jitter in the phantom stage scanning motor. The FWTM is calculated to be a factor of 1.87 and 1.88 larger than the FWHM of the 3D-Mesa SSD and EBT3 respectively.

The use of a Gaussian fit to model the response of a MB peak is reasonably common in the literature, though the Gaussian fit has been known to produce a sharper gradient dose falloff at the edges of the penumbra. To assess the suitability of the Gaussian fit for this data, the Gaussian fit of the 3D-Mesa SSD results is compared against a cubic spline interpolation in Figure 5.2 below.

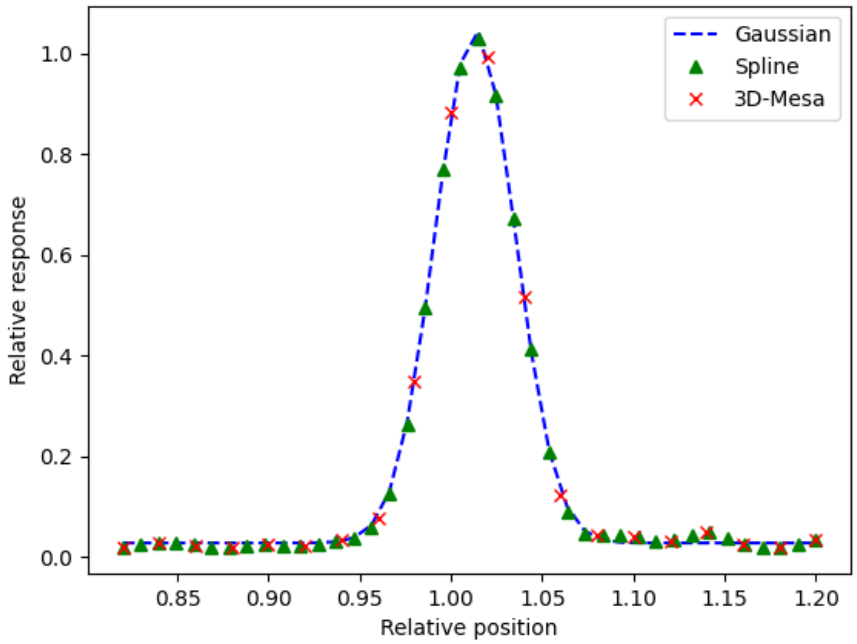

Figure 5.2: Fitting a Gaussian and a cubic spline interpolation to a MB peak.

A visual inspection of the Gaussian and spline fits indicates that the two fits would result in similar calculated FWHM and FWTM. A much finer resolution of 3D-Mesa SSD results would be necessary to perform meaningful statistical analysis to quantitatively determine the goodness of fit, and so it will be assumed that the Gaussian fit is acceptable for simple approximation of FWHM and FWTM of coarse MB data in this thesis.

5.3.2 3.2T-CuCu SNS MRT treatment field

5.3.2.1 Methods

The 3D-Mesa SSD 2s-250µm-#1 was exposed to a 3.2T-CuCu MRT treatment field generated by a 200 mA ring current, at 20 mm depth in a 95 × 100 × 100 mm³ RMI457 phantom. Beam size was

36 × 0.5 mm² and the phantom was scanned vertically through a 36 x 100 mm² field at 20 mm/s. The device was biased to 2 V and was read out using X-Tream with a preamplifier gain of 1.0×10^7 and a sampling frequency of 1 MHz. Figure 5.3 shows the measured treatment field using the SNS procedure with coarse steps of 25 µm in the valley and fine steps of 10 µm in the peak regions over two peaks for the 3D-Mesa SSD. This was compared to EBT3 film scanned once through the treatment field at 20 mm depth under the same conditions. A Gaussian distribution curve was fitted over the measured peaks at Y-position 0.4 mm for both dosimeters to provide relevant dosimetric quantities. The PVDR was measured from the fitted Gaussian maximum on the peak at 0.4 mm and the average of the valley from 0.5–0.7 mm position (Table 5-2).

5.3.2.2 Results

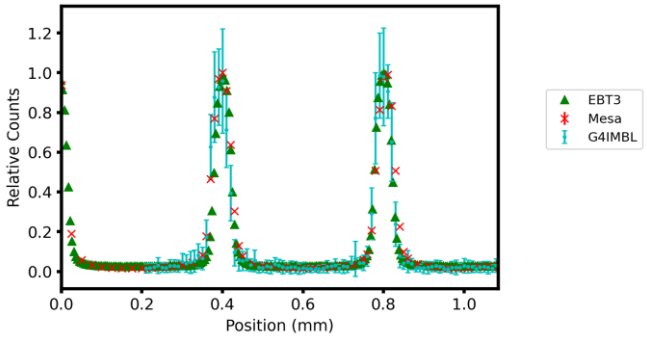

Figure 5.3. 3T-CuCu MRT treatment field lateral response profile.

Table 5-2: 3.2T-CuCu RMI457 MRT treatment field dosimetric quantities.

	PVDR	FWHM	FWTM
3D-Mesa SSD	47.38 ± 9.8	50.6 µm	94 µm
EBT3	35.58 ± 2.4	42.5 µm	80 µm
G4IMBL	38.7 ± 11.2	48.5 µm	90.5 µm

The PVDR uncertainty is improved compared to the 1.4T SNS, and calculated to be 20.7% and 6.8% for the 3D-Mesa SSD and EBT3 respectively. The G4IMBL relative uncertainty is slightly worse at 28.9%. The large uncertainty of the 3D-Mesa SSD PVDR allows agreement of the 3D-Mesa SSD PVDR and the EBT3 PVDR between 38–37.5, though the inaccuracy of the 3D-Mesa SSD PVDR is still too large for clinical use (<10% would be acceptable for preclinical work, <5% would be necessary for clinical measurements according to ICRU Report 24 [69]). As in the 1.4T case, neither FWHM nor FWTM agree between the dosimeters due to the resolution of the fitted curve. If the uncertainty of the FWHM and FWTM were chosen to be the dosimeter resolution then the 3D-Mesa SSD uncertainty would be 10 µm (based off the fine step-size in the peak) and EBT3 uncertainty would be ~6.9 µm — under these assumptions both FWHM and FWTM of both

detectors would agree within uncertainty. The magnitude of uncertainty of the FWHMs would be 19.8% and 16.2% and the uncertainty of the FWTMs would be 10.6% and 8.7% for the 3D-Mesa SSD and EBT3 respectively.

Notably, EBT3 provides a FWHM that is 7.5 µm less than the expected width of the field produced by 50 µm slit width. This may occur due to non-optimised MSC rotation, which geometrically narrows the slit width as seen by the incident beam, but this is unlikely in this case as the 3D-Mesa SSD measures a FWHM of 50.6 µm, which is plausible for an optimized MSC rotation. The granular structure of the film may also have introduced error if the grain artificially increased the average optical density in the peak, which would have the effect of increasing the half-maximum to a narrower region of the peak.

The FWTMs are calculated to be factors of 1.86 and 1.87 larger than the FWHM for 3D-Mesa SSD and EBT3 respectively, which are consistent with 1.4T-AlAl results, as expected due to the use of the same Gaussian curve fitting function to determine the FWTMs.

5.3.3 3T-CuAl SNS MRT treatment field

5.3.3.1 Methods

The 3D-Mesa SSD 1s-250µm-#13 was exposed to a 3T-CuAl MRT treatment field generated by a 200 mA ring current, at 20 mm depth in a 100 × 100 × 100 mm³ RMI457 phantom. The beam size was 20 × 2.014 mm² and the phantom was scanned vertically through a 20 x 20 mm² field at 10 mm/s. The device was read out using the UNIDOS webline Universal Dosemeter and so was biased at 0 V. Figure 5.4 shows the measured treatment field using the SNS procedure with fine steps of 10 µm over five peaks for the 3D-Mesa SSD. EBT3 film was not scanned during this experiment and so cannot provide a point of comparison. A Gaussian curve was fitted over the measured peaks at position 0.4 mm for the 3D-Mesa SSD and valley counts were averaged of the range 200 µm in the valley to provide relevant dosimetric quantities. The PVDR measured from the fitted Gaussian maximum on the peak at 0.45 and the average of the valley from 0.55–0.75 mm position (Table 5-3).

5.3.3.2 Results

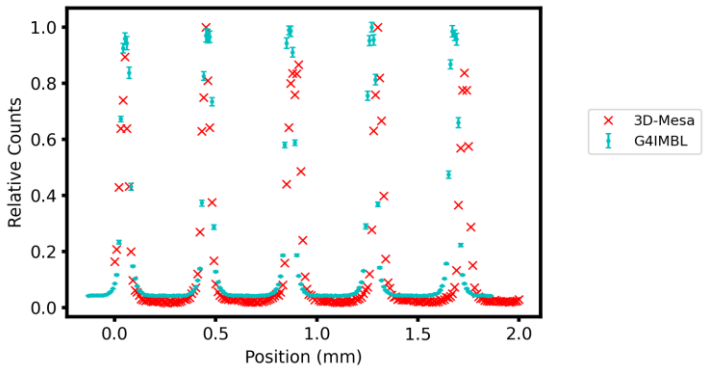

Figure 5.4: 3T-CuAl MRT treatment field lateral response profile.

Table 5-3: 3T-CuAl RMI457 MRT treatment field dosimetric quantities.

	PVDR	FWHM	FWTM
3D-Mesa SSD	42.1 ± 8.0	50 µm	94 µm
G4IMBL	23.0 ± 2.3	51 µm	97 µm

The 3D-Mesa SSD PVDR for the 3T-CuAl SNS is calculated to be 42.1 with a relative uncertainty of 19%. Without comparison to another dosimeter under the same conditions experimental validation of the PVDR measurement is not possible, though comparison to G4IMBL simulation results has been made under the acknowledgement that the simulation has not yet been validated against experimental results for this beam configuration. Simulations were performed for the 3T-CuAl MB treatment field in a 140 × 100 × 100 mm³ RMI457 phantom for a 20 × 20 mm² field, with a 1.053 mm BDA. The 140 × 2 × 2 mm³ voxelised SV is positioned on the central beam axis with 1 × 0.01 × 0.1 mm³ resolution. ~1.7×10^7 photons were simulated across ~3000 jobs and results were then merged. The PVDR calculated at 20 mm depth in the centre of the field was 23.0 ± <10%, which does not agree with the experimental 3D-Mesa SSD PVDR (42.1) within uncertainty. This smaller PVDR arises from the consistent overresponse of the G4IMBL valley dose with respect to the 3D-Mesa SSD valley measurements, though comparison against an independent dosimeter is necessary to validate the simulated profile. Deviation from expected results may be contributed to by the smaller simulated beam size (1.053 mm height was used, as no 2.014 mm-height MB PSF was available) but validation of the simulation under these beam conditions is necessary before confidence in simulated PVDR can be assured.

The FWTM is calculated to be a factor of 1.88 larger than the FWHM. If the uncertainty of the FWHM and FWTM were chosen to be the step size of 10 µm then the relative magnitude of uncertainty would be 20.0% and 10.6% respectively.

5.3.4 3T-AlAl SNS MRT treatment field

5.3.4.1 Methods

The 3D-Mesa SSD 1s-250µm-#100 was exposed to a 3T-AlAl MRT treatment field generated by a 200 mA ring current, at 25 mm depth in a 50 × 50 × 75 mm³ RMI457 phantom. This was a specially designed phantom used to model dosimetry of MRT treatment for rats with brain cancer. The beam size was 20 × 0.532 mm² and the phantom was scanned vertically through a 20 x 20 mm² field at 10 mm/s. The device was biased to 2 V and was read out using X-Tream with a preamplifier gain of 1.8×10^5 and a sampling frequency of 1 MHz. Figure 5.5 shows the measured treatment field using the SNS procedure with coarse steps of 20 µm in the valley and fine steps of 5 µm in the peak regions over two peaks for the 3D-Mesa SSD. The PVDR measured from the fitted Gaussian maximum on the peak at 0.45 and the average of the valley from 0.5–0.7 mm position (Table 5-4).

5.3.4.2 Results

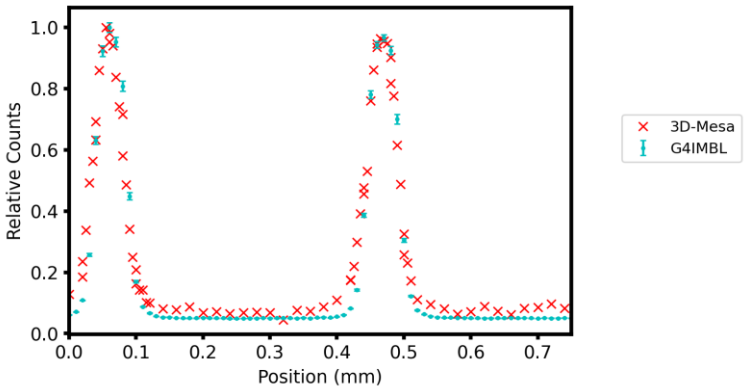

Figure 5.5: 3T-AlAl MRT treatment field lateral response profile.

Table 5-4. 3T-AlAl RMI457 MRT Treatment field dosimetric quantities

	PVDR	FWHM	FWTM
3D-Mesa SSD	12.3 ± 1.9	53.0 µm	115 µm
G4IMBL	19.0 ± 1.4	50.2 µm	96.9 µm

The uncertainty of the PVDR is 15.4% for the 3D-Mesa SSD, which is comparable to other beam configurations measured, but the magnitude of 12.27 is much smaller than all other field sizes. This may be due to a combination of factors. Firstly, that the phantom used for this SNS was 50 × 50 × 75 mm³, which is much smaller than the water tank or RMI457 phantoms of size 100× 100 × 100 mm³ (values rounded for ease of comparison) and so has less backscatter and thus differences in the photon spectrum within the phantom compared to a larger one. Secondly, the softest filtration of Al-Al provides the softest beam, with a mean energy at about 40 keV, which may be favourable to

photoelectric interactions than harder spectra of the other 3T configurations. This would increase the number of scattered photons within the MRT valleys, thus increasing the relative valley dose relative to the peak dose and reducing PVDR. This may also be compounded with energy dependence effects on the Si detector at these lower energies, thus leading to overresponse in the valleys and thus lower PVDR.

The G4IMBL PVDR is calculated to be 19.0 with a relative uncertainty of 7.4%. The 3D-Mesa SSD and G4IMBL PVDRs do not agree within uncertainty, as may be predicted from the consistent underresponse of the G4IMBL valley dose with respect to the 3D-Mesa SSD valley doses. Comparison against an independent detector is necessary to determine which PVDR is more correct.

The FWTM is a factor of 2.17 larger than the FWHM — a larger factor than all other treatment fields measured. As 3T-AlAl was the least-used configuration there is still much not known about the resulting field and its properties. This shall be the subject of future investigation.

If the uncertainty of the FWHM and FWTM was chosen to be the dosimeter resolution, then 3D-Mesa SSD uncertainty would be 5 μm (based off the fine step-size in the peak) and the magnitude of uncertainty of the FWHM and FWTM would be 9.4% and 4.4% respectively.

5.3.5 Conclusion

In summation, 3D-Mesa SSD results are promising but require further investigation and comparison against detectors of similar spatial resolution in order to verify reliability of the 3D-Mesa SSD PVDR measurement for different depths, phantoms, and radiation fields. G4IMBL simulations require validation against independent dosimeters (such as the microDiamond or EPI SSD) under these beam conditions in order to provide confidence in the simulated results, but good agreement was found when comparing PVDR to EBT3 results.

5.4 MRT intrinsic field studies — lateral scans

MRT intrinsic field dosimetry is significantly faster than MRT treatment field dosimetry after accounting for the required BB dose calibration of the detector and height (Z-position) optimization of the detector prior to any data acquisition. Though less useful for patient-specific dosimetry, intrinsic MRT field dosimetry is important as it allows for fast characterization of beam conditions (height, width, roll-off characteristics, MSC rotation verification, and identification of beam perturbation or excess attenuation). It can also be repeated regularly to ensure experimental reproducibility. Standard MRT dosimetric quantities may be obtained for the intrinsic field; but while the FWHM and FWTM are mostly constant between treatment and intrinsic fields, PVDRs of the treatment field is affected by a significant portion of scattered dose in the valley regions that is absent in the intrinsic field setup. Thus, PVDRs of the intrinsic field are generally larger than treatment field PVDRs and direct comparison between the two quantities is difficult due to the dependence on beam size, field size, phantom scanning speed, depth in phantom, and amount of backscatter.

5.4.1 Intrinsic MRT field acquisition methods

Acquisition of intrinsic Y-profile scans of the MRT field requires accurate positioning of the 3D-Mesa SSD device in the centre of the intrinsic field. This is accomplished in the BB setup (usually directly after BB treatment field calibration scans) using a combination of manual positioning of the phantom with assistance from laser guidelines and Z-motor stage displacement. The detector height is verified by short-exposure acquisitions across a small range of Z-displacements and the position of the largest response is chosen as the optimised central height of the beam. The MSC is then translated into the field and the phantom stage is moved to the +Y extremity motion. Intrinsic MRT field acquisition is then performed by scanning the phantom at fixed height to the opposite –Y extremity of stage motion while beam shutters are open. MRT field scans are performed in the same direction every time for consistency of stage motion and must be reset to the +Y extremity after each scan. Generally, a 1 s delay before exposure is enforced to allow for acquisition of baseline ADC response. Repositioning of detector at a different depth in the RMI457 phantom requires re-optimisation of detector height at centre of beam every time to account for any movement of the device in the milled channel relative to the previous depth.

Analysis may be performed manually using RadPlot or using automated python-based scripts with

a range of functions for manipulation of the data file and extraction of important dosimetric quantities.

Acquisition using the X-Tream readout system allows a sampling frequency of 1 MHz, which permits calculation of uncertainty using an averaging factor 'x' such that every x points are averaged, and a standard deviation provided as the uncertainty in the averaged quantity. Applying an averaging factor of 500 reduces the sampling frequency to 2 kHz. Data loss due to this smoothing is considered negligible, as a measurement is recorded for every 8 µm at the maximum lateral scan speed of 4 mm/s under this method and thus there are still 6 data points within each peak. Choosing a maximum horizontal scan speed of 2 mm/s allows 4 µm resolution, and thus 12 data points in each peak, which is sufficient to resolve all features.

The uncertainty of FWHMs is determined by finding the first position to rise above half-maximum when approaching from the valleys on either side of the peak and then finding the first position to fall below the half-maximum when approaching from the centre of the peak on either side. The difference in these two quantities is the calculated uncertainty of that peak's FWHM. Calculation of the FWTM uncertainty is performed similarly. The uncertainty of the PVDR is determined by relative propagation of errors of the peak (P) and valley (V) values as in (5.2).

Due to the large number of data points displayed when discussing FWHM, FWTM, and PVDR a unique colour has been assigned to each individual peak in order to assist in distinguishing them.

5.4.2 Z-height optimisation study

Figure 5.6 shows the intrinsic scan results of the 2s-250µm-#2 3D-Mesa SSD through the field produced by the Hutch 2B 50-400 MSC. The beam was produced using 1.4T-AlAl (equivalent BB treatment field dose rate of 464.4 Gy/s at 20 mm depth) and a 165 mA ring current. The beam was measured at 0 mm depth in a 140 × 100 × 100 RMI457 phantom. Intrinsic beam size was defined by the tertiary shaping slits to be 20 × 1.28 mm² and the 3D-Mesa SSD was positioned vertically at the centre of the beam. The 3D-Mesa SSD was scanned across the width of the field at 1.89 mm/s and read out using X-Tream with an applied bias of 2 V and a preamplifier gain of 1.0×10^8. The measurement uncertainty is calculated to be less than 2% for all positions with an averaging factor of 500.

5.4.2.1 Results at Z-centre of field, 0 mm depth

The full profile in Figure 5.6a shows ~20% roll-off in at the edges of the field compared to the centre

but the field remains roughly symmetrical — a good indicator that the MSC is at optimal rotation with respect to the beam, which allows the microbeams to achieve both maximum dose delivery and FWHM size. Two peaks and valleys near the centre of the field are shown in Figure 5.6.b and match the expected Gaussian appearance of the microbeam – with no unexpected structures in the valley. An adjusted vertical scale (Figure 5.6.c) shows the valley response 6—14 counts above the baseline (readjusted to 0 counts) with greater valley response tending towards the centre of the field. PVDRs range from 50–100 with an outlier at 160 (Figure 5.6.d – outlier not shown to preserve useful axis scaling), FWHMs range from 46–52 μm (Figure 5.6.e), and FWTMs range from 82.5–93 μm (Figure 5.6.f).

The mean PVDR of the field is calculated to be 78.2 ± 15.6, the mean FWHM to be 49.7 ± 1.6 μm, and the mean FWTM to be 90.4 ± 2.3 μm.

It should be noted that this PVDR is measured at 0 mm depth in the phantom as opposed to the treatment field measurements, which were at 20 mm depth. Therefore, the two should not be directly compared due to the differing scattered-radiation fields that exist at the different depths in the phantom. Nevertheless, a rough comparison is provided due to the interest in investigating treatment field PVDRs and their relation to intrinsic PVDRs.

The measured mean PVDR does not agree with 1.4T-AlAl treatment field results (a PVDR of 40.76), even accounting for ~20% uncertainty in the mean intrinsic field PVDR, and the intrinsic PVDR is a factor of 1.9 times larger than the treatment field PVDR under similar beam conditions. It would be useful to determine a relationship between treatment field PVDR and intrinsic field PVDR in order to utilise the faster intrinsic field scanning method to determine treatment field PVDR for pre-treatment quality assurance dosimetry, but this requires further investigation at a large number of different beam configurations.

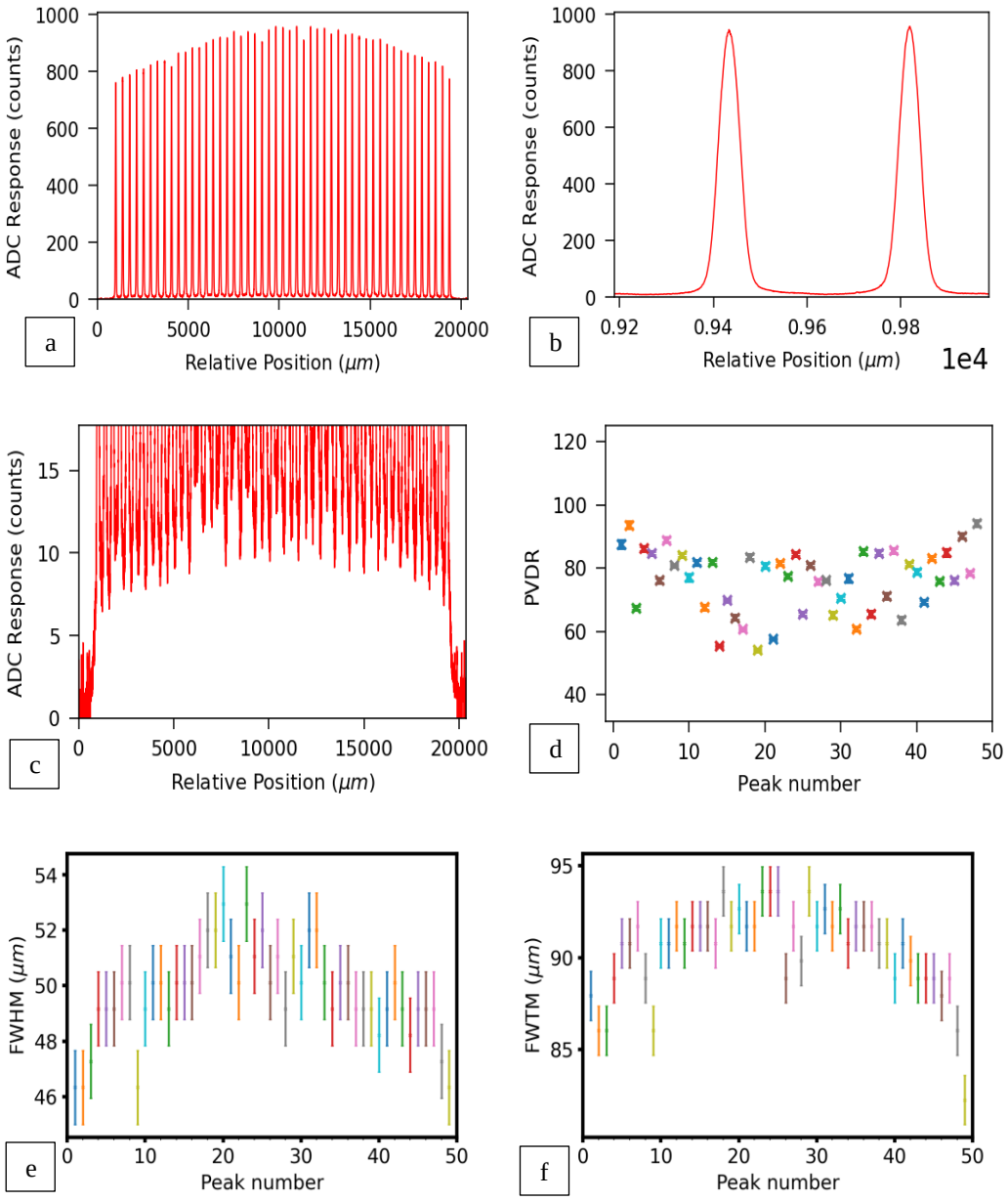

Figure 5.6: 1.4T-AlAl, RMI457 intrinsic MRT lateral profile, 0 mm depth, centre of beam.
a. Full MRT profile; b. Zoom of centre of profile showing shape of two peaks
c. Zoom of profile showing valley counts and baseline; d. PVDRs of profile
e. FWHMs of profile; f. FWTMs of profile.

The mean FWHM and mean FWTM are consistent with 1.4T-AlAl treatment field measurements (53.7 µm and 100.3 µm, respectively) but do not agree within 3% and 2.6% uncertainty, respectively. The mean FWTM is a factor of 1.82 larger than the mean FWHM, which is consistent with results for the 1.4T-AlAl treatment field (a factor of 1.87).

5.4.2.2 Results at -300 µm Z, 0 mm depth.

The intrinsic MRT profile scan was repeated with a vertical displacement of -300 µm (25% of beam height) under the same conditions to allow comparison to a non-optimised Z-height profile. The full

profile in Figure 5.7.a shows no visible difference from the profile at optimised height. Neither do the peaks and valleys near the centre of the field shown in Figure 5.7.b, nor the valley response in Figure 5.7.c. PVDRs range from 55–104 with an outlier at 150 (Figure 5.7.d – outlier not shown to preserve useful axis scaling). FWHMs range from 47–53 µm (Figure 5.7.e), and FWTMs range from 82.5–93 µm (Figure 5.7.f). The mean PVDR of the field is calculated to be 84.7 ± 16.3, the mean FWHM to be 49.8 ± 1.4, and the mean FWTM to be 90.5 ± 2.0. These values are compared against those of the 0-µm position in Table 5-5.

Table 5-5: Comparison of dosimetric quantities of interest for 0 mm depth intrinsic MRT lateral profiles at two different heights.

	Mean PVDR	Mean FWHM (µm)	Mean FWTM (µm)
0 µm height	78.2 ±15.6	49.7 ± 1.6	90.4 ± 2
-300 µm height	84.7 ± 16.3	49.8 ± 1.4	90.5 ± 2

All dosimetric quantities agree within uncertainty, thus it can be assumed that a deviation of detector placement of up to ±25% of beam height around the centre of the beam for a 1.28 mm beam will show no measureable difference. Effects are more pronounced in the penumbral region of the beam and especially for smaller beams.

5.4.2.3 Results at Z-centre of field, 24 mm depth

MRT valley doses depend mostly upon scatter from peak-field radiation and backscatter from deeper in the phantom. Additionally, it is known that charged-particle equilibrium must be achieved in the valley regions for maximum valley dose rate as seen Figure 2.23 in Chapter 2, where a simulated 3T-CuCu valley dose displays a build-up region to reach maximum dose at ~15 mm depth. An intrinsic MRT profile at optimized centre-of-beam height at 24 mm depth was acquired for comparison with the 0 mm profile to determine the effect of depth on 3D-Mesa SSD MRT response.

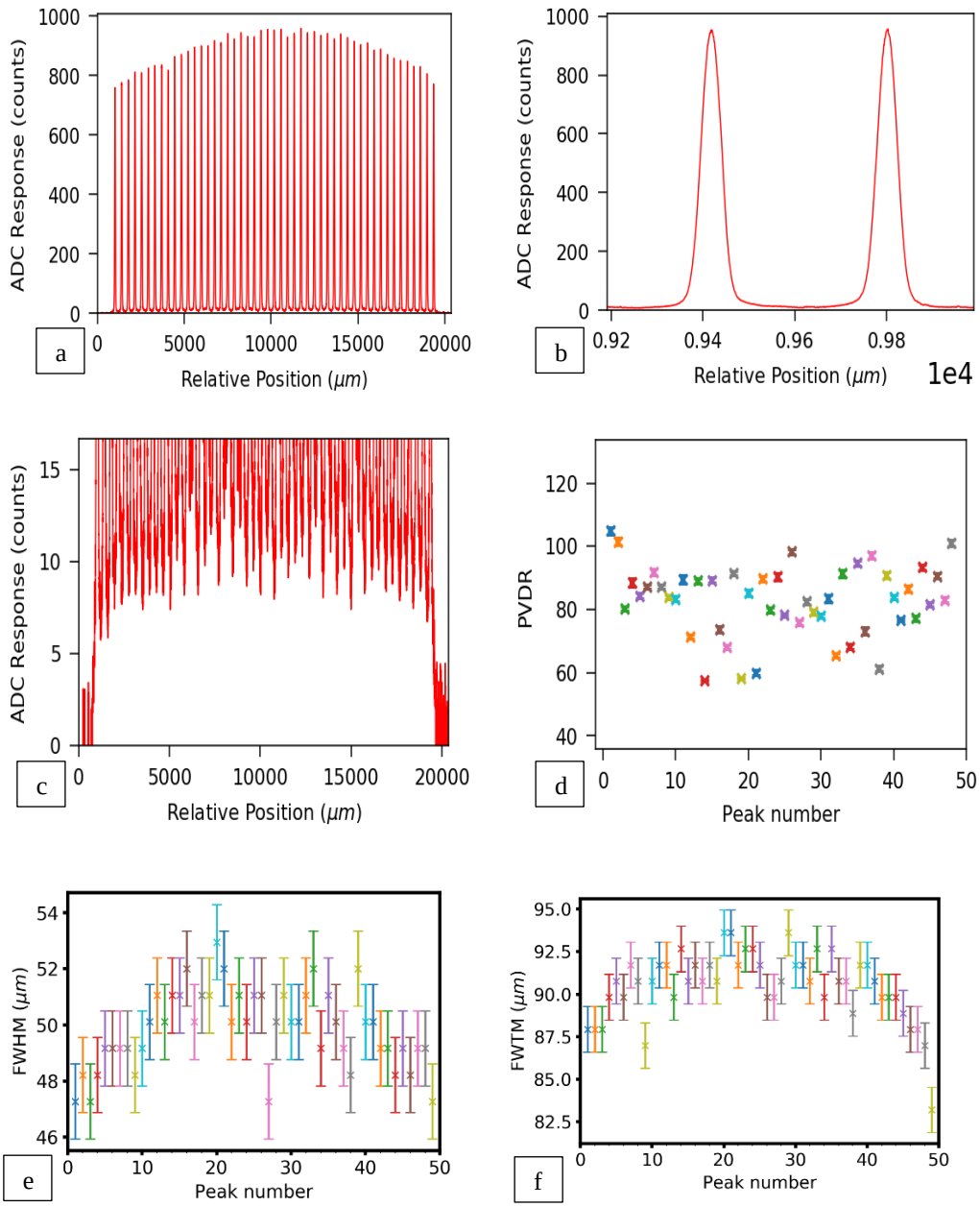

Figure 5.7: 1.4T-AlAl, RMI457 intrinsic MRT lateral profile, 0 mm depth, -300 µm from centre of beam.
a. Full MRT profile; b. Zoom of centre of profile showing the shapes of two peaks
c. Zoom of profile showing valley counts and baseline; d. PVDRs of profile
e. FWHMs of profile; f. FWTMs of profile.

The intrinsic MRT profile scan was repeated at 24 mm depth in the centre of the beam under the same conditions as to allow comparison to the optimised centre-of-beam profile at 0 mm depth. The full profile in Figure 5.8.a shows a maximum response that is half that of the 0 mm depth profile and displays 20% roll-off weighted slightly towards the 0-µm side of the spectrum. Peaks retain the expected Gaussian shape as shown in Figure 5.8.b, but a slight bump in the valley to the +Y side of the peak has appeared that was absent at 0 mm depth. This dosimetric structure in the valley is known as a 'satellite structure' and is most likely due to total external reflection of radiation from

the interior walls of the slits of the MSC that raises the flux in valleys that meet the acceptance angle. The effect of this can be seen by rotating the MSC between Y-scans and thus altering the angle of incidence of radiation for all slits, which has the effect of moving the satellite structures and area of raised flux to different valleys. This movement of the satellite structures is because the new rotation angle may no longer agree with the conditions for total external reflection for slits that previously allowed total external reflection, or vice-versa. The lateral intrinsic (Y) scan of the MRT dose profile allows fast and simple investigation of these satellite structures. Further investigation into this phenomenon is ongoing, but is considered to be beyond the scope of this thesis.

The deduced valley response range in Figure 5.8.c has changed to 6–12.5 ADC counts. PVDRs range from 30–50 with an outlier at 68 (Figure 5.8.d – outlier not shown to preserve useful axis scaling), FWHMs range from 50–56 μm (Figure 5.8.e), and FWTMs range from 105–125 μm (Figure 5.8.f). The mean PVDR of the field is calculated to be 38. ± 5.9, the mean FWHM to be 53.5 ± 1.5, and the mean FWTM to be 116.9 ± 4.1. These values are compared against those of the 0 mm depth in Table 5-6.

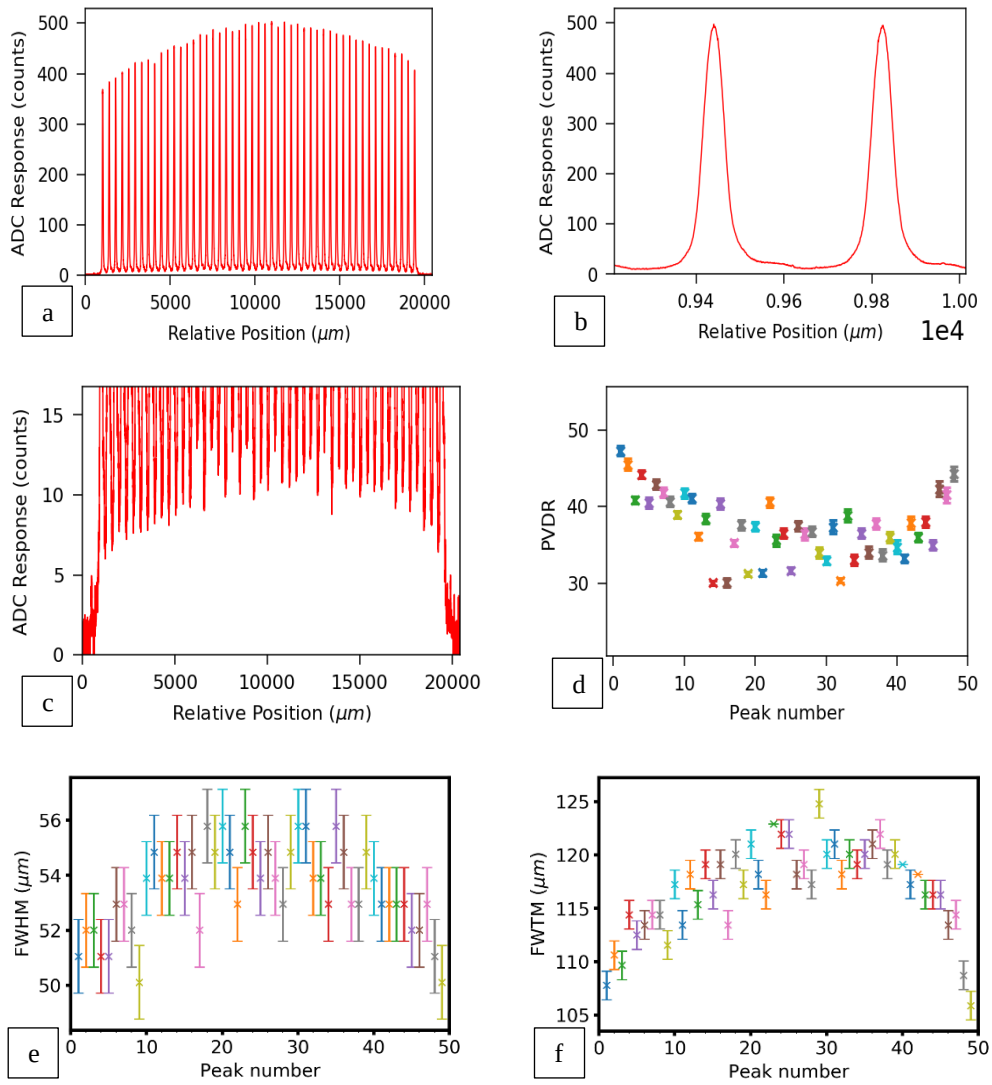

Figure 5.8: 1.4T-AlAl, RMI457 intrinsic MRT lateral profile, 24 mm depth, centre of beam.
a. Full MRT profile; *b. Zoom of centre of profile showing shape of two peaks*
c. Zoom of profile showing valley counts and baseline; *d. PVDRs of profile*
e. FWHMs of profile; *f. FWTMs of profile*

Table 5-6: Comparison of dosimetric quantities of interest for optimised Z-position intrinsic MRT lateral profiles at two different depths.

	Mean PVDR	Mean FWHM (μm)	Mean FWTM (μm)
0 mm depth	78.2 ±15.6	49.7 ± 1.6	90.4 ± 2.3
24 mm depth	38.0 ± 5.9	53.5 ± 1.5	116.9 ± 4.1

At 24 mm depth, the PVDR is reduced by 52% due to the greater scattered dose in the valley and the attenuation of peak intensity. The FWHM is 3.75 μm larger, and the FWTM is 26.5 μm larger as compared to 0 mm depth.

These results show the ability of the 3D-Mesa SSD to perform field characterisation quickly at multiple depths.

5.4.2.4 Comparison to G4IMBL

In its current state, it is impractical for G4IMBL Stage II simulations to record MRT profiles for more than the five central peaks with a Y resolution of 10 µm. This is because the size of the output arrays necessary to contain energy deposition data for the entire field at multiple depths scales very quickly to become unacceptably large output files. Additionally, simulation of intrinsic fields with G4IMBL is less ideal than simulation of treatment fields, as the ability to perform averaging along the vertical Z axis to improve statistics is no longer available, due to the smaller vertical size of the intrinsic field.

To provide a simulated point of comparison for intrinsic field measurements only the central 5 peaks of the intrinsic field were recorded and the uncertainty was determined by finding the average and standard deviation of each voxel response across 100 identical simulations (barring the unique random seed). FWHMs and FWTMs were calculated with the use of a Gaussian Fit and a Cubic Spline Interpolation, to provide two possible measurements of the FWTM, acknowledging that the Gaussian Fit may not accurately model the penumbral region of MB peaks accurately. These quantities are shown in Table 5-7 for both experimentally investigated depths.

Table 5-7: G4IMBL simulated 1.4T-AlAl intrinsic central MB dosimetric quantities at 0.5 mm and 24.5 mm depths.

	0.5 mm depth	24.5 mm depth
Normalised peak response	1.00 ± 1.49%	1.00 ± 2.2%
Normalised valley response	0.02 ± 13.95%	0.04 ± 12.47%
Average PVDR	65.35 ±14.03%	25.54 ±12.66%
Gaussian FWHM (µm)	52.9	52.35
Gaussian FWTM (µm)	97.72	101.02
Cubic Spline FWHM (µm)	51.65	52.47
Cubic Spline FWTM (µm)	69.03	77.05

The G4IMBL simulated PVDR at 0 mm depth agrees with the calculated 3D-Mesa SSD mean PVDR, but the 24 mm G4IMBL PVDR does not agree with the experimental PVDR within uncertainty. Neither Gaussian nor Cubic Spline FWHMs agree within the 0 mm experimental FWHM, but both FWHMs at 24 mm agree with the experimental FWHM within uncertainty. No G4IMBL FWTMs agree with experimental FWTMs at any depth.

The lack of agreement is most likely a symptom of the restricted number of recorded peaks in the G4IMBL measurement. A trend can be seen that all experimental PVDRs were greater than simulated PVDRs, implying that the G4IMBL valleys are over responding compared to the 3D-Mesa SSD results. A greater understanding of valley energy spectrum conditions and validation of G4IMBL MRT results in the 1.4T-AlAl configuration against an independent dosimeter are

necessary before these results can be interpreted with greater confidence.

5.4.3 Comparison of 3D-Mesa SSD designs under constant conditions

The calibrated response of the 3D-Mesa SSD should ideally be consistent regardless of the 3D-Mesa SSD SV architecture for reliable and repeatable dosimetry. However, we expect the uncalibrated response (i.e. the amount of charge released) to differ in proportion to the physical volume of the SV under identical operating conditions. To test this, 3D-Mesa SSD samples of each SV architecture were used to characterise a known field and results were compared.

5.4.3.1 Methods

The field that is used for the next set of results is a 3.2T-CuCu intrinsic MRT field, generated by a 200 mA electron ring current, at 0 mm depth in a 95 x 100 x 100 mm^3 RMI457 phantom with an intrinsic field (BB) dose rate of ~110 Gy/s at 20 mm depth. The beam size is 36 x 0.5 mm^2 and the 3D-Mesa SSD is scanned across the width at the vertical centre of field at 2 mm/s. All 3D-Mesa SSD devices were read out with the X-Tream system at 2 V Bias with a 1.0×10^7 preamplifier gain. The uncertainty of the measurements for all 3D-Mesa SSDs was calculated to be less than 2% across all positions when an averaging factor of 500 was applied.

5.4.3.2 Peak response results

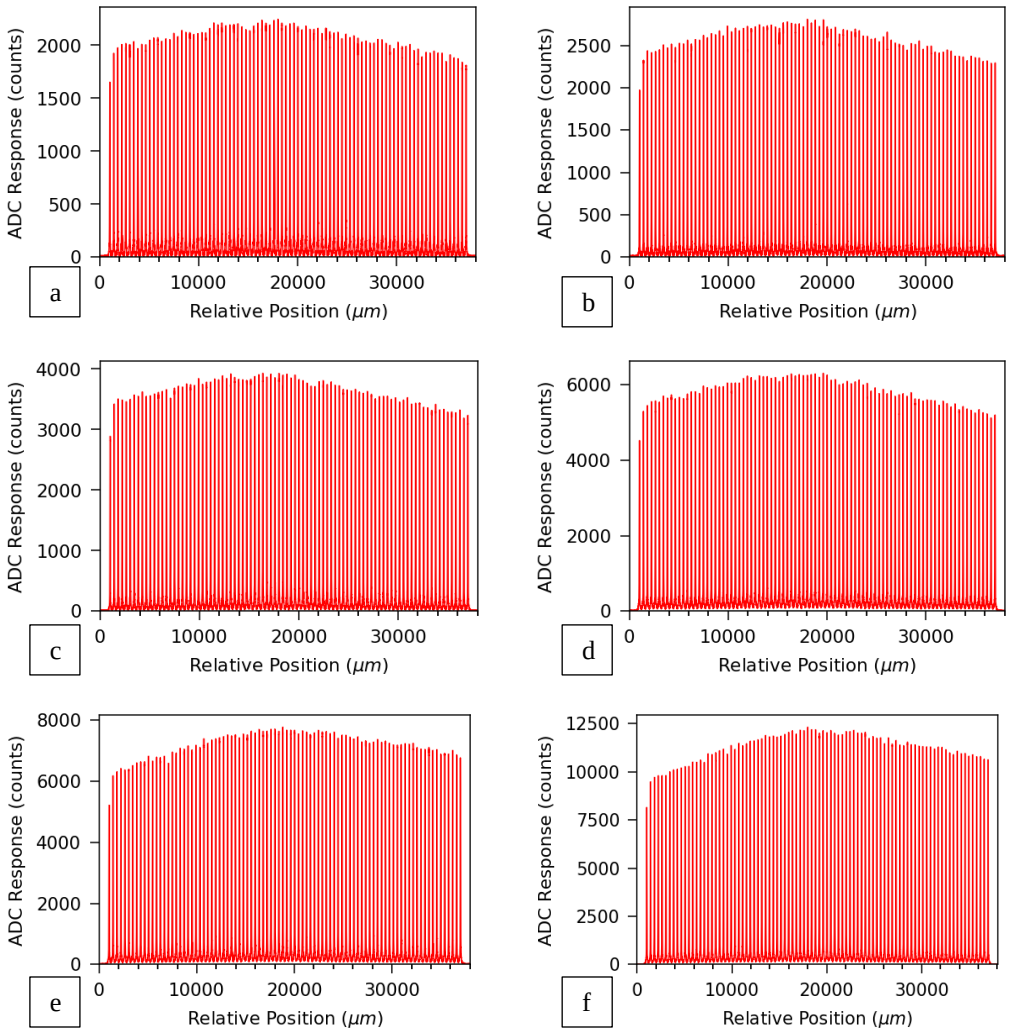

Figure 5.9: Comparison of 3.2T-CuCu, RMI457 intrinsic MRT lateral profiles at 0 mm depth for different 3D-Mesa SSD samples.
a) 1s-50μm-#1; b) 2s-50μm-#1; c) 1s-100μm-#2;
d) 2s-100μm-#1; e) 1s-250μm-#2; f) 2s-250μm-#2.

Figure 5.9 shows MRT profiles under identical conditions for one sample of each design and length of 3D-Mesa SSD SV. The maximum and minimum peak ADC responses across the entire field and the range of peak ADC responses are shown in Table 5-8. The minimum and maximum ADC responses and the magnitude of the range of peak are all seen to increase as volume of the SV increases, consistent with results from Chapter 4 in the BB calibration study.

Table 5-8: Comparison of maximum and minimum peak ADC response between samples. (Range in parentheses.)

Response (ADC)	50 μm	100 μm	250 μm
1s	1651–2245 (594)	2889–3930 (1041)	5213–7775 (2562)
2s	1973–2808 (836)	4514–6294 (1779)	8148–12313 (4165)

The maximum ADC response has been plotted against volume of the device SV in Figure 5.10

below, with $V = 10 \times W \times L$ in µm³ for a volume (V) with a SV length L µm, a height of 10 µm, and a width of 22.5 µm or 36 µm, for 1s and 2s respectively. The uncertainty is displayed as one standard deviation from the mean. A least-squares straight line-of-best-fit has been plotted with an equation of $y = 0.12x + 655.95$. This shows that maximum response is on average proportional to volume of device SV, as expected.

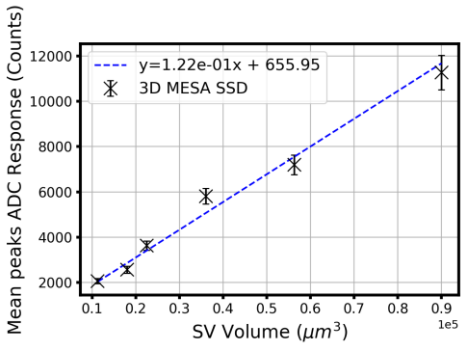

Figure 5.10: Averaged 3D-Mesa SSD peak ADC response as a function of SV size for 3.2T-CuCu intrinsic MB lateral profiles.

Central peaks of the MB field are shown in Figure 5.11 for all samples. The expected Gaussian shape is present in all profiles and there appear to be no satellite structures due to total external reflection present in the valleys on either side of the central microbeams.

5.4.3.3 Valley response results

The magnitude of valley ADC response across all valleys for all samples is shown in Figure 5.12. The decreasing trend in the response at the centre of each valley as the detector moves laterally away from the centre of the field is expected. It is due to a disequilibrium of photon scattering from the centre outwards and thus a net reduction in primary and secondary photons as the detector moves laterally away from the centre of the X-ray field.

Satellite structures in the valleys are clearly present in Figure 5.12, where adjacent valleys are shown to vary significantly and without clear trend (sudden rises and falls). These structures cannot be resolved in Figure 5.11 due to the magnitude of the vertical linear scale (with maximum response of 2000—12,500 ADC counts compared to 30—200 ADC counts in Figure 5.12) and restricted horizontal scale (0.8 mm as opposed to 40 mm in Figure 5.12).

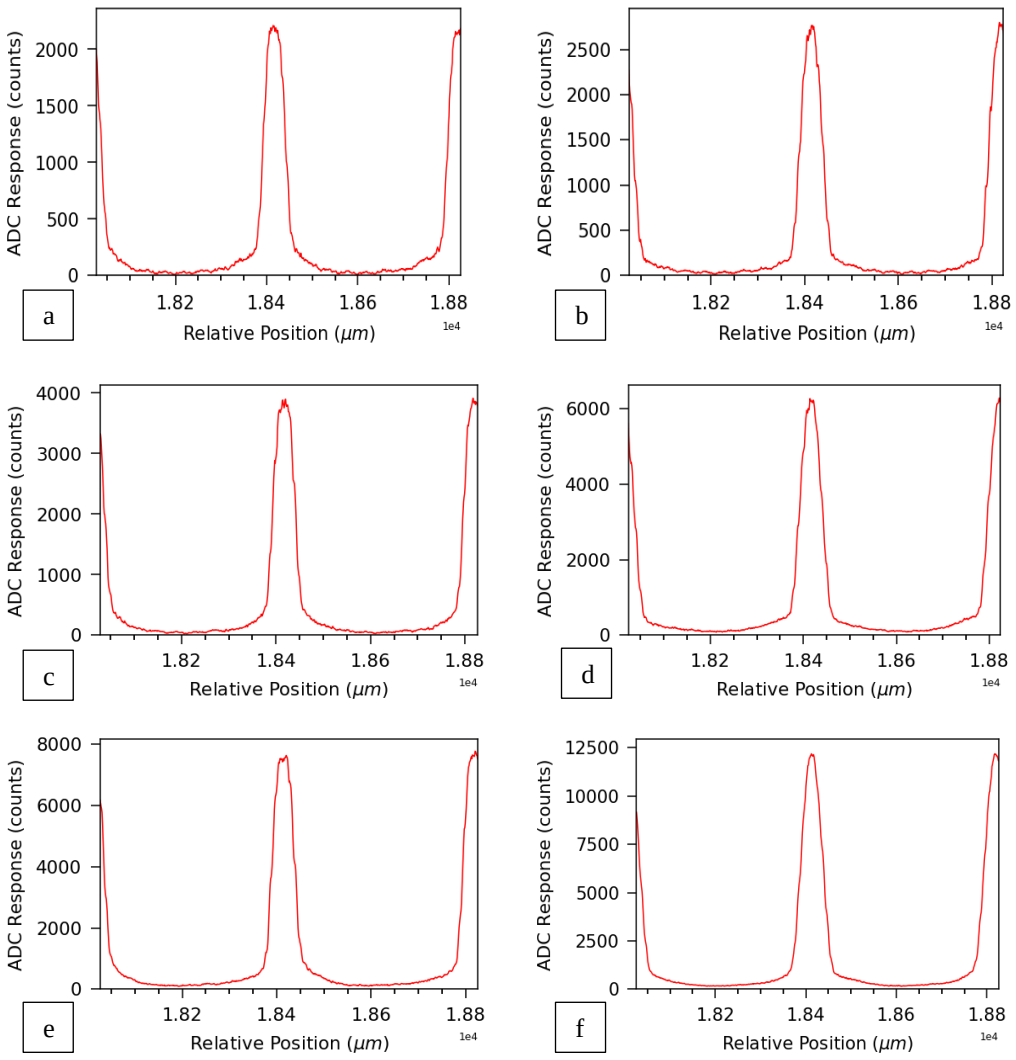

Figure 5.11: Comparison of central peak of 3T-CuCu, RMI457 intrinsic MRT lateral profiles at 0 mm depth for multiple 3D-Mesa SSD samples.
a) 1s-50μm-#1; *b) 2s-50μm-#1;* *c) 1s-100μm-#2;*
d) 2s-100μm-#1; e) 1s-250μm-#2; f) 2s-250μm-#2.

Calculation of the valley dose for PVDR involves averaging of valley doses over a 50-μm region approximately 200 μm from a peak position and so the range of averaged valley values may not agree with the minimum or maximum ADC values shown in Figure 5.12. The minimum and maximum average valley ADC values and the range of average valley ADC values are tabulated in Table 5-9 for all samples.

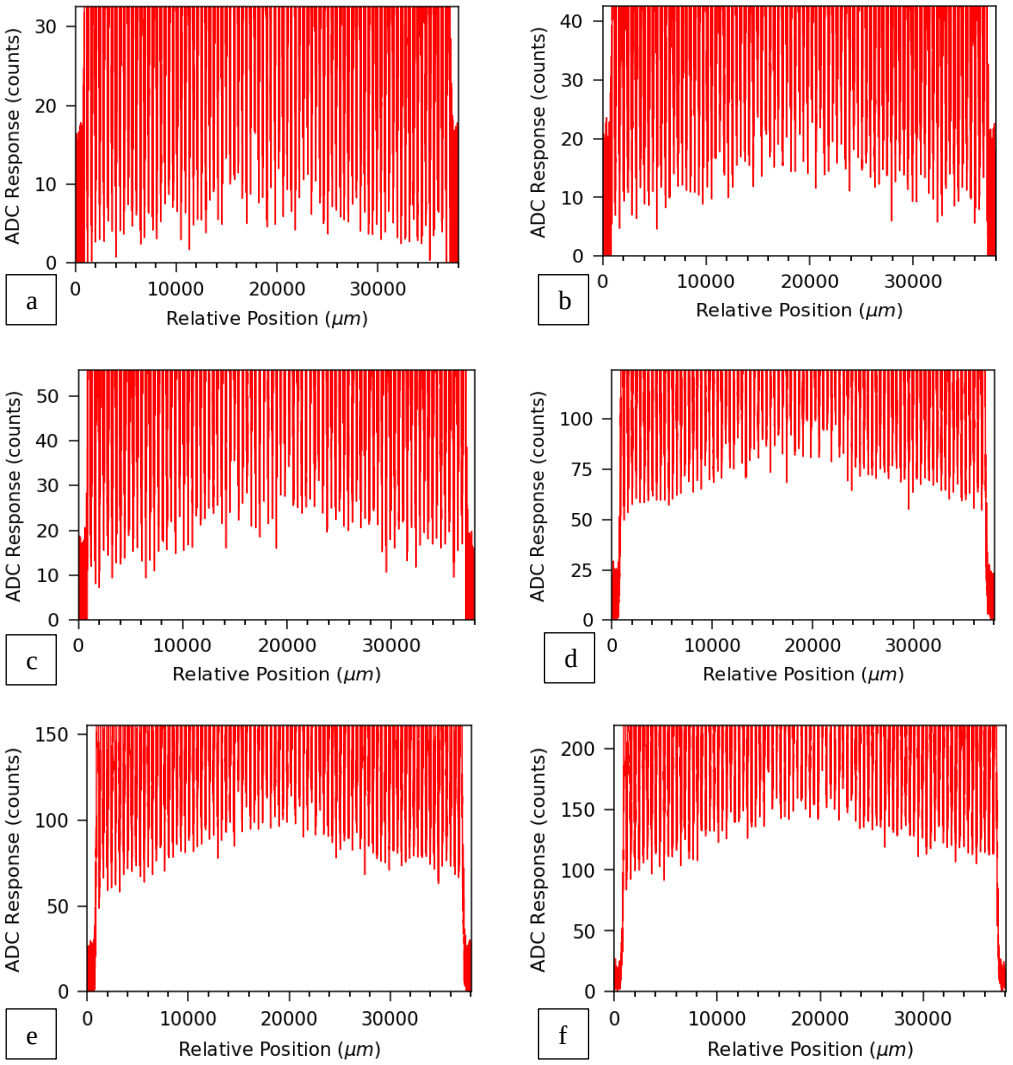

Figure 5.12: Comparison of valleys of 3T-CuCu, RMI457 intrinsic MRT lateral profiles for multiple 3D-Mesa SSD samples.
a) 1s-50μm-#1; b) 2s-50μm-#1; c) 1s-100μm-#2;
d) 2s-100μm-#1; e) 1s-250μm-#2; f) 2s-250μm-#2.

The valley response increases with the increasing volume of the device SV, as expected from the maximum ADC response shown above, and the range of possible valley responses increases with increased SV size. The range of the valley response only slightly decreases with increasing SV length as any local variations, vertically, in the X-ray field that may be smoothed out by volume averaging in the longer SV devices are not significant.

Table 5-9: Comparison of maximum and minimum averaged valley ADC response between samples. (Range in parentheses.)

ADC Response (counts)	50 μm	100 μm	250 μm
1s	16–31 (15)	28–55 (26)	89–152 (63)
2s	22–41 (19)	69–121 (52)	116–213 (97)

As in the case for peak ADC values (Table 5-8), the averages of all valley values across the field

for all samples have been plotted in Figure 5.13 with an uncertainty of one standard deviation from the mean. A least-squares straight line-of-best-fit has been plotted with an equation of $y = 1.97 \times 10^{-3}x - 1.75$.

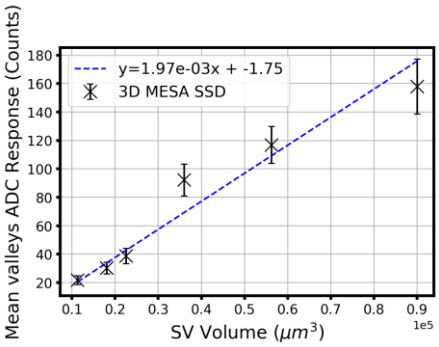

Figure 5.13: Averaged 3D-Mesa SSD valley ADC response as a function of SV size for 3.2T-CuCu MB lateral profiles.

The ratio of the gradient of the averaged peak responses to the gradient of the averaged valley responses is 62.24, which shows that the peak ADC response depends more strongly upon the size of the SV than the valley ADC response. The two should not be expected to agree due to the differing methods of calculation: the peak value is measured as the maximum ADC response in each peak, whereas the valley is an average of multiple ADC responses over a region. The discrepancy in gradients may also be explained by dose-rate dependence arising from the much higher dose rate in the peaks than the valleys (e.g. a factor of 10–100). Dose rate dependence of the 3D-Mesa SSD would ideally be investigated in a BB configuration for a known beam by adjusting the electron ring current to change dose rate at the phantom without perturbing spatial or spectral characteristics of the field.

The issue becomes further complicated because the relevant detector SV component that is changing, the length (height) here, is significant compared to the field height. This may imply is that the vertical variation in the valley dose is significantly greater than the (vertical) variation in the peak dose for the intrinsic X-ray field. For the treatment field the equivalent variation should be much less due to the greater amount of scattered dose in the valley (except at the top and bottom of the treatment field).

Comparison with equivalent simulation data will be necessary to understand this discrepancy in gradients.

Nevertheless, a recommendation may be made that larger SVs should be used where possible due to the increased sensitivity of larger SVs, which leads to larger differences between valley ADC

response and electronic baseline noise and therefore better calculation of intrinsic PVDR.

5.4.3.4 PVDR results

The PVDRs of each peak for each sample are shown in Figure 5.14 and the minimum and maximum values of PVDR in each field are tabulated in Table 5-10. The mean PVDR of each sample is calculated with an uncertainty of one standard deviation from the mean and tabulated in Table 5-11.

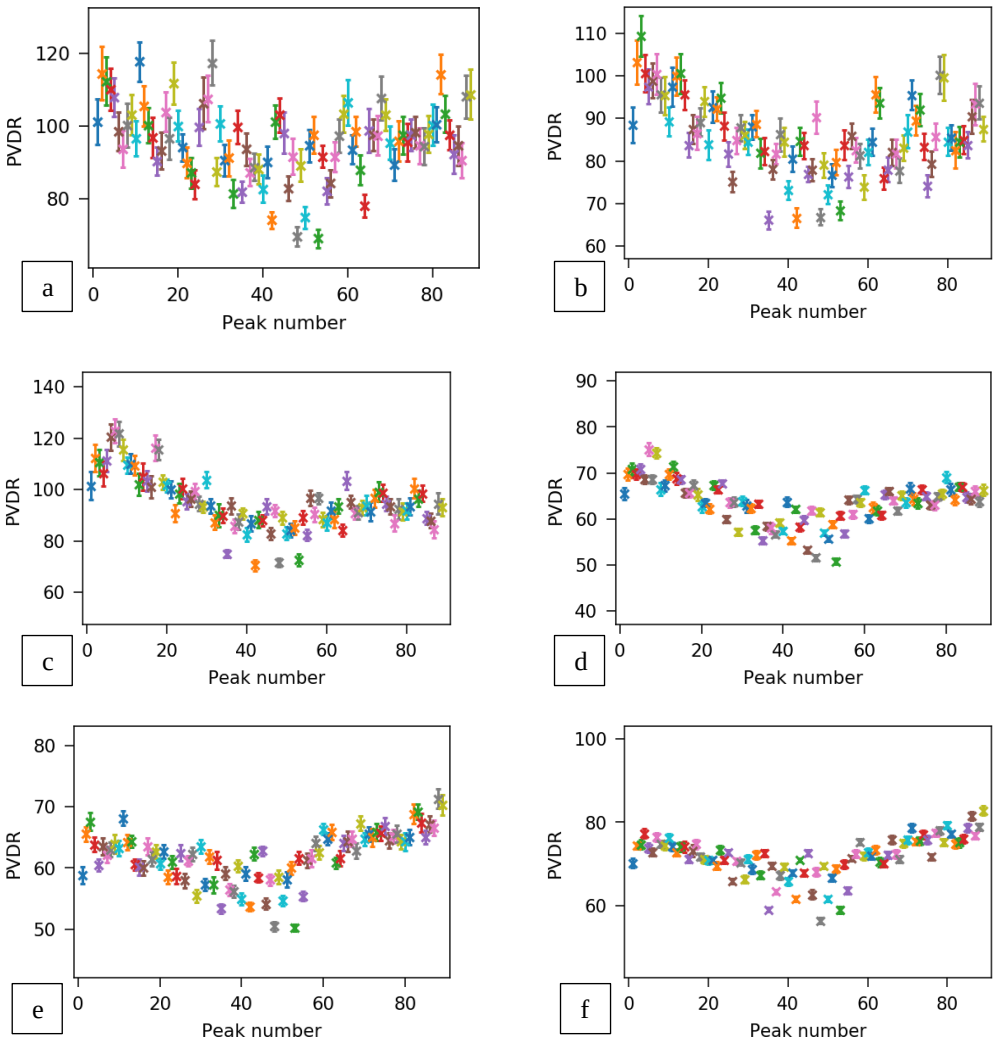

Figure 5.14: Comparison of PVDRs for 3T-CuCu, RMI457 intrinsic MRT lateral profiles for multiple 3D-Mesa SSD samples.
a) 1s-50µm-#1; b) 2s-50µm-#1; c) 1s-100µm-#2;
d) 2s-100µm-#1; e) 1s-250µm-#2; f) 2s-250µm-#2.

Table 5-10: Comparison of maximum and minimum PVDRs across 3D-Mesa SSD samples. (Range in parentheses.)

PVDR range	50 µm	100 µm	250 µm
1s	69–118 (49)	71–123 (52)	50–71 (21)
2s	66–109 (43)	51–75 (24)	56–83 (26)

The range of PVDRs within each field tend to decrease with increasing SV size, disregarding PVDR outliers. This may be attributed to the increasing valley dose, which increases by a factor of 8 from

the smallest SV to the largest SV. Because the peak dose increases by a factor of 5.75 from smallest SV to largest SV, the proportional rate of growth of the valley is greater, thus reducing PVDR. The range of values halves from the smallest to the largest SVs, which may be due to increased sensitivity of the 3D-Mesa SSD allowing more uniform measurements. The shape of the PVDR distribution is an inverse of the dose distribution, with smallest PVDR at the centre of the field where the greatest dose is delivered. This is expected, as the valley dose is greatest at the centre of the field where scatter dose from the left and right of the field contributes equally.

Table 5-11: Comparison of mean PVDRs across 3D-Mesa SSD samples.

Mean PVDR	50 µm	100 µm	250 µm
1s	96 ± 10	95 ± 10	62 ± 4
2s	86 ± 9	64 ± 5	72 ± 5

The mean PVDRs do not agree within uncertainties of 6–10% and do not follow any observable trend when plotted with respect to total SV volume (see Figure 5.15). The three smallest SV sizes show agreement within 10% uncertainty at ~90 and the three largest SV sizes show agreement within 6% at ~67. Uncertainties tend to decrease with increasing SV size, which is attributed to the decreased range of PVDR values evident for large SVs.

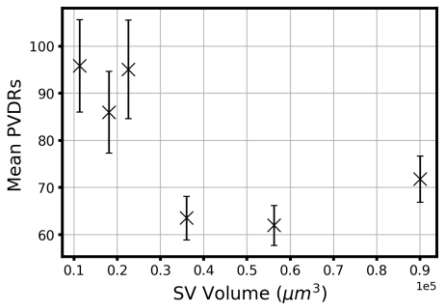

Figure 5.15: Averaged 3D-Mesa SSD intrinsic PVDRs as a function of SV size for 3.2T-CuCu MB lateral profiles.

These intrinsic field PVDRs should not be directly compared to the treatment field PVDR under the same beam configuration due to the different depth of measurement and therefore different fields of scattered radiation. If the difference in radiation field is taken into account, the intrinsic PVDRs range from factors of 1.3–2.0 times larger than the treatment field PVDR of 47. Further investigation under identical radiation field conditions (depth, spectrum, backscatter volume) at different beam heights and field sizes would be necessary to determine if reliable conversion factors between intrinsic and treatment field PVDRs can be found.

5.4.3.5 FWHM results

The FWHMs of each peak for each sample are shown in Figure 5.16 and the minimum and maximum values of FWHM in each field are tabulated in Table 5-12. The mean FWHM of each sample is calculated with an uncertainty of one standard deviation from the mean and tabulated in Table 5-13.

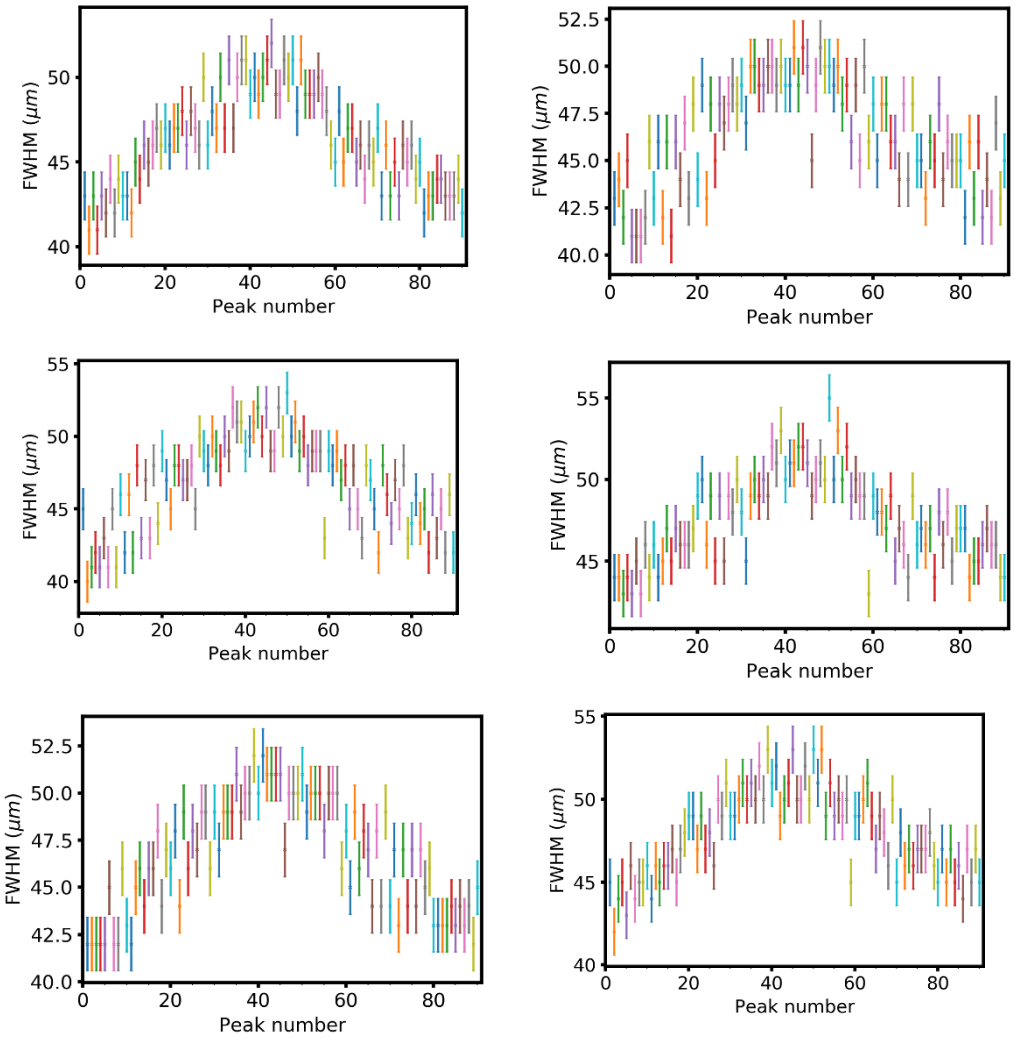

Figure 5.16: Comparison of FWHMs of 3T-CuCu, RMI457 intrinsic MRT lateral profiles for multiple 3D-Mesa SSD samples.
a) 1s-50μm-#1; b) 2s-50μm-#1; c) 1s-100μm-#2;
d) 2s-100μm-#1; e) 1s-250μm-#2; f) 2s-250μm-#2.

All 3D-Mesa SSDs show a trend of increased FWHM magnitude towards the centre of the field due to geometric interaction of the diverging photon field with the MSC slits. At the centre of the beam, the lateral component of momentum is smallest, leading to the least divergence. Further from the centre, the divergence increases and so the probability of photons entering the slits at a larger angle increases until the angle is large enough that photons may interact with the walls of the slits and thus scatter or be attenuated.

Table 5-12: Comparison of maximum and minimum of FWHMs across 3D-Mesa SSD samples. (Range in parentheses.)

FWHM range (µm)	50 µm	100 µm	250 µm
1s	41–52 (11)	40–53 (13)	42–52 (10)
2s	41–51 (10)	43–55 (12)	42–53 (11)

The minimum, maximum, and range of FWHMs is constant across all devices in this field with a variation of the range of values of 3 µm. All mean FWHMs agree across all samples within uncertainties of 5–6%. All mean FWHMs are smaller than the MSC slit size of 50 µm, but this is due to non-uniformity of the radiation field in the later Y-direction about the centre of the field. Slits towards the edges of the MSC encounter radiation at greater angles than slits at the centre of the field. Thus, the cross-sectional area of the slits approaching the edges of the field as seen by the beam are smaller, therefore leading to slight decreases in microbeam width near the edges of the field to be smaller than the apertures. The presence of smaller width microbeams near the edges of the field drags down the average FWHM to be less than the aperture width.

Table 5-13: Comparison of mean FWHMs across 3D-Mesa SSD samples.

Mean FWHM (µm)	50 µm	100 µm	250 µm
1s	46.25 ± 2.81	46.71 ± 3.15	46.66 ± 2.94
2s	46.35 ± 2.77	47.50 ± 2.69	47.95 ± 2.55

5.4.3.6 FWTM results

The FWTMs of each peak for each sample are shown in Figure 5.17 and the minimum and maximum values of the FWTM in each field are tabulated in Table 5-14. The mean FWTM of each sample is calculated with an uncertainty of one standard deviation from the mean and tabulated in Table 5-15. As in the case for FWHMs, the FWTMs display a trend of increased magnitude close to the centre of the field, a consistent maximum magnitude with a range that decreases with increasing SV, and consistent mean FWTMs that agree within 3–5%. FWTMs are 73%–83% larger than each SV's associated mean FWHM.

Table 5-14: Comparison of maximum and minimum FWTMs across 3D-Mesa SSD samples. (Range in parentheses.)

FWTM range (µm)	50 µm	100 µm	250 µm
1s	75–94 (19)	72–91 (19)	77–92 (15)
2s	73–87 (14)	77–91 (14)	80–92 (12)

Table 5-15: Comparison of mean FWTMs across 3D-Mesa SSD samples.

Mean FWTM (µm)	50 µm	100 µm	250 µm
1s	84.44 ± 4.36	82.01 ± 4.07	83.76 ± 3.58
2s	80.33 ± 3.07	83.96 ± 3.17	84.85 ± 2.78

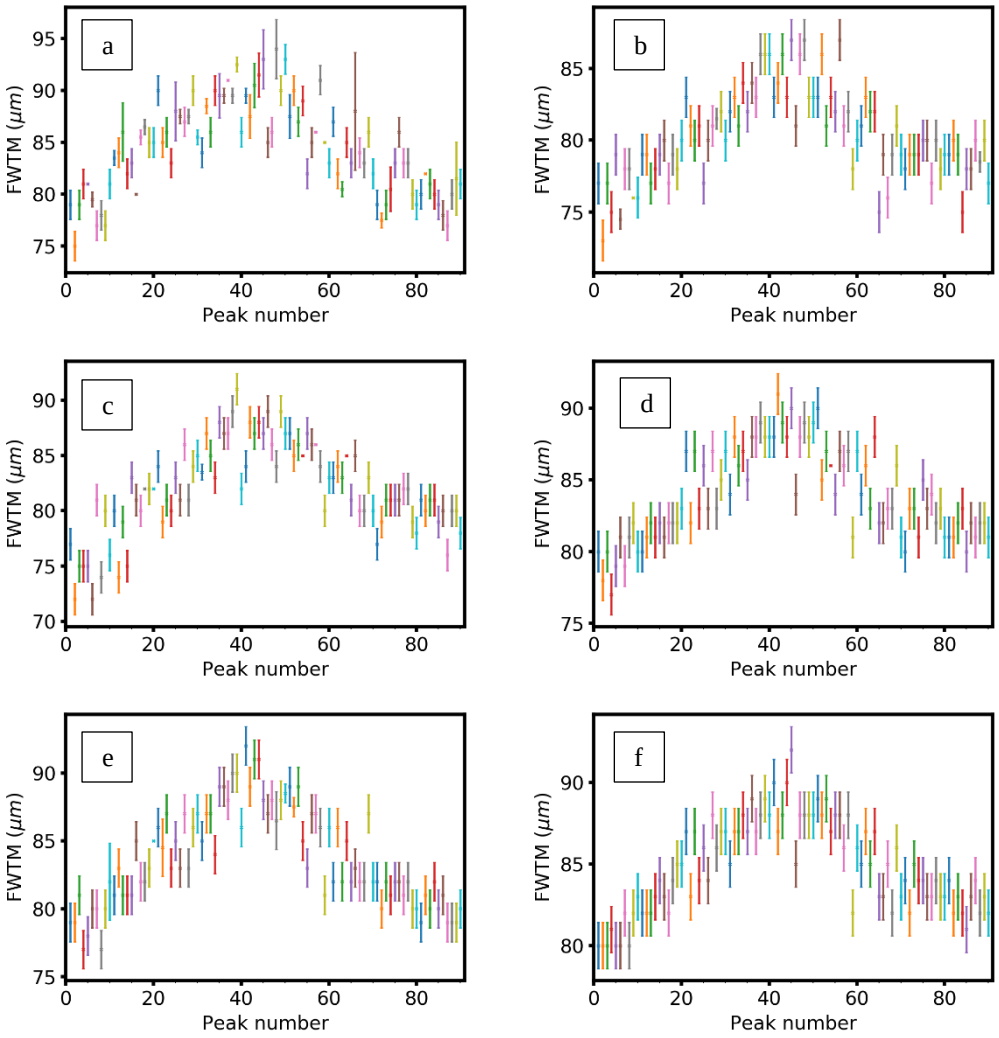

Figure 5.17: Comparison of FWTMs of 3T-CuCu, RMI457 intrinsic MRT lateral profiles for multiple 3D-Mesa SSD samples.
a) 1s-50μm-#1; b) 2s-50μm-#1; c) 1s-100μm-#2;
d) 2s-100μm-#1; e) 1s-250μm-#2; f) 2s-250μm-#2

5.4.3.7 Comparison to G4IMBL

G4IMBL Stage II simulations have been performed as described in 5.4.2.4 to provide a point of comparison for 3T-CuCu MRT results. Dosimetric quantities of interest are recorded in Table 5-16.

Table 5-16: G4IMBL 3.0T-CuCu intrinsic central MB dosimetric properties at 0.5 mm depth.

Normalised peak response	1 + 1.02%	Gaussian FWHM (μm)	54.3	Cublic spline FWHM (μm)	50.23
Normalised valley response	0.02 + 7.51%	Gaussian FWTM (μm)	101.75	Cubic spline FWTM (μm)	76.08
PVDR	56.57 +7.58%				

The G4IMBL PVDR agrees with only the mean PVDRs measured by the 2s-100μm and 1s-250μm samples within uncertainty, but does fall within the range of individual PVDRs for the 2s-250μm sample as well. Neither Gaussian FWHM nor Gaussian FWTM agree with 3D-Mesa SSD mean

FWHM or FWTM and are larger than the maximum measured 3D-Mesa SSD FWHM and FWTMs for all samples. This clearly shows that the Gaussian fit is not suitable for modelling intrinsic MBs. The cubic spline interpolated FWHM and FWTM do not agree with 3D-Mesa SSD mean FWHMs or FWTMs. However, the cubic spline interpolated FWHMs and FWTMs do fall within the range of measured FWHMs for all samples and within the range of measured FWTMs for all samples (except 1s-250μm-#2 and 2s-250μm-#2), respectively. This implies that a cubic spline interpolation may be used to provide a superior approximation of the peaks of an intrinsic MB profile when compared to a Gaussian fit. Validation of G4IMBL under these beam conditions against intrinsic MRT dosimetry by an independent dosimeter (e.g. EPI SSD, EBT3) is necessary for greater confidence in G4IMBL results.

5.4.4 Summary

In summary, 3D-Mesa SSDs were compared for all designs under the same conditions. Spatial resolution was comparable across all designs as FWHMs and FWTMs all agreed within <6% uncertainty. PVDRs generally saw decreased range and magnitude for larger SVs most likely due to increased sensitivity of larger SVs. Possible dose rate dependence was identified as the gradient of ADC response to SV size was not consistent between peak values and valley values and so requires further investigation. Because no significant deviation in spatial resolution was observed, it is recommended that larger SV designs be used for intrinsic field quality assurance (e.g. optimisation of MSC rotation, verification of field size, peak width, and confirmation of lack of artifacts in the valley regions).

5.5 Intrinsic microbeam PDDs in a water phantom

5.5.1 Methods

The behaviour of dosimetric quantities with respect to depth in a phantom is an area of interest for MRT but consistent setup at different depths is difficult in a water-equivalent plastic phantom. Use of a water tank phantom allows motorized control of depth with reliable repeatability. A 3D-Mesa SSD detector was used to examine 3T-AlAl, 20 × 2.014 mm² MB intrinsic field profiles at a variety of depths in a water tank phantom for two field sizes and relevant dosimetric quantities were calculated. Due to the edge-on setup and the mounting of the device in the detector holder, a minimum achievable depth of 20 mm was enforced, which must be taken into account for the following results. All following results were obtained for a 3T-AlAl intrinsic MRT field, generated by a 200 mA electron ring current, in a 137 x 158 x 120 mm³ water tank phantom with a treatment field dose rate of ~3 kGy/s at 20 mm depth. The beam size is 2.014 mm high and either 20 mm or 10 mm wide depending on the conformal mask chosen. The 3D-Mesa SSD (1s-250µm-#100) is scanned in face-on mode across the width of the beam at the vertical centre of the field at 2 mm/s. All 3D-Mesa SSD devices were read out with the X-Tream system at 2 V Bias with a 1.8×10^5 preamplifier gain and a sampling frequency of 1 MHz.

5.5.2 Peak response results

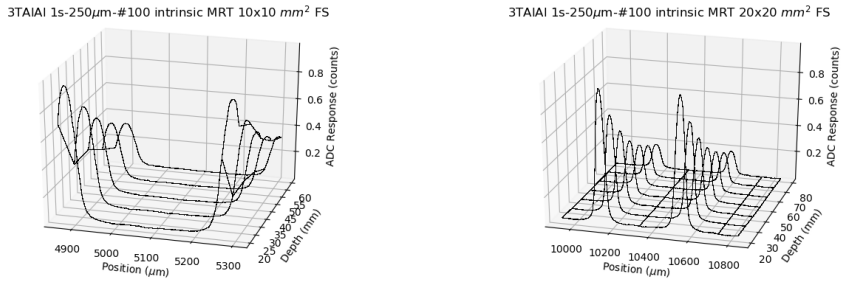

Figure 5.18: 3T-AlAl intrinsic water tank MRT 3D PDDs.
Left: 10 × 2.014 mm² field; right: 20 × 2.014mm² field.

The 10 × 2.014 mm² field produces 24 full-sized peaks and a half-sized peak at each depth and the 20 × 2.014 mm² field produces 49 full-sized peaks only. In order to eliminate response-averaging artifacts, the 10 × 2.014 mm² half-peak is ignored in calculation of PVDR, FWHM, and FWTM. Snippets of the 3D profiles of the two field sizes are shown in Figure 5.18, with the attenuation of the peak responses with depth easily visible.

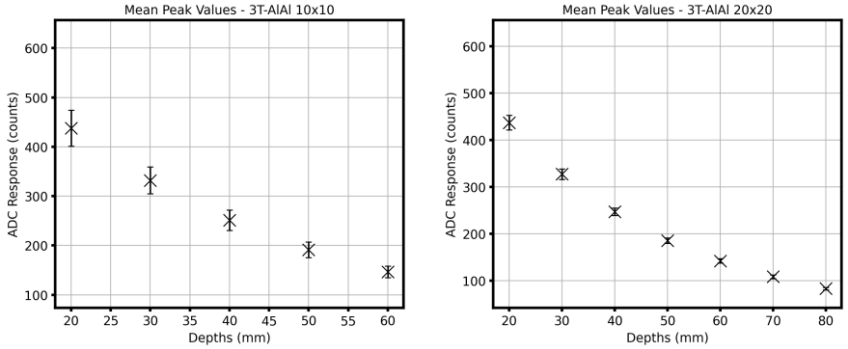

Figure 5.19: 3T-AlAl intrinsic water tank MRT peak depth-response profile.
Left: 10 × 2.014 mm² field, right: 20 × 2.014 mm² field.

Mean peak ADC response values for the two field sizes at each depth are shown in Figure 5.19. The data in this figure have not been normalised to 20 mm depth (as is standard for most of this thesis) in order to better show the effect of field-size variation. Note that as no data was obtained close to the surface of the water tank phantom, the standard shape of the MB peak PDD is truncated less than 20 mm. The two field sizes behave similarly over the range of 20–60 mm, with the 20 × 2.014 mm² field displaying larger uncertainty than the smaller field.

The maximum, minimum, and range of all peak values in the MRT profile at each depth for each field are tabulated in Table 5-17. The maximum peak ADC is consistent between field sizes within 6 counts (<3% of total response) at each depth, whereas the 20 × 2.014 mm² field minimum peak responses are smaller by 45–16 counts than the 10 × 2.014 mm² field, with larger variations close to the surface. This demonstrates the contribution of scattered radiation from the larger field is more impactful at shallower depths and less impactful deep in the phantom where backscatter is more prevalent.

Table 5-17: MRT profile maximum and minimum peak response in ADC units for intrinsic MBs in a water tank at each depth.
(Range in parentheses.)

	20 mm	30 mm	40 mm	50 mm	60 mm	70 mm	80 mm
10 × 2.014 mm²	430—456 (26)	330—344 (14)	249—262 (14)	190—200 (10)	145—153 (8)	N/A	N/A
20 × 2.014 mm²	385—457 (72)	289—342 (53)	220—259 (39)	166—194 (28)	129—148 (19)	96—113 (17)	75—87 (12)

5.5.3 Valley response results

Mean valley ADC response values for the two field sizes at each depth are shown in Figure 5.20. As no data was obtained close to the surface of the water tank phantom, the MB valley PDD does not display the expected build-up region at shallow depths in the phantom. Uncertainties are significantly larger than in the peak datasets as expected due to the low dose delivered in MB

valleys. The two field sizes behave similarly over the range of 20–60 mm, with the response at 60 mm measured as greater than 50 mm (~0.5 and ~0.4, respectively). The 20 × 2.014 mm² field displays a sharper gradient of response between 20 and 40 mm, with relative responses at 30 mm and 40 mm measured as 0.8 and 0.55 respectively for the 20 × 2.014 mm² field and 0.8 and 0.65 for the 10 × 2.014 mm² field. Aside from the 30 mm and 40 mm depths, all responses agree within 5% between the two field sizes; for instance, at 60 mm depth the response of both fields is ~4 ADC counts.

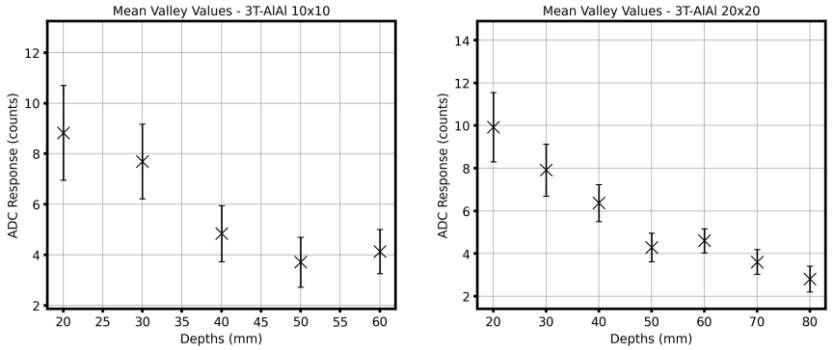

Figure 5.20: 3T-AlAl intrinsic water tank MRT valley PDDs.
Left: 10 × 2.014 mm² field; right: 20 × 2.014 mm² field.

The maximum, minimum, and range of all valley values in the MRT profile at each depth for each field are tabulated in Table 5-18. The maximum, minimum, and range of valley values agree within 2 ADC counts for all depths common to the two field sizes. A trend is observed that the maximum valley responses decrease as depth increases (from 13–5 in 10 × 2.014 mm² field), but the minimum valley response is relatively constant, comparatively (from 4–1). However, relative to the initial valley response, the minimum response decreases proportionally more (75% decrease from 4–1 for minimums, compared to 62% decrease from 13–5 for maximums). This leads to the range of values decreasing with depth, as expected due to the increased amount of scatter that is contributed by points both shallower and deeper in the phantom. Closer to the surface the scattered component is mostly due to backscatter from deeper in the phantom, thus there is less total scatter contribution at the surface, and so there is a wider range of values in the valleys near the surface.

Table 5-18: MRT profile maximum and minimum valley response in ADC units for intrinsic MBs in a water tank at each depth.
(Range in parentheses.)

	20 mm	30 mm	40 mm	50 mm	60 mm	70 mm	80 mm
10 × 2.014 mm²	4—13 (8)	5—11 (6)	3—7 (3)	1—5 (4)	3—6 (3)	N/A	N/A
20 × 2.014 mm²	4—14 (9)	4—11 (7)	4—9 (5)	3—6 (3)	2—6 (3)	2—5 (3)	1—4 (3)

5.5.4 PVDR results

Mean PVDRs for each field size and at each depth in the phantom are shown in Figure 5.21 and tabulated in Table 5-19. Mean PVDRs are seen to agree between the two field sizes within uncertainty at all depths. This is due in part to the large uncertainties (up to ~20%) that arise due to variation of PVDR among all peaks of a particular depth. There is a trend of decreasing mean PVDR proportional to depth in the phantom in the 20 × 2.014 mm² field (with an outlier at 50 mm) but this trend is not seen in the 10 × 2.014 mm² field.

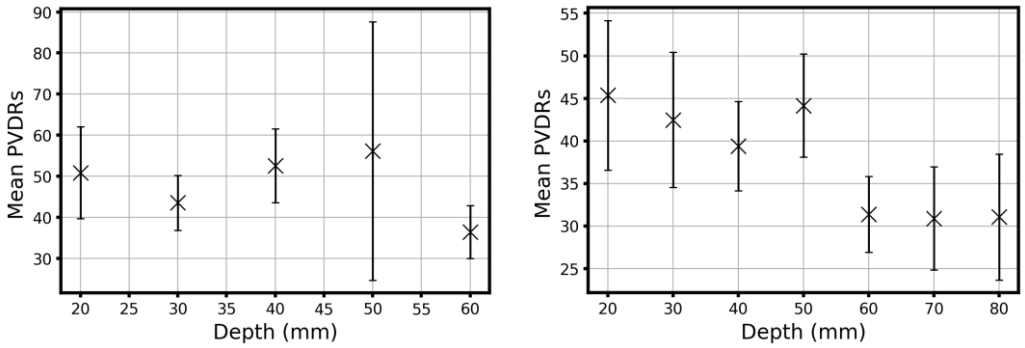

Figure 5.21: 3T-AlAl intrinsic water tank MRT PDD.
Left: 10 × 2.014 mm² field; right: 20 × 2.014 mm² field.

Table 5-19: MRT profile mean PVDRs for intrinsic MBs in a water tank at each depth.

mean PVDR	20 mm	30 mm	40 mm	50 mm	60 mm	70 mm	80 mm
10 × 2.014 mm²	51 ± 11	44 ±7	53 ± 9	56 ± 31	36 ± 6	N/A	N/A
20 × 2.014 mm²	45 ± 9	42 ± 8	39 ± 5	44 ± 6	31 ± 4	31 ± 6	31 ± 7

Examination of the maximum, minimum, and range of PVDRs at each depth is useful for comparison and is shown in Table 5-20. There is a general trend of decreasing maximum PVDR magnitude with depth in the 20 × 2.014 mm² field (allowing for slight increases at 50 mm and 70 mm) which is not present in the 10 × 2.014 mm² field (due to the increases at 40 mm and 50 mm). The minimum PVDR in both cases is reasonably constant at ~30 for depths above 50 mm and then exhibits a slight decrease to ~25 at 60 mm and deeper.

Table 5-20: MRT profile maximum and minimum PVDRs for intrinsic MBs in a water tank at each depth. (Range in parentheses.)

PVDRs	20 mm	30 mm	40 mm	50 mm	60 mm	70 mm	80 mm
10 × 2.014 mm²	35—98 (62)	31—69 (38)	37—76 (39)	37—205 (168)	25—53 (27)	N/A	N/A
20 × 2.014 mm²	32—94 (62)	31—82 (51)	28—61 (34)	31—63 (32)	25—55 (30)	23—61 (38)	21—55 (34)

The minimum PVDRs are generally in the centre of the field and are more constant due to

symmetrical scatter contribution stabilising the valley response, whereas the maximum PVDRs occur at the edges of the field where the relative magnitude of scatter is much less in comparison to the peak dose. This explains why the PVDRs of the larger field size do not exhibit the same outliers as the smaller field size.

5.5.5 FWHM results

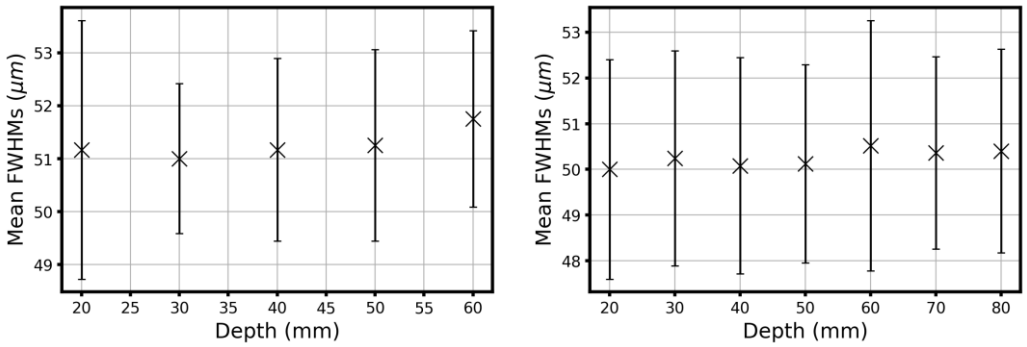

Figure 5.22: 3T-AlAl intrinsic water tank MRT mean FWHMs.
Left: 10 × 2.014 mm² field size; right: 20 × 2.014 mm² field size.

Mean FWHMs for the two field sizes at each depth are shown in Figure 5.22 and are constant for all depths and field sizes (allowing for divergence), agreeing within uncertainties of ±5 μm (10%) and ±3 μm (6%) for 10 × 2.014 mm² and 20 × 2.014 mm² fields respectively. The uncertainties are determined by one standard deviation of the mean discounting the half-peak in the 10 × 2.014 mm² field and represent the variation in individual FWHMs of the component peaks of the radiation field at each depth. A more accurate determination of the uncertainty of the mean value of all peaks at each depth would be obtained by calculation of the standard error of the mean, but this was judged unnecessary, as the mean FWHMs are very consistent with depth.

Table 5-21: MRT profile maximum and minimum FWHMs for intrinsic MBs in a water tank at each depth. (Range in parentheses.)

FWHM (μm)	20 mm	30 mm	40 mm	50 mm	60 mm	70 mm	80 mm
10 × 2.014 mm²	46—56 (10)	48—54 (6)	48—54 (6)	48—56 (8)	48—54 (6)	N/A	N/A
20 × 2.014 mm²	46—56 (10)	46—56 (10)	46—54 (8)	46—54 (8)	44—58 (14)	46—54 (8)	46—56 (10)

The maximum, minimum, and range of all FWHMs in the MRT profile at each depth for each field are tabulated in Table 5-21. The maximum difference of the ranges of FWHMs across all depths is 4 μm for the 10 × 2.014 mm² field and 6 μm for the 20 × 2.014 mm² field, which is approximately 10% of the expected mean FWHM of 51 μm. This is a good measure of the consistency of the range of FWHM values. Generally, the FWHM is greatest in the centre of the field where the direction of

travel of the synchrotron photons is normal to the opening of the slits of the MSC and smallest towards the edges of the field where the photons may not pass through unattenuated at angles greater than normal to the opening of the slit. The small range of deviation is likely because the conformal mask blocks the edges of the intrinsic 30 mm wide (Y) beam where the likelihood of attenuation due to the path of traversal of the slit is greater; which also explains why the smaller field size shows a smaller deviation than the larger.

5.5.6 FWTM results

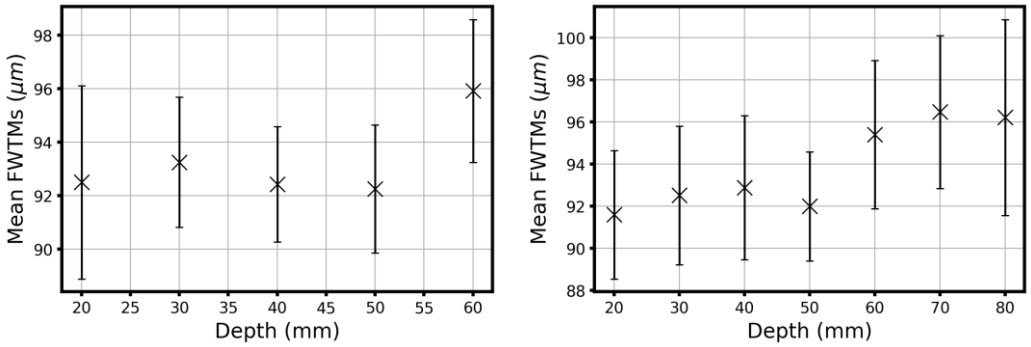

Figure 5.23: 3T-AlAl intrinsic water tank MRT FWTMs.
Left: 10 × 2.014 mm² field size; right: 20 × 2.014 mm² field size.

Mean FWTMs for the two field sizes at each depth are shown in Figure 5.23. Mean FWTMs vary from 92–96 μm for both field sizes and results at each depth agree between field sizes within 1 μm. There is a rough trend of increasing mean FWTM with increasing depth in the phantom, though 40 mm and 50 mm do not agree with this trend in the 10 × 2.014 mm² field, and 50 mm and 80 mm do not agree in the 20 × 2.014 mm² field. The uncertainties range from 2–4 μm, which corresponds to ~3% uncertainty relative to a 93 μm FWTM. As in the case of the FWHM, the uncertainties displayed represent the standard deviation of the population of FWTMs rather than the standard error of the mean. Additionally, the mean FWTM of 93 μm is 80% larger than the mean FWHM of 51 μm, which is consistent with prior intrinsic and treatment field MRT profiles.

Table 5-22: MRT profile maximum and minimum FWTMs for intrinsic MBs in a water tank at each depth. (Range in parentheses.)

FWTM (μm)	20 mm	30 mm	40 mm	50 mm	60 mm	70 mm	80 mm
10 × 2.014 mm²	86—100 (14)	88—98 (10)	88—96 (8)	88—98 (10)	92—100 (8)	N/A	N/A
20 × 2.014 mm²	84—98 (14)	86—100 (14)	86—100 (14)	86—96 (10)	90—102 (12)	90—104 (14)	86—106 (20)

The maximum, minimum, and range of all FWTM values in the MRT profile at each depth for each field are tabulated in Table 5-22. The maximum difference of the ranges of FWTMs across all depths

is 6 μm for the 10 × 2.014 mm² field and 10 μm for the 20 × 2.014 mm² field and thus the ranges are quite consistent. There is little variation in maximum or minimum values across depths and field sizes. This consistency implies that the FWTM is less dependent on MSC geometry (i.e. the angle relative to the incident beam) than the FWHM and may instead be more dependent upon the energy of scattered radiation – which governs the probability and range of scatter of photons and secondary particles.

5.5.7 Comparison to G4IMBL

G4IMBL Stage II intrinsic MRT simulations were performed under these beam conditions for both field sizes in a water phantom. A comparison of normalised peak and valley 3D-Mesa SSD measurements against the central G4IMBL peak for both field sizes is shown in Figure 5.24. In both the 10 × 10 mm² and 20 × 20 mm² fields the normalised G4IMBL peak agrees well with the 3D-Mesa SSD results at all depths within 3% uncertainty. However, in neither field size does the G4IMBL normalised valley response agree with the 3D-Mesa SSD valley measurements within uncertainty. This continues the trend found in section 5.4 that G4IMBL intrinsic valley doses do not agree with 3D-Mesa SSD measurements. Without validation of the simulation against MRT results using EBT3, EPI SSD, or the PTW microDiamond detector, it is impossible to determine if the consistent disagreement is due to the 3D-Mesa SSD incorrectly measuring the dose in the valley due to dose rate or energy dependencies, or if G4IMBL does not accurately model dose distribution within MRT valley regions.

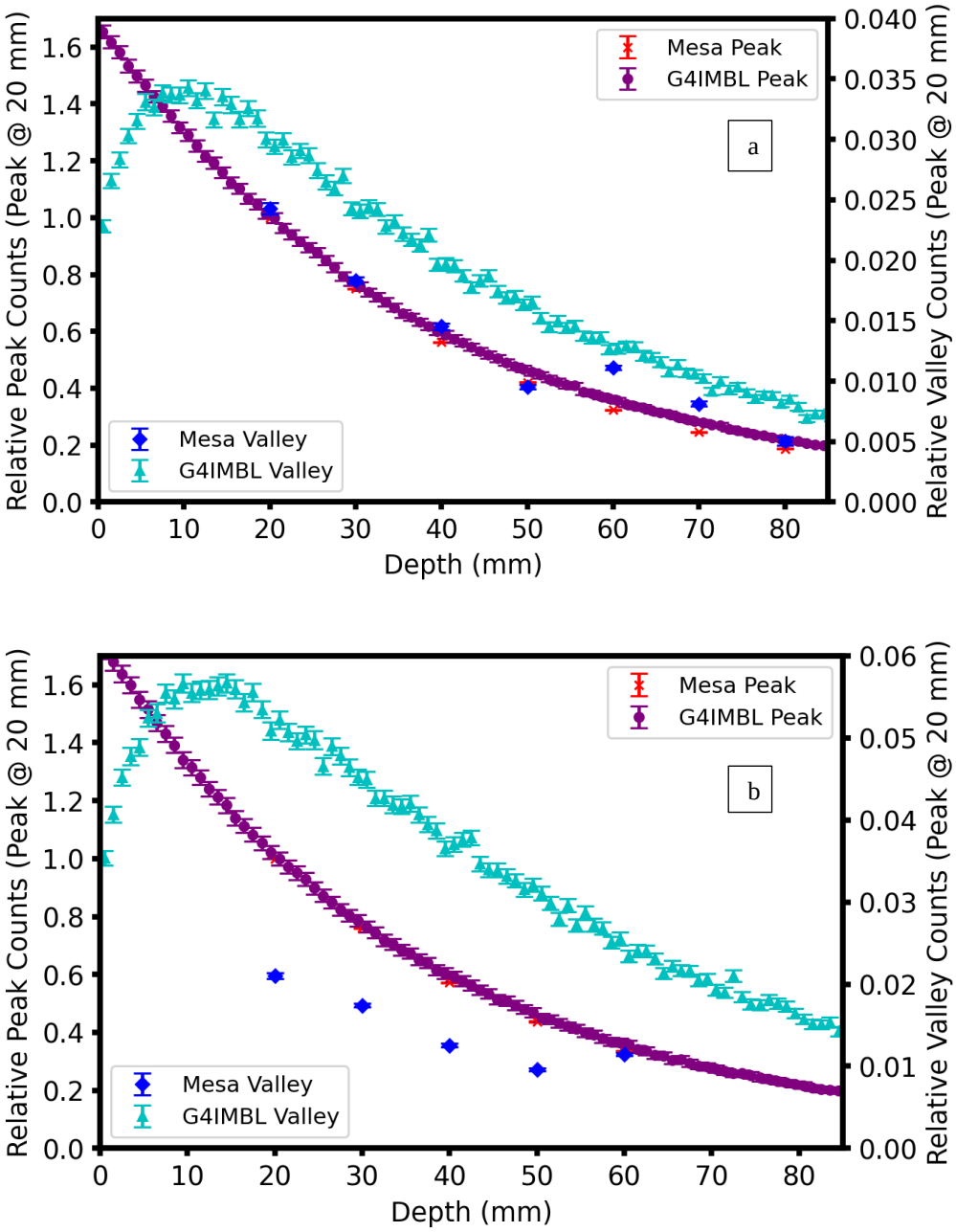

Figure 5.24: Comparison of normalised 3D-Mesa SSD peak and valley response to G4IMBL.
a) 10 × 10 mm² field; b) 20 × 20 mm² field.
Peak and valley correspond to left and right axes, respectively.

5.6 Summary of microbeam results

The 3D-Mesa SSD was used for dosimetry of treatment field and intrinsic field MBs for a variety of depths, field sizes, and energy spectra.

3D-Mesa SSD treatment field MRT scans were compared against EBT3 film and G4IMBL simulations for 1.4T-AlAl and 3.2T-CuCu MRT treatment fields and against G4IMBL simulations only for 3T-CuAl and 3T-AlAl MRT treatment fields. While PVDRs agreed between film, G4IMBL, and 3D-Mesa SSD results for 1.4T-AlAl and 3.2T-CuCu treatment fields, the

uncertainties were too large to be clinically acceptable. The 3T-CuAl PVDR is of similar magnitude to prior 3D-Mesa SSD results (~30), but does not agree with the G4IMBL PVDR within uncertainty. The 3T-AlAl PVDR is significantly different from prior results at ~12 — approximately a third of the average of prior 3D-Mesa SSD PVDRs — and also does not agree with the G4IMBL PVDR within uncertainty. This may be attributed to the different beam conditions of this configuration. Measurements were performed with a smaller beam, smaller phantom, at a different depth, and with a softer and higher intensity beam compared to prior results.

The coarse step-size of the treatment field dosimetry required a Gaussian distribution to be fitted to the data in order to determine FWHM and FWTM of the MB peaks. The parameters of the fit produced negligible uncertainties of the FWHM and FWTM and so 3D-Mesa SSD and EBT3 film FWHMs and FWTMs did not agree within uncertainty. Using a larger measure of uncertainty (such as the coarse step-size of the SNS) did allow for agreement between FWHMs and FWTMS, but these uncertainties were also too large for clinical use (~20%).

The 3D-Mesa SSD was used to investigate the properties of the intrinsic MRT profile to determine the effect of vertical alignment within the beam and the effect of depth on the dosimetric quantities of interest. It was found that all dosimetric quantities of interest of a 1.4T-AlAl MRT profile agreed within uncertainty between the centre of the beam and a position 300 μm away from the centre (25% of the beam height). This suggests that larger beams (~2 mm) may exhibit identical detector response within ±25% of the beam centre, thus allowing for easier positioning (provided that there is no excessive non-uniformity in the field). These results were then compared against experimental results at 24 mm depth and G4IMBL simulated results to examine the effect of depth on the dosimetric quantities of interest. It was determined that G4IMBL PVDR, FWHM and FWTM did not agree with 3D-Mesa SSD results at either depth within uncertainty. Without validation of results against a second dosimeter it is impossible to determine whether G4IMBL or 3D-Mesa SSD results are more correct.

A number of 3D-Mesa SSD samples of differing SV design were compared under constant field conditions (3T-CuCu MRT) to investigate the effect of the device geometry upon the electrical response. It was found that the peak and valley both increased in sensitivity as the volume of the SV increased (as expected from similar broadbeam studies) but that they did not increase at the same rate. The sensitivity of the valley increased at a slower rate than the peak, suggesting dose-rate

effects may contribute to uncertainty in the measured dose. This also effected the measurement of PVDR, where the differing rates of change of sensitivity in peak and valley resulted in PVDR variations of up to 30% (relative to the largest mean PVDR). However, FWHMs and FWTMs agreed within 5% for all samples under these beam conditions, thus providing evidence that the spatial resolution of the 3D-Mesa SSD is not particularly affected by length or shape of the SV. This is promising for larger SVs as sensitivity does not need to be sacrificed for improved spatial resolution. Therefore, it is recommended that larger 3D-Mesa SSD detectors be employed for measurements of MRT fields due to improved sensitivity — a recommendation that is consistent with BB results.

These dosimetric quantities were once again compared to G4IMBL and it was found that G4IMBL PVDRs only agreed with two of the four 3D-Mesa SSD samples, but G4IMBL FWHMs and FWTMs both fell within the range of measured 3D-Mesa SSD results.

Intrinsic MRT PDDs were acquired in a water tank phantom using the 3D-Mesa SSD for two separate field sizes and compared against G4IMBL simulations to examine the effect of field size on dosimetric quantities of interest. It was found that while G4IMBL matched the peak PDDs well, G4IMBL produced a larger overresponse in the valley PDDs with respect to 3D-Mesa SSD measurements. Based on the performance of G4IMBL in the intrinsic MRT studies it is recommended that G4IMBL not be used for comparison against intrinsic MRT valleys until the behaviour of the simulated valleys is well understood.

Further study is required at the more intense configurations at IBML, in order to verify the 3T-AlAl results of the 3D-Mesa SSD. 3T-AlAl and all 4T spectra remain areas of interest in which the 3D-Mesa SSD (with its lower sensitivity and good radiation hardness) may be expected to perform better than lower intensity configurations.

Chapter 6

Conclusion

This aim of this thesis was to develop software and instrumentation tools for use in quality assurance of Microbeam Radiation Therapy (MRT). The development of software to assist in quality assurance of MRT was accomplished by the design and benchmarkrking a Geant4 model of the Australian Synchrotron Imaging and Medical Beamline, G4IMBL, against theoretical and experimental results. The development of instrumentation tools for use in dosimetry of MRT was accomplished with the electrical and dosimetric characterisation of the novel 3D-Mesa SSD silicon detector in broadbeam and microbeam radiation fields. This chapter provides an overview of the conclusions reached regarding G4IMBL and the 3D-Mesa SSD, divided into sections below; identifies areas of interest for future investigation; then concludes with final recommendations relating to the use of G4IMBL and the 3D-Mesa SSD for synchrotron radiation dosimetry.

6.1 G4IMBL conclusions

6.1.1 Stage I studies

Stage I synchrotron radiation transport simulations allowed the study of the Geant4 model used for generation of synchrotron radiation beyond its stated limits of validity (i.e. in non-constant magnetic fields). This was accomplished by analysis of generated energy spectra that were compared to theoretical predictions as calculated using SPEC. It was found that while normalised energy spectra agreed well with theoretical spectra for a number of different beamline configurations, the non-normalised simulated spectra flux disagreed with theoretical flux by factors of ~0.5. This was determined to be the result of a preferential production of low energy (<40 keV) synchrotron radiation by the Geant4 model when compared with SPEC calculations. Further investigation is required to determine the suitability of the current Geant4 Synchrotron Radiation physics model for use in insertion devices. A recommendation is made that all PSF spectra produced by G4IMBL be used only after normalisation to the integral of the spectrum.

6.1.2 Stage II studies

Stage II energy deposition simulations within a phantom allowed the study of the change of an incident spectrum with respect to depth in a phantom, and determination of the contribution of backscattered photons to the energy spectrum close to the surface of the phantom. The mean energy

of the spectrum was found to vary with depth by up to 5 keV due to a combination of attenuation and backscatter. This demonstrates the ability of G4IMBL to examine spectral properties within a phantom, which is important for planning experiments that require targeted energies at certain depths (e.g. MRT nanotherapy enhancement) and for assessing the contribution of energy dependence to a detector response. In particular, the spectral change in MRT radiation fields between the peak and the valley are the subject of much interest to determine the difference in behaviour of energy-dependent detectors between peaks and valleys and improve confidence in MRT dosimetry. G4IMBL serves as a good scaffold to pursue this line of inquiry in future research.

Stage II energy deposition simulations also allowed the production of BB and MB PDDs that allow the simulation to be validated against experimental measurements. Proper validation allows G4IMBL to be used as a theoretical point-of-comparison for experimental measurements and eventually use in predicative or post-experimental QA. A 3T-CuCu 20 × 20 mm² treatment field was validated against EBT3 and PTW™ IC measurements. Good agreement was found within uncertainty at all depths for BB measurements and in the MB peak and valley, within uncertainty. Further validation against new beamline configurations against commercially available dosimeters and CMRP-designed EPI SSDs is underway.

Future developments of the simulation will include extension of the model to include the imaging Hutches 3A and 3B at 130 m from the source, the addition of heterogeneous phantom compatibility, and the implementation of DICOM-based functionality to allow for use of CT image files to construct patient-specific geometries.

6.2 3D-Mesa SSD conclusions

This thesis has successfully characterised and tested a novel silicon detector, the 3D-Mesa SSD, for use in MRT QA. An electron microscopy study confirmed successful fabrication and milling of the 3D-Mesa structure protruding above the SiO_2 insulating layer of the SSD. IBIC studies and sentaurus TCAD simulations identify excess unwanted charge collection under the bridge and pads at reverse bias voltages greater than 3 V. This has informed the design of next generation 3D-Mesa SSDs, will address the issue of parasitic MOS capacitance due to the bridge structure via the implantation of an “N stop” layer underneath the bridge and pads, which will likely allow a stable response at greater operating bias and thus a superior SNR.

6.2.1 Broadbeam studies

The 3D-Mesa SSD underwent a series of studies to characterise its performance in BB field conditions.

The 3D-Mesa SSD was found to meet the requirements of radiation hardness as multiple samples were exposed the >100 kGy and remained functional. Based on the results of the lifetime study it is recommended that the 3D-Mesa SSD be exposed to ~40 kGy prior to use in order to stabilise the response, with recalibration performed every 30 kGy.

The 3D-Mesa SSD was found to exhibit response linearity for in a ~100 Gy/s intrinsic radiation field. The results of this study indicate the treatment field dose rate measured by an ionisation chamber and the intrinsic field dose rate as measured by a high spatial resolution dosimeter may differ by a factor of up to 2.5. It is recommended that the distinction between intrinsic and treatment field dose rates must be acknowledged when performing dosimetry of large fields where the contribution of scatter to the treatment field dose rate is comparable to the contribution from the intrinsic beam. These results show that the 3D-Mesa SSD and X-Tream data acquisition system allow for deep understanding of the structure of the synchrotron radiation field.

The 3D-Mesa SSD was found to exhibit energy dependence in a monoenergetic response study. This was expected due to the known over-response of Si compared to water at low energies as explained by the ratio of mass energy absorption coefficients. The results of a limited number of samples showed that the energy dependence at ~30 keV was better than predicted (a factor of ~3 as opposed to a factor of 6). Further investigation is needed to characterise energy dependence of the full range of fabrication options of the 3D-Mesa SSS, and will be the subject of future studies on the next generation of 3D-Mesa SSDs.

The 3D-Mesa SSD was used to perform BB PDDs for a number of field sizes and beamline configurations and was compared against G4IMBL, PinPoint™ IC, microDiamond, EPI SSD, EBT3, and HDV2 results. The 3D-Mesa SSD generally had good agreement within 10% uncertainty with commercial dosimeters between 10 mm and 50 mm depth in RMI457 Solid Water and water tank phantoms. Particularly good agreement with PinPoint™ IC measurements was found for 2T-CuAl in a RMI457 phantom, and small fields for 3T-CuCu and 3T-CuAl in a water tank phantom.

As a result of comparison of G4IMBL against commercial dosimeters, G4IMBL may be considered to be preliminarily validated for BB PDDS of certain field sizes of 1.4T-AlAl, 2T-CuAl, 3T-CuCu,

and 3T-CuAl beamline configurations. The validation of G4IMBL and the 3D-Mesa SSD against higher dose-rate configurations (e.g. 4.0 T wiggler) will pave the way for the use of G4IMBL and the next generation of 3D-Mesa SSD in BB QA dosimetry at the AS IMBL.

6.2.2 Microbeam studies

Following the successful completion of synchrotron BB studies, the 3D-Mesa SSD undertook a series of MRT studies to evaluate the device performance with respect to MRT dosimetry.

A study was performed to acquire treatment field lateral dose profiles using the SNS method and 3D-Mesa SSD results were compared to EBT3 film and G4IMBL measurements.

3D-Mesa SSD measurements were compared against G4IMBL simulations for 3T-CuAl and 3T-AlAl configurations, but no EBT3 film results exist under the same conditions to allow for comparison to another experimental dosimeter. Next generation thin epitaxial silicon detectors were exposed under these conditions and may be used as an extra point of experimental comparison. However, those results are the subject of a separate CMRP PhD thesis and so are not able to be referred to until publication. Instead, 3D-Mesa SSD results were compared only against G4IMBL simulations. G4IMBL simulations agreed with 3D-Mesa SSD treatment field FWHMs but not with PVDRs or FWTMs within uncertainty.

Intrinisc MB studies were performed to assess the effect of 3D-Mesa SSD design architecture of six unique samples upon the response under identical conditions. It was found that FWHMs and FWTMs show no particular volume dependence, though the peak and valley response (and thus PVDR) do show some volume dependence. Without comparison to another dosimeter it is impossible to determine the most suitable 3D-Mesa SSD design to measure the most accurate PVDRs. These results were compared with G4IMBL simulations, but the simulated PVDR agreed with 3D-Mesa SSD PVDRs in two of the six cases.

An intrinsic MB depth-dose study was performed for two separate field sizes and compared with G4IMBL to examine the effect of treatment field width against peak and valley response. It was found that G4IMBL agreed well with normalised peak PDDs but significantly over responded compared to 3D-Mesa SSD valley measurements.

The results of the microbeam studies indicate that more investigation into the simulation of valley doses by G4IMBL is necessary before it may be used for MRT treatment planning or verification.

6.3 Final recommendations

It is believed that, with further development to address the issue of excess charge collection under the bridge and pads, the next generation of 3D-Mesa SSDs should become an excellent candidate for MRT QA worldwide.

G4IMBL has performed very well in simulating BB PDDs and MB peak PDDs, though further work is required for the validation of MB valley simulations. It serves as a good proof-of-concept for simulated treatment planning and verification and may be used as a scaffold to create Monte Carlo models of other beamlines for benchmarking of future treatment planning systems.

List of References

[1] Australian Institute of Health and Welfare, “Cancer in Australia 2019,” *Cancer Ser.* , vol. 119, no. CAN 123, 2019.

[2] M. B. Barton *et al.*, “Estimating the demand for radiotherapy from the evidence: A review of changes from 2003 to 2012,” *Radiother. Oncol.*, vol. 112, pp. 140–144, 2014.

[3] T. Mitin and A. L. Zietman, “Promise and pitfalls of heavy-particles therapy,” *Journal of Clinical Oncology*, vol. 32, no. 26. American Society of Clinical Oncology, pp. 2855–2863, 10-Sep-2014.

[4] J. D. Jackson, *Classical Electrodynamics*, Second. Wiley, 1975.

[5] H. Winick, “Synchrotron radiation sources a primer,” *Ser. Synchrot. Radiat. Tech. Appl.*, vol. 1, 1994.

[6] K.-J. Kim, “Characteristics of Synchrotron Radiation,” in *X-ray Data Booklet.*, 2nd ed., A. C. Thompson and D. Vaughan, Eds. Lawrence Berkeley National Laboratory, 2001, p. 16.

[7] E. Bräuer-Krisch *et al.*, “Effects of pulsed, spatially fractionated, microscopic synchrotron X-ray beams on normal and tumoral brain tissue,” *Mutat. Res. - Rev. Mutat. Res.*, vol. 704, no. 1–3, pp. 160–166, 2010.

[8] W. Zeman, H. J. Curtis, and C. P. Baker, “Histopathologic Effect of High-Energy-Particle Microbeams on the Visual Cortex of the Mouse Brain,” *Radiat. Res.*, vol. 15, no. 4, pp. 496–514, 1961.

[9] A. Bravin, P. Olko, E. Schültke, and J. J. Wilkens, “SYRA3 COST Action - Microbeam radiation therapy: Roots and prospects,” *Phys. Medica*, vol. 31, no. 6, pp. 561–563, 2015.

[10] M. De Felici, R. Felici, M. S. Del Rio, C. Ferrero, T. Bacarian, and F. A. Dilmanian, “Dose distribution from x-ray microbeam arrays applied to radiation therapy: An EGS4 Monte Carlo study,” *Med. Phys.*, vol. 32, no. 8, pp. 2455–2463, 2005.

[11] J. Livingstone, A. W. Stevenson, D. J. Butler, D. Häusermann, and J. F. Adam, “Characterization of a synthetic single crystal diamond detector for dosimetry in spatially fractionated synchrotron x-ray fields,” *Med. Phys.*, vol. 43, no. 7, pp. 4283–4293, 2016.

[12] J. C. Crosbie, I. Svalbe, S. M. Midgley, N. Yagi, P. A. W. Rogers, and R. A. Lewis, “A method of dosimetry for synchrotron microbeam radiation therapy using radiochromic films of different sensitivity,” *Phys. Med. Biol.*, vol. 53, no. 23, pp. 6861–6877, 2008.

[13] M. A. Grotzer, E. Schültke, E. Bräuer-Krisch, and J. A. Laissue, “Microbeam radiation therapy: Clinical perspectives,” *Phys. Medica*, vol. 31, no. 6, pp. 564–567, 2015.

[14] C. Fernandez-Palomo *et al.*, “Use of synchrotron medical microbeam irradiation to investigate radiation-induced bystander and abscopal effects in vivo,” *Phys. Medica*, vol. 31, no. 6, pp. 584–595, 2015.

[15] E. Bräuer-Krisch *et al.*, “Potential high resolution dosimeters for MRT,” in *AIP Conference Proceedings*, 2010, vol. 1266, pp. 89–97.

[16] A. Dipuglia *et al.*, “Validation of a Monte Carlo simulation for Microbeam Radiation Therapy on the Imaging and Medical Beamline at the Australian Synchrotron,” *Sci. Rep.*, vol. 9, 2019.

[17] J. Archer *et al.*, “X-ray microbeam measurements with a high resolution scintillator fibre-optic dosimeter,” *Sci. Rep.*, vol. 7, no. 1, pp. 1–7, 2017.

[18] J. Archer *et al.*, “Synchrotron X-ray microbeam dosimetry with a 20 micrometre resolution scintillator fibre-optic dosimeter,” *J. Synchrotron Radiat.*, vol. 25, no. 3, pp. 826–832, 2018.

[19] A. B. Rosenfeld *et al.*, “Edge-on Face-to-Face MOSFET for synchrotron microbeam dosimetry: MC modeling,” *IEEE Trans. Nucl. Sci.*, vol. 52, no. 6, pp. 2562–2569, 2005.

[20] J. Kalliopuska, A. Cullen, M. Lerch, M. Petasecca, M. Santala, and A. Rosenfeld, “Evaluation of a thin microstrip detector for high spatial resolution dosimetry,” *Radiat. Meas.*, vol. 46, no. 12, pp. 1643–1645, 2011.

[21] M. Petasecca *et al.*, “X-tream: A novel dosimetry system for synchrotron microbeam radiation therapy,” *J. Instrum.*, vol. 7, no. 7, pp. 1–15, 2012.

[22] M. L. F. Lerch *et al.*, “Dosimetry of intensive synchrotron microbeams,” *Radiat. Meas.*, vol. 46, no. 12, pp. 1560–1565, 2011.

[23] M. L. F. Lerch *et al.*, “New 3D Silicon detectors for dosimetry in Microbeam Radiation Therapy,” *J. Phys. Conf. Ser.*, vol. 777, no. 1, p. 012009, 2017.

[24] P. Fournier *et al.*, “X-Tream dosimetry of highly brilliant X-ray microbeams in the MRT hutch of the Australian Synchrotron,” *Radiat. Meas.*, vol. 106, pp. 405–411, 2017.

[25] L. T. Tran *et al.*, “3D-mesa ‘bridge’ silicon microdosimeter: Charge collection study and application to rbe studies in 12rm c radiation therapy,” *IEEE Trans. Nucl. Sci.*, vol. 62, no. 2, pp. 504–511, 2015.

[26] J. Livingstone *et al.*, “Charge collection in n-SOI planar microdosimeters,” *IEEE Trans. Nucl. Sci.*, vol. 60, no. 6, pp. 4289–4296, 2013.

[27] A. J. Cullen, “A real time solid state dosimetry system for QA in synchrotron x-A real time solid state dosimetry system for QA in synchrotron x-ray microbeam radiosurgery ray microbeam radiosurgery,” 2017.

[28] Synopsys Inc, “TCAD - Technology Computer Aided Design.” Synopsys Inc., 2019.

[29] S. Agostinelli *et al.*, “GEANT4 - A simulation toolkit,” *Nucl. Instruments Methods Phys. Res. Sect. A Accel. Spectrometers, Detect. Assoc. Equip.*, vol. 506, no. 3, pp. 250–303, 2003.

[30] J. Allison *et al.*, “Recent developments in GEANT4,” *Nucl. Instruments Methods Phys. Res. Sect. A Accel. Spectrometers, Detect. Assoc. Equip.*, vol. 835, pp. 186–225, 2016.

[31] I. Cornelius *et al.*, “Benchmarking and validation of a Geant4-SHADOW Monte Carlo simulation for dose calculations in microbeam radiation therapy,” *J. Synchrotron Radiat.*, vol. 21, no. 3, pp. 518–528, 2014.

[32] M. Sanchez Del Rio, N. Canestrari, F. Jiang, and F. Cerrina, “SHADOW3: A new version of the synchrotron X-ray optics modelling package,” *J. Synchrotron Radiat.*, vol. 18, no. 5, pp. 708–716, 2011.

[33] J. Baro, J. Sempau, J. M. Fernandez-Varea, and F. Salvat, “PENELOPE: An algorithm for Monte Carlo simulation of the penetration and energy loss of electrons and positrons in matter,” 1995.

[34] I. Martínez-Rovira, J. Sempau, and Y. Prezado, “Development and commissioning of a Monte Carlo photon beam model for the forthcoming clinical trials in microbeam radiation therapy,”

Med. Phys., vol. 39, no. 1, pp. 119–131, 2012.

[35] A. W. Stevenson, J. C. Crosbie, C. J. Hall, D. Häusermann, J. Livingstone, and J. E. Lye, "Quantitative characterization of the X-ray beam at the Australian Synchrotron Imaging and Medical Beamline (IMBL)," *J. Synchrotron Radiat.*, vol. 24, no. 1, pp. 110–141, 2017.

[36] E. Bräuer-Krisch *et al.*, "New technology enables high precision multislit collimators for microbeam radiation therapy," *Rev. Sci. Instrum.*, vol. 80, no. 7, p. 074301, Jul. 2009.

[37] V. Ivanchenko *et al.*, "Recent Improvements in Geant4 Electromagnetic Physics Models and Interfaces," 2011.

[38] G. A. P. Cirrone, G. Cuttone, F. Di Rosa, L. Pandola, F. Romano, and Q. Zhang, "Validation of the Geant4 electromagnetic photon cross-sections for elements and compounds," *Nucl. Inst. Methods Phys. Res. A*, vol. 618, pp. 315–322, 2010.

[39] K. Amako *et al.*, "Validation of Geant4 electromagnetic physics versus protocol data," *2004 IIEEE Nucl. Sci. Symp. Med. Imaging Conf.*, vol. 4, pp. 1–5, 2004.

[40] Geant4 Collaboration, "Physics Reference Manual." 2017.

[41] H. Burkhardt, "Monte Carlo generation of the energy spectrum of synchrotron radiation." EUROTeV Report 018, Geneva, 2007.

[42] M. J. Cameron *et al.*, "Characterisation of 3D-Mesa silicon single strip detectors for use in synchrotron microbeam radiation therapy," *IEEE Trans. Radiat. Plasma Med. Sci.*, pp. 1–1, Oct. 2019.

[43] C. J. Kenney *et al.*, "Active-edge planar radiation sensors," *Nucl. Instruments Methods Phys. Res. Sect. A Accel. Spectrometers, Detect. Assoc. Equip.*, vol. 565, no. 1, pp. 272–277, 2006.

[44] J. Kalliopuska, S. Eränen, and T. Virolainen, "Alternative fabrication process for edgeless detectors on 6 in. wafers," *Nucl. Instruments Methods Phys. Res. Sect. A Accel. Spectrometers, Detect. Assoc. Equip.*, vol. 633, no. SUPPL. 1, pp. S50–S54, 2011.

[45] JEOL, "High Performance SEM for Nanoscience." JEOL Ltd., Tokyo, pp. 1–20, 2007.

[46] Boonton Electronics Corporation, "Model 7200 Capacitance Meter Instruction Manual." Boonton Electronics Corporation, Parsippany, New Jersey, 1996.

[47] R. Siegele, D. D. Cohen, and N. Dytlewski, "The ANSTO high energy heavy ion microprobe," *Nucl. Instruments Methods Phys. Res. Sect. B Beam Interact. with Mater. Atoms*, vol. 158, no. 1–4, pp. 31–38, 1999.

[48] J. F. Ziegler, M. D. Ziegler, and J. P. Biersack, "SRIM - The stopping and range of ions in matter (2010)," *Nucl. Instruments Methods Phys. Res. Sect. B Beam Interact. with Mater. Atoms*, vol. 268, no. 11–12, pp. 1818–1823, 2010.

[49] M. B. H. Breese, "A theory of ion beam induced charge collection," *J. Appl. Phys.*, vol. 74, no. 6, pp. 3789–3799, 1993.

[50] J. D. Hunter, "Matplotlib: A 2D graphics environment," *Comput. Sci. Eng.*, vol. 9, no. 3, pp. 99–104, 2007.

[51] G. Masetti, M. Severi, and S. Solmi, "Modeling of Carrier Mobility Against Carrier Concentration in Arsenic-, Phosphorus-, and Boron-Doped Silicon," *IEEE Trans. Electron Devices*, vol. 30, no. 7, pp. 764–769, Jul. 1983.

[52] C. Canali, G. Majni, R. Minder, and G. Ottaviani, “Electron and Hole Drift Velocity Measurements in Silicon and Their Empirical Relation to Electric Field and Temperature,” *IEEE Trans. Electron Devices*, vol. 22, no. 11, pp. 1045–1047, Nov. 1975.

[53] C. Lombardi, S. Manzini, A. Saporito, and M. Vanzi, “A Physically Based Mobility Model for Numerical Simulation of Nonplanar Devices,” *IEEE Trans. Comput. Des. Integr. Circuits Syst.*, vol. 7, no. 11, pp. 1164–1171, 1988.

[54] M. N. Darwish, J. L. Lentz, M. R. Pinto, P. M. Zeitzoff, T. J. Krutsick, and H. H. Vuong, “An improved electron and hole mobility model for general purpose device simulation,” *IEEE Trans. Electron Devices*, vol. 44, no. 9, pp. 1529–1538, 1997.

[55] D. J. Roulston, N. D. Arora, and S. G. Chamberlain, “Modeling and Measurement of Minority-Carrier Lifetime versus Doping in Diffused Layers of n +-p Silicon Diodes,” *IEEE Trans. Electron Devices*, vol. 29, no. 2, pp. 284–291, 1982.

[56] J. G. Fossum, “Computer-aided numerical analysis of silicon solar cells,” *Solid State Electron.*, vol. 19, no. 4, pp. 269–277, 1976.

[57] J. G. Fossum and D. S. Lee, “A physical model for the dependence of carrier lifetime on doping density in nondegenerate silicon,” *Solid State Electron.*, vol. 25, no. 8, pp. 741–747, 1982.

[58] J. G. Fossum, R. P. Mertens, D. S. Lee, and J. F. Nijs, “Carrier recombination and lifetime in highly doped silicon,” *Solid State Electron.*, vol. 26, no. 6, pp. 569–576, 1983.

[59] L. Huldt, N. G. Nilsson, and K. G. Svantesson, “The temperature dependence of band-to-band Auger recombination in silicon,” *Appl. Phys. Lett.*, vol. 35, no. 10, pp. 776–777, 1979.

[60] W. Lochmann and A. Haug, “Phonon-assisted Auger recombination in Si with direct calculation of the overlap integrals,” *Solid State Commun.*, vol. 35, no. 7, pp. 553–556, 1980.

[61] H. S. Bennett and C. L. Wilson, “Statistical comparisons of data on band-gap narrowing in heavily doped silicon: Electrical and optical measurements,” *J. Appl. Phys.*, vol. 55, no. 10, pp. 3582–3587, 1984.

[62] A. H. Aldosari *et al.*, “Characterization of an innovative p-type epitaxial diode for dosimetry in modern external beam radiotherapy,” *IEEE Trans. Nucl. Sci.*, vol. 60, no. 6, pp. 4705–4712, 2013.

[63] Y. Prezado *et al.*, “Dosimetry protocol for the forthcoming clinical trials in synchrotron stereotactic radiation therapy (SSRT),” *Med. Phys.*, vol. 38, no. 3, pp. 1709–1717, Mar. 2011.

[64] IAEA, “IAEA TRS 398: Dosimetry and Medical Radiation Physics Section,” vol. 2006, no. June, 2006.

[65] P. Fournier *et al.*, “Absorbed dose-to-water protocol applied to synchrotron-generated x-rays at very high dose rates,” *Phys. Med. Biol.*, vol. 61, no. 14, pp. N349–N361, 2016.

[66] J. H. Hubbell and S. M. Seltzer, “NIST: X-Ray Mass Attenuation Coefficients,” *Physical Reference Data*, 1996. [Online]. Available: https://www.nist.gov/pml/x-ray-mass-attenuation-coefficients. [Accessed: 30-Aug-2019].

[67] A. W. Stevenson *et al.*, “Analysis and interpretation of the first monochromatic X-ray tomography data collected at the Australian synchrotron imaging and medical beamline,” *J. Synchrotron Radiat.*, vol. 19, no. 5, pp. 728–750, 2012.

[68] D. J. Butler, “Private Communication.” 2019.

[69] International Commission on Radiation Units and Measurements, “Determination of Absorbed Dose in a Patient Irradiated by Beams of X or Gamma rays in Radiotherapy Procedures,” vol. 34. Bethesda, MD, 1976.